Electrode Engineering of Metal-Oxide-Based Materials for Optimized Lithium-ion Batteries

---

Dissertation

zur Erlangung des Grades

des Doktors der Naturwissenschaften

der Naturwissenschaftlich-Technischen Fakultät

der Universität des Saarlandes

vorgelegt von

M.Sc. Amir Haghipour

Aus Dezful, Iran

Saarbrücken, September 2024

Tag des Kolloquiums: 27.01.2025

Dekan: Prof. Dr.-Ing. Dirk Bähre

Berichterstatter: Prof. Dr. Volker Presser, Priv.-Doz. Dr.-Ing. Guido Falk, Prof. Dr.-Ing. Ralf Moos Akad

Akad. Mitglied: Dr. Yazdan Rashidi

Vorsitz: Prof. Dr. Tobias Kraus

ACKNOWLEDGEMENTS

I would like to express my sincere gratitude to all those who supported me in the preparation of this doctoral thesis, offering invaluable advice and assistance:

First and foremost, I extend my heartfelt gratitude to my supervisor and doctoral advisor, Prof. Dr. Volker Presser, for granting me the opportunity to undertake this compelling doctoral project within the Research Department „Energy Materials" Group at INM - Leibniz Institute for New Materials. His patience, guidance, and encouragement have been instrumental in my achievements over the past three years. These accomplishments include publications and the privilege to participate in prestigious international conferences. Thank you, Prof. Presser!

I also thank Prof. Dr. Falk from Saarland University for serving as my scientific advisor during my PhD. I have immensely appreciated his valuable scientific discussions, advice during our meetings, and preparation for the second review of this thesis.

During my time at the INM, I worked with many wonderful and helpful people who always supported me in my endeavors. Many thanks go to: Dr. Stefanie Arnold, Dr. Lisa Beran, Dr. Behnoosh Bornamehr, Peter Burger, Dr. Samantha Husmann, Yunjie Li, Thi Thao Le, Prof. Dr. Tobias Kraus, Cansu Kök, Dr. Mingren Liu, Chiraz Layouni, Dr. Kaitlyn Prenger, Anna Quinten, Panyu Ren, Dr. Amr Radwan, Jean Gustavo de Andrade Ruthes, Dominik Sebastian Schmidt, Dr. Sarah Saleem, Dr. Gracita Tomboc, Dr. Delvina Japhet Tarimo, Dr. Mohammad Torkamanzadeh, Dr. Qingsong Wang, Dr. Tamara Winter, Liying Xue, Dr. Emmanuel Pameté Yambou, and Dr. Yuan Zhang for your endless support, the many scientific discussions and the wonderful time outside the INM.

Many thanks to the great technical and analytical help of Dr. Mesut Aslan, Mr. Robert Drumm Zeyu Fu, Dr. Ingrid Grobelsek, Andrea Jung, Dr. Karsten Moh, and all members of the workshop.

We acknowledge funding of the DigiBatMat (03XP0367A) within the competence cluster for battery cell production (ProZell) by the Federal Ministry of Education and Research (Bundesministerium für Bildung und Forschung).

I extend my heartfelt gratitude to my esteemed cooperation partners beyond INM for their friendly and active support in my research Prof. Dr. Volker Knoblauch, Junior Professor Dr. Lola González-García, Dr. Hitoshi Nakamura, and Jonas Oehm Their insightful discussions and constructive feedback have significantly broadened my perspective in the field of science.

Lastly, I am profoundly grateful to my friends and family outside INM and Saarland University for their unwavering personal support and motivation throughout my doctoral journey.

TABLE OF CONTENTS

ZUSAMMENFASSUNG

Diese Dissertation befasst sich mit den Fortschritten bei der Entwicklung und Herstellung von Lithium-Ionen-Batterien (LIB), wobei der Schwerpunkt auf Materialien auf Metalloxidbasis und Techniken zur Verbesserung ihrer Leistung liegt. Es werden die Verfahren zur Steigerung der Effizienz und der Umweltfreundlichkeit erörtert. Das Hauptziel besteht darin, die Herausforderungen von Metalloxidelektroden in LIBs anzugehen, insbesondere die Kapazitätsverschlechterung bei hohen Lade-/Entladeraten und die Erweiterung ihres Betriebsspannungsbereichs. Wir sind zuversichtlich, dass wir die Eigenschaften dieser Elektroden durch Präparationsmethoden verbessern können. Unsere Forschung untersucht, wie verschiedene Mischtechniken und Variablen die Leistung und Haltbarkeit dieser Elektroden verbessern können. Darüber hinaus beschreibt diese Arbeit unsere Bemühungen, den Herstellungsprozess von Batterien zu digitalisieren, indem wir die DigiBatMat-Plattform einführen, eine Plattform für Batteriematerialien und Herstellungsprozesse. DigiBatMat treibt den Fortschritt in der Batterietechnologie voran, indem es die LIBs durch Datenerfassung und -analyse optimiert, was seine entscheidende Rolle in diesem Bereich hervorhebt. Letztendlich bietet diese Arbeit Einblicke in die Batterieelektrodenentwicklung und unterstützt Initiativen zur Verbesserung von Energiespeichertechnologien und zur Förderung von Nachhaltigkeitsbestrebungen.

ABSTRACT

This dissertation explores the advancements in the design and manufacturing of lithium-ion batteries (LIB), with a focus on metal oxide-based materials and techniques used to enhance their performance. It discusses the processes to boost efficiency and environmental friendliness. The primary goal is to address the challenges of metal oxide electrodes in LIBs, particularly capacity degradation at high charge/discharge rates and expanding their operating voltage range. We are confident in our ability to enhance the characteristics of these electrodes through preparation methods. Our research investigates how different mixing techniques and variables can improve the performance and durability of these electrodes. Furthermore, this thesis describes our efforts to digitize the battery manufacturing process by introducing the DigiBatMat platform, a platform for battery materials and manufacturing processes. DigiBatMat drives advancements in battery technology by optimizing LIBs through data gathering and analysis, highlighting its crucial role in this field. Ultimately, this thesis provides insights into battery electrode engineering and supports initiatives to improve energy storage technologies and advance sustainability efforts.

1. INTRODUCTION AND MOTIVATION

In recent years, there has been an increase in the focus on energy storage, driven by government goals and regulations. The growing electricity demand fueled by living standards and population growth makes necessary advancements in energy storage solutions. In 2023, approximately 272.4 TWh of electricity was produced from solar, wind, hydro, and biomass, making up 52% of electricity generation. The expanding electricity usage across sectors highlights the importance of power sources that can operate independently of factors such as darkness or low wind speeds.[1]

The reliance on energy sources influenced by conditions emphasizes the significance of effective energy storage systems. These systems play a role in ensuring an energy supply under different weather conditions at any given moment. Energy storage technologies extend across mechanical, electrical, and electrochemical methods, which stand as the most prominent global energy storage technology after thermal storage.

Electrochemical storage involves batteries where electrical charge carriers are stored and released through reduction and oxidation processes at electrodes connected to an electrolyte. Since its introduction in the 1970s and availability, in 1991 lithium-ion batteries (LIBs) technology has increasingly emerged as an energy storage solution. The current materials used in these types of batteries, such as lithium oxide (LMO) and lithium iron phosphate (LFP) for cathodes, along with lithium titanate (LTO) for anodes, work based on the concept of lithium ions entering the host structure.[2]

LIBs are recognized for their energy density and power performance. Ongoing research efforts are continuously improving its functionalities. Over the years, the specific energy storage capacity (watt-hours per kilogram) of existing systems has nearly tripled. However, challenges remain due to the dependence on materials like cobalt, found in LIB electrodes sourced from sensitive areas, raising environmental concerns.[3]

Additionally, the increasing costs of lithium reserves highlight the necessity to explore energy storage solutions beyond lithium. This study focuses on enhancing electrodes in metal oxide-based LIBs to enhance their efficiency and sustainability. The research emphasizes refining manufacturing processes to enable the development of energy storage alternatives. The ultimate goal is to enhance capabilities and support the transition, towards energy sources.

2. THEORETICAL BACKGROUND

Historically, the first energy sources converted into electricity and used by humankind were coal, oil, and natural gas.[4-6] The world's current economic and social development is impossible without fossil fuels.[4, 5, 7] The destructive effects of using fossil fuels, such as the carbon dioxide produced during this process, have become a plague on our society today.[4, 7] However, fossil fuels still dominate the world's energy supply with more than 84.7%.[4, 7-10] With the development and advancement of new technologies, the need for sustainable energy sources is increasing.

However, global warming caused by using fossil fuels in 2023 broke a new record and became the warmest year in 174 years.[11] Scientists, industries, politicians, and global efforts have shifted to environment-friendly energies to estimate the ever-increasing need.[12] In this regard, renewable energy storage systems can suit this need.[13] As shown in **Figure 1**, energy storage systems can be divided into five categories based on the leading applications.[4, 14] The electrochemical and electric storage technologies are usually sustainable for quickly storing and consuming large-scale energy sources.[4, 14] Mechanical, thermal, and chemical storage technologies are usually used for minor purposes and extended periods (hours to days, depending on the term).[4, 14]

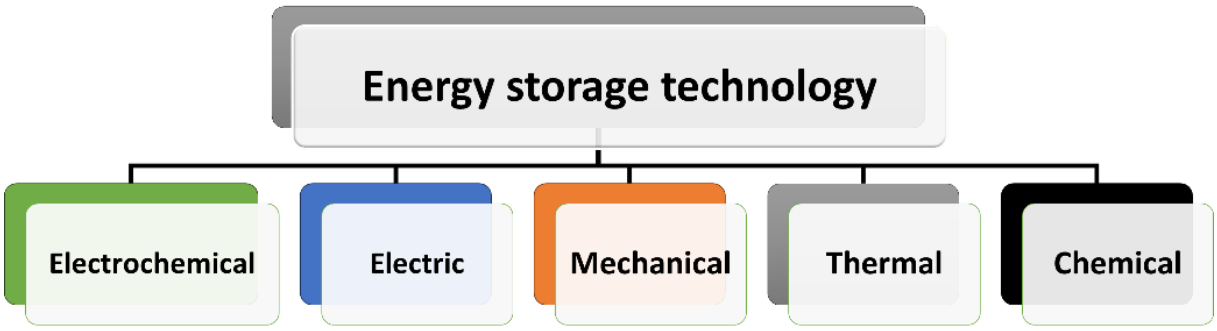

Figure 1. Classification of energy storage technologies (adapted from Ref.[4]).

2.1. Electrochemical Energy Storage (EES)

Electrochemical energy storage stands as one of the forms of energy storage technology that remains widely utilized today, with a history that spans over two centuries. We can categorize the EES technologies into supercapacitors, batteries, and hybrids, as depicted in **Figure 2**.[15] These systems have garnered interest owing to their qualities, such as abundant raw materials availability, robust safety measures, long-lasting durability, and efficient performance.[8, 15, 16] They serve as power sources. Support various grid applications.[8, 15, 16] **Figure 3** presents a

Ragone plot comparing the energy and power characteristics of energy storage devices with fuel cells.[15, 17-19] The plot illustrates the energy and power densities of these devices and their conversion efficiencies via fuel cells.[20-22] It is also widely used to evaluate the performance of energy storage materials like anodes and cathodes.[15, 17-19]

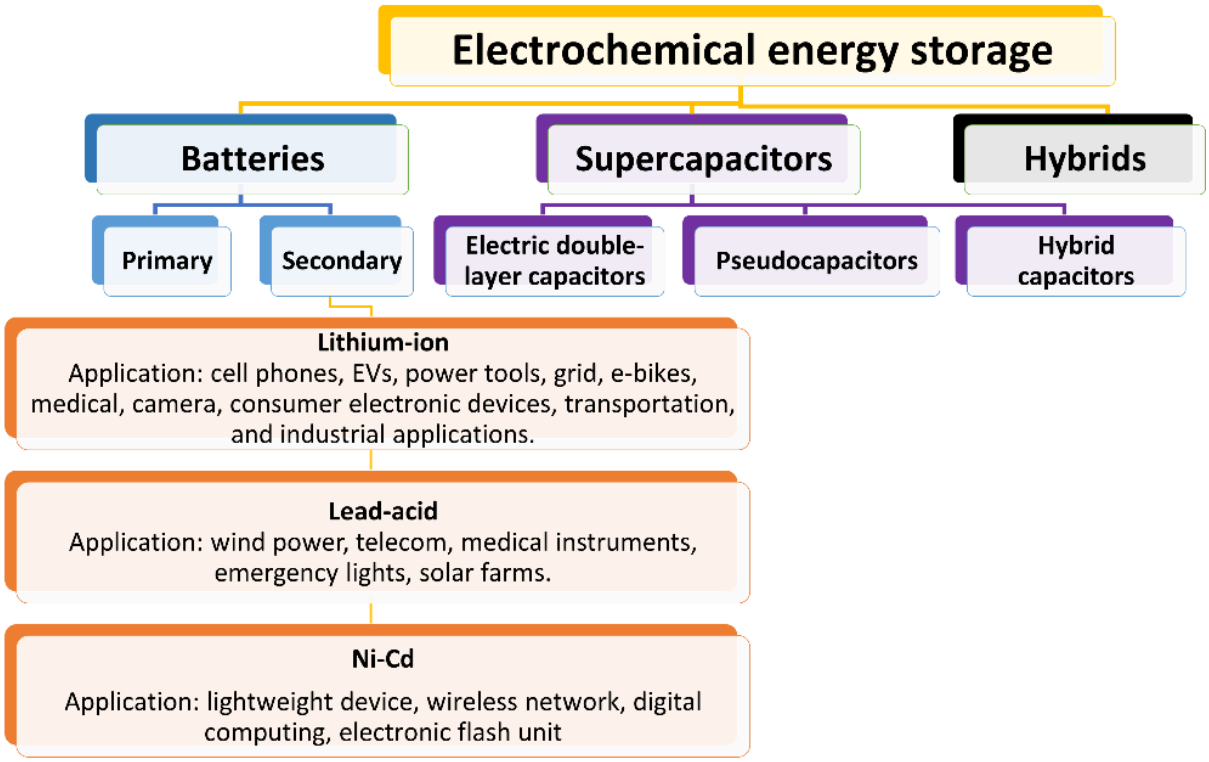

Figure 2. Classification of electrochemical energy storage technologies (adapted from Ref.[16, 23, 24]). In this figure, three very specific chemistry systems have been randomly shown for secondary batteries.

The Ragone plot typically normalizes energy and power by either mass or volume to facilitate direct comparisons across different types of energy storage systems.[25] When normalized by mass, the resulting metrics are specific energy and specific power.[25] Alternatively, when normalized by volume, the metrics become energy density and power density.[25] In this graph, logarithmic values are used for both axes, which allows the performance of different devices to be compared. **Equation 1** and **Equation 2** were used to calculate specific energy and specific power, respectively, where (V) is the nominal battery voltage, (I) represents electric current, (t) is the unit of time in seconds, and (m) is the mass of the active material in kilograms.[26, 27]

$$\boldsymbol{Specific\ Energy} = \frac{\boldsymbol{VIt}}{\boldsymbol{m}} \qquad \textbf{Equation 1}$$

$$\boldsymbol{Specific\ Power} = \frac{\boldsymbol{VI}}{\boldsymbol{m}} \qquad \textbf{Equation 2}$$

In the Ragone plot, the specific power (W kg^{-1}) is plotted against the energy (kW kg^{-1}).[28] Typically, logarithmic units are used for the horizontal axes, allowing for an evaluation of

various devices.[28] This plotting method was first introduced by D. V. Ragone in 1968 to compare vehicle battery systems.[29] As shown in **Figure 3**, the horizontal axis represents energy, while the vertical axis indicates the rate at which energy can be delivered.[29] Capacitors exhibit power compared to other devices, enabling rapid charging and discharging within fractions of a second.[30] On the contrary, batteries with energy storage capacity require time for charging and discharging processes.[30] Combining these materials is possible and often suitable Considering the growing need for batteries with high energy and power simultaneously.[17-19] In response to the increasing demand for batteries, with energy and power capabilities simultaneously, researchers have explored materials to develop innovative devices that can occupy the upper left quadrant of the Ragone plot.[15, 17-19]

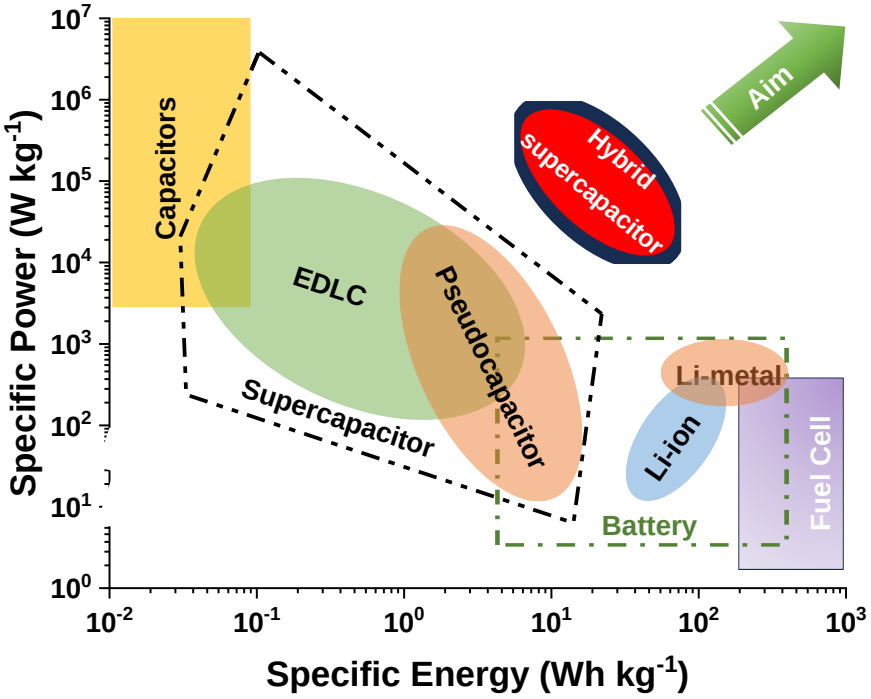

Figure 3. Ragone plot for various electrochemical energy storage devices' energy and power performance metrics (adapted from Ref.[20-22]).

Hence, scientists have explored approaches, including merging two energy storage systems, like gadgets that integrate battery and supercapacitor components.[15, 17-19, 31, 32] To enhance comprehension of batteries, supercapacitors, and hybrid devices, a concise overview of these energy storage system categories will be provided.

2.2. Batteries

Batteries are EES devices that store energy and are used in different applications, sizes, and shapes.[16, 33, 34] In today's sense, the term battery became popular by Benjamin Franklin in 1748.[16, 34] The Battery market is expected to reach over 400 billion dollars by 2030.[35] The widespread use of research batteries in this field has encouraged research on various materials to produce more economical and environmentally friendly batteries with higher efficiency.[35] A battery consists of one or more cells that generate an electric current through chemical reactions, effectively storing energy in a chemical form.[16] This process typically occurs when two different electrodes (metal or metal compounds) are submerged in an electrolyte capable of transporting ions.[16, 36] Within the system, electrons transfer from one electrode to another. Redox reactions are employed in the battery system for energy storage purposes.[16, 36, 37]

In this process, one electrode takes electrons and becomes negatively charged, while the other releases electrons and becomes positively charged.[36-38] This sets up a voltage difference between the two electrodes, and when they are connected, an electric current is established.[36] As the flows, the electrons return to their position (discharge).[39] To prevent ions from recombining, a porous separator known as a separator is placed between the cathode and anode in batteries.[36, 38] **Figure 4** illustrates the battery materials during the charging and discharging process.

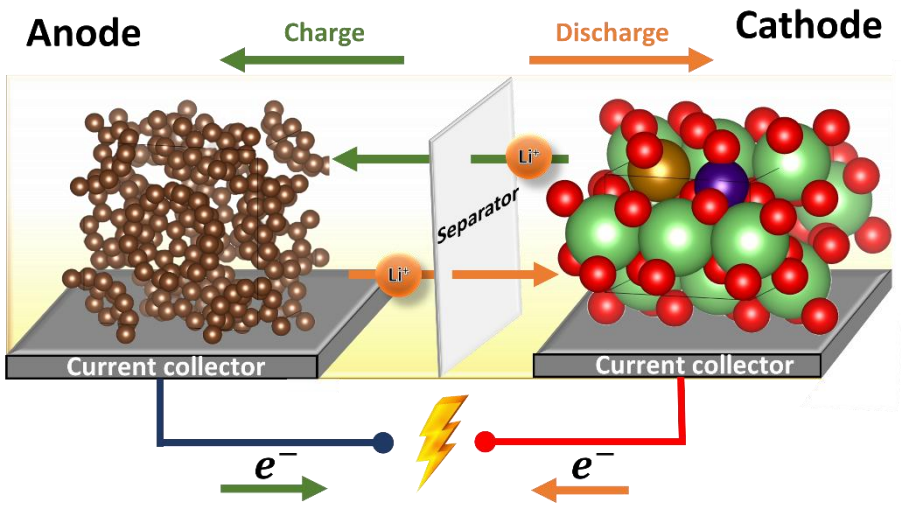

Figure 4. The components in a typical battery, along with charging and discharging phenomena.[40]

Batteries are generally divided into primary and secondary categories, as shown in **Figure 2**.[16, 36, 41] Primary batteries are batteries that have a fixed amount of reactants, determined during the manufacturing process, and cannot be recharged once their stored energy is depleted.[42]

Secondary batteries can be recharged after each use. This is because they have reversible chemical reactions at the electrodes, allowing them to be used multiple times.[43] As shown in **Figure 2**, this category of batteries includes several types, with LIB specifically discussed in **section 2.2.3**.

2.2.1. Metrics and definitions of the batteries

Battery performance metrics should be standardized across research, industry, and laboratories.[44] However, the methods used to measure these metrics vary significantly.[44] For instance, some studies and publications calculate performance based on the total electrode mass, which includes active material, binder, and conductive agent.[44] In contrast, other research bases calculations solely on the active material.[37]

In the following, some definitions and metrics of batteries are discussed by providing meaningful suggestions for reporting.[37] Charge and discharge curves contain key metrics for cells and batteries and valuable information can be obtained from them.[45] To explain the following concepts, the charge/discharge of the LFP//LTO full cell plot with an applied current of 200 mA g^{-1} (as shown in **Figure 5**) is used.

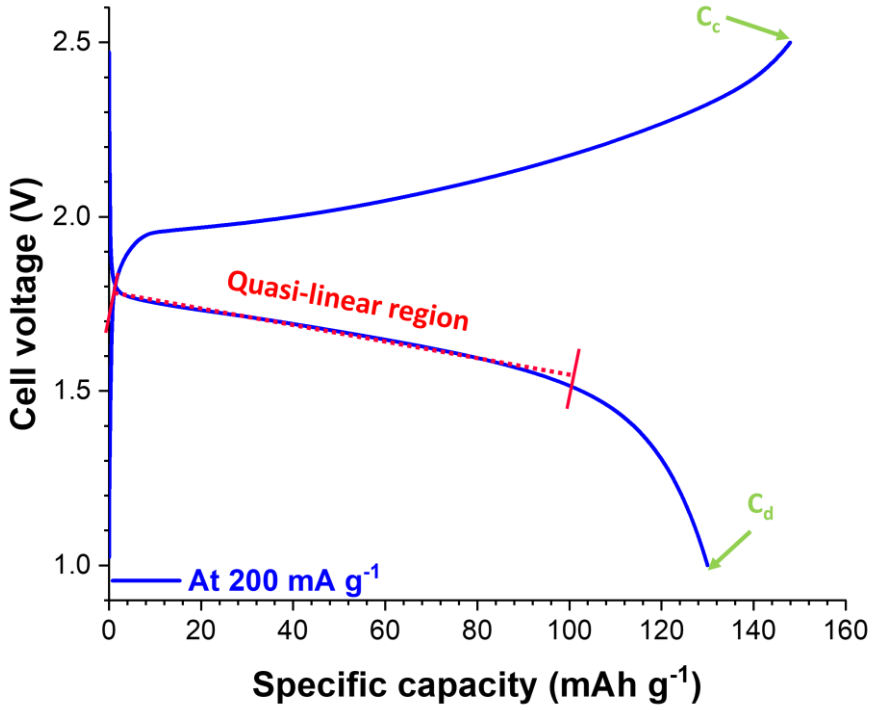

Figure 5. LFP//LTO full cell charge and discharge curves. C_d is the discharge capacity, and C_c is the charge capacity of the cell.

2.2.1.1. Capacity

The capacity unit is ampere hour, normalized based on mole, mass, or volume.[46] Normalizing the capacity based on mass is called specific capacity or gravimetric capacity, which is displayed in mAh g^{-1} unit.[46] This value can be calculated based on the amount of charge stored per unit mass of the material through Faraday's law shown in **Equation 3**. [46, 47] Where (n) is the number of electrons in the reaction, (F) is the Faraday constant, and (Mw) is the molecular weight of the active material.[46, 47]

$$Q_{theoretical} = \frac{n \cdot F}{3600 \times M_w} \qquad \textbf{Equation 3}$$

The mass electrode is needed to calculate active materials, and then the battery's charge/discharge process takes place based on the applied current.[48] The applied current is usually constant during charging/discharging to acquire the specific capacity of charge/discharge displayed in mAh g^{-1}.[48]

Therefore, it is possible to obtain the specific capacity of charge or discharge without ambiguity from the specific capacities at the end of the charge or discharge diagram, as shown in **Figure 5**. For example, for the LFP//LTO battery, at the applied current of 200 mA g^{-1}, the specific charge capacity is 147 mAh g^{-1}, and the specific discharge capacity is around 130 mAh g^{-1}.

2.2.1.2. Coulombic efficiency

Another concept used in batteries is the cell's Coulombic efficiency (CE).[49, 50] This battery parameter quantifies the reversibility and indicates side reactions. CE is calculated as follows in **Equation 4**, where (C_d) is the cell's discharge capacity at the single half cycle, and (C_c) is the cell's charge capacity in the next half cycle.[49, 50]

$$\eta(\%) = \frac{C_d}{C_c} \times 100 \qquad \textbf{Equation 4}$$

Therefore, as explained earlier, CE can be calculated by extracting the discharge/charge capacity from the charge/discharge diagram, as shown in **Figure 5**.[37] For the LFP//LTO battery, at the applied current of 200 mA g^{-1}, the Coulombic efficiency is 88.4%.

2.2.1.3. Voltage

Another important parameter in batteries is voltage.[51] The voltage can be determined from the relation between the discharge and charge curves.[51] In typical batteries, the voltage during discharge enters a region that decreases linearly, known as the quasi-linear region.[37] This

region can be seen after the initial non-linear reduction of the voltage, and after crossing the quasi-linear region, the voltage decreases rapidly.[52] The average of the quasi-linear region for the discharge process, as shown in **Figure 5**, can be a reasonable estimate of the battery voltage.[53] For the LFP//LTO battery at the applied specific current of 200 mA g^{-1}, the cell voltage can be calculated as approximately 1.65 V.

2.2.1.4. Cycling stability and cycle life

When the charge and discharge of a battery are within a certain voltage range using a set current, it is called galvanostatic cycling. The discharge capacity has been tracked over multiple cycles.[54, 55] Usually, this capacity decreases as the cycles progress, influenced by various factors such as the applied current used for charging and discharging, temperature, voltage range, electrode material, and the stability of the electrolyte.[56] According to the definition, the number of times the battery can be charged and discharged during its lifetime is the cycle life.[53] According to the industry standard, when the battery loses 20% of its initial specific capacity, it has reached the end of its lifetime.[57] Batteries need pre-cycles to gain equilibrium, which is called the formation of the electrodes.[18] Therefore, it is clear that the initial capacity of batteries or cells should be calculated after completing the formation process (which is a process in which the battery or cell goes through some pre-cycles of charge and discharge).[57]

2.2.1.5. Electrochemical signature

Two common electrochemical signatures are galvanostatic cycling with potential limitation (**Figure 6**) and cyclic voltammetry (**Figure 7**).[58, 59] These standard electrochemistry tests are used to identify and describe energy storage devices.[58, 59] These tests help us understand various aspects, such as capacitance, capacity, voltage range, cell kinetics, and how well the device holds up over multiple charge and discharge cycles.[60] Both galvanostatic cycling with potential limitation (GCPL) profiles and Cyclic Voltammetry (CV) showcase a cell's unique electrochemical fingerprint.[61]

In a GCPL test, we apply a constant current to the device and then measure the resulting voltage within a specific range over time.[62] Voltage plateaus indicate chemical reactions in the electrode material when plotting the voltage against the amount of charge inserted or extracted, giving insight into the device's behavior during operation.[62] To assess the device's

longevity, the charging and discharging process is repeated multiple times to see how it holds up over cycles.[63]

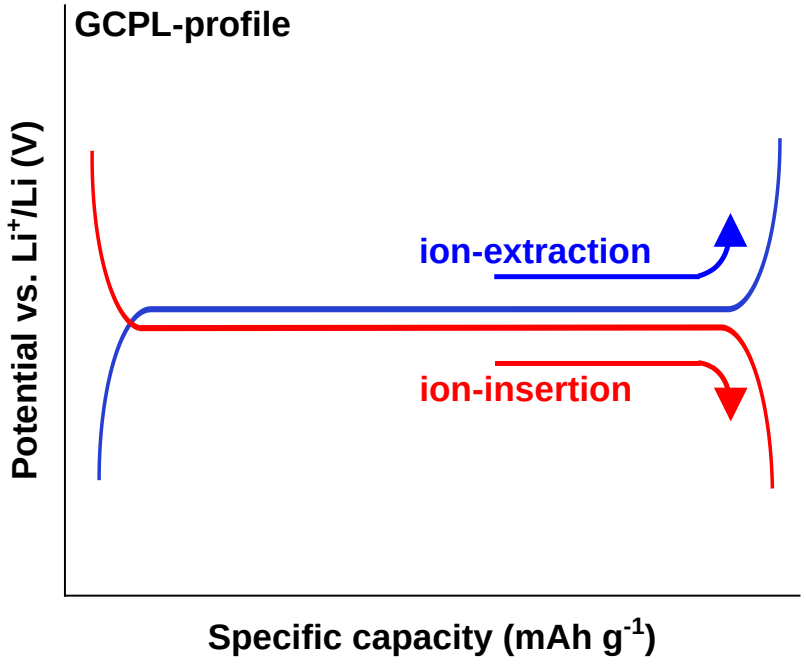

Figure 6. A galvanostatic charge and discharge profiles are recorded at constant currents.

The CV measurements apply a gradually increasing voltage to the cell.[64] Then, measure the current needed to follow this voltage change and plot it against the voltage.[65]

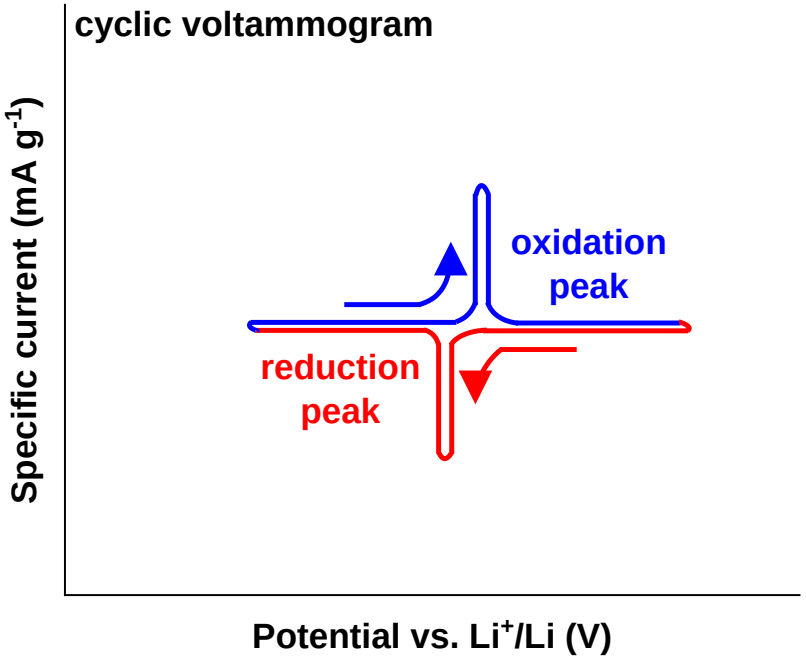

Figure 7. A schematic of a cyclic voltammogram collected by applying a constant voltage ramp.

Once it hits a specific target voltage, it reverses the voltage ramp to return to the starting point or another predefined voltage level.[66] Any peaks in the resulting cyclic voltammogram indicate the occurrence of certain chemical reactions at particular voltage levels.[67] These peaks give an insight into the redox reactions happening within the cell.[67]

2.2.1.6. HOMO and LUMO

In any rechargeable battery, like LIBs, the cathode and anode serve as the oxidizing and reducing agents, respectively, concerning the energy separation in the electrolyte.[68] This energy separation is the range of operating voltage for the electrolyte, defined by the energy difference between its lowest unoccupied molecular orbital (LUMO) and its highest occupied molecular orbital (HOMO).[69] To ensure the electrolyte's stability, the electrochemical potentials of the anode and cathode must stay within this energy range (**Figure 8**).[70] To ensure thermodynamic stability, the electrochemical potentials of the anode and cathode must stay within the energy range of the electrolyte.[69]

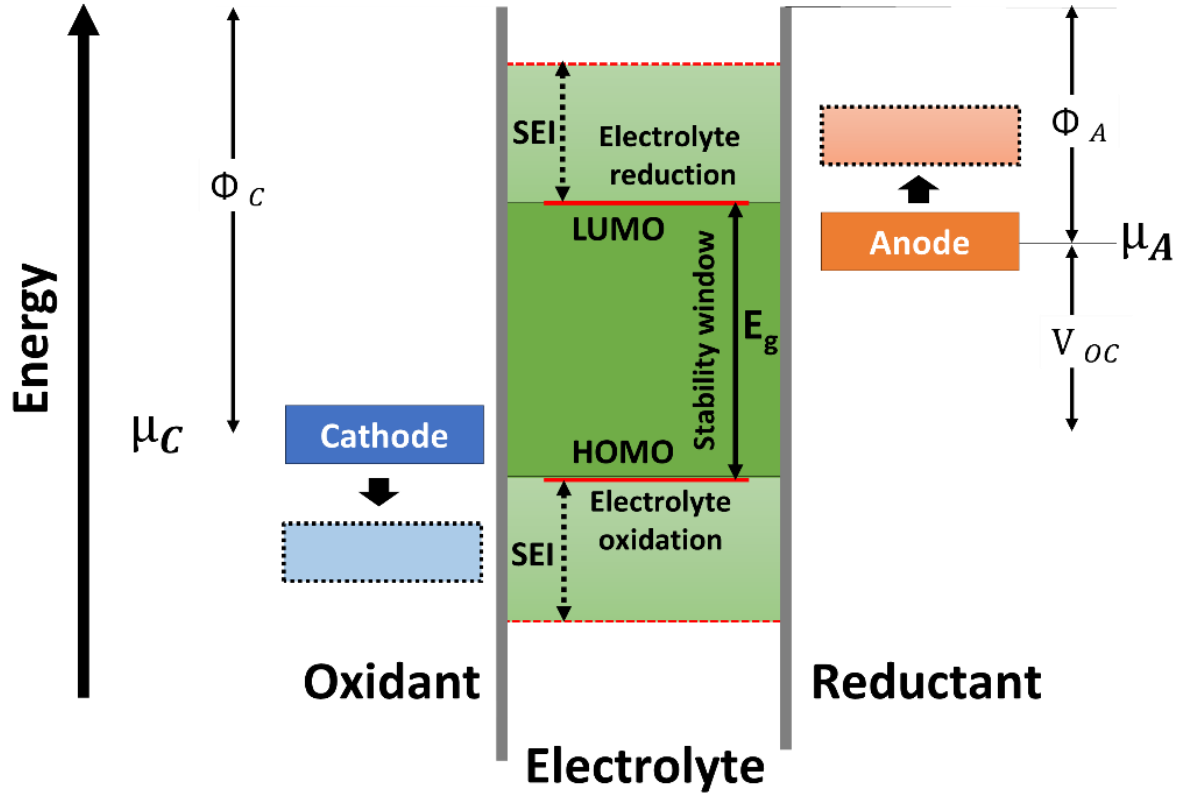

Figure 8. Depicts a diagrammatic representation of the energy levels of the electrodes and the electrolyte. (adapted from Ref.[70, 71])

2.2.2. Mechanisms

Ion batteries function by exchanging charges between the anode and cathode, allowing ions to move back and forth.[39] As a result, parameters like cell potential influence the battery's storage capacity.[72] This difference in potential arises from the response of ions present in both electrodes and the number of electrons involved.[73] Different types of mechanisms exist for charge transfer, which are accidental based on how electrodes interact with ions and will be further explored below.[73]

2.2.2.1. Insertion mechanism

One of the ion transfer processes for ion batteries is dedicated to the intercalation of ions into the layered structure of materials such as graphite or transition metal oxides.[37, 38, 74] In this process, the insertion/extraction of ions in the interlayer structure usually causes a change in the van der Waals gap.[37, 75] The empty spaces within the structure of an electrode, known as insertion storage sites, are where lithium ions (Li-ion) can be stored.[68] These sites provide higher capacity, quicker charging abilities, safer battery function, and longer life span.[68] There are two distinct ways for intercalation/deintercalation: heterogeneous and homogeneous insertion, as shown in **Figure 9**.[71, 76]

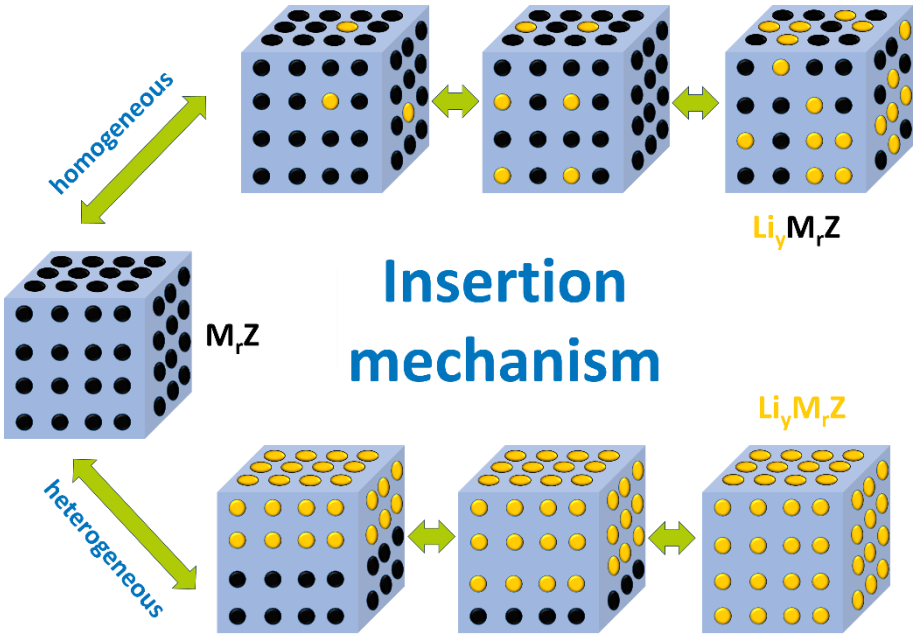

Figure 9. Insertion mechanism and its corresponding merits and demerits (adapted from Ref. [71])

In heterogeneous insertion, the electrical potential remains stable throughout the process.[71, 76] In contrast, in inhomogeneous insertion, the potential shifts as the composition of the

electrode material changes.[77] This dynamic shift in potential during homogeneous insertion offers faster reaction rates and enhances the stability of the electrode's structure.[77, 78]

Despite these benefits, both insertion methods have a limitation in capacity because the number of sites available for Li-ions is limited, generally allowing only one electron per ionic center.[76, 79] This insertion/extraction does not change the host structure in some materials.[37, 75] The ions intercalated into the host structure or deintercalated and left the host structure.[80] Therefore, the redox reaction for layered materials depends on the number of π-electrons in the intercalation flow of the material or the transition metal center.[81]

2.2.2.2. Conversion mechanism

Another type of mechanism for batteries is the conversion, in which new chemical species are formed from electrochemical reactions, as shown in **Equation 5**.[38, 71] Furthermore, the conversion mechanism and its corresponding merits and demerits have been depicted schematically in **Figure 10**.[71] The structure of this new material is different from the structure of the original material, and this process can be displayed as a reversible process.[82]

$$M_aX_b + (b.c)Li^+ + (b.c)e^- \leftrightarrow aM^0 + bLi_cX$$ **Equation 5**

where (M) is a TM (transition metal), and (X) is an atomic species such as sulfide, oxide, or fluoride.[82]

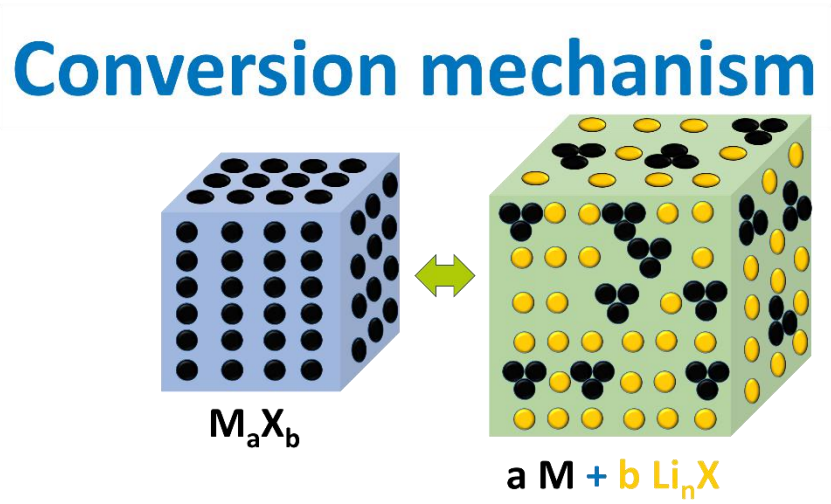

Figure 10. Conversion mechanism and its corresponding merits and demerits (adapted from Ref.[71]).

In the redox conversation process, more electrons are involved because, unlike the intercalation process, the transition metal center is reduced to a zero oxidation state, which leads to a higher theoretical capacity.[48, 83] If the conversion process is defined based on anionic

species oxidation/reduction, it can be shown more comprehensively as **Equation 6** that there will be no need for a transition metal.[38, 82, 84]

$$X + aLi^{+} + ae^{-} \leftrightarrow aM^{0} + Li_{a}X \qquad \textbf{Equation 6}$$

2.2.2.3. Alloying mechanism

Another type of charge transfer that ends in forming a Li-M lithium alloy is the alloying mechanism, which can be considered a type of conversion shown in **Figure 11**.[71, 85] This process is mainly studied in anodes such as Si, Sn, and Sb.[85] For example, in Si anodes that have a specific capacity of about 4200 mAh g^{-1}, the stoichiometry of $Li_{4.4}Si$ is formed by alloying Li with Si.[86] Composites of graphene, porous carbons, carbon nanotubes, etc., are used in alloy materials to increase the conductivity of this category of electrodes.[86]

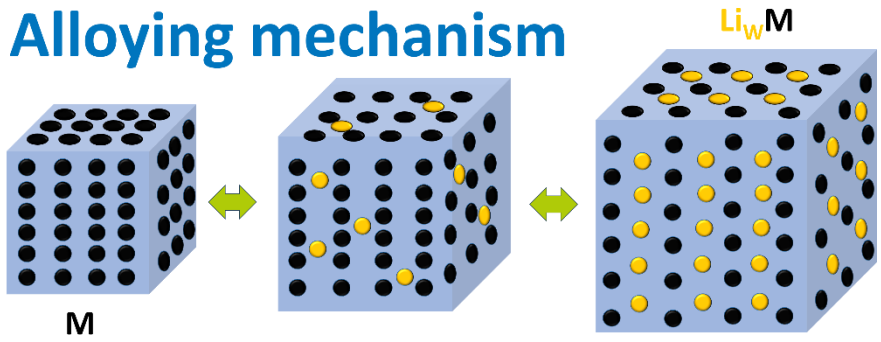

Figure 11. Alloying mechanism and its corresponding merits and demerits (adapted from[71]).

2.2.3. Lithium-ion batteries (LIBs)

Lithium is the 33rd most abundant element in the earth's crust. It has a high electrochemical potential (-3.02 V vs. standard hydrogen electrode (SHE)) and a high energy density by weight (200-300 Wh kg^{-1} for LIBs).[87] Lithium is the lightest metal available in nature, with a molar mass of 6.9 g mol^{-1}. It is silver-white and very soft.[88] This metal also has a very low density of 0.53 g cm^{-3} and an electrochemical equivalent of 259 mg Ah^{-1}.[89, 90] In addition to the mentioned characteristics, LIBs' wide range of thermal tolerance, compared to any other types, has achieved high demand in the energy storage industry.[90]

In 2023, 46% of all extracted lithium will be used in battery production.[91] LIBs have attracted much attention due to their unique capabilities in developing energy storage technologies.[91] It is estimated that more than one million cells equivalent to 700 GWh are available in the market, more than half of which are used in light vehicles.[92] As shown in **Figure 12**, the position

of LIBs in terms of gravitational and volumetric energy density is higher than that of other existing technologies.[49, 87-91, 93]

In addition to high energy density and high energy power, features such as long lifetime, very low self-discharge, fast charging, low self-discharge, high open circle potential, a wide range of chemical potentials accessible with various electrode designs, and high Coulombic efficiency have added to the importance of LIBs.[38, 94]

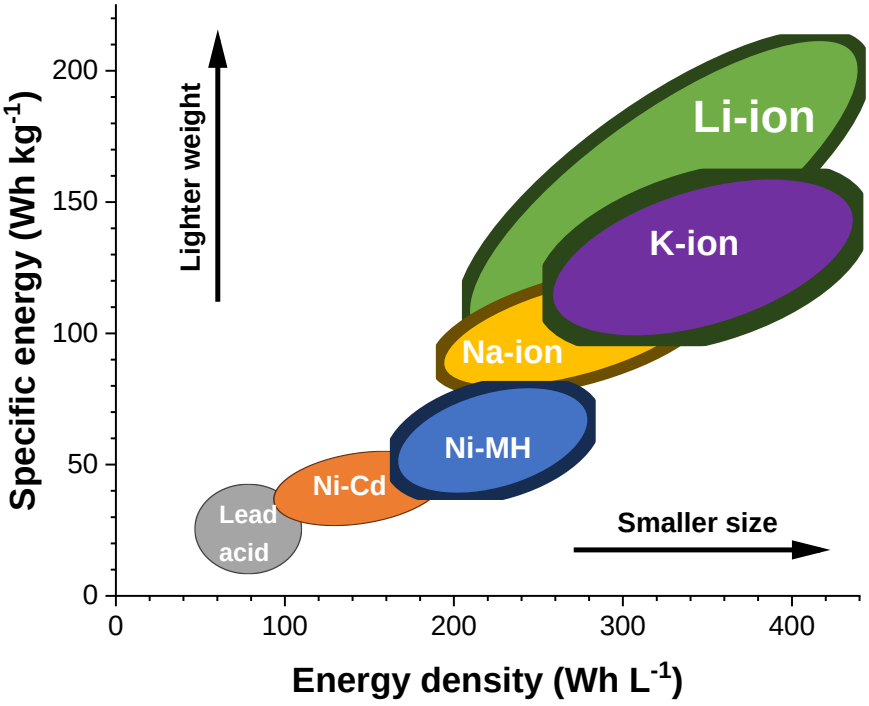

Figure 12. The energy performance of various secondary batteries (adapted from Ref.[49, 93]).

These features make them suitable for multiple vehicle uses, including electric cars, hybrid electric cars, ships, aerospace applications, and energy storage sources.[38, 94] Whittingham introduced the concept of LIBs as it is today in the early 1970s and was later acquired by Goodenough.[38, 54, 95, 96] In 1991, Sony launched the first commercial LIB.[97, 98] Research in the innovation of LIBs has increased significantly over the last years.[97, 98] Efforts to produce LIBs with higher energy storage capacity, lower weight, higher safety, less toxicity, lower production cost, high Coulombic energy, etc.[54, 94]

As shown in **Figure 13**, different electrodes with different capabilities have been presented over the years to produce more optimized LIBs.[94] Also, according to the growing need for electric vehicles, hybrid electric vehicles, and aerospace industries, batteries with fast charging, high power, and high energy capabilities have been researched and produced.[97, 98] LIBs are among rechargeable batteries or secondary batteries.[99] The conventional Li-battery

operation is based on the reversible process of inserting lithium cations in the anode and cathode materials and electrons flowing through the external circuit.[99] In the charging process, lithium-ion (Li-ion) is de-intercalated from the cathode active material, diffused in the electrolyte, and then passed through nanopores of the separator and intercalated into the anode active material.[100]

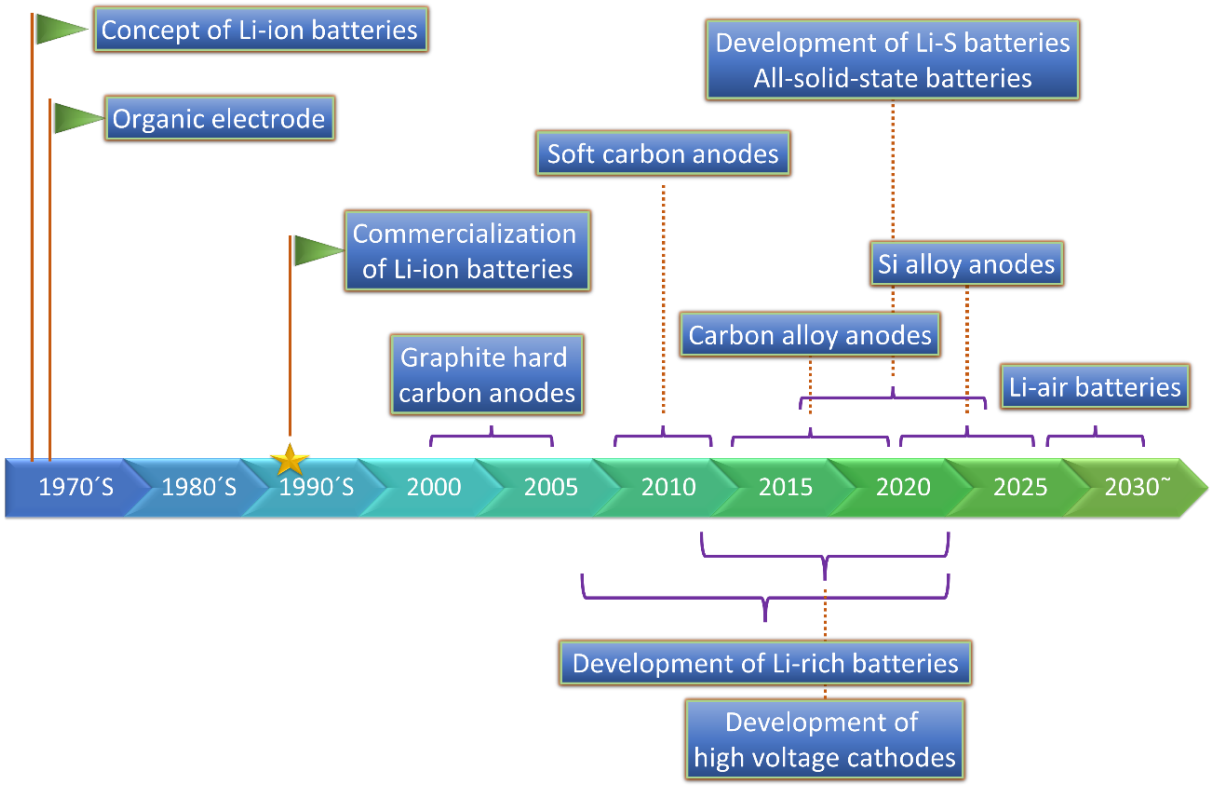

Figure 13. Historical evolution of LIBs technologies (adapted from Ref.[97, 98]).

At the same time, electrons conversely move through the external circuit.[100] While in the discharge process, Li-ion is released due to the oxidation of the anode active material and is inserted back into the cathode active material.[101]

Therefore, Li-ion is forced to move to the anode by applying external energy in the charging process.[46, 47] Following the charge and discharge process has been shown for $LiCoO_2$ as an example of LIBs in **Equation 7-9**.[46, 47]

$$\boldsymbol{Cathode}: \boldsymbol{LiCoO_2 \leftrightarrow Li_{1-x}CoO_2 + xLi^+ + xe^-} \qquad \textbf{Equation 7}$$

$$\boldsymbol{Athode}: \boldsymbol{6C + xLi^+ + xe^{-1} + xe^- \leftrightarrow Li_xC_6} \qquad \textbf{Equation 8}$$

$$\boldsymbol{Overall}: \boldsymbol{LiCoO_2 + 6C \leftrightarrow Li_{1-x}CoO_2 + Li_xC_6} \qquad \textbf{Equation 9}$$

In LIBs, charging and discharging include the movement of both Li-ions and electrons between the electrodes.[102] During charging, Li-ions are released from the cathode (terminal) and move through the electrolyte and separator to reach the anode side (negative terminal).[103] As the Li-ions flow, electrons are also released at the cathode.[104] The positive current collector collects these electrons and that move through the external circuit to the anode.[104] Both Li-ions and electrons are stored in the anode.[104, 105] During discharge, this process is reversed.[104, 105] The Li-ions move back to the cathode, converting chemical energy into electrical energy. LIBs are made up of various parts, including the cathode, the anode, the electrolyte, the separator, and the current collectors.[103]

A summary of the requirements for each of these elements is provided in **Table 1**.[71, 103] The anode and cathode are usually coated on a thin layer of copper foil or aluminum foil, respectively.[46, 47] This layer is called a current collector and affects connected electrodes' physical properties and conductivity.[106] LIBs are usually classified based on capacity, which is charge storage capacity.[106] The CE ratio of Li-ion extraction capacity to Li-ion insertion capacity in electrode active mass and electrolyte decomposition (in a single cycle is influenced by chemical and physical variations).[107]

Another factor that plays a significant role in the capacity of LIBs is the applied current to the cell.[107] It means that the higher the applied current is for charge or discharge, the more it affects the cathode and anode, and as a result, the irreversible damaging effect on the electrodes increases.[108] Therefore, the applied current determines volumetric and specific capacity and power density.[108] The electrode manufacturing process and production efficiency play an important role in optimizing the electrodes in producing LIBs.[109]

Table 1. The key points that should be considered from the materials utilized in batteries (adapted from Ref.[71]).

Battery	Anode	Cathode	Electrolyte	Separator
Free of toxic materials, high reliability, and easy to recycle	High energy density	High energy density	High ionic conductivity	Chemically stable
Smaller in size will serve better	High structural stability	High structure stability	High internal resistance	Mechanical stability
Self-heating should be as low as possible	High specific capacity	High specific capacity	High chemical stability	High porosity
Raw materials should be abundantly available and cheaper	Environmental friendly	High oxidation potential	High boiling point	High resistance to Electronic conductivity
High energy content with respect to weight and volume	Low cost	High power density	Low melting point	Low resistance to Ionic transport

The following section of this review dives into developing various components used in LIBs, including the anode, cathode, electrolyte, and others.

2.2.3.1. Anode materials for LIBs

The anode is one of the main components in LIBs, whose morphology and structure can significantly impact the final product's optimal performance.[83, 107] Graphite is widely used as an anode in the rechargeable battery industry due to its electrochemical properties, environmental friendliness, and cost.[110-112] Among these features, we can mention the hierarchical structure of graphite. In fact, during the charging process, Li-ion can easily insert carbon atoms in the reasonably large interstice between two adjoining layers.[107] **Figure 14** shows anode materials with nanostructures and mixed valances used in LIBs in the potential range of 0.01-3.00 V vs. Li^+/Li.[97, 98, 113, 114]

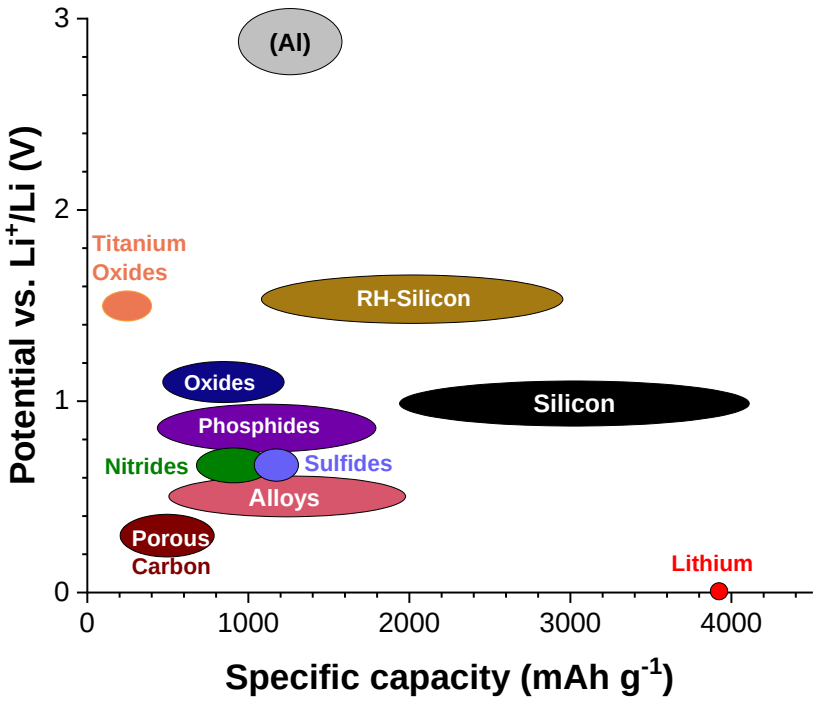

Figure 14. Comparison chart for some anodes used in LIBs based on potential versus specific capacity (adapted from Ref.[97, 98, 113, 114]).

In evaluating LIBs factors like charging and discharging rates, cycling capacity, and Coulombic efficiency are given priority.[107] The performance of LIBs can be affected by processes that cause a decrease in battery characteristics during operation.[107] Ideally, a cell could function indefinitely if the Coulombic efficiency remains at 100%.[50, 115] A significant aspect influencing LIB performance is the development of an interphase (SEI) layer.[47, 116] The SEI forms when

electrodes come into contact with the electrolyte, playing a role in determining LIB performance by acting as a barrier between the electrode and electrolyte that hinders electron flow while allowing ion movement.[47, 116]

The formation of SEI facilitates the movement of Li-ions within the system, prevents solvent penetration into the electrode, and results in irreversible capacity loss in the battery.[107] Extensive research has been conducted to develop materials for components to enhance LIB technology. When selecting materials for anodes in LIBs, the following key considerations should be included:[83, 107, 110, 111]

- **Compatibility with the electrolyte**: Ensure that anode energy levels are lower than those of the electrolyte to maintain battery stability and avoid reduction.
- **Electrochemical potential**: The difference in potential between the anode and cathode plays a role in enhancing lithium intercalation and boosting energy storage capacity. It is optimal for the anode potential to stay around or below 0.5 V compared to Li^+/Li.
- **Material selection criteria**: When selecting materials, the choice depends on factors like crystal structure, capacity, electrical conductivity, stability, and chemical properties.
- **Atomic mass and density**: A material should have low atomic weight and density while maintaining a high lithium-to-formula unit ratio.
- **Cyclability and reversible capacity**: The anode must exhibit cyclability, offer capacity, and remain stable during prolonged use.
- **Operating voltage**: The anode must align its voltage with lithium metal to support battery operation at voltages.
- **Ensuring the stability of chemicals**: The anode material must remain chemically stable without reacting with the electrolyte or breaking down in solvents.
- **Considering safety aspects:** the anode material should be environmentally friendly cost-effective, safe for use, and possess electrical and lithium ion conductivity characteristics.

Different materials used as anodes LIBs can be classified into alloy materials, conversion type substances, silicon-based components, carbon-based compounds, and lithium titanium oxide.[83, 107, 110-112]

2.2.3.1.1. Alloying materials

Huggin and Besenhard presented the concept of using binary metal alloys as electrode materials for energy storage devices for the first time.[83, 117] Extensive research was then done on metal and metal oxide alloys and their performance in LIBs.[118, 119] In this regard, the first Lithium-based alloys (Li_xM) in which (M) represented a secondary metal (electrochemically active or inactive) have been investigated.[83, 120] These secondary metals include silicon, aluminum, tin, magnesium, silver, antimony, and their derived alloys.[107, 119] A schematic of the $LiSn_2$ structure as an example of silicon-based components is shown in **Figure 15.**[121]

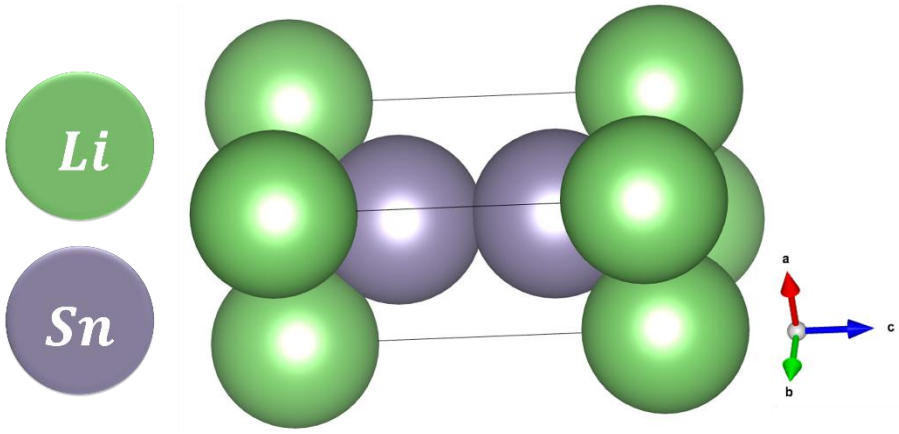

Figure 15. Polyhedral illustration of a $LiSi_2$ unit cell. (adapted from Ref. [121])

This category of anodes usually has high lithiation and delithiation capabilities and unique processing quality.[107, 112] The working concept of these anodes is based on the insertion process of Li-ion and the chemical reaction of Li-ion with the active metal.[83, 107, 110, 111] This category of anodes has problems such as massive volumetric expansions, poor electrical conductivity, substantial capacity loss during the first cycle, and rapid capacity loss in the subsequent cycles.[107, 122] For example, these processes for lithiation and delithiation can be shown as crystalline-to-amorphous mechanism equations in the following steps (**Equation 10-11**).[83, 107, 110, 111, 123, 124]

During the delithiation:

$$\boldsymbol{Si\ (Crystalline) + xLi^{+} + xe^{-} \rightarrow Li_xSi\ (amorphous) + (3.75 - x)Li^{+} + (3.75 - x)e^{-} \rightarrow Li_{15}Si_4(crystalline)} \quad \textbf{Equation 10}$$

During the lithiation:

$$\boldsymbol{Li_{15}Si_4(crystalline) \rightarrow Si\ (amorphous) + yLi^{+} + xe^{-} \rightarrow Li_{15}Si_4(residual)} \quad \textbf{Equation 11}$$

2.2.3.1.2. Silicon-based components

Silicon (Si) is another material available for LIBs technology, which has particular characteristics for the anode.[107, 125] Silicon is seen as a top choice for anode material because it offers high theoretical capacity, low toxicity, and relatively low cost.[126] This anode has a working potential of about 370 mV vs. Li^+/Li and a theoretical specific capacity of 4200 mAh g^{-1} (corresponding to a fully lithiated state).[107, 125, 127] Among all elements, Si has the highest gravimetric and volumetric capacity despite its low cost.[125] Also, despite its low working potential and its abundance in the earth's crust, it has high safety as one of its advantages.[128]

The use and industrial production of silicon anodes are still challenging due to massive volume expansion (>400%) during lithiation and delithiation, which occurs as a conversation reaction.[107, 125] This volume expansion reduces reversibility and rapidly declining capacity.[129] In this type of anode, carbon additive or Si/C composite materials are usually used to increase the conductivity of the current collector.[107, 125, 130] A schematic of the $Li_{4.11}Si$ structure as an example of silicon-based components is shown in **Figure 16.**[107, 125, 127]

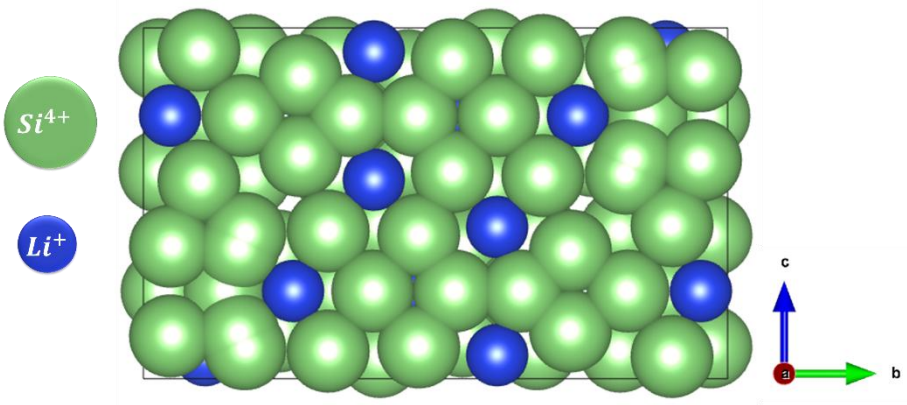

Figure 16. Polyhedral illustration of a $Li_{4.11}Si$ unit cell. (adapted from Ref. [131])

2.2.3.1.3. Carbon-based compounds

Currently, carbon is widely used as the primary anode for LIBs. This type of anode has many advantages, including high conductivity, hierarchical arrangements suitable for Li-ion insertion, low cost, and low working potential.[132] In addition to the advantages mentioned, carbon anodes have some limitations, such as low rate capacity and safety risks.[107, 125, 133] These anodes can be generally divided into graphitic carbon and non-graphitic carbons.[134] This category of carbonaceous materials is called hard carbon; conversely, GCs are called soft carbon.[107, 125, 135]

The Li-ion insertion/extraction process is performed for carbon anodes, as shown in **Equation 12**. In this equation, (n) can vary between 6 and 12 depending on the morphology and structure of carbon.[107, 125]

$$Li^{+} + e + nC = LiC_n \qquad \textbf{Equation 12}$$

The microstructure, morphology, and crystallinity of carbon directly affect its electrochemical properties during the cycling process.[107, 125] For example, graphene's high capacity and high energy density can be compared to the stability of excellent cycles of hard carbon.[136] A schematic of the carbon structure as an example of carbon-based components is shown in **Figure 17.**[131]

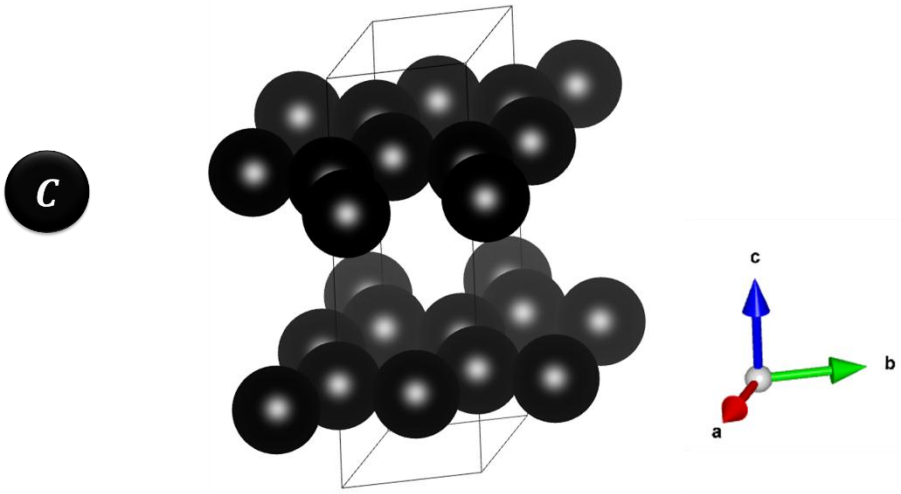

Figure 17. Polyhedral illustration of a carbon unit cell. (adapted from Ref.[131])

2.2.3.1.4. Conversion-type materials

Conversion-type anode materials are promising due to their attractive compositions and high theoretical specific capacity for Li-ion batteries.[137] Low production cost compared to other anodes is one of the advantages of these anodes, which include alloy anode materials such as Fe_2O_3, FeS_2, and FeP.[138] This approach enhances the safety of lithium-ion batteries by preventing the formation of lithium dendrites, even when operating at a lower lithium-intercalation potential.[139] This category of anodes has limitations such as continuous electrolyte decomposition, significant volume expansion (<200%), and poor electric and ionic conductivity.[139] A schematic of the Fe_2O_3 structure as an example of silicon-based components is shown in **Figure 18.**[40]

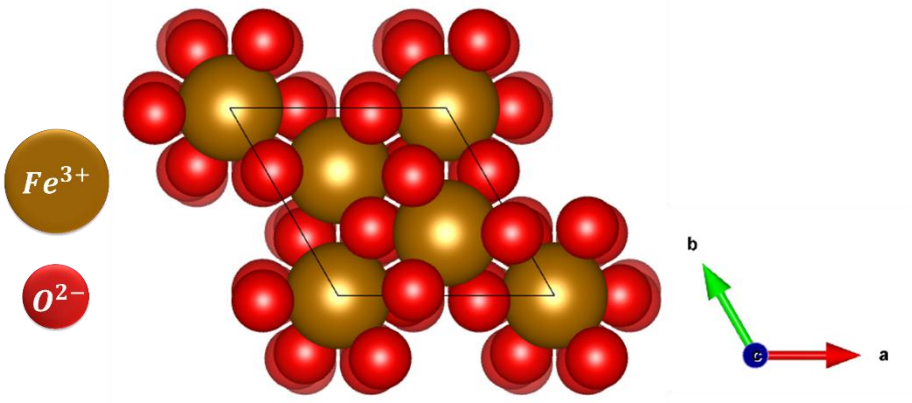

Figure 18. Polyhedral illustration of a Fe_2O_3 unit cell. (adapted from Ref.[40])

2.2.3.1.5. Transition metal oxalates

Transition metal oxalate anodes have been gaining attention as an alternative to graphite anodes due to their electrochemical properties.[107, 140, 141] This category of anodes includes combinations of cobalt oxalates (CoC_2O_4), zinc oxalates (ZnC_2O_4), iron oxalates (FeC_2O_4), nickel oxalates (NiC_2O_4), and manganese oxalates (MnC_2O_4).[142, 143] These anodes exhibit a capacity and do not form metal lithium alloys during the lithiation process.[144, 145] Anodes in this category face challenges such as cycling performance and expansion issues during the insertion and extraction of Li-ion, which can be enhanced by adjusting the shape, design, and size of the particles.[107, 143] A schematic of the zinc oxalate structure as an example of transition metal oxalate components is shown in **Figure 19**

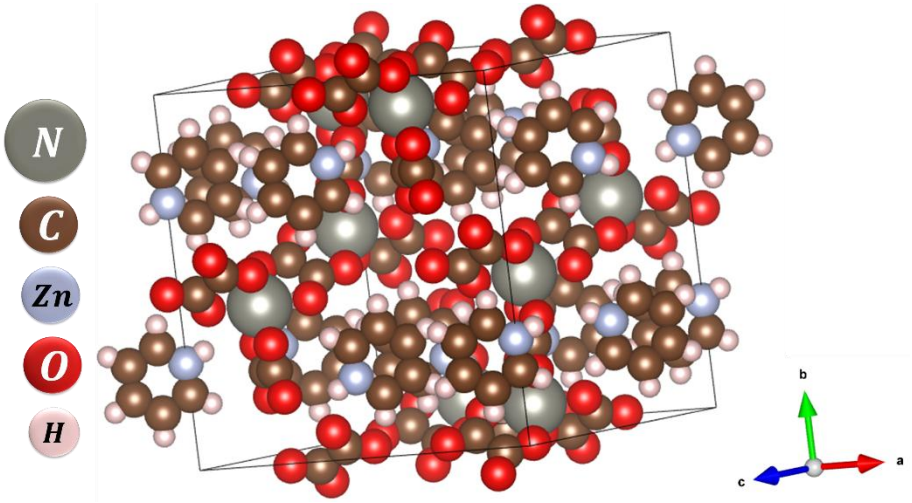

Figure 19. Polyhedral illustration of a zinc oxalate unit cell (adapted from Ref.[146]).

Transition metal oxides, like iron oxide (Fe_2O_3, Fe_3O_4), cobalt oxide (Co_3O_4), manganese oxide (MnO_2, Mn_3O_4), and nickel oxide (NiO), offer higher theoretical capacities compared to

traditional graphite anodes.[147] Iron oxides such as Fe_2O_3 and Fe_3O_4 have theoretical capacities of approximately 1000 mAh g^{-1} and 926 mAh g^{-1}, respectively, due to their reaction with Li-ions, yielding lithium oxide and metallic iron upon discharge.[147] Cobalt oxide, Co_3O_4, has a theoretical capacity of about 890 mAh g^{-1}, along with good cycling stability and high capacity retention.[148] Manganese oxides, such as MnO_2 and Mn_3O_4, have theoretical capacities of about 1230 mAh g^{-1} and 1013 mAh g^{-1}, respectively, distinct redox reactions contributing to their high capacities.[149] Nickel oxide, NiO, has a theoretical capacity of around 718 mAh g^{-1} and is known for its high capacity and stability.[150]

2.2.3.1.6. Transition metal chalcogenides

This category of anodes stores Li-ion in an electrochemical conversation mechanism and includes tin sulfide (SnS), molybdenum disulfide (MoS_2), cobalt sulfide (CoS_2), and iron disulfide (FeS_2).[107, 151] These transition metal compounds have attracted attention due to their high theoretical capacity.[107, 152] This category of anode has limitations, including significant alterations during lithiation and delithiation and low rate and cycling capacity. However, it can be modified using highly conductive materials such as graphene and surface coating.[107, 152, 153] Transition metal chalcogenides offer a compelling platform for developing advanced anodes for LIBs.[154, 155] Ongoing research focuses on innovative solutions, such as nanostructuring, composites and coatings, and doping and alloying paving the way for next-generation LIBs with higher specific energy, longer cycle life, and enhanced safety.[156, 157] A schematic of the MoS_2 structure as an example of silicon-based components is shown in **Figure 20.**

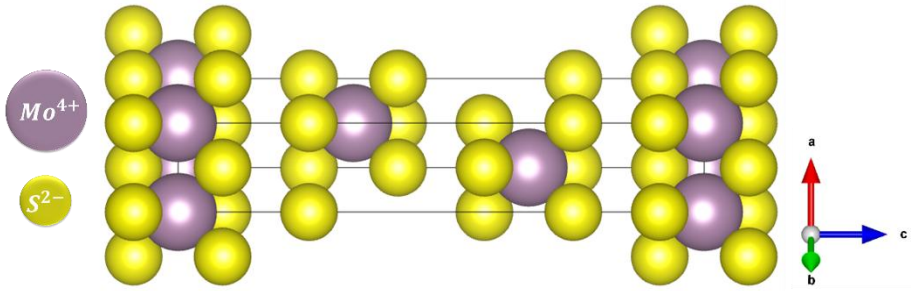

Figure 20. Polyhedral illustration of a MoS_2 unit cell (adapted from Ref.[40]).

2.2.3.1.7. MXenes

Recently there has been a lot of interest in MXenes, a type of anode that consists of 2D carbide, nitride, and carbonitrides.[107, 112, 158, 159] These materials were first discovered in 2011 and have since found applications across the industry, including in LIBs.[107, 159, 160] MXenes are typically

produced through an etching process on a MAX phase material, where (M) represents a transition metal element, (A) includes IIIA or IVA elements, and (X) stands for either carbon or nitrogen and is formulated as $M_{n+1}AX_n$.[158, 161] In this formula, (n) can be assigned 1, 2, or 3, (M) stands for a transition metal element, A includes a group of IIIA or IVA elements, and X stands for (C) or (N), which is shown in **Figure 21**.[158, 161]

MXenes with a particular 2D structure with high electrical conductivity, low Li-ion diffusion impedance, and high chemical stability showed potential for LIBs.[158, 159, 161, 162] MXenes (such as Ti_3C_2) can achieve a high specific capacity of as much as 320 mAh g^{-1} at a specific current of 100 mA g^{-1} after 760 cycles.[161, 162] Finally, these anodes suffer from restacking during the cycles, which limits Li-ion storage.[163] According to the studies, synthesizing a few-layered MXene, altering MXenes' functional groups, and increasing interlayer spacing can improve the capacity of MXene for storing Li-ion.[164, 165]

Usually, two strategies can be used to improve the synergistic effect of MXenes and other composite compounds and to produce high-capacity anode materials, which include reducing the restacking of MXene, as well as preventing electrical contact and buffering the volumetric expansion.[162, 166, 167] Based on the combination of transition metal dichalcogenides, silicon, and metal oxides with MXenes, it can be considered a practical and promising strategy to produce anodes used in LIBs.[107, 162, 168]

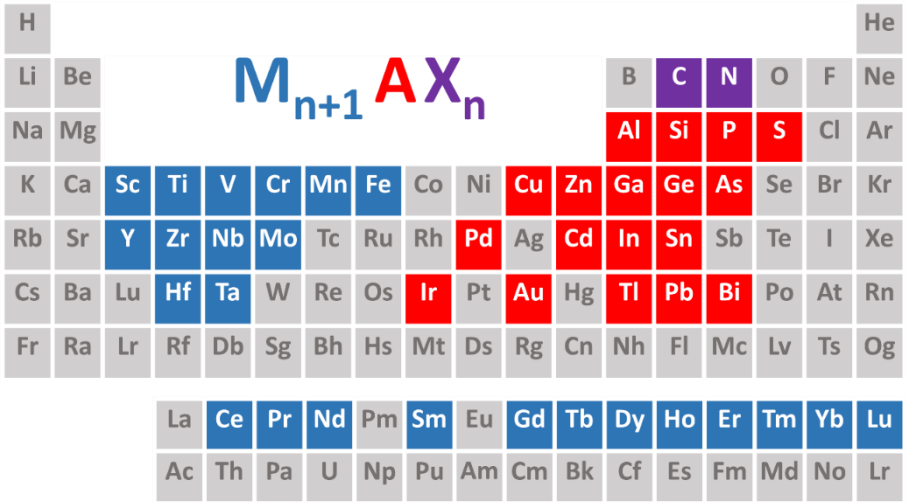

Figure 21. A periodic table shows the elements in MAX phases and MXenes, surface terminations, and intercalant cations (adapted from Ref.[169, 170])

2.2.3.1.8. Transition metal oxides and their composites

Transition metal oxide (TMOs) has a very high specific capacity, and, unlike graphite, Li-ion insertion/extraction process inside metal oxides without forming metal-lithium alloy.[107, 125]

TMOs are becoming increasingly popular for use in energy storage and conversion applications, largely due to their affordability, natural abundance, non-toxic, and high storage capacity.[107, 125, 140] The capacity of these materials can reach anywhere between 700-1200 mAh g^{-1}.[171] That's almost triple the capacity of the standard graphite-based materials used in today's commercial batteries.[141] However, they also come with some significant drawbacks.[172] TMOs typically have low electrical conductivity and ion diffusion kinetics, and they tend to undergo major structural changes, which can lead to a decline in performance over time.[107, 141] They can also experience significant volume expansion, high-voltage hysteresis, and other issues that can negatively impact their long-term capacity.[173, 174]

Researchers have made significant strides in addressing these challenges.[107, 171] One prevalent method involves the creation of nanostructures, which mitigate the adverse effects of volume expansion by offering shorter diffusion paths and increased contact areas.[175] Another technique is the incorporation of TMO nanoparticles with conductive materials like carbon, reduced graphene oxide, or carbon nanotubes (CNTs).[176] These composites not only enhance electrical conductivity but also fortify structural stability, thereby preserving capacity over multiple charge cycles. The lithiation/delithiation process for this category of anodes is done according to **Equation 13**.[107, 173]

$$\boldsymbol{MO + xLi^{+} + xe^{-} \leftrightarrow Li_2O + M} \qquad \textbf{Equation 13}$$

In this equation, (M) includes a transition metal that can be considered iron, titanium, zinc, copper, nickel, and cobalt.[107, 125, 173, 174] A schematic of the lithium titanium oxide structure as an example of transition metal oxalate components is shown in **Figure 22.**

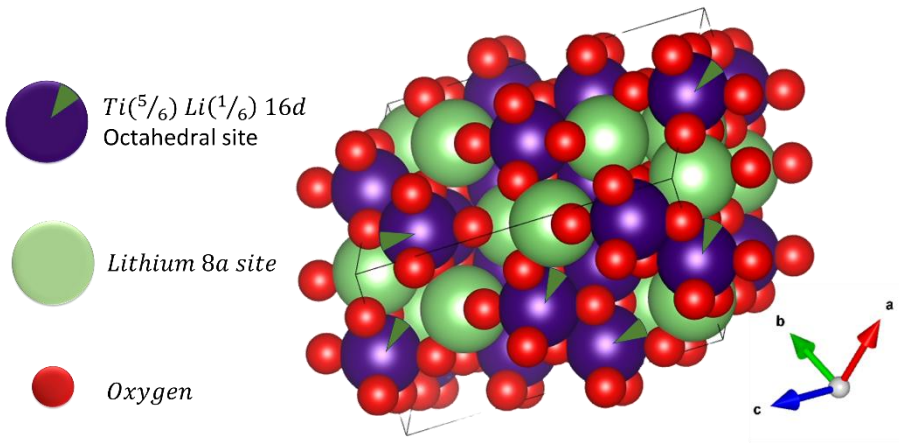

Figure 22. Polyhedral illustration of the crystal structure of pristine lithium titanium oxide (adapted from Ref.[40, 177])

2.2.3.1.8.1. Lithium titanium oxide

Spinal lithium titanium oxide (LTO), with the chemical formula $Li_4Ti_5O_{12}$, is currently the second most used anode in the industry.[178, 179] Due to the 3D network-like channel structure (**Figure 22**), this anode creates a very suitable space for the intercalation-deintercalation of Li-ion.[178, 179] Besides, due to the reversibility of this intercalation-deintercalation, this feature provides fast lithiation and delithiation for this material due to its stable structure.[180] Recently, there has been a lot of focus on this anode for high-rate LIBs due to their cycling performance, high rate capacity, minimal degradation of active material, wide thermal range, and safety features.[180] LTO is counted as a zero-strain material due to the slight shrinkage of the lattice parameter from 8.36 Å to 8.35 Å and a minimal change of about 0.2%.[181]

The theoretical capacity of LTO was defined based on its crystalline structure in 1995 and was considered 175 mAh g^{-1}. [177-183] This value was calculated from the potential range of 1.0 V to 2.5 V vs. Li^+/Li, where only three Li-ion intercalations are in the LTO structure.[177-183] Most researchers used to believe Li-ion intercalates in LTO at a potential of less than 1 V vs. Li^+/Li. However, some researchers showed that increasing the potential range of LTO can achieve a theoretical capacity higher than 175 mAh g^{-1} while broadening the potential range from 0.01-3.0 V vs. Li^+/Li.[181, 182]

The structure of $[Li_3]^{8a}[Li_1Ti_5]^{16d}[\square]^{16c}[O_{12}]^{32e}$ or LTO spinel compounds belongs to the $Fd\bar{3}m$ group, so some Li-ion is placed in the 8a sites.[179, 183-185] The remaining Li-ion and titanium-ions are placed in the 16d sites in a ratio of 1:5, respectively, and finally, oxygen-ions are in the (32e) sites.[89, 186] According to the above definition, $Li_4Ti_5O_{12}$ can be rewritten as $[LiTi_5^{4+}]_{(16d)}O_{12(32e)}$.[89, 182] Based on the conventional view, it was thought that only (16c) available octahedral sites could accommodate Li-ion in their lattice.[179, 187, 188] Li-ion moves from tetrahedral (8a) sites to octahedral (16c) sites simultaneously.

Based on this classical view and according to **Equation 14**, LTO can hold three moles of Li-ion, which becomes $Li_7Ti_5O_{12}$ or $[\square]^{8a}[Li_1Ti_5]^{16d}[Li_6]^{16c}[O_{12}]^{32e}$. In that case, only 60% of titanium ions in the crystal can be reduced to Ti^{+3}.[179, 185] By considering the full utilization of the Ti^{3+}/Ti^{4+} redox process, LTO can accept two more Li-ion per unit formulas.[183, 185] Besides, it has been proven that in the 0.01-0.6 V vs. Li^+/Li range, LTO accommodates extra ions, and this additional reversible capacity oversteps the classic view.[179, 185]

$$\boldsymbol{Li_{3(8a)}\left[LiTi_5^{4+}\right]_{(16d)}O_{12(32e)} + 3e^- + 3Li^+ \leftrightarrow (rock\ salt)Li_{6(16c)}[LiTi_3^{3+}Ti_2^{4+}]_{(16d)}O_{12(32e)}} \quad \textbf{Equation 14}$$

Considering the above, LTO can be $Li_9Ti_5O_{12}$ or $Li_{10}Ti_5O_{12}$ in the lithiation process, which means LTO can achieve 293 mAh g^{-1} and 350 mAh g^{-1} theoretical specific capacities.[179, 183, 189, 190] In this regard, research has been done, some of which is as follows.[182, 191, 192] Ge et al., for the first, work on increasing LTO capacity by broadening the potential range. [179, 183-185] By examining in situ X-ray and lithiation of LTO in the potential range of 0.01-3.00 V vs. Li^+/Li, they concluded that the number of tetravalent titanium ions limits the theoretical capacity of LTO.[179, 191, 193, 194] Therefore, LTO can achieve a specific capacity of 293 mAh g^{-1} by storing five Li-ion. Liu et al. also investigated this by using electrochemical and structural characterization methods.[182, 183, 185] They concluded that LTO could receive four Li-ion when cycled to 0.01 V vs. Li^+/Li. Han et al. have shown a theoretical specific capacity of 293 mAh g^{-1} in the potential range of 0.01-3.00 V vs. Li^+/Li.[179, 183-185]

Since factors such as specific surface area, morphology, purity, and compositions of the materials, as well as crystallinity, directly affect the electrochemical performance of the materials, the synthesis method is of particular importance.[179, 183-185] Many methods exist by which LTO can be synthesized.[195] These techniques include solid-state, microwave, spray pyrolysis, sol-gel hydrothermal, combustion, sonochemical, and molten salt. For the solid-state technique, many researchers have applied different conditions for sintering with varying time and temperature.[196] Chauque et al. reported that titanium dioxide and lithium carbonate were used to synthesize the LTO.[197] The overall equation of this process can be shown below in **Equation 15**.[197]

$$\mathbf{5}\ \boldsymbol{TiO_2} + \mathbf{2}\ \boldsymbol{Li_2CO_3} \rightarrow \boldsymbol{Li_4Ti_5O_{12}} + \mathbf{2}\ \boldsymbol{CO_2} \qquad \textbf{Equation 15}$$

Another method used to synthesize LTO is sol-gel. Sintering temperature plays a significant role in this method and is usually set in the 700-800 °C range.[195] The product obtained by the sol-gel method is remarkably homogeneous, the particle size is minimal in the nanometer range, and there is reasonable stoichiometric control.[195] Sandhya et al. reported that lithium acetate dihydrate and CTAB initially dissolved in an ethanol solution containing 2% (by mass) acetic acid.[198] Then, titanium isopropoxide was added drop by drop to the above solution with continuous stirring until white sol was obtained. [198] Then, the temperature was kept at 80°C in an oil bath until a gel was formed.[198] The gel was dried in a vacuum oven for 24 h, and the resulting precursor was calcined for 12 h.[198]

2.2.3.2. Cathode materials for LIBs

The cathode covers more than 30% of the cost of LIBs and is usually composed of lithium, nickel, cobalt, and manganese with different percentage combinations.[199, 200] Cathodes are usually composed of complex lithium composite materials, and these different materials have different performances.[201] The combination of these materials creates impedance compared to metallic lithium due to low ionic conductivity and diffusion coefficients.[201]. Currently, LIBs are named based on the cathode used on an industrial scale.[202] This is because the performance of LIBs is ultimately limited on the cathode, and it is the limiting factor.[202] **Figure 23** shows some cathode materials used in LIBs in the potential range of 2-5 V vs. Li^+/Li.[93] Nowadays, improving the performance of cathodes plays a crucial role in enhancing LIB energy and power density.[199, 200] Also, reducing the production cost of the cathode materials can play a decisive role in the further expansion of LIBs in various industries.[199, 200] Another critical factor in improving the cathode material is reaching a higher potential to increase cell operational potential.[96] The cell voltage is determined by the difference in redox energy between the cathode and the anode, so the amount of this energy must be lower for the cathode and very high for the anode.[96, 203, 204] This way, the cathode is stabilized in the lower-lying band with a higher oxidation state, and vice versa for the anode.[96, 203, 204] To be an ideal candidate for a LIBs cathode, a material must meet several key requirements as follows:[205]

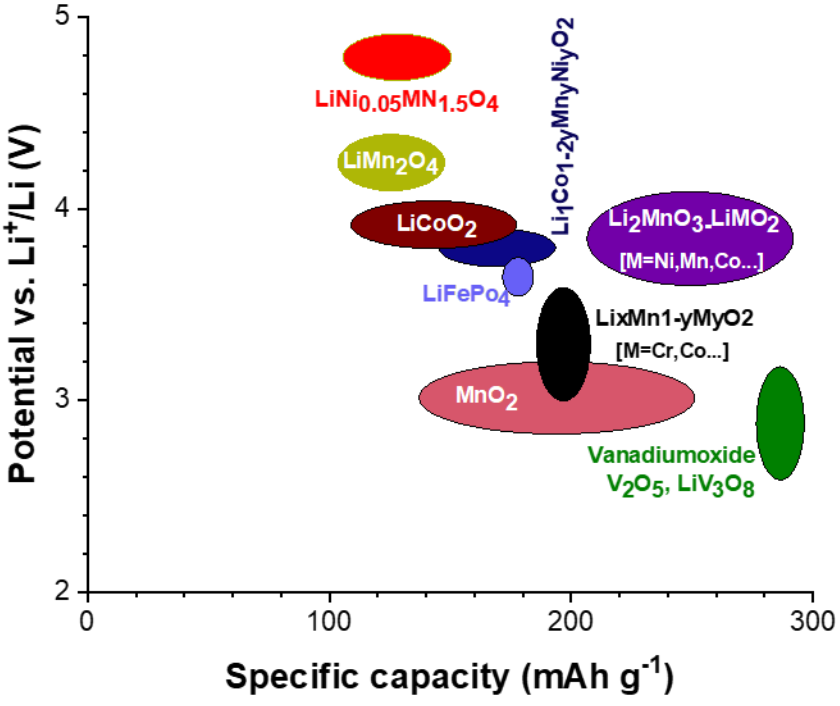

Figure 23. Comparison chart for some cathodes used in LIBs based on potential versus specific capacity (adapted from Ref.[93, 204, 206]).

Redox capability: It should contain ions, such as those from transition metals, that are easily oxidized or reduced. Reversibility with lithium: The active material inside the anode must allow reversible reactions of Li-ions. High free energy reaction: A strong reaction with lithium, characterized by high capacity (one lithium per transition metal) and high voltage (4 V or more), is crucial for energy storage in LIBs. Fast reaction rate: The material should enable quick lithium insertion and dissipation for efficient charging and discharging. Conductivity: It should exhibit good ionic and electronic conductivity. Cost, availability, and safety: The material should be affordable, readily available, and environmentally friendly.

So, the cathode stabilization should be done in the higher-lying band with lower oxidation states, providing the cell access to a higher voltage.[96, 203, 204] This idea was the starting point for Goodenough and his colleagues, in the 1980s at Oxford University to develop three classes of oxide cathode materials as a higher-voltage for LIBs (**Figure 24**).[96]

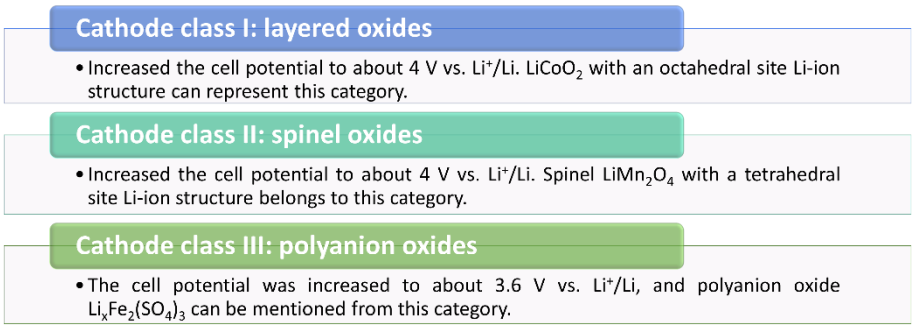

Figure 24. Three categories of cathodes for LIBs by Manthiram et al. (adapted from Ref.[96]).

Common materials currently used as LIB cathodes include layered lithium transition metal oxides, polyanionic compounds, and Mn-based spinel ($LiMn_2O_4$) oxide.[207] In the following, some of the classes of cathodes will be examined in detail with examples of each.

2.2.3.2.1. Layered lithium transition metal oxides

One of the challenges for LIB scientists is to develop and discover new cathode materials with superior performance. In the 1970s, the topotactic reaction was found.[208] Since then, the layered lithium transition metal oxides, due to their appealing merits, have been developed through research and innovation in intercalation materials.[207, 208] Layered lithium transition metal oxides can be represented by the general formula of $LiNi_xCo_yMn_zO$ (where $x+y+z\approx1$).[207] The formula can be simplified as $LiMO_2$, where the (M) is usually an electrochemically active

transition ion (M=Co, Ni, and Mn) and electrochemically inactive substituent cations (Li, Al, and Mn).[207, 209]

Layered lithium transition metal oxides are normally a trigonal crystal system. The M-cation's average oxidation state is (+3) (such as Co, Ni, and Mn).[209] In this structure, Li-ion and (M) are positioned in octahedral sites in the lithium layers, and a cubic close-packed oxygen array is situated in slabs of octahedra formed by (M) and oxygen atoms.[207, 210] Layered lithium transition metal oxides can be divided into two types of naming: basic layered transition metal oxides and polyanionic compounds, which will briefly be discussed in the following.[207, 210] In basic layered transition metal oxides, three materials can be referred to as lithium manganese oxide ($LiMnO_2$), lithium nickel oxide ($LiNiO_2$), and lithium cobalt oxide ($LiCoO_2$).[207] $LiCoO_2$ is more attractive in this category due to its convenient manufacturing process and synthesis using chemical and solid-state techniques.[211, 212]

$LiCoO_2$ (LCO) is the first cathode used as a cathode material for LIBs on an industrial scale since 1980.[211, 212] This cathode delivers a practical capacity of around 140 mAh g^{-1} at a potential of 2.4 V vs. Li^+/Li.[211, 212] The issues with LCO are the high price of cobalt and its high toxicity, which has reduced interest in its use.[211, 212] The schematic structure of LCO has been shown in **Figure 25** as one of the basic layered transition metal oxide cathode materials.[213] $LiNiO_2$ was first introduced in 1954 and was considered an alternative to LCO due to its low price and low toxicity.[214, 215] This cathode has a structure similar to LCO in which Co^{3+} is substituted with Ni^{3+}, and with an average operating potential of 4 V vs. Li^+/Li, it shows a capacity equivalent to 250 mAh g^{-1} along with a high-rate capacity.[214, 215]

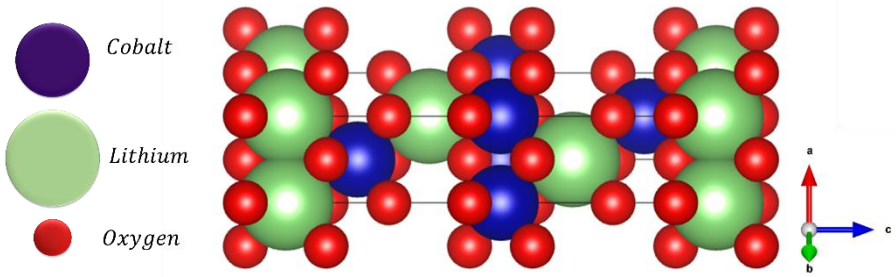

Figure 25. Polyhedral illustration of a $LiCoO_2$ unit cell (adapted from Ref. [40]).

$LiNiO_2$ with the basic formula of $Li_xNi_{1+x}O_2$ instead of Li_xNiO_2 is limited due to the blocking of the path of Li-ion due to the tendency of Ni^{2+} ions with Li^+ sites during the manufacturing and delithiation process.[216-219] Moreover, the other limiting factors for these types of cathodes are not fully reversible rhombohedral phase transition, limiting cut-off potential, and poor thermal

tolerance. Also, the pure form is unfavorable for this cathode for safety reasons.[216-219] Consequently, other materials such as nickel, aluminum, and magnesium have been substituted partially in $LiNiO_2$ cathode materials.[216-219]

Due to the lower price of manganese and its lower toxicity in comparison with other layered oxide materials, such as $LiMnO_2$, were widely researched.[220] This class of materials includes much more complex structures because they can form multiple structures.[220] $LiMnO_2$ pure-form synthesis is difficult and possesses unstable structures during the delithiation process compared to other layered oxide materials, such as LCO.[220] The basic structure of these types of cathodes is electrochemically active, and they have a zigzag-type orthorhombic with Pmnm symmetry and a monoclinic with C/2m symmetry structure.[38, 221, 222] The layered oxide materials in the potential range of 2.5-4.3 V vs. Li^+/Li can deliver a theoretical capacity of 285 mAh g^{-1} with a practical specific capacity of around 200 mAh g^{-1}. The layered oxide materials are limited due to capacity fading. At the same time, the spinel structure is formed.[38, 221, 222]

Ternary layered lithium transition metal oxides have been extensively researched due to their high energy density, easy processing, viability for commercial production, and high operating potential.[223] Ternary layered lithium transition metal oxides contain three sub-categories.[106] These sub-categories are nickel-layered oxide ($LiNi_{1/3}Mn_{1/3}Co_{1/3}O_2$), nickel-rich layered lithium transition metal oxides, and Al-substituted NCM.[142] The working potential range between 2.5-4.5 V vs. Li^+/Li can deliver a capacity of around 200 mAh g^{-1}.[223-225]

In recent years, Li-rich layered cathode material has received much attention due to its high specific capacity at room temperature (250 mAh g^{-1}).[226] Currently, overcoming low power density, low cycling stability, and voltage decline for these cathode materials with existing technologies such as modification and surface coating is available.[227, 228] These materials are shown by $xLi_2MnO_3 \cdot (1 \cdot x)LiMO_2$ formula where M includes manganese, nickel, cobalt, or a combination.[226] The high cost, limited resources, and toxicity of cobalt have become the reason for the popularity of the Li-Ni-Mn-O system among Li-rich materials.[229, 230]

2.2.3.2.2. Polyanionic compounds

Polyanionic compounds include a component with strong covalent bonding between the tetrahedral polyanion structure and their derivatives with transition metal oxide (**Figure 26**).[231, 232]

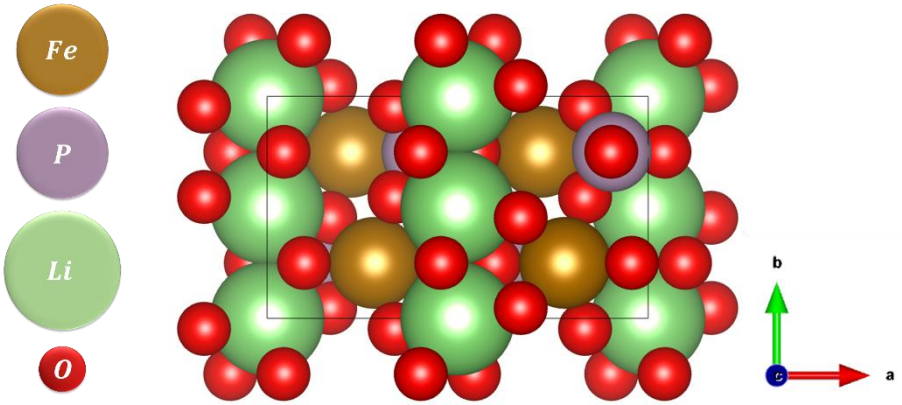

Figure 26. Polyhedral illustration of a $LiFePO_4$ unit cell (adapted from Ref.[40]).

Compared with conventional layered transition metal oxides, polyanionic compounds have stability and higher thermal tolerance, which makes them more attractive to employ in LIBs.[211, 233-235] The interest in polyanion compounds started with the $LiFePO_4$ electrochemical performance report.[209, 235, 236] Polyanic compounds include the Olivine structure (including carbon nanoparticle-coated $LiFePO_4$ and polymer-coated $LiFePO_4$), tavorite structure (including fluorosulfates and fluorophosphate), orthosilicate, and borate.[237-239]

The Olivine-type cathode working potential ranges at 2.0-5.0 V vs. Li^+/Li and can deliver a reversible capacity of 110-175 mAh g^{-1}.[233-241] Tavorite-structure cathodes with the general $M(PO_4)$ or $M(SO_4)$ formula are gaining attention due to their high stability and long cycling performance.[242-249] The tavorite structure cathode working potential ranges between 2.0-5.2 V vs. Li^+/Li and can deliver capacities around 100-150 mAh g^{-1}.[242-249] Borate components, such as hexagonal-$LiMnBO_3$, have working potentials ranging between 1.2-4.8 V vs. Li^+/Li and can provide a capacity between 90-140 mAh g^{-1}.[242, 250, 251] The orthosilicate components, such as Li_2MSiO_4 (M=Fe, Mn, Co, Ni) as the cathode, operate in the working potential ranges between 1.5-4.8 V vs. Li^+/Li and can deliver a capacity up to around 250 mAh g^{-1}.[252-255]

2.2.3.2.3. Mn-based spinel oxide

Face-centered cubic (FCC) spinel lithium manganese oxide (LMO) with the formula of $LiMn_2O_4$ has been widely explored for cathode materials.[256] LMO has a theoretical capacity of 148 mAh g^{-1} with an electrical conductivity of 10^{-4} S cm^{-1}, an ion conductivity of 10^{-6} S cm^{-1}, and working potential of around 4.1 V vs. Li^+/Li.[257, 258] LMO has advantages over other cathode materials, such as high thermal stability and high energy density due to high working potential, high capacity, low toxicity, long cycle of life, and good safety.[259, 260] One reason LMO has

received widespread attention is its three-dimensional 3D structure for Li^+ insertion, which is depicted in **Figure 27**.[261] The 3D host network functions well and can improve ion transport and capability, especially at high rates.[260, 262]

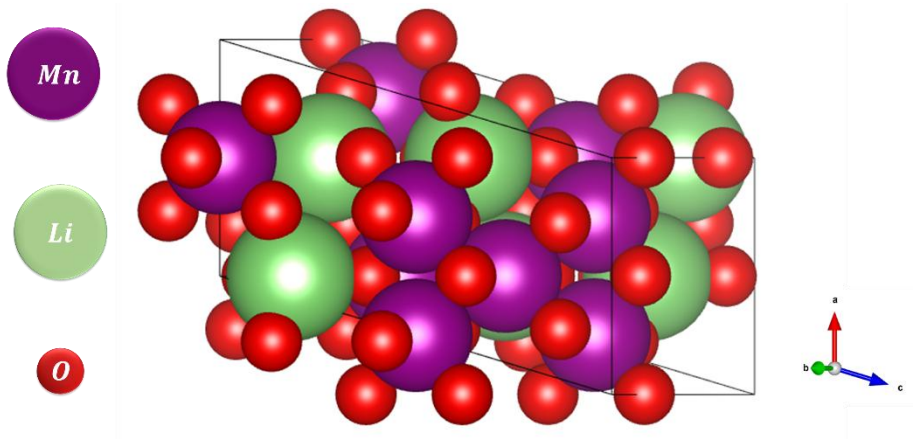

Figure 27: Polyhedral illustration of the structure of the spinel $LiMn_2O_4$ (adapted from Ref.[40]).

MOs have a cubic structure, and in terms of crystallography, they belong to the $Fd\bar{3}m$ symmetry group. The structural formula for LMO is ($[Li^+]_{(8a)}[Mn^{3+}, Mn^{4+}]_{(16d)}O_4$), and it can be represented by the crystal lattice of $Li_{(8a)}[Mn_2]_{(16d)}O_4$ model.[262] Thus, 16d, 8a, and 32e sites are occupied by manganese, lithium, and oxygen, respectively.[262] LMO has limitations, such as capacity fading caused by structural transformation and transition metal dissolution.[263]

The dissolution of manganese ions during the cycling process occurs in the organic electrolyte due to the disproportionate reaction, as shown in **Equation 16**.[263]

$$\boldsymbol{2Mn^{3+} \rightarrow Mn^{4+} + Mm^{2+}} \qquad \textbf{Equation 16}$$

One of the challenges to fully understanding the electrochemical capabilities of the LMO cathode and its application in LIBs is metal dissolution based on the Jahn-Teller distortion phenomenon.[95, 258, 264] The structural Jahn-Teller (J-T) distortion in the discharge state is related to different structures of manganese.[57, 179] LMO involves many structures and tie-lines associated with the nature of manganese, which can have different oxidation states.[95, 258, 264] The most important oxidation states are II, IV, and VII, where II is the most stable.[265] The reason is that the average oxidation state of manganese (n_{Mn}) is 3.5+ due to the equal ratio of Mn^{3+} and Mn^{4+} in octahedral site cubic spinel LMO.[258]

$Li_{1+x}Mn_2O_4$ (Redox couple of Mn^{4+}/Mn^{3+}) is responsible for the charge compensation for the LMO lithiation.[95] The octahedral Mn^{3+}, which is (1+x; x>0), is the mentioned formula and is a J-T ion, unlike the Mn^{4+} (1-x; x>0).[95] During cycling, degradation of LMO occurs while more than half of the total magnesium percent is Mn^{3+}.[89, 264] The Mn^{3+} insertion inside the cubic

lattice changes it to a tetragonal shape. In reverse, the delithiation cubic symmetry of LMO in the complete range of (0 < y < 1) for $Li_{1-y}Mn_2O_4$ can be maintained.[139, 264, 266, 267] In LMO, ideally, when (y = 0.5) Li-ion in both interpenetrating FCC Li patterns subsets occupies a diamond-like array at 8a sites.[259] The lithiation of Li^+ in an anode vs. LMO can be explained as a two-stage electrochemical process as shown in **Figure 28**. [258]

The main reason for the two plateaus in the LMO lithiation/delithiation is the behavior of Li-ion ordering in the Mn^{+4}/Mn^{+3} redox couple.[258] In the first stage, it is faced with a decrease of about 0.15 V to the limit of 4.1 V vs. Li^+/Li, and then, with a tetrahedral-to-octahedral Li sublattice shift, it shows a further decline.[258] This phenomenon affects LMO cycling, limiting it to one lithium atom for every two manganese atoms in each cycle.[264]

In the first stage, the single-phase reaction happens at a voltage plateau of around 4.1 V vs. Li/Li+, as shown in **Equation 17**.[258, 264] The second process, around 2.8 V vs. Li/Li^+, is related to the two-phase single reaction in the second stage, as shown in **Equation 18**. [258, 264]

$$LiMn_2O_4 \rightarrow Li_{1-X}Mn_2O_4 + x0.5Li^+ + x0.5e^- \ (x < 0.5) \qquad \textbf{Equation 17}$$

$$Li_{1-X}Mn_2O_4 \rightarrow 2MnO_2 + (1-x)Li^+ + (1-x)e^- \ (x > 0.5) \qquad \textbf{Equation 18}$$

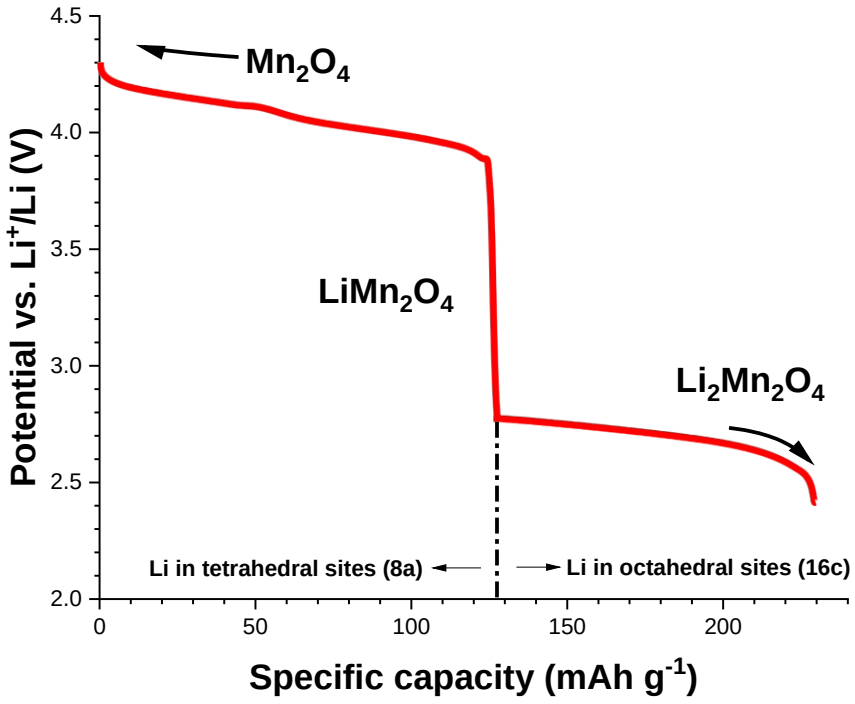

Figure 28. Galvanostatic charge curves for Li-ion lithiation and delithiation of LMO cathode material (adapted from Ref.[95]).

2.2.3.3. LIB Electrolytes

Electrolytes act as storage and carriers of the ions and have been extensively researched for their use in LIBs.[84, 268] Some crucial factors such as voltage range, conductivity, viscosity, thermal stability wetting properties, compatibility, and cost play a role in determining the suitable electrolyte to be used.[84, 268] To qualify as an electrolyte, a substance must fulfill criteria:[24]

- It should efficiently conduct ions without conducting electricity.
- It should not react with electrodes.
- It should withstand temperature changes without degradation.
- It should be safe to handle and also cost-effective.

Four categories of electrolytes utilized in LIBs can be mentioned organic electrolytes, aqueous electrolytes, ionic liquid electrolytes, and solid-state electrolytes.[269] Below is an overview of the types of electrolytes employed in battery technology.

2.2.3.3.1. Organic electrolytes

Organic electrolytes are currently the most common type of electrolyte used in batteries in cellphones, laptops, and electric and hybrid vehicles.[270] An organic electrolyte usually dissolves a metal salt with weak and large coordinating anions to a standard 1 mol dm^{-3} concentration.[271] These types of electrolytes, such as ethylene carbonate (EC), propylene carbonate (PC), and dimethyl carbonate (DMC), and their mixtures have ionic conductivity of around 10 mS cm^{-1} plus with a wide electrochemical window around 4 V.[270, 271] The main consideration for applying this type of electrolyte on a commercial and industrial scale is safety due to the flammability of organic electrolytes.[272] There is a great demand for safer solvents, such as γ-butyrolactone and sulfolane, with cost-effective pathways and a smaller environmental footprint.[273]

2.2.3.3.2. Aqueous electrolytes

Aqueous electrolytes are often a cost-effective option compared to organic electrolytes.[274-276] However, a challenge arises when the potentials surpass 2.5 V, leading to water splitting into hydrogen and oxygen gases, which poses an obstacle for using electrolytes.[274, 275] To address this issue, utilizing materials that can prevent the oxidation and reduction of water can help

widen the window.[277, 278] Another significant difficulty for these electrolytes is finding materials that are compatible with redox reactions within the restricted electrochemical window.[276, 279] For instance, graphite material is not suitable for use in LIBs due to the intercalation of Li^+ into graphite occurring below the potential of hydrogen evolution at -2.9 V vs. SHE.[276, 280] In studies, researchers select this electrolyte over nonaqueous ones when investigating cathode materials.[274, 275, 280, 281] This decision was influenced by the belief that the simple nature of this electrolyte can provide a conducive environment for exploring the fundamental aspects of the Li-ion intercalation/deintercalation process compared to nonaqueous alternatives.[274, 275, 280, 281]

2.2.3.3.3. Solid electrolytes

The flow of ions between the electrodes is the main role of an electrolyte, and liquid electrolytes can facilitate that aim.[282] However, some cons, such as electrochemical and thermal instability, cost, and safety, justify considering a new class of electrolyte.[282] Solid electrolytes can be classified into two categories, inorganic and organic, and can be used for metallic anodes and sulfur cathodes with high capacity.[85] One example of an inorganic solid electrolyte is β-alumina, a polymorph of Al_2O_3 with an unusual, layered structure commercialized in the 1960s and can be used in high operation temperatures where both anode and cathode material are molten. In inorganic electrolytes, constant swelling and shrinking of the material where the electrodes undergo large volume changes.[283]

This is the main issue with inorganic electrolytes and can result in a lack of contact with the electrode, and the cell will die if the contact is disrupted.[284] Organic material development back in 1973 was shown, channeling the ions possible in these classes of electrolytes.[285-288] Poly(acrylonitrile),[285] poly (vinylidene fluoride)[287], and poly (methyl methacrylate) are the usual types of organic solid electrolytes, and poly (ethylene oxide) (PEO) is the most popular one used for LIBs.[288] Organic solid electrolytes, compared with inorganic solid electrolytes, are less thermally stable, and as a result, they can operate in lower potential windows. [285-288]

2.2.3.3.4. Ionic liquid electrolytes

Ionic liquids, such as aluminum trifluoromethane sulfonate and $AlCl_3$ mixed with 1-ethyl-3-methylimidazolium chloride, are also electrolytes that can be utilized in LIBs.[289, 290] These liquids exhibit better conductivity compared to organic electrolytes because of their high ion content and can resist an electrochemical stability range of up to 3.25 V. [289, 290] Researchers are

exploring the potential use of ionic liquids as safer substitutes for organic electrolytes, in rechargeable LIB systems to improve device safety.[291, 292] Ionic liquids are known for their ion transport and wide chemical, electrochemical, and thermal stability.[293, 294] Although individual ionic liquids may not consistently meet all device requirements or operating conditions, their properties can be precisely adjusted by modifying their structure.[295, 296]

2.2.3.4. Other components for LIBs

When designing batteries, enhancing the specific energy of LIBs is all about increasing the proportion of materials or components that actively participate in electrochemical reactions, aiming for as close to unity as possible.[37] Simultaneously, efforts are made to reduce the percentage of materials and components that do not contribute to these reactions.[297] The path forward for LIBs involves advancing and refining the production methods and exploring new materials that don't actively participate in the electrochemical processes.[297] A full battery includes many necessary components, even though the anode, cathode, and electrolyte normally are the center of focus for LIBs research.[297, 298] Some components, including separators, binders, current collectors, and conductive agents, will be briefly discussed.

2.2.3.4.1. Conductive agent

Other important agents in cell components whose type and morphologies greatly impact the LIBs storage performance are conductive agents, even though they occupy a tiny mass percentage.[299, 300] Building a multidimensional conducting network is the goal for conductive agents, which is greatly affected by the mass ratio.[299, 301, 302] The increased performance is due to different mechanisms caused by the conductive agents, such as polarization prevention during lithiation and delithiation at high rates and cell internal resistance reduction, which improves electrolyte absorption.[301] There are various types of conductive agents used in LIBs, including vast groups of nanostructured carbon materials such as 1D-carbon nanotubes, 2D-graphene, and the most popular one, 0D-carbon black, or a combination.[300, 302]

2.2.3.4.2. Current collector

The current collectors are usually metallic substrates in LIBs and act as agents that hold the electrode materials together and collect and deliver the electrons to the electrode mass loading.[303] The main conditions for selecting the current collector materials include inactivity

during the cell operation (to avoid corrosion) and conductivity.[304] In LIBs, due to their low cost and anti-corrosion behavior, aluminum foil (Al-foil) is the most frequently used current collector for cathode electrodes and some anodes.[304] Also, copper foil (Cu-foil) is used due to the inactivity of low potential in LIBs system for anode material.[305, 306] Other substrates, such as molybdenum or tungsten, can be used as a current collector, but they can increase the cost by up to 70%.[305, 306] Despite being susceptible to corrosion, steel could be suitable due to cost efficiency, and also carbon-based materials can be a good option.[303, 305, 306] However, what is evident is that development in the current collectors can be highly dependent on electrolyte advances.[303]

2.2.3.4.3. Binders

Binder materials keep the components of electrodes, such as active material, conductive agent, etc., together by boasting mechanical properties and adhesion abilities.[307-309] The binder can have a crucial effect on battery performance if we consider the following points caused by binder degradation.[310-313]

- There is a risk of losing contact due to the weakening of the mechanical stability of the electrode.[310-312]
- Decrease of practical capacity in forming LiF species immobilizing lithium.[310-312]
- Increase the total impedance of the cell ascribable to highly electronically and ionically resistive LiF.[310-312]

These components include SBR, which are strands of styrene-butadiene rubber, PTFE (polytetrafluoroethylene), and PVdF (polyvinylidene fluoride, the structure of which is shown in **Figure 29**).[307-310, 314-316]

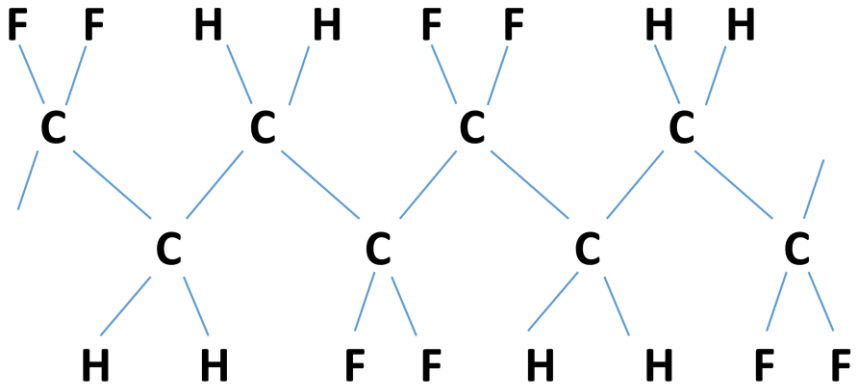

Figure 29. The structural formula of the polyvinylidene fluoride (adapted from Ref.[319]).

PVdF, due to its combination of electrochemical and thermal stability, can be used for anode and cathode electrodes in LIBs.[310-312, 314, 317, 318]

2.2.3.4.4. Separators

Separators can be defined as glass microfiber (in the lab or on a small scale) or carbon-based polymers, particularly polyolefin barriers (on an industrial and commercial scale).[320] The separator is moistened with electrolytes and acts as a catalyst to help ions move from the cathode to the anode during charging, and in the opposite direction during discharging.[321] Ions, which are atoms that have lost or gained electrons, become electrically charged.[321] Although ions move freely between the electrodes, the separator itself is an insulator and does not conduct electricity.[322] Separators are usually placed between the anode and cathode to preserve conditions such as allowing the active species to flow and avoiding short circuits.[320] Advances in separator materials are in different directions.[323] For example, on an industrial scale, polymer separators have been customized to melt and act as a complete barrier in case the temperature gets too high.[324] In this, any further ion flow will be completely cut, resulting in the battery shut down in a fail-safe mechanism.[320, 323, 325] From another perspective, technological developments in thinner materials, which ease the flow of the active species, and eco-friendly sources, such as cellulose, which reduce the environmental impact of functionalized polymers, are in demand.[326]

2.3. Supercapacitors

Supercapacitors also referred to as ultracapacitors and electric double-layer capacitors, have attracted attention for their charge/discharge speeds (1-10 s) and enhanced cyclic stability (>30,000 cycles) for their toughness and ability to function in a temperature range (-40 °C to +70 °C), and markable power from a power standpoint.[327-335] A supercapacitor operates as a system for pulse currents utilizing levels to achieve exceptional specific power.[327-335] From a power standpoint, a supercapacitor operates as a system for pulse currents utilizing levels to achieve very high specific power (10,000 W Kg^{-1}) in under a minute.[332, 336] The introduction of supercapacitors dates back to 1978 when NEC Corporation (Nippon Electric Company, Limited) implemented them as power sources for computer memory.[330]

Since then, supercapacitors have developed into energy storage solutions with applications that leverage various energy storage mechanisms and deliver performance that complements

LIBs.[327, 328] A supercapacitor consists of two electrodes, an electrolyte, and a separator, as illustrated in **Figure 30**.[337]

On one side, the properties of the materials can impact the range of the electrodes and greatly influence how well the supercapacitor works.[330, 331] Conversely, the electrolyte, typically a mix of salt and solvent, helps balance the charge on both electrodes by aiding conductivity within a cell.[335, 336] The electrolyte is crucial for predicting supercapacitor performance and plays a role in storing electric charge.[330, 332, 333] Various electrolytes with sizes/types and ion/solvent concentrations are utilized for supercapacitors, such as aqueous organic and ionic liquid electrolytes.[330, 332, 333, 338] In terms supercapacitors are categorized into three groups based on how they store energy; Electrical double-layer capacitors (EDLCs), Pseudocapacitors (PCs), and hybrid supercapacitor batteries (HSC).

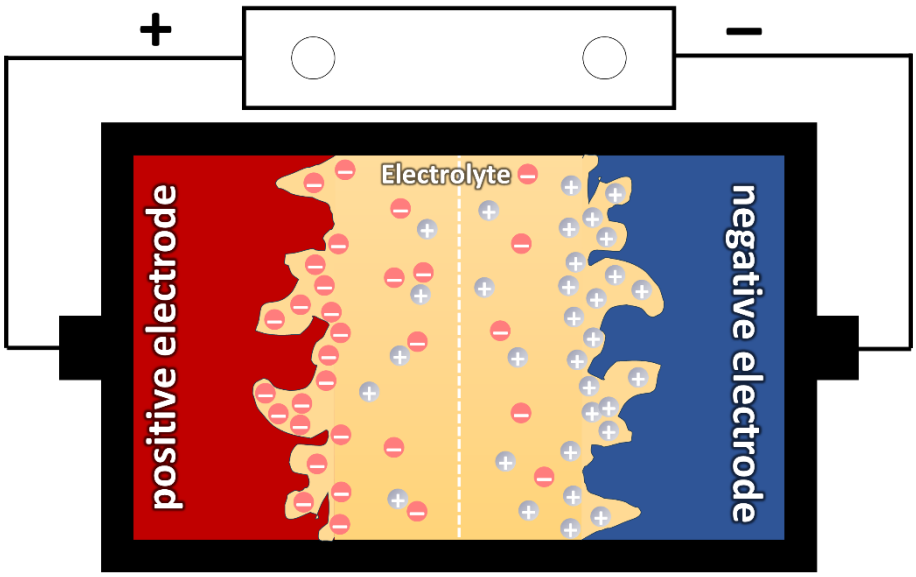

Figure 30. Schematic view of a symmetric electrical double-layer capacitor using porous electrodes in the charged state (adapted from Ref.[337]).

- **Electrical double-layer capacitors** store energy using ion electrosorption. The electrical energy stores the energy at the interface of the electrode and the electrolyte, where the electrical double-layer capacitance forms because of the electrostatic attraction between the polarized electrode and the electrolyte counter-ions.[332-335] The accumulation of electrons at the electrode is a non-Faradaic process; hence, no redox reaction occurs.[332-335] In EDLCs, used electrode materials include carbon-based substances like activated carbon (AC) and graphene due to their affordability, high electrical conductivity, and easily created structures.[332-335]

- **Pseudocapacitors** operate through the process where electrons are directly transferred through oxidation at one electrode and then reduction at the redox reaction.[332, 333] In pseudocapacitors, capacitance is achieved by exchanging charge between the electrolyte and the electrodes in a similar manner to how batteries work.[327-335] Pseudocapacitors are used for high-power applications requiring rapid charge/discharge and long cycle life but offer lower energy density. Batteries are better suited for applications with high energy density and longer-term energy storage, but there are trade-offs in power density and cycle life.[327-335] Pseudocapacitors provide more competitive capacitance compared to EDLCs due to their higher energy density. This makes them more promising for enhancing the specific energy and power density of supercapacitors.[330, 332, 333] The most studied pseudocapacitive materials by far are transition metal oxides, conducting polymers, and composite materials.[327-335] Materials with fast reaction kinetics, improved dynamic reaction, structural stability, and conductivity are highly crucial to achieving a long lifespan of supercapacitors.[339, 340]
- **Hybrid supercapacitor batteries** have been developed and investigated to compensate for the limitations of EDLCs and LIBs.[303, 339, 341, 342] **Figure 31A-C** schematic illustration of LIB, EDLC, and asymmetric hybrid battery capacitors to simply demonstrate the major differences between the three energy storage devices.[303, 339, 341, 342] Mainly, Hybrid supercapacitor batteries use both battery-type and capacitor-type electrodes, making it a high energy and power output and fast charging device: it acquires the energy output from the battery-type electrode, while the power output and quick charge/discharge rate come from the capacitor-type electrode.[339, 340, 343] They offer a compelling solution for applications requiring both high energy and power densities, alongside long-term durability and safety.[303, 339, 341, 344] However, the drawback of HSCs is even though they exhibit high specific energy at low current density, this advantage diminishes significantly at higher current densities, limiting their practical applications.[303, 339, 341, 344]
- The Li-ion capacitor composed of graphite anodes and active carbon cathodes in an organic electrolyte based on carbonates is the most recognized example of an asymmetric HSC; at present, this cell type is already on the market.[345, 346] Theoretically, it is possible to reverse this electrochemical arrangement and establish a hybrid supercapacitor with a positive electrode from a LIB and a negative electrode from an electrical double-layer capacitor.[347] The first asymmetric HSC in this configuration can be assembled using LTO as an anode

material and activated carbon as a cathode material.[348] An electrical double layer is created at the interface between the activated carbon cathode and the electrolyte. At the same time, Li-ion migrates from the Li-ion-containing electrolyte and integrates into the crystal structure of the LTO anode.[347]

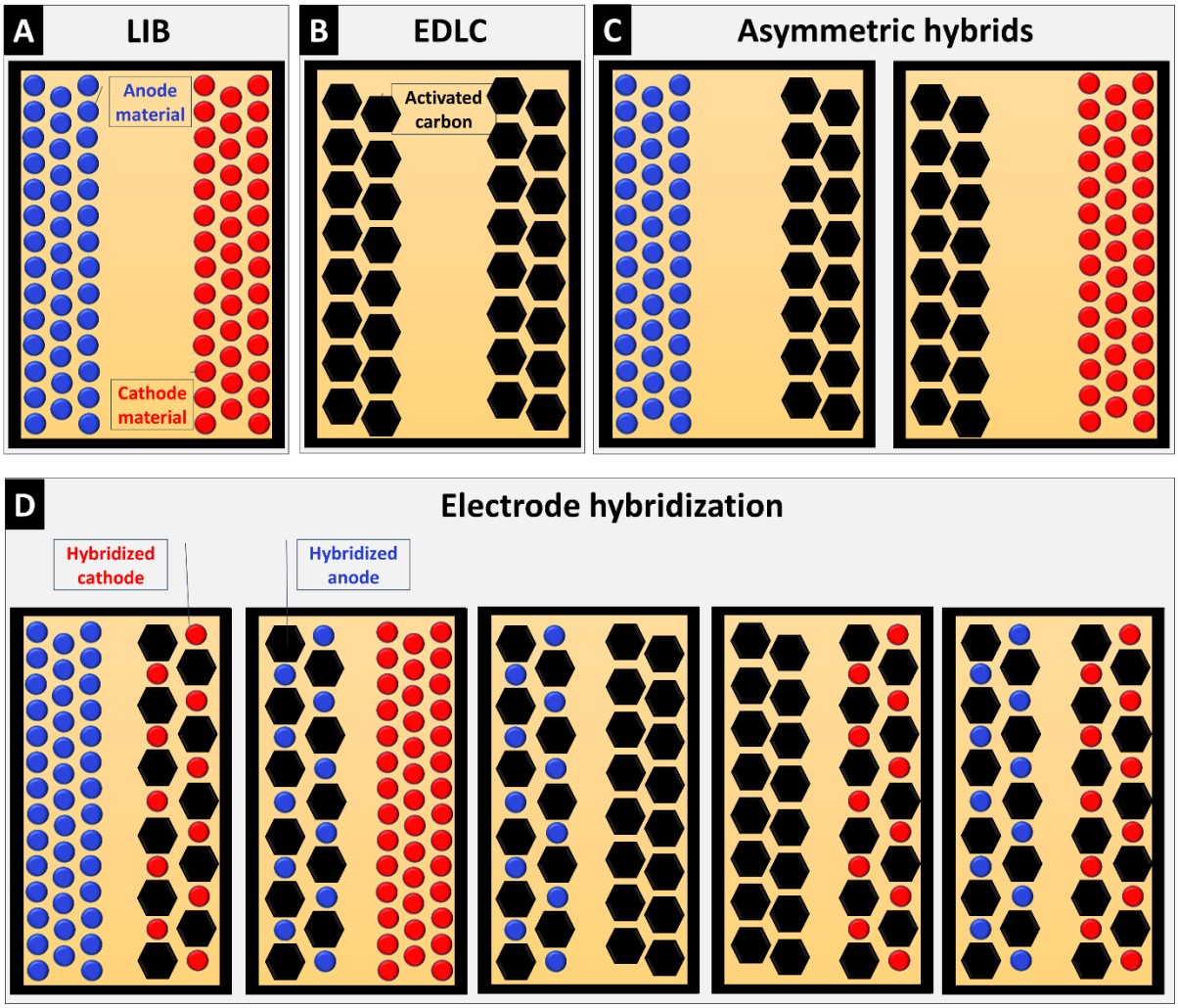

Figure 31. Schematic view of **(A)** LIB, **(B)** EDLC, **(C)** asymmetric hybrid, and **(D)** hybridization of the electrode. Blue/red spherical particles indicate active material particles, while activated carbon is shown as regular black hexagons.

- Another way to achieve hybridization involves combining Faradaic charge storage materials with highly porous carbon materials in the same electrode.[349, 350] Two distinct approaches to achieve this electrode hybridization are utilizing hybrid materials or forming composite electrodes.[349, 350] In the former approach, Faradaic energy storage materials are directly incorporated during the synthesis of materials onto materials such as activated carbon, carbon nanotubes, carbon nanofibers, onion-like carbons, or graphene.[351-357] Concurrently, the capacity and energy are boosted by the presence of the Faradaic charge storage

material.[349] The hybrid material approach offers precise control over electrochemical performance by adjusting process parameters, allowing the tuning of charge storage mechanisms.[349] The latter approach to hybridize electrodes involves mixing LIB materials with activated carbon, all in the same electrode, through mechanical mixing as shown in **Figure 31D**.[358, 359]

This combination not only sidesteps the issue of blocking pores in the activated carbon but also lowers the cost with readily available materials.[358, 359] It would be possible to hybridize both electrodes simultaneously or mix and match by pairing a composite electrode with a LIB or an EDLC electrode.[360, 361] The materials already used for HSC are $LiMn_2O_4$, lithium phosphate, $LiFe_PO_4$, and hard carbon; all possess stable structures and exhibit no side reactions with electrolytes.[331, 339-341, 348, 362-365] The LTO characteristics such as zero-strain material because of minor volume changes (about 0.2%) during lithiation and delithiation, stability, and long cycling performance have been vastly used in hybrid supercapacitor batteries as anode material.[341, 354] Meanwhile, spinel LMO has been considered a favorable cathode material candidate due to its 3D-ion diffusion channels, low cost, safety, high natural abundance of manganese, and relatively high capacity.[339-341, 348, 364, 365]

2.4. Dry electrode process

The dry electrode technology is quickly gaining recognition as an advancement for the generation of batteries, especially LIBs.[366] Its introduction into the battery industry has brought about changes in production methods and electrode microstructure.[366] At the core of this technology is the removal of solvents. Unlike LIB manufacturing, which involves creating a slurry with materials and solvents, the dry electrode process directly applies a dry powder of active materials onto the current collector, eliminating the need for solvents.[366, 367] This streamlined approach reduces production steps compared to methods that require solvent mixing, coating, drying, and solvent recovery processes along with equipment and energy inputs.[368, 369] The dry electrode method simplifies manufacturing by eliminating these stages, making the production line more efficient.[369] Various techniques have been developed for the electrode process, with some common ones being the spraying deposition process, polymer fibrillation process, extrusion and melt process, and mechanical compression process. Descriptions of these techniques have been provided here.[367]

- **Extrusion and melt process: The** process involves using heat and mechanical pressure to mix active materials, conductive additives, and polymer binders as illustrated in **Figure 32**.[367, 369, 370]

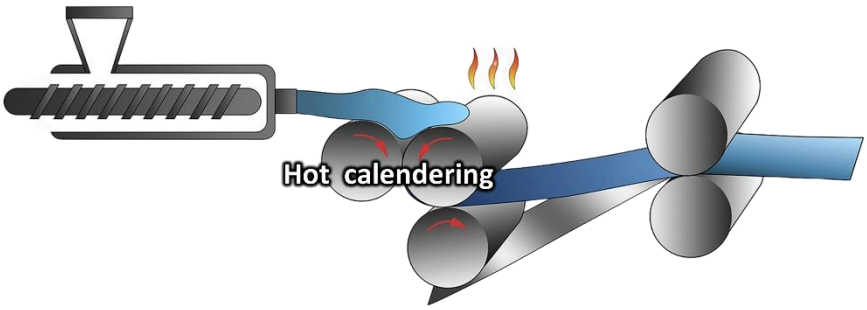

Figure 32. Schematic view of a typical procedure for applying extrusion and melt method for electrode preparation (adapted from Ref. Copyright Elsevier 2024[369]).

In this process, all the components are introduced into an extruder device where they are heated until the polymer binders melt for the mixing process. The resulting molten mixture is then extruded through a die to shape it into a sheet or a specific form before being cooled.[371] This method allows for control over composition, thickness, uniformity, and mechanical strength.[371, 372] However, it is important to adjust temperature settings and extrusion parameters to ensure material consistency and optimized performance when it comes to large-scale production.[372]

- **Dry spray deposition process**: As shown in **Figure 33**, this process involves converting materials into aerosols and applying them onto a substrate. In the next step, heat or pressure activates binders for particle adhesion and mechanical stability.[369, 373-375]

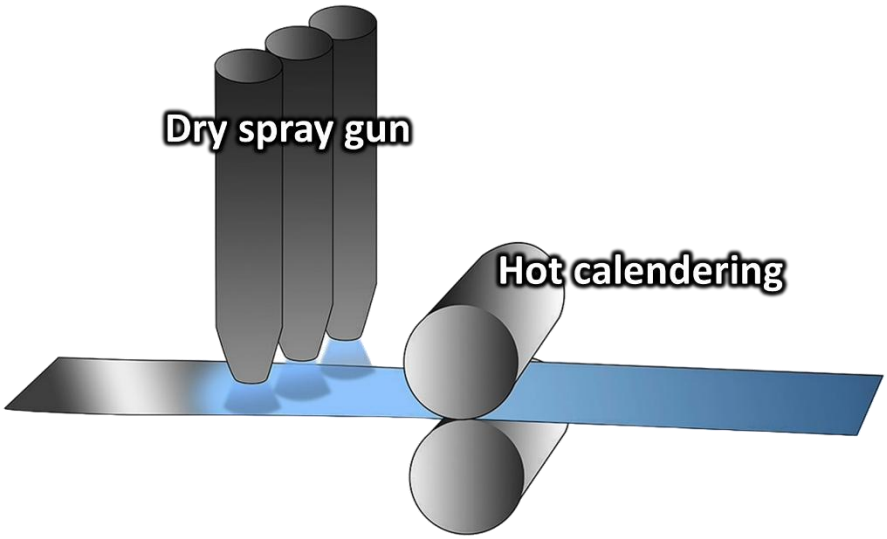

Figure 33. Schematic view of a typical procedure for applying dry spray deposition method for electrode preparation (adapted from Ref. Copyright Elsevier 2024[369]).

This technique aids in reducing compound emissions and minimizing energy and material costs, potentially improving the homogeneity of materials and performance.[375] However, challenges such as managing powder flowability and ensuring proper deposition control may be faced.[376, 377] The difficulties mentioned in adapting the process remain a challenge.[376, 377]

- **Polymer fibrillation process**: The process of polymer fibrillation can be explained as converting polymer binders into networks to improve the properties and structural integrity of battery electrodes, as illustrated in **Figure 34**.[368] In the first step, active materials, conductive agents, and polymer binders are mixed.[378, 379] These components go through stress from extrusion calendering or shearing processes, causing the polymer binders to form fibrils that twine with parts to create a structure.[380] Key challenges include ensuring fibrillation and optimizing processes for quality and performance during large-scale production should be met.[380]

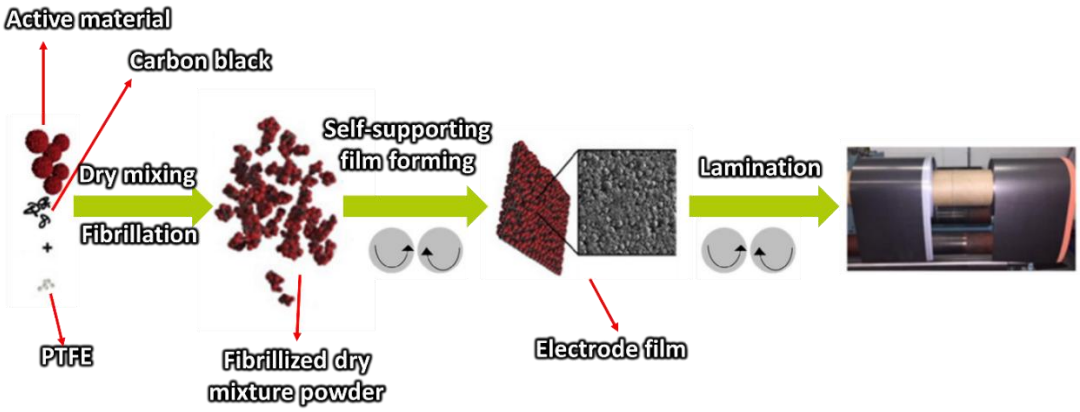

Figure 34. Schematic view of a typical procedure for applying polymer fibrillation method (PTFE fibrillation) for electrode preparation (adapted with permission from Ref. Copyright Elsevier 2023 [368]).

Mechanical compression process: As illustrated in **Figure 35**, involves pressing a mixture of active materials, conductive additives, and polymer binders to create a solid and united electrode.[368, 381-383] To start, the dry powder blend is evenly spread on a collector. Then, it is compressed under high pressure using methods such as calendering.[381] This compression step helps to compact the materials into a layer and ensures that there is contact between particles and even distribution of binders.[384] By enhancing the strength and electrical conductivity of the electrode, mechanical compression plays an important role in its performance.[384] However, challenges appear in maintaining pressure distribution and optimizing compression

parameters for large-scale production to become confident that material unity and performance reliability.[384, 385]

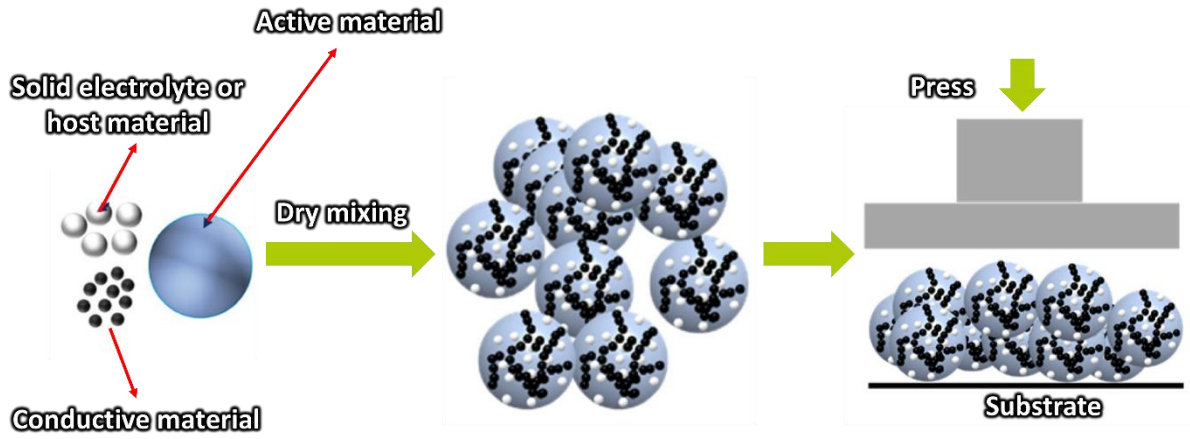

Figure 35. Schematic view of a typical procedure for applying mechanical compression method for electrode preparation, adapted with permission from Ref. (Copyright Elsevier 2023) [368]

The dry electrode process offers cost benefits due to the elimination of solvent-related steps that cut down energy use and reduce the need for costly equipment used in drying and solvent recovery.[386] This results in production expenses and more cost-effective batteries.[366, 386] Additionally, the dry process is eco-friendly as it reduces emissions that can contribute to pollution.[387] By excluding the usage of solvents, this method helps reduce pollution and minimizes the risks associated with handling these chemicals.[387, 388] Apart from cost and environmental advantages, the dry electrode process plays a role in boosting battery performance in many ways.[387, 389] Greater energy density translates to battery life.[388, 389] Improved power storage capacity, vital for applications across consumer electronics and electric vehicles.[390, 391]

Furthermore, the dry electrode process can modify microstructures to enhance ion transport efficiency and mechanical strength.[390, 392] This could result in batteries that do not perform better but have extended lifespans.[393] However, implementing the process in LIB manufacturing comes with challenges that must be addressed for a transition from wet processes.[393] Key concerns include binder selection since binders must offer cohesion without solvents while maintaining integrity and electrical connectivity.[393]

Creating mixtures of materials with densities is a challenging task without the use of a liquid medium as it can lead to potential separation.[394] Moreover, it is important for the process to

strike a balance between cohesion and adhesion since solvents, which are commonly used as adhesives, are not present.[392, 394] Specialized equipment is essential for handling and blending particulate materials while compacting them into uniform films.[391] Additionally, integrating the process with wet production lines may require significant adjustments that call for substantial investment.[391] While the dry method holds promise in terms of advantages, it is crucial to address these obstacles before incorporation into LIB manufacturing.[392]

2.5. Digitalization of battery manufacturing

The increase in electric vehicles (EVs) is related to expansion, technological progress, growing consumer interest, and substantial investments from car manufacturers.[395, 396] Despite facing some challenges, the overall outlook for this industry looks promising, with an expected 70 percent of all travelers choosing EVs as their pick of transportation by 2040.[397] Significant advancements have been achieved in LIBs technology with improvements in energy capacities extended lifespan and reduced battery costs.[398, 399] The manufacturing and assembly processes play a role in enhancing the performance of these batteries.[400, 401] Enhancements in these areas impact the development of environmentally friendly energy storage systems. The nature of modern technology necessitates that manufacturing systems transition towards intelligent procedures, driven by advancements in tools, machinery, interface components, and the workforce.[400, 401]

This shift focuses on aspects like enhanced intelligence and customized sustainable manufacturing methods to Integrate battery research and innovation to drive advancements toward Industry 4.0.[398, 399, 402] Despite the successful giga-scale production of LIBs that led to significant cost reduction, it still faces challenges in maintaining operational and quality standards.[403, 404] With the precise sequential steps in the battery manufacturing chain and the complex adaptability of these steps with many individual process parameters, there is a key need for optimization beyond the conventional trial-and-error approach.[401, 405] This is exactly where digitization-based automation can play an important role. Creating virtual copies of the actual manufacturing process can accelerate time to market and increase profitability by

reducing cell prototyping and optimizing costs.[400, 405] These virtual improvements can minimize the costs associated with redesign and tool changes if problems are identified before the pre-series launch. [399, 402]

Additionally, the operations of digitalized giga factories are expected to optimize production in real time, enhancing productivity, product reliability, and overall quality.[406] The concept of digitalization has proven successful in various domains, such as converting analog product features into digital values.[396, 402] These facilitate electronic and informational transfer, storage, and data processing.[407] While some aspirations for digitizing the battery manufacturing process are ambitious, the vision is to progress toward automated decision-making, unmarked mechanical automation, and symbiotic integration with human input.[406, 407] The ultimate goal is to have battery manufacturing facilities that are entirely interconnected and smart, spanning from raw materials to the production of finished battery cells.[407]

The future of battery manufacturing relies on digitalizing the process using digital twins (DTs).[407, 408] This transformation significantly benefits product quality, resource efficiency, production time, and cost.[408, 409] However, the extensive use of data in DTs requires careful consideration of data accuracy, security, and evolving technology challenges to meet goals in battery manufacturing digitalization.[408, 410] Battery manufacturing proposed a three-structure with main steps, including electrode preparation, cell assembly, and battery activation by formation.[408, 411] Three levels can be defined to achieve these aims, including digital manufacturing framework, models, and standards (**Figure 36**).[412]

The first level is the digital manufacturing framework, which is associated with data collection from the physical manufacturing and adjustment with the communication network, relying on real-time data sharing.[410, 412, 413] The digital manufacturing framework is like a smart system that helps machines communicate and process information.[396, 409] Ensuring machines can communicate with each other is important for creating DTs.[409, 413] These DTs need to share real-time information with the machines. At the same time, special sensors are used to measure important things during the manufacturing process.[413]

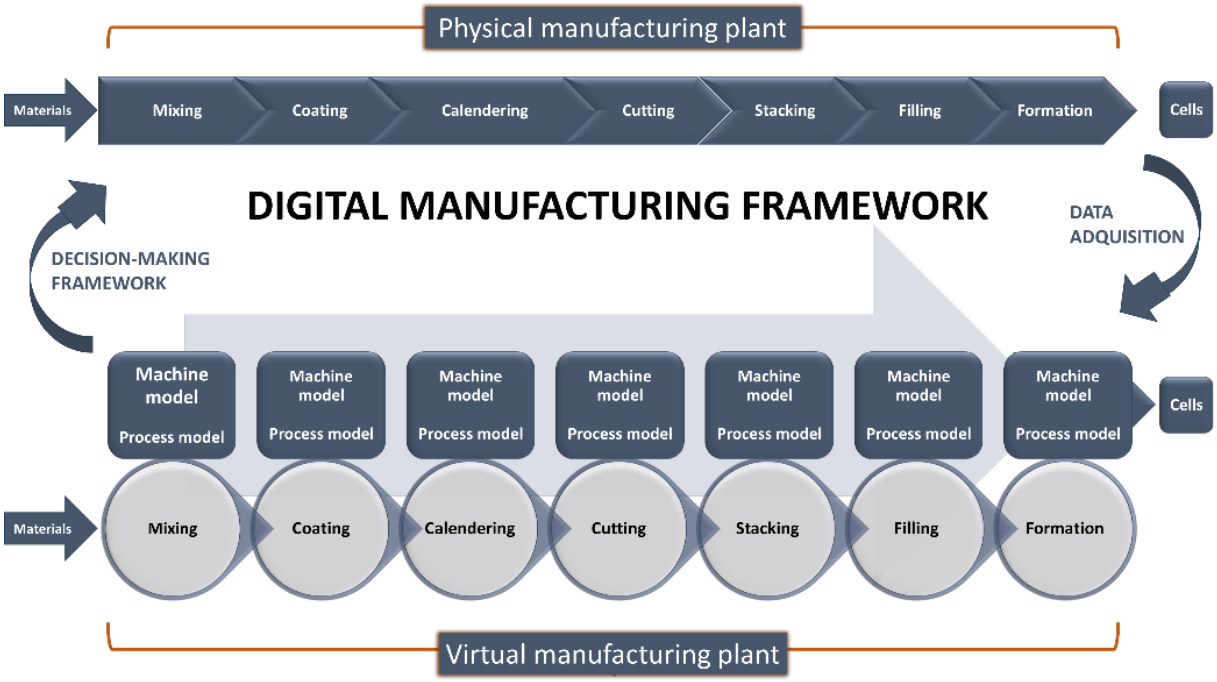

Figure 36: Illustration of a protocol for manufacturing LIBs that integrates digitalized machine learning and artificial intelligence (adapted from Ref.[395]).

All this information is stored in a central place so we can look at it later to improve the manufacturing process or resolve any problems.[395] The digital manufacturing framework includes data acquisition, interoperability, communication protocols, ontologies for battery manufacturing, and digitalization frameworks and APIs.[395] The model's second level defines the **manufacturing routes** of structural parameters, machines, and equipment, while the third one is associated with **standards** that provide extensive mechanisms to determine the stages necessary for the full digital approach.[412, 414] Overall, to address the challenges in manufacturing, experts from both academic and industrial backgrounds should explore various options to develop a user-friendly tool that organizes and integrates with the newly revolutionized manufacturing process.[415, 416]

An example of a manufacturing process is illustrated in **Figure 37** to explain the mentioned processes in more detail.[398] The manufacturing process includes numerous inter-connected variables such as physical, chemical, interfaces, electronic, and ionic transport properties.[398]

- Firstly, creating a digital tool with AI algorithms to validate physics-based and multiscale models is essential for the long-term plan. [406, 415] This process aims to integrate the diverse next generation of manufacturing technologies beyond just batteries and across various fields.[406, 415]
- Secondly, supporting battery second-life applications involves recycling, swapping, fast charging, life cycle, and thermal management systems.[415, 416] Next, application-oriented manufacturing involves effective database management, data visualization, and virtual manufacturing techniques.[415]
- Finally, tools for processing and recycling spent LIBs were created to enhance battery capacity's quality, reliability, and lifespan.[415] It is important to implement accurate multisensory monitoring across the interface, cell, and system levels.[416, 417]

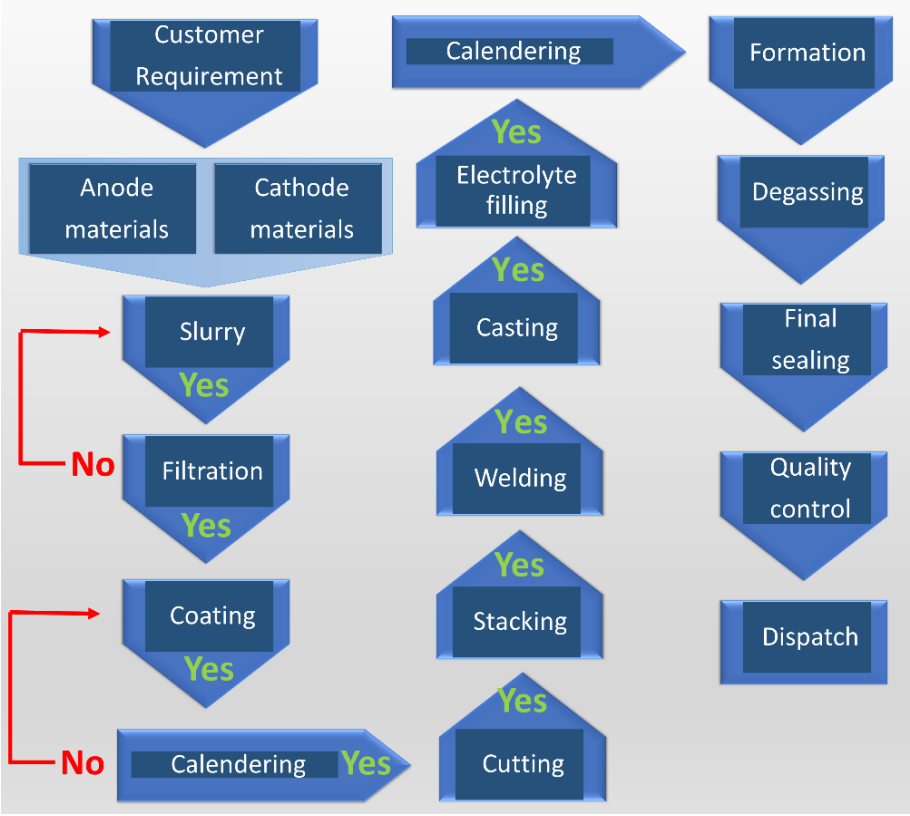

Figure 37: Illustration of a protocol for manufacturing LIBs that integrates digitalized machine learning and artificial intelligence (adapted from Ref.[398]).

In real-world working conditions, these parameters are pushed to their limits to meet end-users requirements.[417, 418] Consequently, the challenge lies in the absence of real-time monitoring data that can comprehensively explain the complexity, hindering the

development of an efficient battery management system (BMS).[418, 419] BMS typically oversees system-level metrics like temperature, current, and voltage to forecast battery quality, reliability, lifespan, thermal runaway, and safety.[419, 420]

3. MATERIAL, STRUCTURAL, AND ELECTROCHEMICAL CHARACTERIZATION METHODS

3.1. Dynamic light scattering

Dynamic light scattering (DLS) was employed to estimate the particle size distributions in suspension, specifically the hydrodynamic diameters. This was done using a Malvern Mastersizer 2000 device equipped with a Hydro 2000S module. The preparation process involved stirring the mixture powders in 30 g of ethanol for 2 h. Following this, the mixture was sonicated for 30 min to ensure thorough dispersion. The sonicated mixture was then gradually added to a reservoir containing approximately 150 mL of de-ionized water. This addition continued until a laser obscuration of 7% was achieved. During the DLS measurements, a refractive index of 1.33 for water and 2.42 for carbon was considered, while the refractive index of ethanol was neglected.

To maintain consistency during the measurements, the diluted suspension was stirred at a speed of 2000 rpm and sonicated with an output power of 100%. The results were gathered using particle size distribution histograms and detectors positioned to capture front, back, and side light scattering. It was observed that carbon deposition on the device's walls led to a decrease in laser obscuration over time, which could affect the accuracy of the measurements. This factor was taken into consideration when interpreting the results. The collected data provided detailed insights into the particle size distribution, aiding in the understanding of the suspension characteristics.

3.2. Rheology measurements

Rheological tests were conducted using an Anton-Paar MCR302e rheometer to determine the flow and deformation behavior of the samples. Stainless steel cone plates with an opening angle of 1° and a diameter of 25 mm were employed for the measurements, which were carried out at a controlled temperature of 25°C. Before each test, the samples were pre-sheared at a shear rate of 10 s^{-1} for 2 min to ensure uniformity and eliminate any previous shear history. Following the pre-shearing, the sample was allowed to rest for 15 min to stabilize. During the measurements, the time allocated for each data point was adjusted in a logarithmic manner. For lower shear rates, each point was measured for 100 s to capture detailed viscosity behavior.

Conversely, for higher shear rates, the measurement time per point was reduced to 2 s to gather data across a wide range of shear rates efficiently. This meticulous testing procedure ensured that accurate and reliable rheological data were obtained, providing valuable insights into the material's properties under different flow conditions. The gathered data were critical for understanding the material's performance and potential applications.

3.3. Grindometer measurements

A BEVS Fineness of Single-Channel Grind Gauge 1903/100 was utilized as a grindometer, following the ISO 1524 standard. For the test, 0.3 mL samples were placed in the deepest part of the trough. To avoid the formation of air bubbles, some of the samples overflowed the edge. The scraper was then drawn across the gauge at a steady speed of 1-2 cm s^{-1}, held perpendicular to the gauge top, and aligned with the long side of the gutter, moving towards the shallow end. The gauge was examined immediately after spreading the coating while it was still wet. This examination was conducted at an angle of 30 (±2) degrees relative to the top of the indicator. The particle size was determined by observing the initial appearance of scratches in clusters on the specimen, specifically in linear locations forming about a 3 mm transverse strip.

Additionally, optical photographs were captured using a Dino-Lite Premier video microscope. These photographs provided further visual documentation and analysis of the particle size and distribution within the sample. This accurate approach ensured precise measurement and thorough analysis of the particle sizes according to the standardized method.

3.4. Scanning electron microscopy

For the top-sectional view scanning electron microscopy (SEM) was performed using a Gemini 500 system from Zeiss. The samples were first placed on copper adhesive tape and then mounted on aluminum stubs. The samples were examined without the application of an additional conductive sputter coating. The analysis was conducted at acceleration voltages ranging from 1-10 kV. Because of the high-resolution imaging capabilities of the Gemini 500 system and thorough sample preparation, precise scanning electron micrograph analysis results were ensured.

For the cross-sectional view, a ZEISS Sigma 300 VP FE-SEM SE detector was utilized at an acceleration voltage of 10 kV. The working distance was set between 3-6 mm. These samples

were embedded in epoxy resin to provide stability and support. The embedded samples were then metallographically prepared through a process of grinding and polishing to achieve a smooth surface for analysis. This preparation and analysis method allowed for detailed examination of the samples' surface and cross-sectional structures, providing valuable insights into their morphology and microstructural features.

3.5. X-Ray diffraction

X-ray diffraction (XRD) was performed using a D8 Discover diffractometer (Bruker AXS) equipped with a copper X-ray source operating at 40 kV and 40 mA and a two-dimensional VANTEC-500 detector. A Göbel mirror with a 1 mm point focus was utilized for the measurements. The samples were analyzed at angles ranging from 20°-80° 2θ, with a step width of 20° 2θ and a measurement time of 1000 s per step. The powder samples were affixed onto an optical glass sample holder with a depth of 0.5 mm. All scans were normalized to a range of 0 to 1. System calibration was carried out by adjusting positions and measuring a NIST 1976b corundum standard. This accurate procedure ensured precise and reliable XRD measurements, providing detailed insights into the crystalline structure of the samples.

3.6. Raman spectroscopy

Raman spectroscopy was carried out using a Renishaw inVia Raman system that had an Nd: YAG laser with a wavelength of 532 nm and a power output of 0.05 mW focused on the sample with a numerical aperture of 0.75. Each sample was analyzed at five points, with each spectrum captured for 30 s and accumulated five times to enhance signal clarity. This method improved the quality and reliability of the data collected. Two Voigt peaks were assumed for the D-mode and G-mode to analyze the spectra. The powder samples were mounted on glass microscope slides during measurement procedures. The recorded spectra underwent cosmic rays. Normalization to a scale ranging from 0 to 1. Calibration using a silicon standard was performed before. After measurements are taken to ensure precision and consistency in the results obtained.

3.7. Electrochemical characterization

A BioLogic BCS-810 battery cycler was used to perform cyclic voltammetry (CV) and galvanostatic charge and discharge measurements. For the LTO anode half-cell, a potential

window of 0.01-3.00 V vs. Li^+/Li was used, with scan rates of 0.1 mV s^{-1} and 5.0 mV s^{-1}. For galvanostatic charge and discharge measurements of the LTO anode half-cell, a potential range of 0.01-3.00 V vs. Li^+/Li was used, with specific currents varying from 0.1 A g^{-1} to 20.0 A g^{-1}.

Electrochemical impedance spectroscopy (EIS) was performed using a VMP3 multi-channel potentiostat and galvanostat from Bio-Logic, equipped with EC-Lab software. EIS analysis for the LTO anode half-cell was conducted after 100 full lithiation/delithiation cycles at a specific current of 2.5 A g^{-1}. The frequency range was 10^{-2} Hz to 10^5 Hz, with an alternating-current oscillation of 5.00 mV. All electrochemical tests were conducted under constant temperature conditions of 25± °C in Binder climate chambers.

For the post-mortem investigations, the LTO half cells were held at 3.00 V vs. Li^+/L for 12 h to ensure delithiation consistently. Following this, the cells were taken apart in a glovebox. The LTO electrodes were rinsed with 5 mL of dimethyl carbonate (DMC) and air-dried at room temperature under vacuum conditions. This process guaranteed that the electrodes were adequately prepared for analysis.

The LFP cathode half-cell was analyzed within a potential window of 2.2 V vs. Li^+/Li and 4.2 V vs. Li^+/Li, at scan rates ranging from 0.1 mV s^{-1} to 1.0 mV s^{-1}. For LMO and LMO//AC, a potential window of 3.0 V vs. Li^+/Li to 4.5 V vs. Li^+/Li was employed, with scan rates also between 0.1 mV s^{-1} and 1.0 mV s^{-1}.

The LTO//LFP full cells were tested within a cell voltage range of 1.00-2.50 V, using scan rates between 0.10 mV s^{-1} and 1.00 mV s^{-1}. For galvanostatic charge and discharge tests, the LTO//LFP and LTO//LMO full cells were examined within a voltage range of 1.00-2.50 V, with a specific current of 0.2 A g^{-1} and 0.5A g^{-1}, respectively.

For full cells, the EIS measurements were taken on pristine samples, as well as after 100 and 500 full lithiation/delithiation cycles at 0.2 A g^{-1}. The frequency range for both cell types was 10^{-2} to 10^5 Hz, with an alternating-current oscillation of 5.00 mV. All electrochemical tests were conducted under constant temperature conditions of 25±1°C in Binder climate chambers.

4. OPTIMIZED LITHIUM TITANATE OXIDE ANODE MANUFACTURING

4.1. Materials

All chemicals were purchased commercially and used as received without any purification. $Li_4Ti_5O_{12}$ nanopowder (LTO, ~200 nm) was purchased from Sigma-Aldrich. Super C65 (C65) conductive carbon black was from IMERYS Graphite & Carbon. Dimethyl sulfoxide solvent (DMSO, ≥99.9%, anhydrous) and Polyvinylidene fluoride binder (PVdF) were procured from Sigma-Aldrich, respectively. Battery-grade copper foil current collector with 25 µm thickness was obtained from MTI Corporation.

4.2. LTO anode preparation

Figure 38 shows the preparation steps for LTO anodes. Initially, 70 mass% LTO nano-powder and 20 mass% C65 conductive carbon black were manually ground in a mortar for five minutes (min) before it was blended in a centrifugal mixer (SpeedMixer (SM), DAC 150 SP Hauschild) for 15 min at 2500 rpm.

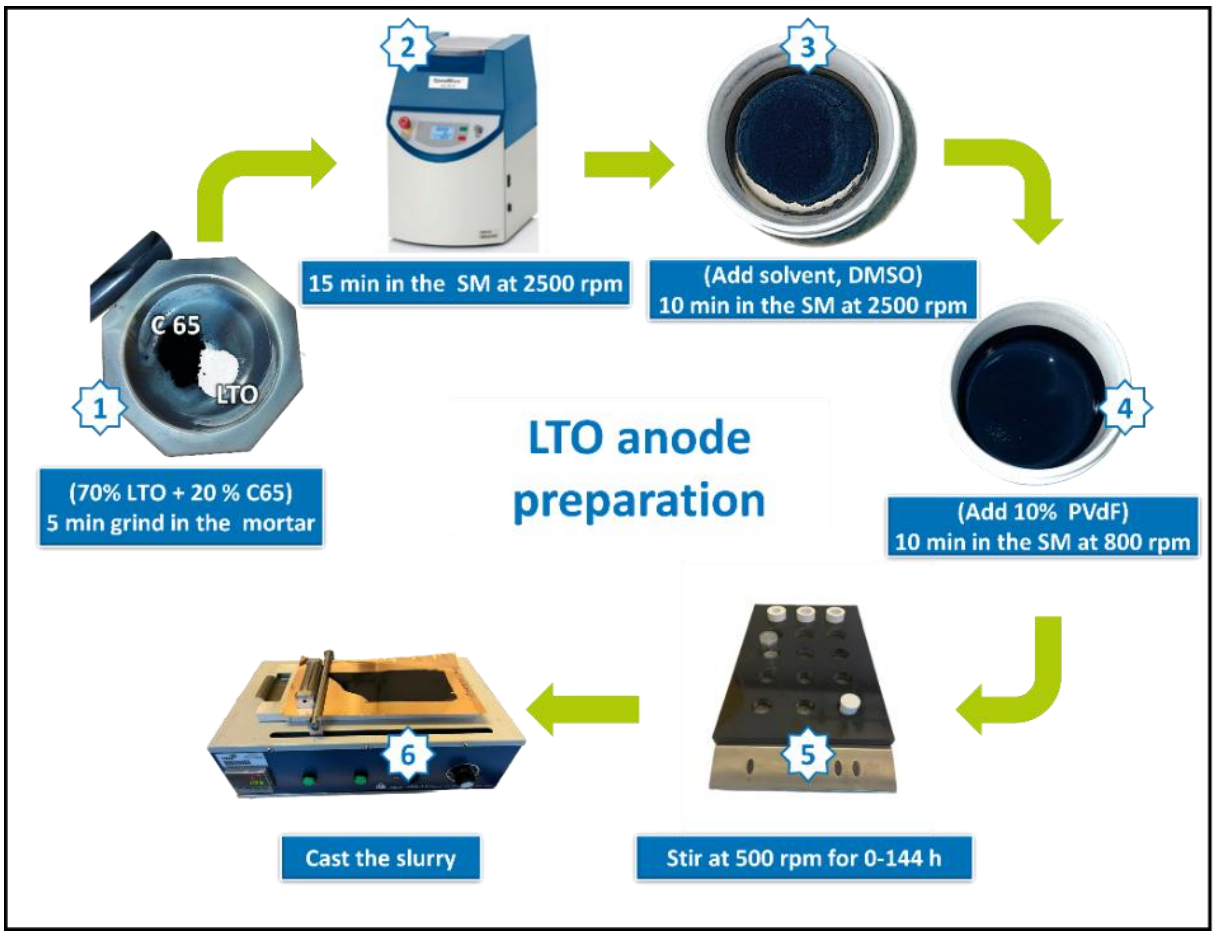

Figure 38. The manufacturing mixing routines of lithium titanate anode.

DMSO solvent was added dropwise to control the consistency of the slurry, and the mixture was put in SM for 10 min at 2500 rpm. Subsequently, 10 mass% PVdF binder solution was added to the above mixture, followed by another round of mixing using the SM for 10 min at 800 rpm. The mixing speed and duration of the dry and wet mixtures were varied to investigate the effect of these parameters in controlling the particle sizes, distribution, and uniformity, as elaborated in the subsequent sections. The final slurries were coated onto a battery-grade copper foil current collector using a micrometer doctor-blade (MSK-AFA-HC 100, MTI Corporation) at a speed of 7.5 mm s^{-1}, achieving a wet thickness of 150 µm. The coated samples were first air-dried in a fume hood for 12 h, followed by a drying step in a vacuum oven at 80 °C and 60 mbar for another 12 h. Ultimately, the dried coatings were calendered using a rolling press (MSK-HRP-01, MTI Corporation), with the press gap set to 42% of the initial coating thickness (ranging from 55-90 µm).

4.3. Half-cell assembly using LTO anode

Figure 39 illustrates a CR2032-type Li-ion battery coin cell assembly using an LTO anode. All of our cells are assembled with high precision and quality, making them suitable for use in LIB testing and applications. Our thorough preparation and controlled environment are critical for obtaining consistent, reliable, and reproducible results in subsequent experimental evaluations and practical energy storage solutions. The LTO half-cell assembly was carried out in an MBRAUN Argon-filled glove box, where oxygen and water levels were maintained below 0.1 ppm to ensure a controlled environment. The cells were fabricated in coin cell format using commercial CR2032 cases from PI-KEM. Lithium chips (Ø = 15 mm, MTI Corporation) were used as both the counter and reference electrodes.

The working electrodes were the LTO discs (Ø = 12 mm, approximately 2.7 mg cm^2, and around 31 µm dried thickness). Whatman GF/F glass fiber discs (Ø = 18 mm) were punched and used as separators between the electrodes.

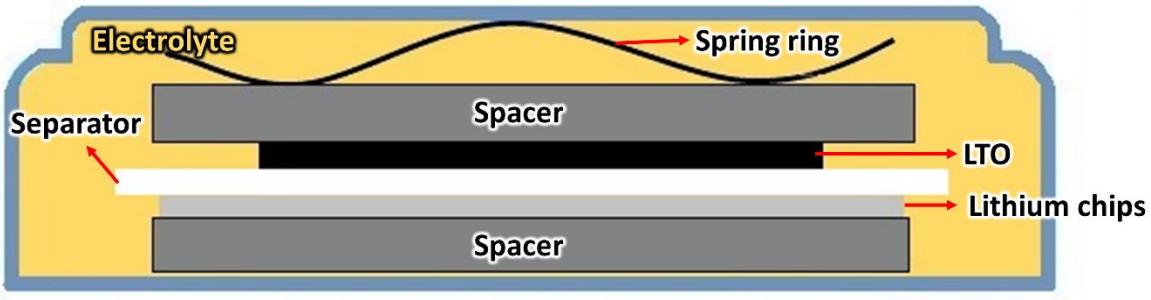

Figure 39. Illustration of a CR2032-type Li-ion battery coin cell assembly using LTO anode.

For each coin cell, 150 µL of an electrolyte solution consisting of 1 M $LiPF_6$ salt in a mixture of ethylene carbonate and dimethyl carbonate (EC, 1:1 by volume, Sigma-Aldrich), was injected. This electrolyte solution is essential for facilitating Li-ion movement within the cell. Two stainless steel 304 spacers (thickness = 0.5 mm, PI-KEM) were used for each coin cell, and the cells were sealed under a pressure of 1000 psi using a hydraulic crimping machine (MSK-110, MTI Corporation).

4.4. Results and discussion

The content in this section is adapted from the article “Enhanced development and potential scope for spinel lithium titanate anode for high-speed lithium-ion batteries.“ The article offers an investigation into the methods and elements used to improve the preparation and efficiency of spinel lithium titanate anodes. All contributions are thoroughly listed and acknowledged in **Section 12**.

4.4.1. Characterization analysis of raw LTO powder

The structure and morphology of raw LTO active material were first investigated via scanning electron micrograph analysis. **Figure 40A-F** displays the low and high-magnification scanning electron micrographs of the raw LTO powder. As shown, LTO powder is composed of agglomerated porous particles ranging from 500 nm to 2 µm in diameter.

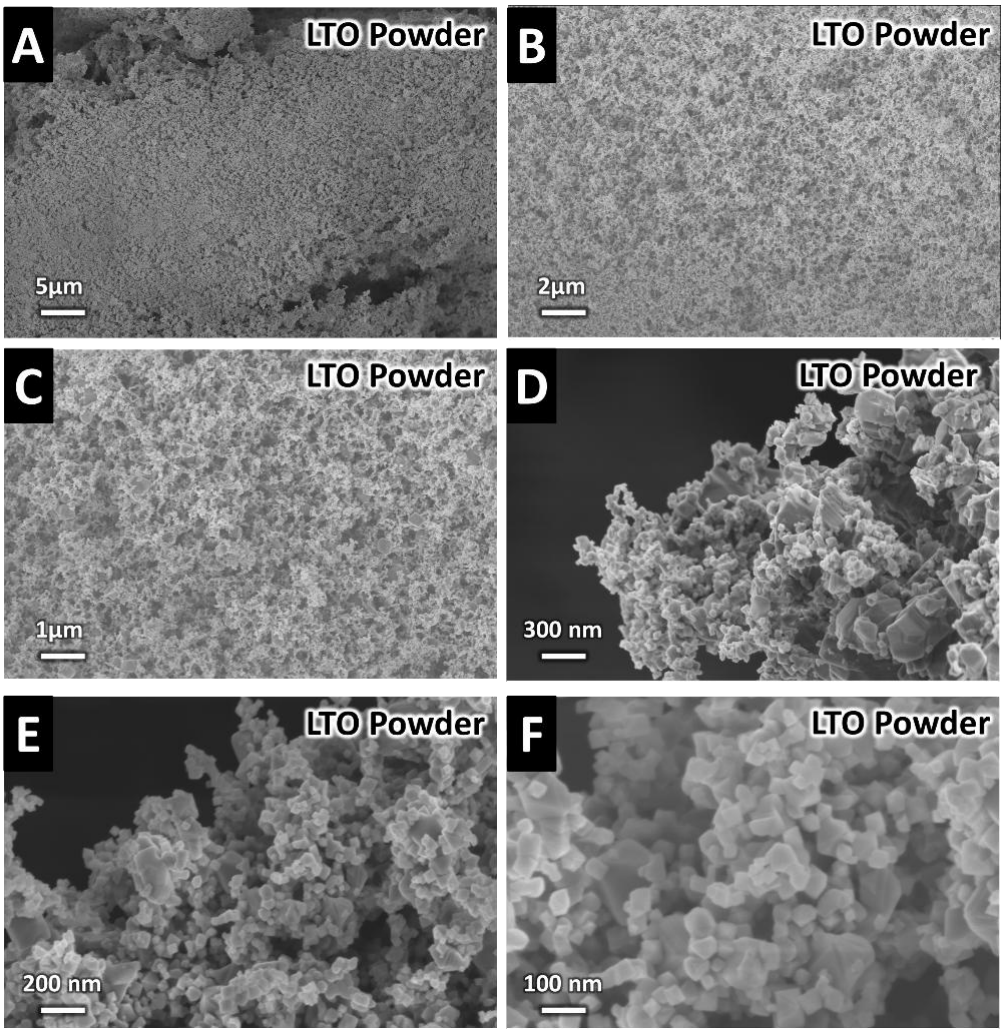

Figure 40. Low and high-magnification scanning electron micrographs of raw LTO powder from Sigma-Aldrich.

It was observed that the nanosized LTO particles tend to aggregate, possibly due to their high surface energy. These densely agglomerated particles can negatively affect the overall performance of LTO-based anodes by hindering uniform Li-ion insertion and extraction within individual grains. Additionally, the LTO nanoparticles within these grains may lose their effectiveness during cycles of high current as the diffusion lengths of Li-ions tend to increase. **Figure 41A** displays the X-ray diffractograms of raw LTO powder. All the diffraction peaks in the XRD pattern of the LTO powder sample exhibited high crystallinity and were indexed as spinel LTO with the $Fd\bar{3}m$ space group, parallel with JCPDS card 49-0207.[421-423]

Diffraction peaks with 2θ values around 18.3°, 30.2°, 35.5°, 37.2°, 43.2°, 47.3°, 57.2°, 62.8°, and 66.0° are assigned to (111), (220), (311), (222), (400), (331), (333), (440), and (531) planes of spinel LTO, respectively. **Figure 41B** shows the Raman pattern of raw LTO powder. This examination presented, in-depth insights, into the behaviors of the particles further confirming the details derived from X-ray diffraction. The Raman pattern of pristine LTO powder resembles a typical pattern with a spinel structure defect.[423, 424] The main interpretation contains six major and minor bands.[425]

In particular, four major bands centered at 232 cm^{-1}, 355 cm^{-1}, 435 cm^{-1}, and 675 cm^{-1} are attributed to F_{2g}, F_{2g}, E_g, and A_{1g} vibrations in TiO_6 octahedra, LiO_6 octahedra, LiO_4 tetrahedra, and TiO_6 octahedra, respectively. The minor band located at 751 cm^{-1} is known as the A_{1g} shoulder. The combined results from these analyses confirmed the consistency of the LTO powder's properties with known standards. The scanning electron micrographs show structure formation, and both X-ray diffraction patterns and Raman pattern indicated that the untreated LTO powder exhibited crystallographic and molecular features.

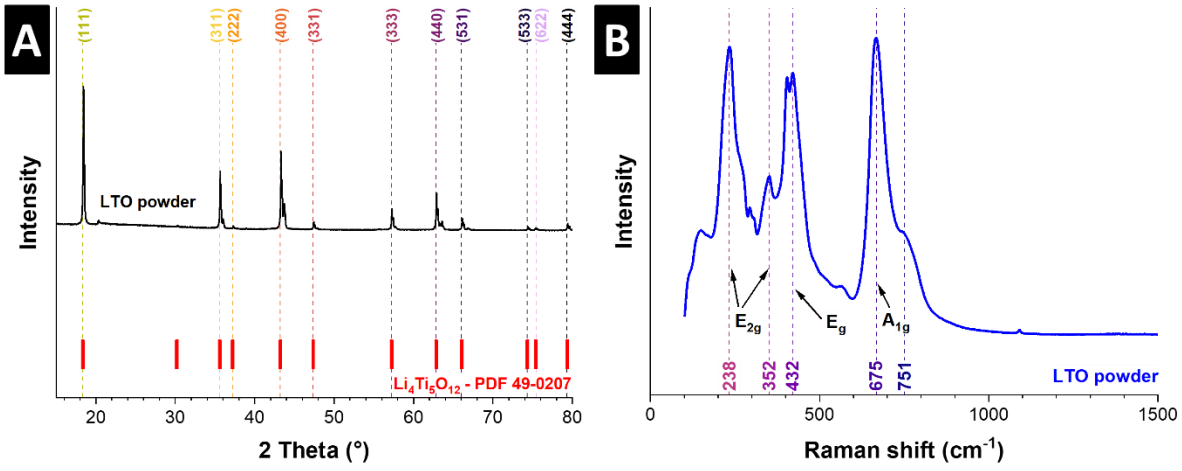

Figure 41. (A) X-ray diffractogram and **(B)** Raman pattern of raw LTO powder.

The detailed study of the shape and structure is important in figuring out how LTO particles behave when used practically. The characteristics we have discovered show the importance of managing the particle size and morphology of LTO powder. We believe that these particular characteristics play a role in improving the battery performance and overall effectiveness of LTO-based anodes in LIBs.

4.4.2. Characterization analysis of Super C65 conductive carbon black

The scanning electron micrograph analyses were employed to gain a better understanding of the morphological aspects and primary particle dimensions of the C65 conductive agent. The scanning electron micrographs in **Figures 42A-F** show the C65 carbon black, with particles ranging from 30-50 nm.

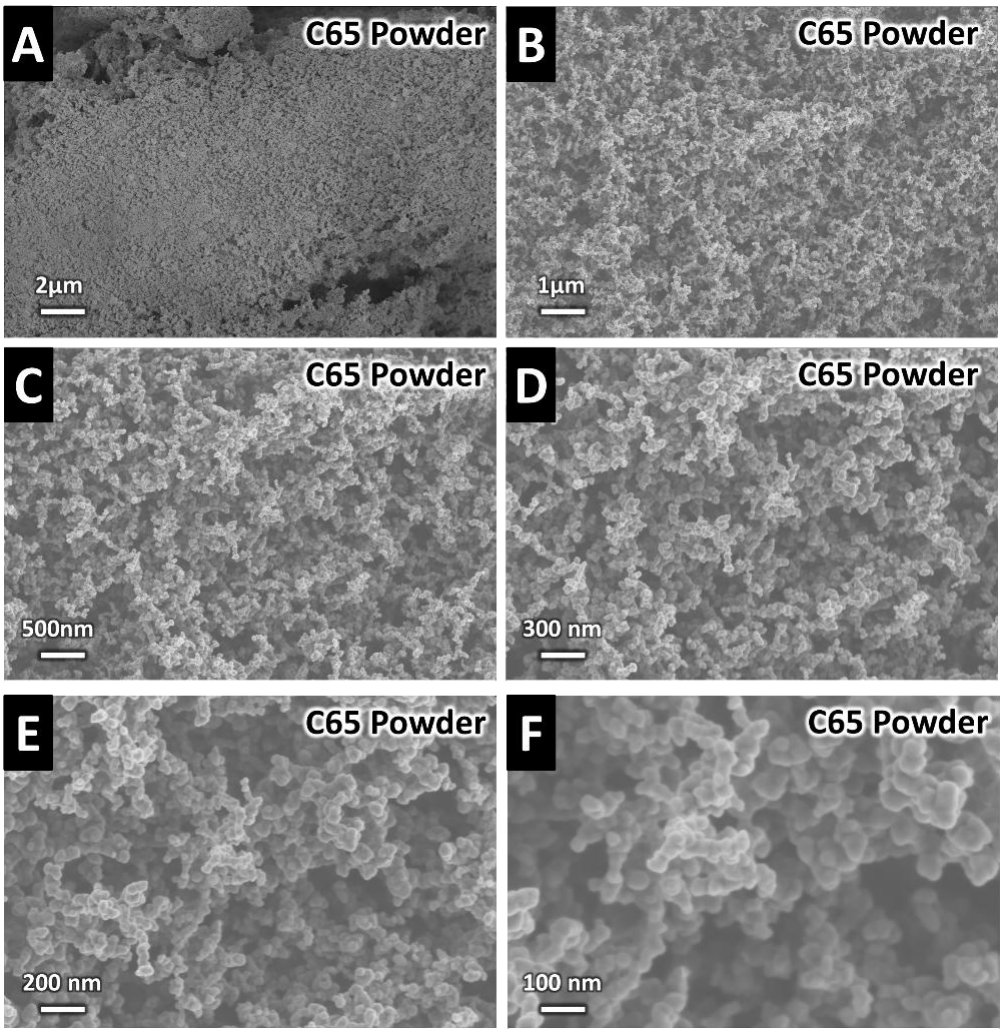

Figure 42. Low and high-magnification scanning electron micrographs of C65 conductive carbon black.

Figure 43A displays the X-ray diffractograms of C65. The XRD pattern exhibits distinct peaks at 25.2° 2θ and 44.2° 2θ, corresponding to the (002) and (011) crystallographic planes, confirming the graphite structure and providing insights into its orientation and lattice spacing. The broad peak at 25.2° 2θ is linked to the disordered nature of graphite revealing disorder, indicating a lack of long-range order in graphite layer stacking. This type of disorder indicates a lack of long-range order in the stacking of the graphite layers.[426] This disorder influences material crystallinity, impacting its conductivity and performance in applications like LIBs.

Figure 43B displays the Raman pattern of C65. In the Raman pattern, the D-band and G-band are particularly important. The G-band peak around 1600 cm^{-1} is associated with the sp^2-bonded carbon atoms in a graphitic lattice. The D-band peak appeared around 1350 cm^{-1}, indicating the presence of sp^3-bonded carbon atoms, reflecting structural defects and disorder within the material.[423, 427]

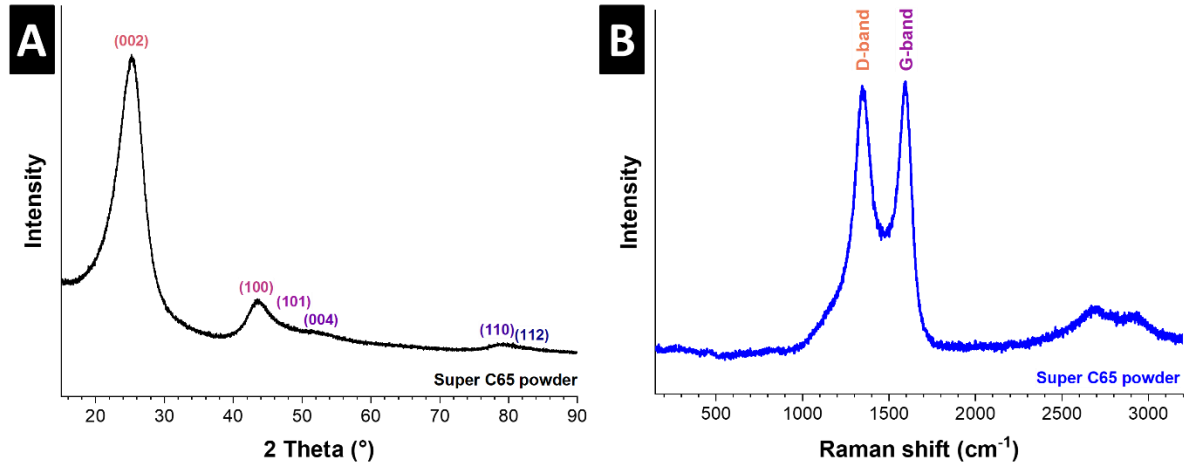

Figure 43. (A) X-ray diffractograms and **(B)** Raman pattern of C65 conductive carbon black.

This sp^2/sp^3 ratio which was calculated to be around 1.18 is directly linked to the level of graphitization and the presence of content in C65 and provides a clear view of the properties of carbon. A higher sp^2 content typically signifies conductivity and structural organization qualities that are desirable for use in LIBs and other electronic devices.[428, 429]

By combining scanning electron micrographs, XRD, and Raman analyses, it can gain an understanding of both the shape and crystallographic structure of this carbon material. Thorough examinations of morphology and structure are essential for evaluating how well C65 performs in applications in improving the conductivity and overall effectiveness of LIBs. We believe that the spherical shape and tiny size of the particles play roles in creating high surface area and conductive properties within the material.

4.4.3. Extensive optimization of LTO electrode preparation details

During the preliminary testing, we aimed to achieve a more homogeneous composition for preparing the LTO electrode to address several issues we observed as follows:

1. The surface of the production electrode was highly uneven.
2. The adhesion of the particles to the current collector was rather weak.
3. The dispersion of active substances per unit surface area was exceptionally low.

To address these issues, different mixtures were prepared in the dry state using LTO powder and C65. The dry mixing speed and time with a speedmixer were then varied, preparing 16 types of dry mixtures, as summarized in **Table 2**.

Table 2. The dry mixing steps for the LTO mixtures (including C65 and LTO powders) in the SpeedMixer.

	Dry mixing in a mortar (Time, min)	Dry mixing with SpeedMixer (Speed, rpm)	Dry mixing with SpeedMixer (Time, min)
Mixture A	**10**	**500**	**5**
Mixture B	**10**	**1500**	**5**
Mixture C	**10**	**2500**	**5**
Mixture D	**10**	**3500**	**5**
Mixture E	**10**	**500**	**10**
Mixture F	**10**	**1500**	**10**
Mixture G	**10**	**2500**	**10**
Mixture H	**10**	**3500**	**10**
Mixture I	**10**	**500**	**15**
Mixture J	**10**	**1500**	**15**
Mixture K	**10**	**2500**	**15**
Mixture L	**10**	**3500**	**15**
Mixture M	**10**	**500**	**20**
Mixture N	**10**	**1500**	**20**
Mixture O	**10**	**2500**	**20**
Mixture P	**10**	**3500**	**20**

4.4.3.1. LTO/C65 dry mixture: Identification of mixing time in mortar

As illustrated in **Figure 39**, the materials were first mixed in a mortar on a fixed weight ratio of 70 mass% LTO powder (which is considered for each electrode preparation 0.7 g) and 20 mass% C65 (which is considered for each electrode preparation 0.2 g). This mass ratio was maintained consistently across all produced electrodes. The mixing time of the LTO and C65 powders in the mortar was varied for 5 min, 10 min, 15 min, 20 min, and 30 min, respectively. We observed that mixing time above 10 min has no significant effect on the particle size and only resulted in the mixtures adhering to the mortar. In this regard mixing for more than 10 min made it impossible to collect the mixture from the mortar completely, leading to unavoidable material loss.

Given this, 10 min of mixing in the mortar was defined as the optimum mixing time for the powder mixture in the dry state. The raw materials, however, appeared as fragile plates in the mortar after mixing, with some amount lost during the process. To compensate for this loss, the initial amount of materials was increased by 5 mass%, resulting in 73.5 mass% for LTO and 21 mass% for C65. This adjusted preparation method aimed to produce a more homogeneous mixture and improve the electrode's surface uniformity, particle adhesion to the current collector, and the amount of active material per unit surface area.

4.4.3.2. LTO/C65 dry mixture: Identification of mixing time and speed in SpeedMixer

Approximately 90 mass% of the dry mixtures were transferred into the special SpeedMixer containers. In the next step, the containers were sealed to secure the mixture and avoid any contamination. They were placed in the chamber of the SpeedMixer (DAC 150 SP Hauschild), as depicted in **Figure 44** and mixed at various mixing speeds (500 rpm, 1500 rpm, 2500 rpm, and 3500 rpm) and times (5 min, 10 min, 15 min, and 20 min).

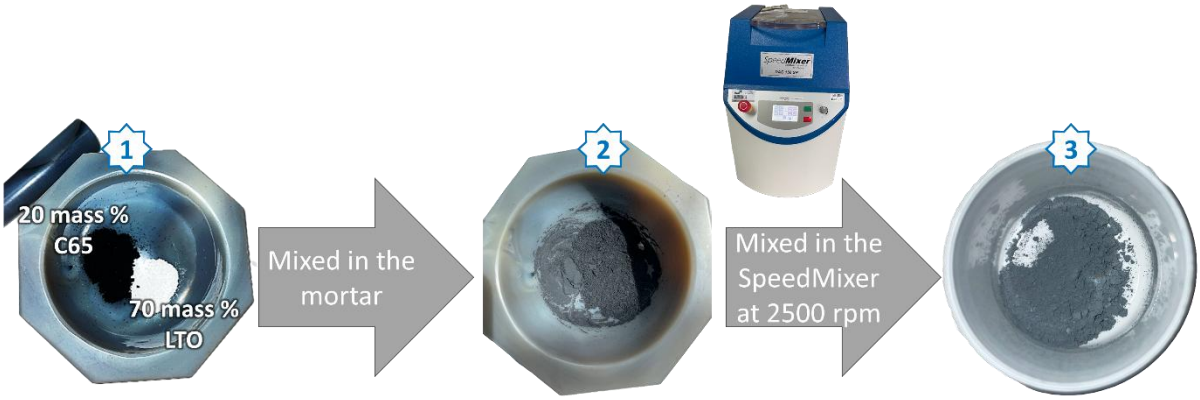

Figure 44. The mixture of C65 and LTO was added to the mortar and, after manual mixing, the dry mixture was transferred to a special container for mixing in the SpeedMixer.

The SpeedMixer offers control over mixing parameters, ensuring consistency and reliability, in preparing materials. This mixing method is subject to forces that enhance component distribution and integration, which is a step in achieving the desired quality and performance of LTO electrodes. Following the mixing process, each sample underwent inspection and morphological analysis using scanning electron microscopy (**Figures 45A-D**).

Notably, speeds below 2500 rpm (500 rpm and 1500 rpm) showed a minor impact on the particle size distribution of materials. Similar results were observed for the mixtures that were prepared at speeds (3500 rpm). Mixtures stirred at 2500 rpm for durations (5 min and 10 min)

exhibited effects on particle size and distribution, while those mixed for 15 min at this speed experienced a significant reduction in particle sizes.

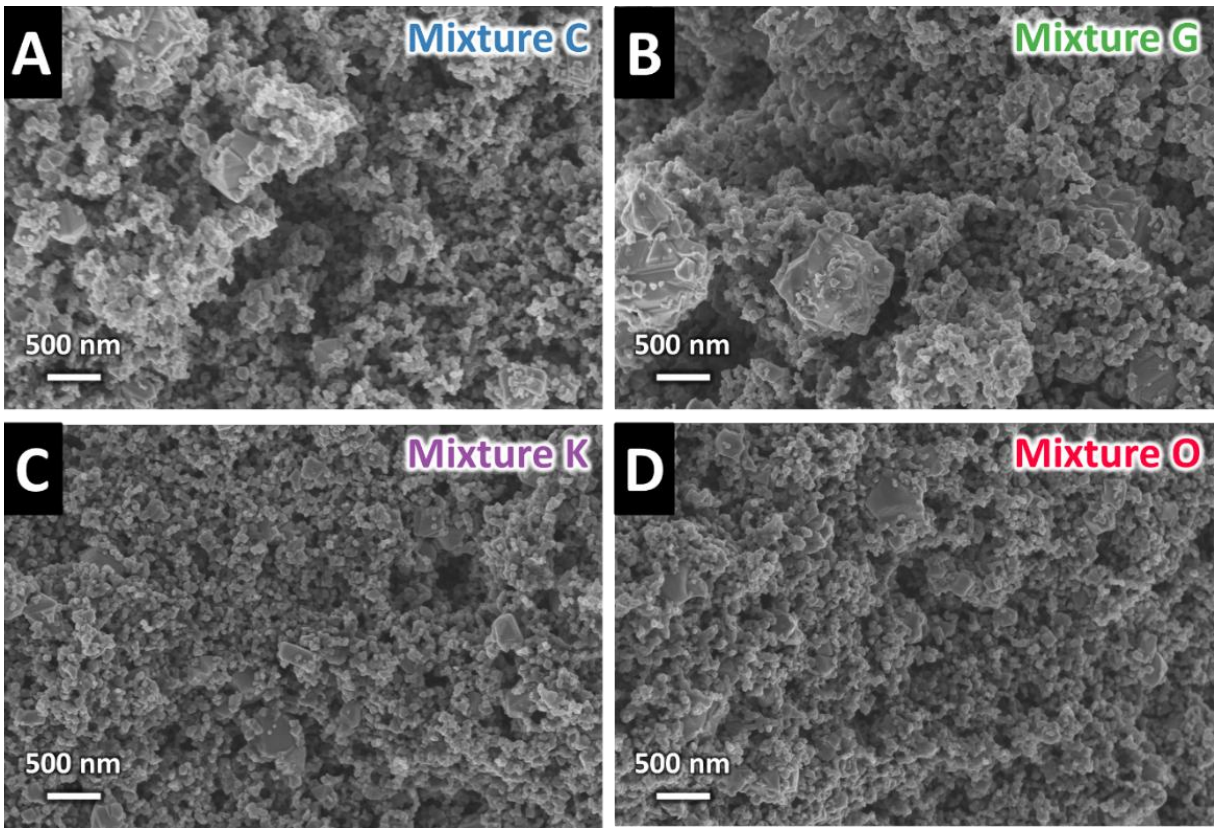

Figure 45. High-magnification scanning electron micrographs of mixtures C, G, K, and O, as defined in **Table 2**.

To further understand the impact of mixing speed in a defined duration, we inspected the dry mixtures visually. **Figure 46** displays the actual photographs of samples mixed in SpeedMixer at 500 rpm, 1500 rpm, 2500 rpm, and 3500 rpm for 15 min, respectively. Large LTO particles were evident in the dry mixture that was mixed at 500 rpm for 15 min. The LTO particles were either completely uncovered or only partially covered by the conductive agent. When the stirring rate was raised to 1500 rpm, a more even distribution (based on visual observation) of the substance with the conducting agents was noticed within the mixing duration. After 15 min of mixing at 2500 rpm, the mixture appeared smoother and more uniform suggesting a mixed and uniform combination of the substances. The dry mixture mixed at a high speed of 3500 rpm for 15 min prompted the agglomeration of the LTO powder, forming a hard conglomeration of solid flake structure that mostly stuck to the SpeedMixer container.

After reviewing the findings, it was determined that setting the mixer to 2500 rpm and mixing for 15 min is the combination for blending the LTO and C65 powders in their form. The analysis

underscored how crucial it is to choose the mixing speed for achieving a mixture of LTO and C65. The ideal speed and duration did not decrease the particle size but ensured that the conductive agent fully coated the LTO particles, improving the electrode material's overall mixing quality and performance.

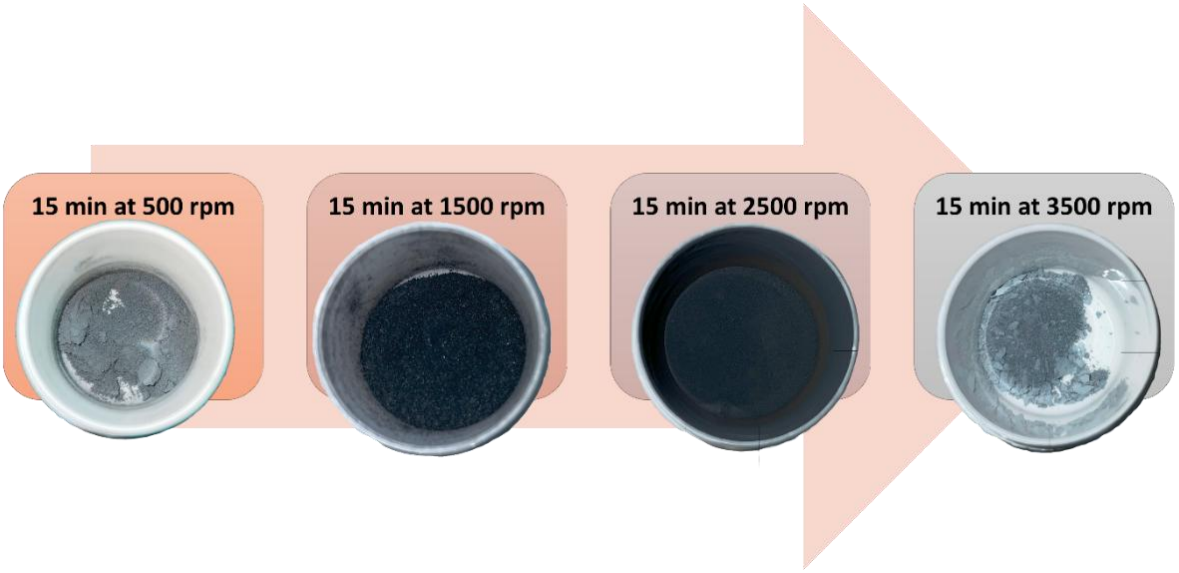

Figure 46. Actual photographs of the samples mixed in SpeedMixer at 500 rpm, 1500 rpm, 2500 rpm, and 3500 rpm for 15 min.

Scanning electron microscopy and Dynamic Light Scattering were employed to provide insights into the particle size distributions and helped confirm the pre-defined mixing duration and time to achieve the most homogeneous mixture. We prepared five samples to use for thorough analysis, as listed in **Table 3**.

The manual mixing of LTO and carbon black powder in the mortar was fixed for 10 min. The mixing speed in SpeedMixer was fixed for 2500 rpm while the mixing duration varies from 0 min, 5 min, 10 min, 15 min, and 20 min. The samples were labeled according to the mixing speed and duration to analyze the particle sizes.

1. **DM 0**, where „DM“ stands for Dry Mixing, refers to the samples without mixing in the SpeedMixer.
2. **DM 2500-5** indicates a sample blended in the SpeedMixer for 5 min at 2500 rpm.
3. **DM 2500-10** refers to a sample mixed for 10 min at 2500 rpm.
4. **DM 2500-15** associated with a sample mixed for 15 min at 2500 rpm.
5. **DM 2500-20** corresponds to a sample mixed for 20 min at 2500 rpm.

It was focused on the effect of varying the duration of mixing at a constant speed of 2500 rpm to the particle sizes and overall homogeneity of the mixtures.

Table 3. Parameters were set to find the optimum dry mixing duration. DM stands for dry mixing, and SM stands for speed mixer. The labeling was as follows:

Sample name	DM in a mortar (Time, min)	DM with SM (rpm, min)
DM 0	10	0
DM 2500-5	10	2500, 5
DM 2500-10	10	2500, 10
DM 2500-15	10	2500, 15
DM 2500-20	10	2500, 20

Figures 47A-F show scanning electron micrographs of the LTO and C65 powders combined at a speed of 2500 rpm for different durations (0 min, 5 min, 10 min, 15 min, and 20 min). These visuals show insights into the surface features and structural interactions between the two materials. The images reveal the shapes and sizes of the LTO and C65 particles, showcasing their morphologies.

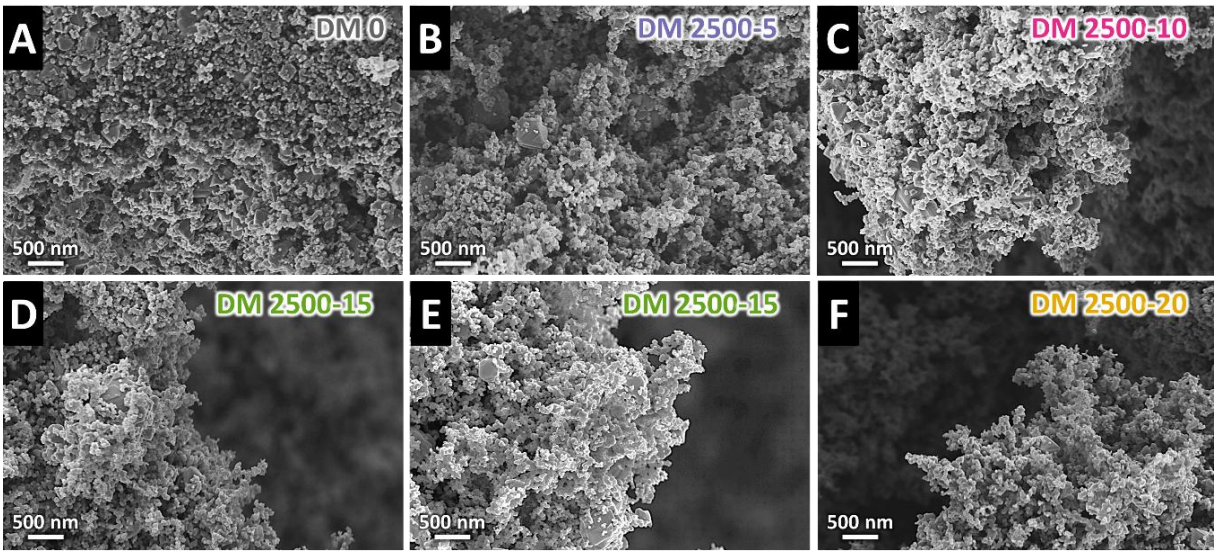

Figure 47. Scanning electron micrographs of different powder samples **(A)** DM 0, **(B)** DM 2500-5, **(C)** DM 2500-10, **(D)** and **(E)** DM 2500-15, and **(F)** DM 2500-20**.**

Further investigation on particle sizes shown in **Figure 48** presents dynamic light scattering data for mixtures of LTO and C65 powders. The DLS analysis validates the findings from scanning electron micrographs and quantifies shifts in particle size distribution, enhancing our understanding of how blending impacts the characteristics of LTO and C65 powders. Most particles in DM 0 samples measured within the range of 50 nm to 2 mm (which indicates the primary particle size). Upon mixing these samples at 2500 rpm in the SpeedMixer, a noticeable reduction in particle sizes was observed. Extending the mixing time to 15 min resulted in

decreases in particle sizes, with more than 80% of particles falling within the range of 30 nm to 1 µm and an average length around approximately 250 nm. When the stirring time surpassed 15 min, there was a rise in the size of the particles.

Therefore, starting with a prolonged mixing time at such high speed can enter large forces on particles and, by reducing the surface energy, cause larger average particle sizes. Through control of the duration and speed of mixing, it has been determined that it is achievable to decrease particle size without the clumping that arises from mixing. Our findings from analyzing scanning electron micrograph data and conducting DLS measurements allowed us to determine the mixing parameters, such as using 2500 rpm for mixing speed and 15 min for mixing time in the mixture's dry state.

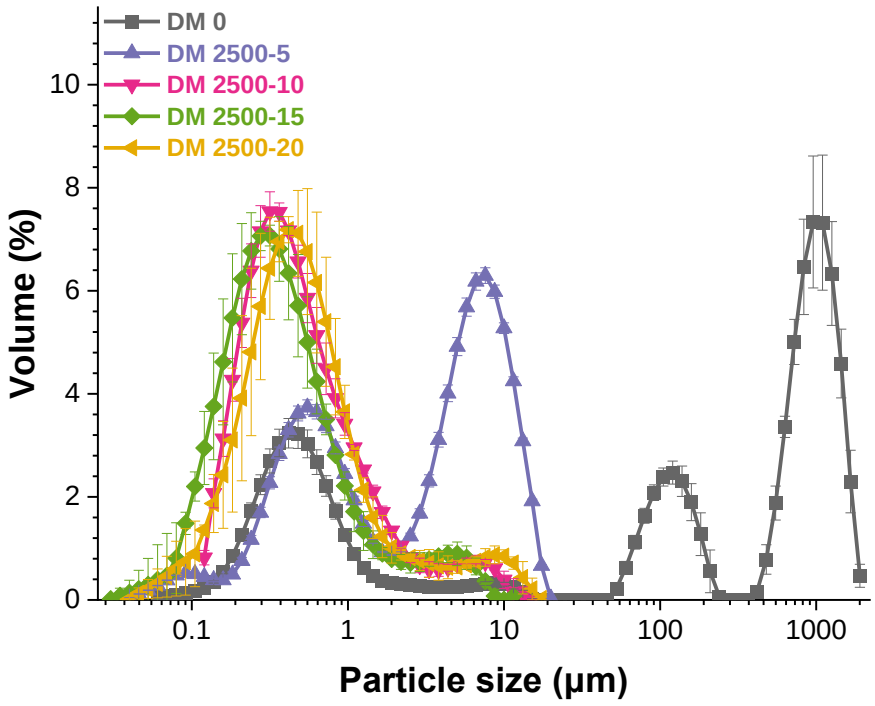

Figure 48. Dynamic light scattering measurements to identify the particle sizes for different applied speeds and durations in the mixture of powder samples, DM 0, DM 2500-5, DM 2500-10, DM 2500-15, and DM 2500-20.

4.4.3.3. Wet mixture: Identification of the amount of solvent added to the dry mixture

The starting steps for creating the LTO slurry can be seen in **Figure 49**. Initially, DMSO solvent was added to the dry mixtures and mixed at 2500 rpm for 10 min using the SpeedMixer. Following this, a binder solution with 10% PVdF by mass was added to the slurry and mixed for 10 min in the SpeedMixer at a reduced speed of 800 rpm to ensure proper dispersion of the

binder. Each resulting slurry was then transferred to the stirrer mixer and stirred for different durations to achieve complete homogenization and optimize mixture consistency. This process involves speed mixing followed by binder addition and slower mixing, aimed at producing a uniform and stable slurry.

.

Figure 49. The wet mixing procedure for the C65 mixture in the SpeedMixer was used to obtain the initial and final slurries.

The use of stirring further ensured the distribution of all components, resulting in a well-blended slurry suitable for electrode preparation.[430] Typically, the drying phase consumes about 47% of the total process energy. By reducing the solvent quantity, manufacturing becomes cost-effective and energy-efficient, leading to a drying period. This increase in efficiency results in reduced costs and a smaller environmental impact. To explore how the mixing method impacts the flow characteristics of the slurry, the quantity of solvent added to each of the five samples was adjusted, as outlined in **Table 4**. Each sample went through a mixing process to ensure a distribution of the solvent, enabling a precise evaluation of the slurry's flow properties after dry mixing.

Table 4. Parameters and the amount of solvent were set during the rheology tests. DM: Dry Mixing, WM: Wet Mixing. SM: SpeedMixer.

Sample name	DM in a mortar (min)	DM with SM (rpm, min)	The ratio of the solvent mass% to the mixtures	WM with SM (rpm, min)
S-DM 0	5	-	16:5	-
S-DM 2500-5	5	2500, 5	11:5	2500, 5
S-DM 2500-10	5	2500, 10	19:10	2500, 5
S-DM 2500-15	5	2500, 15	8:5	2500, 5
S-DM 2500-20	5	2500, 20	8:5	2500, 5

By analyzing how the solvent was distributed and its impact, on flow properties it became more clear how to enhance the efficiency of the dry mixing process. This necessary step played a role in optimizing material production for improved performance in the final product.

We noted that varying amounts of solvent were necessary to achieve slurries with viscosity levels. For example, S-DM 2500-15 requires 50% more solvent than S-DM 0 to reach the desired viscosity. This variation in the amount of solvent can be related to varying sizes between LTO and C65, in the mixtures, directly influencing the amount of solvent needed for viscosity levels.

These discoveries highlight the significance of adjusting quantities based on the characteristics of each blend to ensure consistent slurry viscosity. As shown in **Figure 50**, varying solvent levels maintained the samples' viscosity, between 2.4-3.4 Pa s for a shear rate of 50 s^{-1}.

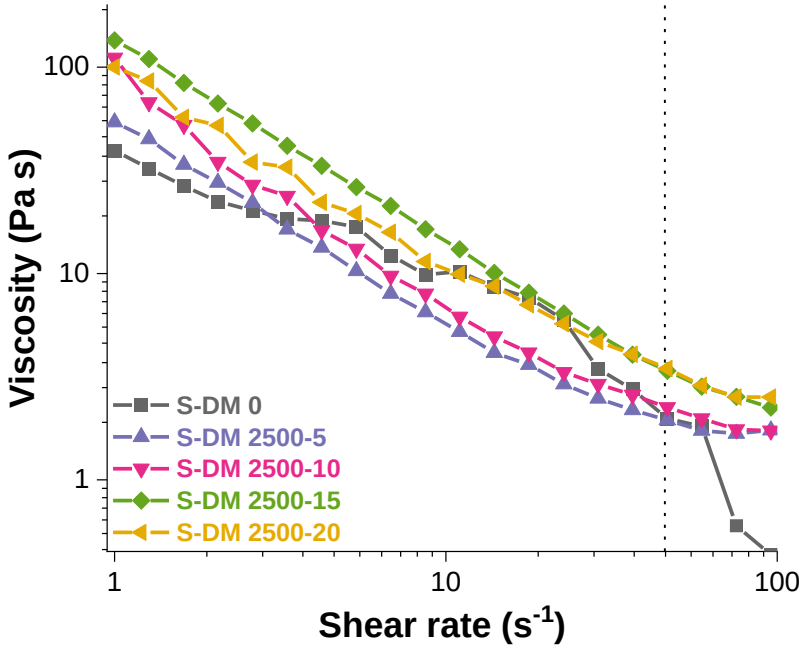

Figure 50. Viscosity vs shear rate for different applied durations in initial slurry samples, S-DM 0, S-DM 2500-5, S-DM 2500-10, S-DM 2500-15, and S-DM 2500-20.

This specific shear rate comparison was selected by calculating the shear rate employed during deposition through doctor blading using **Equation 19**. The coatings were applied with a doctor blade comma gap of 150 µm and a casting coater speed of 7.5 mm s^{-1}. where $(\dot{\gamma})$ is the shear rate in s^{-1}, (v) velocity in mm s^{-1}, and (h) the gap height in mm.

$$\dot{\gamma} = v \cdot h^{-1} \qquad \textbf{(Equation 19)}$$

The consistent viscosity achieved with solvent levels suggests that the mixing process effectively produced a slurry. Keeping viscosity stable within the range of 2.4-3.4 Pa s indicates that solvent distribution filled gaps between LTO and C65 particles resulting in a mixture.

By understanding how various mixing conditions impact sizes and solvent needs, precise and effective formulations can be developed, ultimately enhancing product performance and consistency. It is important to mention that maintaining a viscosity range is vital, for the steps of making electrodes ensuring that the slurry can be applied smoothly and processed without any flow or application problems. Ultimately we establish a ratio of 8:5 solvent mass to the dry mixture, for use in the following stages.

4.4.3.4. Wet mixture: Identification of the mixing time and speed in SpeedMixer

To study how the initial wet mixing process impacts slurry particle size using the Grindometer we utilized the samples detailed in **Table 5**. A generous amount of slurry (10.0 mL) was prepared for consistency with 0.3 mL of slurry separated for each stage. The first wet sample was taken after speed mixing at 2500 rpm for 5 min and was labeled Slurry 2500-5.

Additional slurry samples were prepared and labeled as Slurry 2500-10, Slurry 2500-15, and Slurry 2500-20 after 10 min, 15 min, and 20 min at 2500 rpm, respectively.

Table 5. Parameters were set for the optimum initial wet mixing duration. DM: Dry Mixing, WM: Wet Mixing. SM: SpeedMixer.

Sample name	DM in a Mortar (min)	DM with SM (rpm, min)	The ratio of the solvent mass% to the mixtures	WM with SM (rpm, min)
Slurry 2500-5	10	2500, 15	8:5	2500, 5
Slurry 2500-10	10	2500, 15	8:5	2500, 10
Slurry 2500-15	10	2500, 15	8:5	2500, 15
Slurry 2500-20	10	2500, 15	8:5	2500, 20

In the initial wet mixing process that was conducted for more than 10 min at 2500 rpm before adding the binder, the particle size in the slurry remained consistent, staying under 5 µm, as shown in **Figure 51**. Consequently, a mixing duration of ten minutes at a speed of 2500 rpm seemed optimal. The slurry mixed under these conditions (referred to as Slurry 2500-10) was chosen for the steps. Following this optimized process, a blend of PVdF in DMSO (constituting 10% by mass) was introduced into the slurry. This mixture then underwent mixing in SpeedMixer for 10 min at 800 rpm.

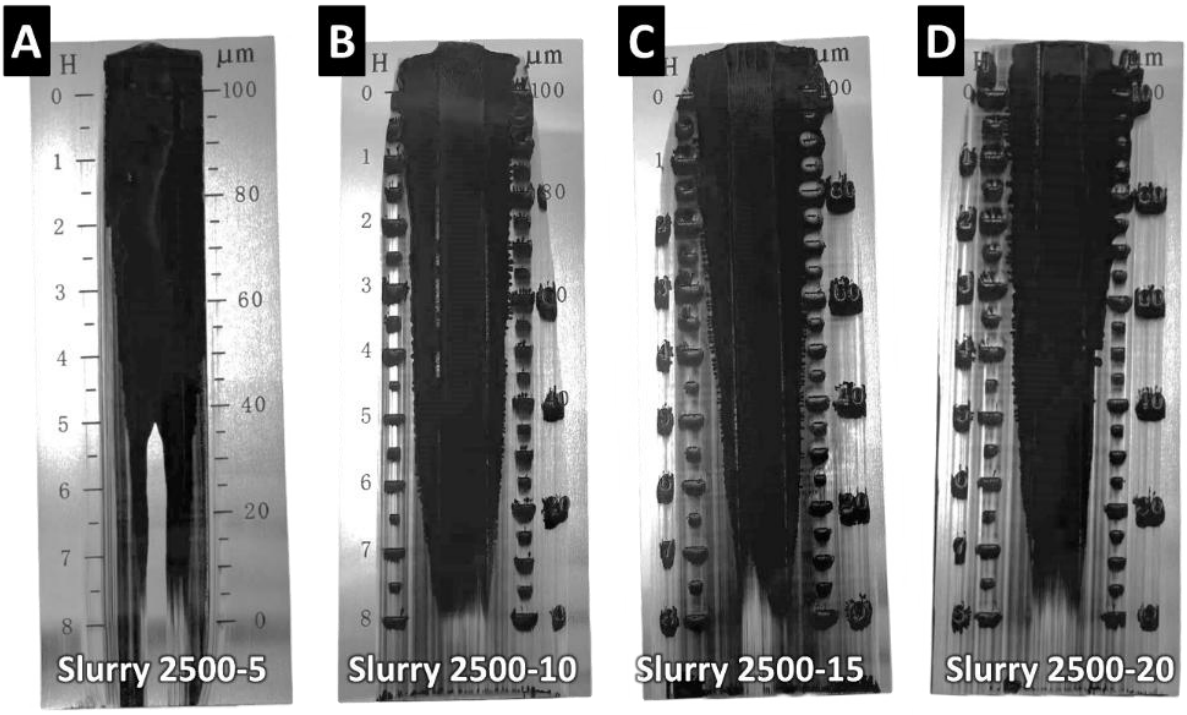

Figure 51. Photographs of grindometer results for **(A)** Slurry 2500-5, **(B)** Slurry 2500- 10, **(C)** Slurry 2500-15, and **(D)** Slurry 2500-20.

4.4.3.5. Wet mixture: Identification of the mixing time and speed in mechanical stirrer

The main goal was to make sure that the final mix reached the desired consistency and uniformity. We recorded each change in stirring time to see how it affected the quality of the mixture. This particular stage was set up to find out the conditions for making the product. By trying out stirring times of 0 h, 24 h, 48 h, 72 h, 96 h, and 144 h, we thoroughly checked how extended stirring impacted the mix. We kept an eye on each time to note any alterations in particle distribution and overall uniformity of the mixture. By understanding these impacts, we could spot the stirring duration, which would ensure that our mix met all necessary standards for fine electrochemical performance. These discoveries offer insights into how to stir and what properties our mixture should have for future production processes.

Every sample, as shown in **Table 6**, underwent an examination to monitor any changes in the viscosity, uniformity, and stability of the mixture. This helped us figure out how long we needed to stir to keep our desired slurry qualities intact, which is important for boosting efficiency and quality in our production process. We delved into how different stirring times affected the characteristics of our slurry, shedding light on the stirring duration needed to achieve superior outcomes.

Table 6. Parameters were set to find the optimum stirring time. DM stands for dry Mixing, WM for wet Mixing, SM for speed Mixer, and MS for magnetic stirrer.

Sample name	DM in a mortar (min)	DM with SM (rpm, min)	WM with SM (rpm, min)	WM with SM (rpm, min)	Stirring on MS (rpm, h)
LTO 0	5	2500, 15	2500, 10	800, 10	0
LTO 24	5	2500, 15	2500, 10	800, 10	500, 24
LTO 48	5	2500, 15	2500, 10	800, 10	500, 48
LTO 72	5	2500, 15	2500, 10	800, 10	500, 72
LTO 96	5	2500, 15	2500, 10	800, 10	500, 96
LTO 144	5	2500, 15	2500, 10	800, 10	500, 144

In **Figure 52,** all the above-mentioned samples are displayed at stages and are explained as follows:

- Sample A (LTO Ref): Reference sample depicting the particle size distribution.
- Sample B (LTO 0): sample showing larger particle sizes.
- Sample C (LTO 24): Stirred for 24 h exhibiting some decrease, in particle size.
- Sample D (LTO 48): Stirred for 48 h indicating a notable reduction in particle size to less than 5 µm.
- Sample E (LTO 72): Stirred for 72 h maintaining small particle sizes (<5 µm).
- Sample F (LTO 96): Stirred for 96 h displaying a reduction, in particle size.
- Sample G (LTO 144); Stirred for 144 h sustaining particle sizes.

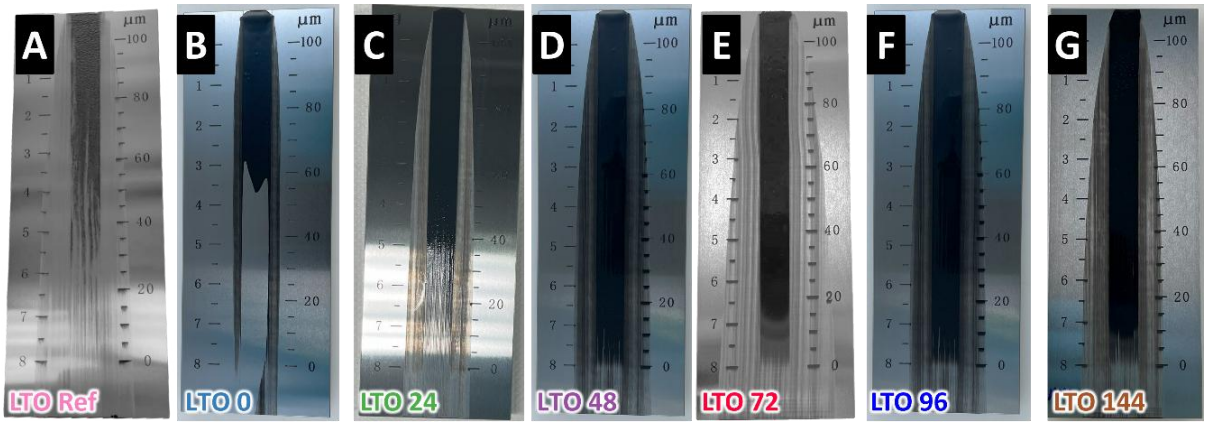

Figure 52. Actual photographs of grindometer results for **(A)** LTO Ref, **(B)** LTO 0, **(C)** LTO 24, **(D)** LTO 48, **(E)** LTO 72, **(F)** LTO 96, and **(G)** LTO 144.

After analyzing the impact of durations, it was found that a minimum of 48 h of stirring could yield similar particle sizes to the original slurry. Specifically, after stirring for 48 h with the binder added, the final slurry achieved particles under 5 µm. Through monitoring and analysis,

we were able to manage the mixing process to achieve the desired particle size and slurry consistency. This valuable data plays a role in enhancing the manufacturing process and improving product quality.

4.4.4. LTO electrode characterization

4.4.4.1. Characterization analysis

Figure 53 illustrates the coatings post-drying and calendering procedures. Each sample underwent a process of drying the slurry to eliminate any solvent, ensuring a solid and stable coating. The samples were categorized based on their stirring durations: LTO 0 for no stirring, LTO 24 for 24 h, LTO 48 for 48 h, LTO 72 for 72 h, LTO 96 for 96 h, and LTO 144 for 144 h of stirring. The impact of durations on the outcome was evaluated by examining the electrode surfaces. The LTO 0 coating displayed an uneven texture with the presence of large particles and irregular distribution. In contrast, the LTO 24 coating exhibited enhancements in particle distribution and uniformity compared to LTO 0; however, large particles were still visible.

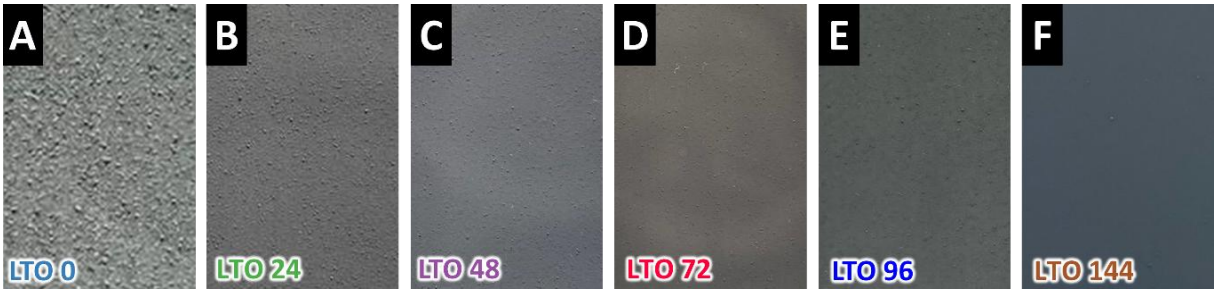

Figure 53. Photographs of electrode surfaces after calendering **(A)** LTO 0, **(B)** LTO 24, **(C)** LTO 48, **(D)** LTO 72, **(E)** LTO 96, and **(F)** LTO 144.

Significantly, the LTO 48 coating demonstrated improvements such as reduced particle sizes and enhanced coating quality. A better quality coating was observed in the case of the LTO 72 sample, with a more uniform surface texture indicating the beneficial impact of extending the stirring time beyond 48 h. Both the LTO 96 and LTO 144 coatings showed quality comparable to that of the LTO 72 sample. The coatings appear to stay consistent and even show no signs of decline in quality, which means extending the time does not have an impact on the coating quality appearance. The observations show that stirring for 48 h creates a good-quality coating with a uniform surface. To confirm the influence of stirring time further, we examined the electrode structure using scanning electron microscopy.

In **Figure 54,** it can be seen images of dried electrodes after calendaring to rate the level of LTO agglomerations on the surface at stirring times. These images revealed that as the stirring time increased from 0 h to 72 h, there was a decrease in particle agglomeration. However, when the stirring duration went beyond 96 h, surface grooves started appearing. These discoveries are important for refining the production process. It emphasizes the need for a balance between mixing and avoiding excessive mechanical strain. Our research showed that an optimal stirring duration falls within the range of 48 h to 72 h, ensuring uniformity and quality in the coating without causing surface harm.

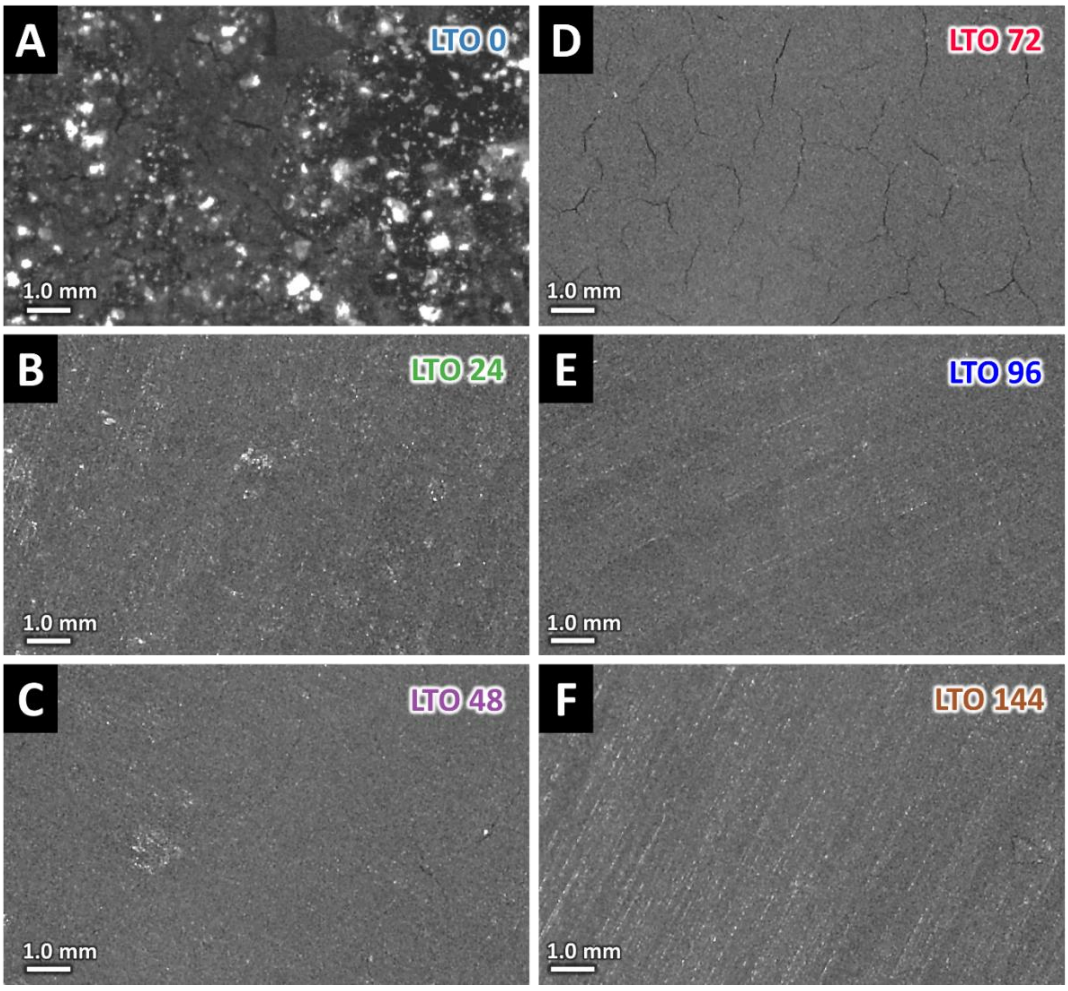

Figure 54. Photographs (Magnification: 30X) of the dried electrodes after calendaring **(A)** LTO 0**, (B)** LTO 24, **(C)** LTO 48, **(D)** LTO 72, **(E)** LTO 96**, (F)** LTO 144.

Figure 55 shows the scanning electron micrographs of calendered LTO samples to offer a more detailed look at particle morphology. The analysis of scanning electron micrographs is summarized as follows:

- **Figure 55A**: LTO 0 sample displays unevenness and clumping of LTO particles, showing mixing and distribution. The presence of particle clusters up to around 20 µm is evident.
- **Figure 55B**: Following 24 h of stirring, the surface of the LTO 24 sample shows improvement with roughness and fewer LTO clumps compared to the initial LTO 0 sample. The particles are distributed evenly, although some larger clusters are still present.
- **Figure 55C**: In the case of LTO 48, a uniform surface was observed, with noticeably fewer agglomerates. The large particles that were visible in samples were now barely discernible, indicating mixing and improved particle distribution.
- **Figure 55D**: Similarly, the surface quality of the LTO 72 sample remains high, similar to that of the LTO 48 sample. The particles are evenly spread out with signs of clusters, demonstrating that optimal stirring duration has been maintained.
- **Figure 55E**: It shows that the LTO 96 sample has surface grooves, which is the result of the stirring. Although the particle distribution is consistent, the presence of grooves suggests that excessive mechanical stress could impact the binder and its overall structure.
- In **Figure 55F,** it is observed that after 144 h of stirring, the surface grooves on LTO 144 are more prominent. Despite the particles being distributed, the increased stirring duration has led to mechanical stress.

Based on the analysis, it is suggested that extending the mixing duration reduces the formation of particle clusters, leading to a more evenly spread distribution of particles on the final electrode. After 48 h of stirring, a few large clusters were visible, resulting in a more uniform surface. Yet surpassing 96 h of mixing introduced surface indentations due to pressure on the binder. These results highlight the significance of a mixing period ranging from 48 h to 72 h for achieving an even quality for the coating without surface harm. The surface morphology of LTO 96, and even more LTO 144, reveals a much stronger entanglement of the LTO and carbon additive particles within the binder matrix. This “smearing“ characteristic correlates with the grooves post-calendaring. It could have negative effects on the electrode‘s electrical properties.

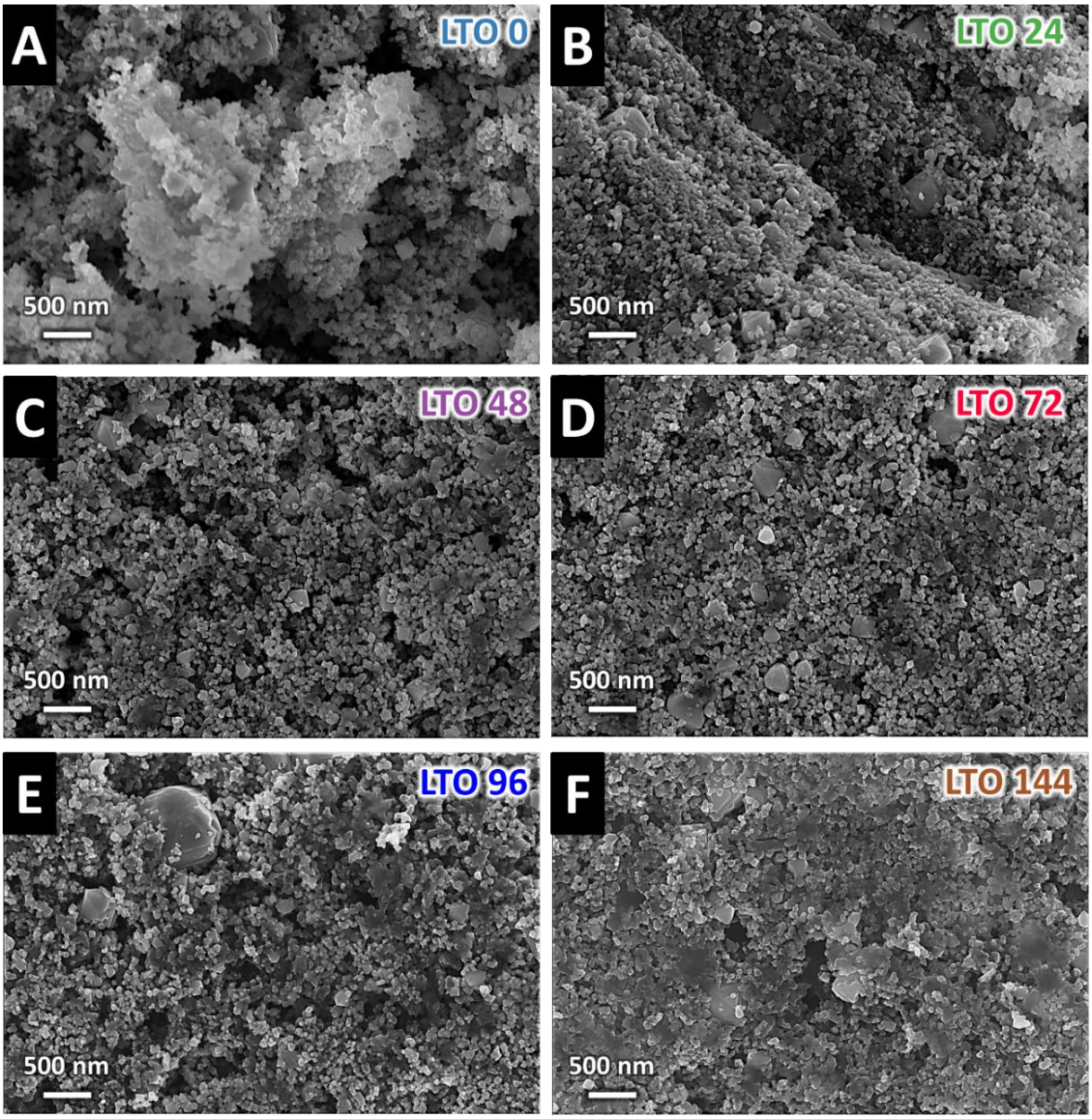

Figure 55. Scanning electron micrographs of LTO 0, LTO 24, LTO 48, LTO 72, LTO 96, and LTO 144 dried electrodes after calendering **(A-F)** top view.

In **Figure 56,** there are scanning electron micrographs that show the shape of samples at 50 µm in a sectional view. The cross-sectional images of samples stirred for a duration further confirm how this process impacts them. In these samples, prolonged stirring resulted in increased agglomeration of LTO and carbon particles within the binder. It was observed that excessive stirring could result in flaws in the final product. The smearing effect is particularly evident in sample LTO 144, where longer stirring also resulted in grooves on the surface.

The bonding between the conductive agent and the binder influences the surface structure and, in turn, affects performance. For instance, grooves and uneven distribution of particles

may disrupt ion paths within the electrode, diminishing conductivity and overall effectiveness. These discoveries show the importance of optimizing stirring duration on the performance of the final product. By understanding these effects, the manufacturing of LTO anodes can be adjusted to ensure that electrodes possess properties that are suitable for their intended use.

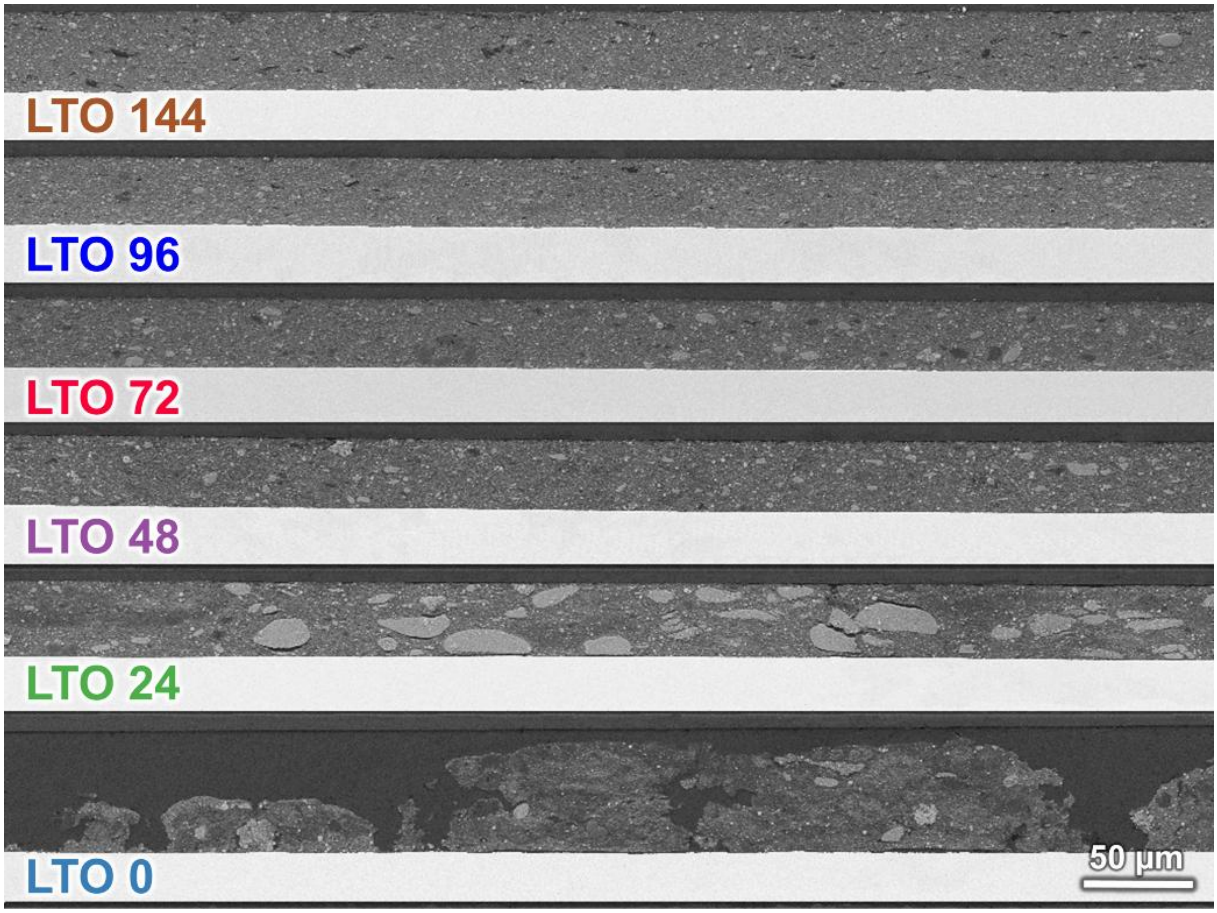

Figure 56. Scanning electron micrographs of LTO 0, LTO 24, LTO 48, LTO 72, LTO 96, and LTO 144 dried electrodes after calendering cross-sectional view.

Figure 57A shows the X-ray diffractogram of the electrode samples exhibiting the crystallized structure of spinel LTO (based on PDF 49-0207; space group $Fd\bar{3}m$). Reflections at 18.3° 2θ, 30.2° 2θ, 35.5° 2θ, 37.2° 2θ, 43.2° 2θ, 47.3° 2θ, 57.2° 2θ, 62.8° 2θ, and 66.0° 2θ indicate the planes of cubic LTO at 111), (220), (311), (222), (400), (331), (333), (440), and (531) respectively. Additional reflections seen at 43.4° 2θ, 50.5° 2θ, and 74.3° 2θ relate to cubic copper as the measurements were conducted with the electrode material cast onto Cu-foil. PDF 49-0207 was used as the starting structure during the Rietveld refinement (TOPAS) analysis. We obtained no significant trend of the unit cell values for the samples as a function of treatment duration. All values were within 8.360-8.366 Å, and the average domain size of all samples was about 82±16 nm (where the values were calculated by TOPAS by Prof. Dr.

Volker Presser). The X-ray diffractogram analysis also reveals that the crystallinity of the spinel LTO structure is maintained across all samples, regardless of the stirring duration.

Figure 57B shows the Raman pattern of the samples revealing five modes present, in all electrodes at specific frequencies: 217 cm^{-1}, 350 cm^{-1}, 428 cm^{-1}, 659 cm^{-1}, 1322 cm^{-1}, and 1590 cm^{-1}. These peaks confirm the spinel structure of LTO electrodes based on $A_{1g} + E_g + 3_{F2g}$ modes. In the following, each specific vibrational mode observed will be explained:

- The minor peak at 217 cm^{-1} indicates vibrations related to O-Ti-O bonds in the LTO structure.
- The peak at 350 cm^{-1} is also linked to O-Ti-O bond vibrations.
- Attributed to Li-O bond vibrations for LTO materials structure and stability is the peak at 428 cm^{-1}.
- Confirming the integrity of the spinel structure is the peak at 659 cm^{-1} associated with Ti-O bond vibrations.
- Additionally peaks around 1349 cm^{-1}. Approximately 1600 cm^{-1} correspond to the D-band and the G-band respectively. These bands confirm carbon presence within the electrodes.

The Raman pattern displays similar peaks in all samples ranging from LTO 0 to LTO 144, indicating that the spinel structure of LTO electrodes remains unchanged regardless of how they were stirred.

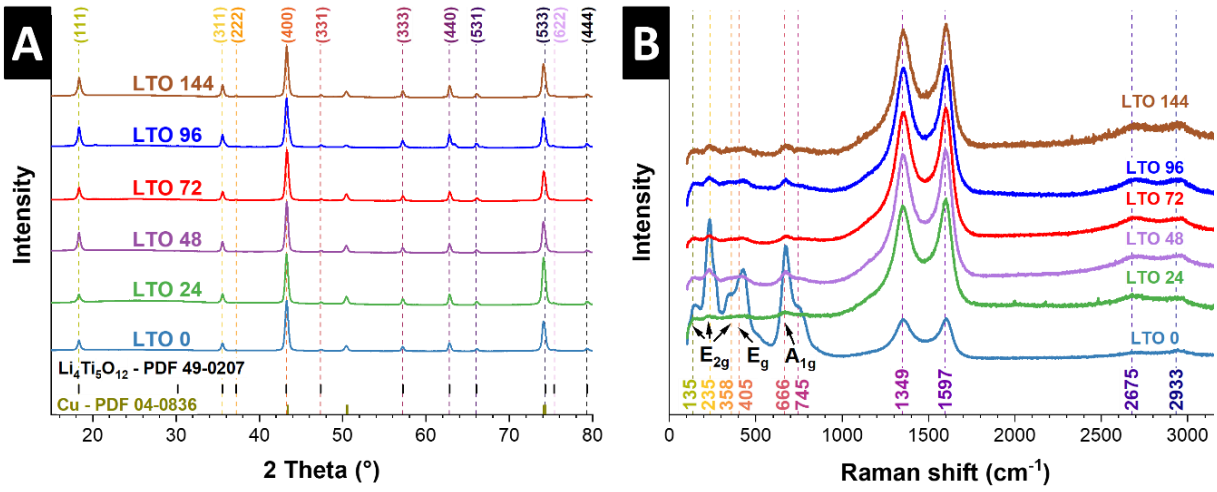

Figure 57. (A) X-ray diffractograms using Cu-Kα radiation (Cu reflections relate to the Cu current collector) and **(B)** Raman patterns of LTO 0, LTO 24, LTO 48, LTO 72, LTO 96, and LTO 144.

4.4.4.2. Electrochemical characterization

A series of tests like cyclic voltammetry, galvanostatic charge and discharge, and EIS measurements have been employed on LTO samples. By comparing samples with stirring times, we were able to see the stirring conditions that enhanced electrochemical performance. This study was crucial in understanding how varying stirring durations impacted the efficiency and stability of the electrodes during operation. To start we looked into the behavior of LTO samples prepared with different stirring durations using a magnetic stirrer (**Table 6**).

In the cyclic voltammogram graphs (shown in **Figures 58A-B**), distinct and reversible redox peaks were observed for all LTO samples. These peaks signify the processes of Li-ion intercalation and deintercalation within the electrodes. Specifically, Li-ion intercalation occurs around 1.50 V vs. Li^+/Li and 1.40 V vs. Li^+/Li whereas deintercalation takes place at 1.70 V vs. Li^+/Li and 1.90 V vs. Li^+/Li. Below 0.60 V vs. Li^+/Li, there is a peak observed for all samples related to the Li-ion intercalation process as described by **Equation 20**.

$$Li_4Ti_5O_{12} + 5Li^+ + 5e^- \rightarrow Li_9Ti_5O_{12} \qquad \textbf{(Equation 20)}$$

The LTO 72 sample shows the current values among the anodes at scan rates of 0.10 mV s^{-1} and 5.00 mV s^{-1}, as depicted in the figures. However, these specific current values decrease gradually with time. This observation implies that prolonged stirring durations could lead to influences that may negatively impact the performance, emphasizing the significance of optimizing the stirring duration.

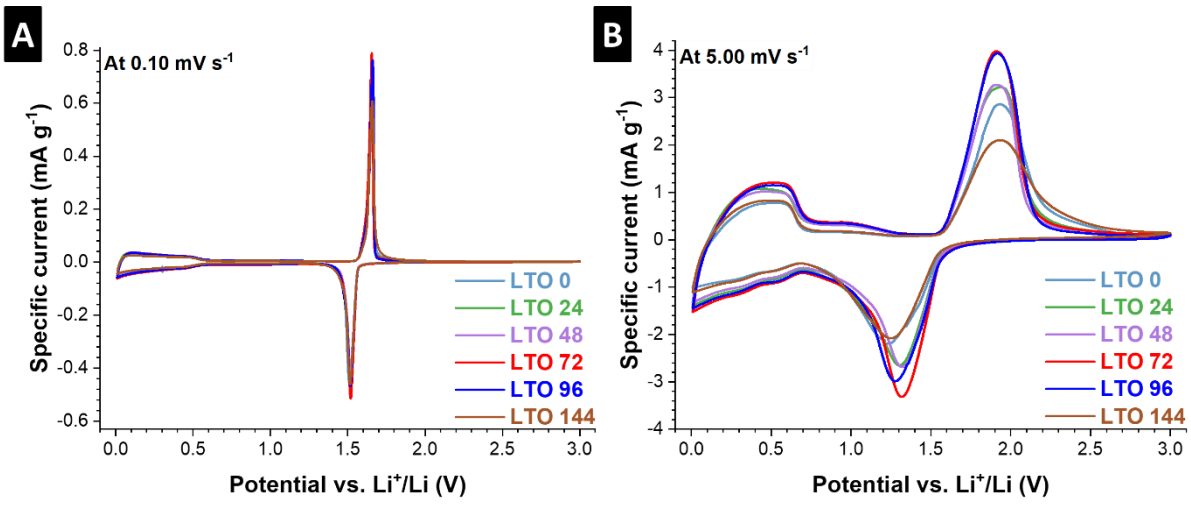

Figure 58. The half-cells data of LTO anode samples. Cyclic voltammetry profile of LTO 0, LTO 24, LTO 48, LTO 72, LTO 96, and LTO 144 **(A)** at a scan rate of 0.1 mV s^{-1}**, (B)** at a scan rate of 5.0 mV s^{-1}.

Moreover, when the stirring time is prolonged, the difference between the points of anodic and cathodic potential peaks decreases, as depicted in **Figure 59**. In the LTO 72 sample, there

is a minimum difference gap between the cathodic peaks, which increases with longer stirring periods. This smaller difference in potential indicates that the LTO 72 sample is efficient in transferring charges, thus facilitating Li-ion intercalation and deintercalation effectively. The obtained specific current values were conducted in **Figure 59** regarding the LTO 72 sample, which supports the other finding as well. The rise in values signals a reduction in electrode resistance and an enhancement of electrochemical performance. Overall, it appears that Li-ion intercalation and deintercalation processes are smoother within the LTO 72 material, resulting in enhanced performance based on cyclic voltammetry outcomes. This progress is linked to the optimized stirring duration that promotes particle distribution across electrodes, decreasing resistance and enhancing reaction speed.

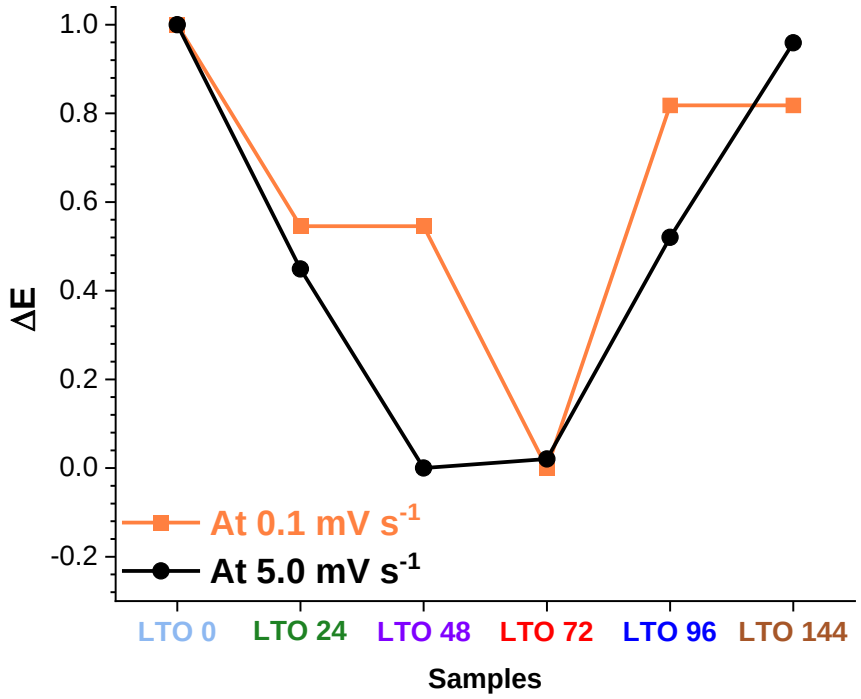

Figure 59. Normalized the difference between the points of anodic and cathodic potential peaks values were obtained from anodic and cathodic peaks for LTO 0, LTO 24, LTO 48, LTO 72, LTO 96, and LTO 144 at scan rates of 0.10 mV s^{-1} and 5.00 mV s^{-1}.

Figure 60A illustrates the performance of different LTO samples, with varying stirring times from 0 h to 144 h alongside an LTO Ref sample. The tests were carried out at currents ranging from 0.1-5.0 A g^{-1} (equivalent to 0.34C to 17C) within a potential range of 0.01-3.00 V vs. Li^+/Li. The findings show that at rates, all samples exhibited specific capacities around 250 mAh g^{-1} except for the LTO 72 and LTO 96 samples, which showed higher values averaging at about 293 mAh g^{-1} and 272 mAh g^{-1}, respectively. However, as the cycle number and current rates

increased, the specific capacity of the LTO Ref sample decreased significantly and experienced a decline.

Furthermore, the performance difference between the samples became more noticeable, with LTO 72 being higher than all others in performance. As shown in **Figure 60B**, at a rate of 5.0 A g^{-1} (around 17C) during the 5th cycle, LTO 72 achieved a capacity of 210 mAh g^{-1}.

This capacity is higher than the capacities of LTO 96, LTO 48, LTO 144, LTO 24, LTO 0, and LTO Ref by 19%, 48%, 78%, 89%, 347%, and 2525%, respectively. The excellent results seen with LTO 72 are due to the amount of stirring time, which leads to optimal outcomes and enhances the uniformity and distribution of active materials within the electrode.

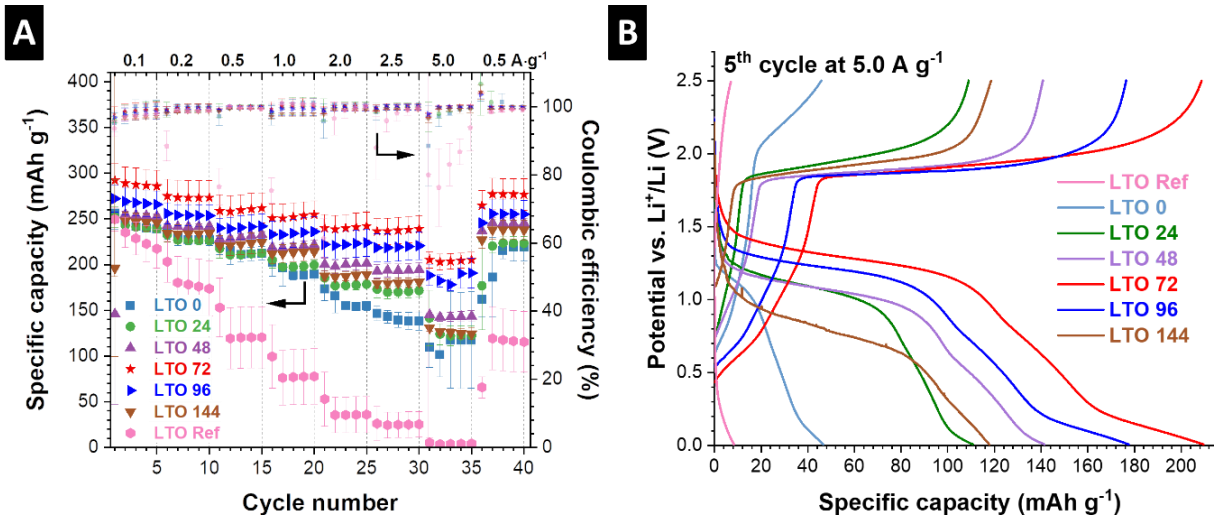

Figure 60. The half-cells data of LTO anode samples. **(A)** Rate performance of LTO Ref, LTO 0, LTO 24, LTO 48, LTO 72, LTO 96, and LTO 144 at 0.1-5.0 A g^{-1}. **(B)** LTO 0, LTO 24, LTO 48, LTO 72, LTO 96, LTO 144, and LTO Ref anode samples show the charge/discharge curve at 5.0 A g^{-1} at the 5th cycle.

The enhanced distribution of particles results (based on scanning electron micrographs) in improved electrochemical performance, which includes increased capacities and enhanced stability at higher current rates (0.1-5 A g^{-1}). Additionally, findings show that stirring longer than 72 h can still damage electrodes, and it does not provide significant performance advantages. It may even lead to issues like smearing and increased surface roughness. Therefore a stirring duration of 72 h is considered optimal for achieving the balance between capacity and stability. Samples exhibiting better rate performance were subjected to cycling at a current rate of 2.5 A g^{-1} (approximately 8.5C). As depicted in **Figure 61A** the initial capacities for LTO 24, LTO 48, LTO 72, LTO 96, and LTO 144 were recorded as 184 mAh g^{-1}, 195 mAh g^{-1}, 218 mAh g^{-1}, 215 mAh g^{-1}, and 181 mAh g^{-1} respectively. After completing 100 cycles, these samples retained around 90%, 90%, 95%, 92%, and 90% of their capacity, respectively. These

findings suggest that the electrodes demonstrate capacity in the cycles, possibly attributed to Li-ion storage on the electrode surfaces. As cycling progresses over time, the capacity stabilizes, indicating the performance of the electrodes under cycling conditions.

The performance of LTO 72 was studied further to test its long-term cycling performance when subjected to high applied current levels. In **Figure 61B**, the results of the LTO 72 electrodes performance after 100 cycles at rates of 2.9 A g^{-1}(approximately 10C), 5.0 A g^{-1} (approximately 17C), 10.0 A g^{-1} (approximately 34C), and 20.0 A g^{-1} (approximately 68C) are depicted. Initially, the capacities at these rates were recorded as follows: 232 mAh g^{-1}, 190 mAh g^{-1}, 162 mAh g^{-1}, and 78 mAh g^{-1}. The LTO 72 electrode managed to maintain around 99%, 98%, 94%, and 90% of its capacity at these rates after completing a cycle of 100 times. This consistency, in capacity retention, highlights the stability and robustness of the LTO 72 electrode when operating under demanding high-applied current conditions.

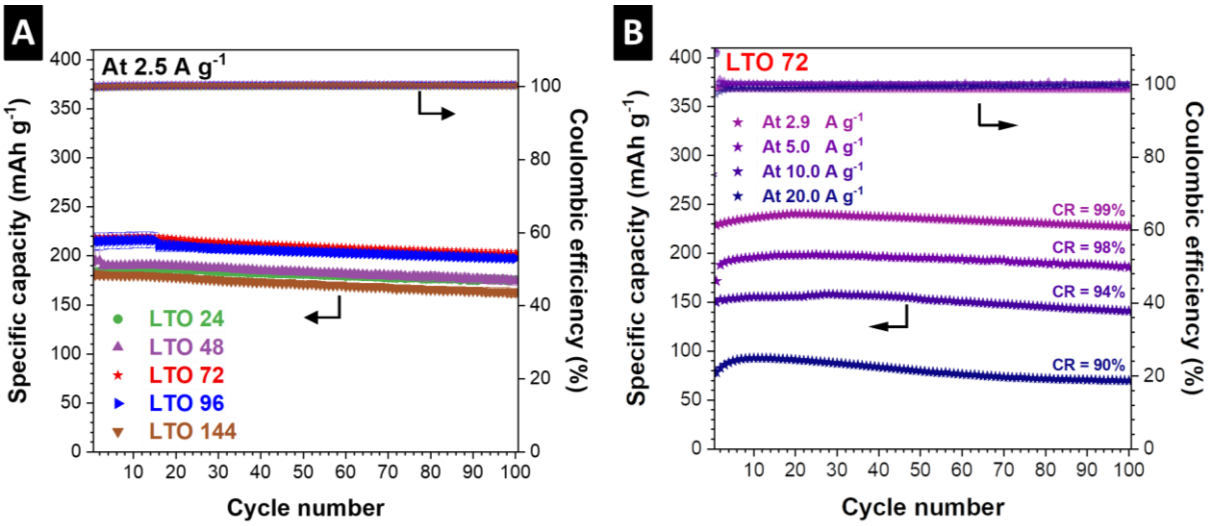

Figure 61. The half-cells data of LTO anode samples. and **(A)** show the cycling performance of LTO 24, LTO 48, LTO 72, LTO 96, and LTO 144 at 2.5 A g^{-1} for 100 cycles. **(B)** Cycling performance of LTO 72 at 2.9 A g^{-1} (≈10C), 5.0 A g^{-1} (≈17C), 10.0 A g^{-1}(≈34C), and 20.0(≈68C) A g^{-1} for 100 cycles.

Additionally, the LTO 72 samples underwent cycling tests at current rates of 5.0 A g^{-1} and 10.0 A g^{-1} to assess the durability and stability of the electrodes over numerous cycles (up to 2000 cycles). The outcomes can be seen in **Figure 62A**. When subjected to a rate of 5.0 A g^{-1}, the LTO 72 samples retained capacities of 84%, 73%, and 60% after completing 300 cycles, 1000 cycles, and 2000 cycles. This suggests that under conditions, the electrodes preserved a substantial portion of their initial capacity over an extended period. When operating at a rate of 10.0 A g^{-1}, the LTO 72 samples exhibited significant capacity retentions of approximately

80% after completing 300 cycles, around 68% after completing 1000 cycles, and roughly 57% after finishing 2000 cycles. Despite a doubling, in applied intensity by up to 100% there was a minor decrease of 3% in electrode capacity retention after 2000 cycles. This showcases the durability of LTO 72 electrodes under strenuous circumstances.

Furthermore, the Coulombic efficiency for the LTO 72 samples remained close to 100% during all cycling performance assessments. This high Coulombic efficiency indicates that the charge and discharge processes were reversible with capacity loss through side reactions or degradation. The results show the durability and consistent performance of the LTO 72 electrode. Its capacity to maintain a level of charge over cycles, with almost 100% Coulombic efficiency, demonstrates the success of the refined mixing technique employed in creating these electrodes.

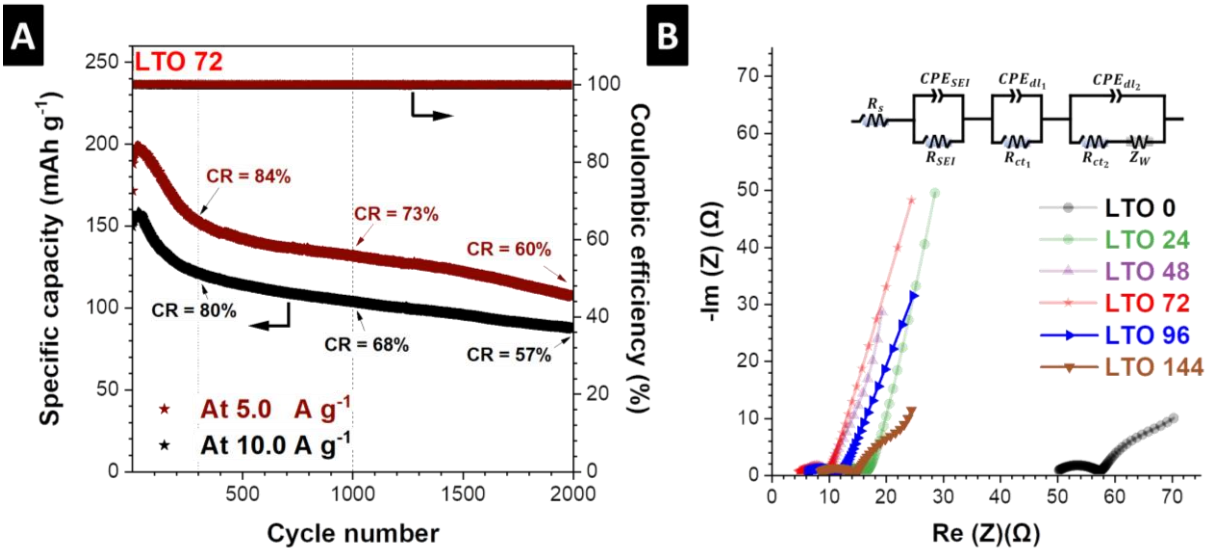

Figure 62. The half-cells data of LTO anode samples. **(A)** at 5.0 A g^{-1}, and 10.0 A g^{-1} for 2000 cycles. **(B)** Electrochemical impedance spectroscopy results after 100 cycles at 2.5 A g^{-1} for LTO 0, LTO 24, LTO 48, LTO 72, LTO 96, and LTO 144, and the equivalent circuit model was used for fitting. CR = capacity retention vs. the first cycle.

The EIS measurements were performed to elaborate on the reasons behind the decreased electrochemical performances of samples stirred longer than 72 h. We explored the kinetic processes and assessed the influence of the internal resistance of LTO samples by model-fitting the Nyquist plots, as shown in **Figure 62B**. The samples were subjected to EIS tests after 100 cycles at 2.5 A g^{-1}, and based on the EIS responses, the equivalent circuit model (ECM) was obtained. In the high-frequency region, an Ohmic resistance associated with the resistances of cables, electrolytes, contact between the active material and current collector, and pore

resistance inside the separators appeared and indicated as R_b. Three semicircles and one 45 ° inclined line were observed.

The high-frequency semicircle in the spectra is directly linked to the movement of Li-ion through the SEI film, which is shown by R_{SEI}. The second semicircle occurring in the middle-to-high frequency range is attributed to the transfer of charge at the interface between the electrode/electrolyte (R_{ct1}). The third semicircle may be associated with the charge-transfer process defined here as (R_{ct2}). Finally, a 45 ° inclined line in the lower-frequency region due to a semi-infinite Li-ion diffusion into the electrode is represented here by Warburg impedances (Z_W). The system's electrochemical performance primarily depends on the cell's total resistance. The total internal resistance (R_{Total}) is determined in **Table 7** for all LTO samples. As summarized in **Table 7**, the total resistance (R_{Total}) is highest for LTO 0 (69.00 Ω across all components, indicating poor conductivity, which is a result of proper mixing). Such resistance significantly decreases as stirring time increases, wherein a minimum resistance of 9.00 Ω was observed for LTO 72. After this point, the resistance values gradually increase again for LTO 96 (12.90 Ω) and LTO 144 (25.50 Ω).

Table 7. Electrochemical impedance spectroscopy results of LTO samples after 100 lithiation and delithiation at 2.5 A g^{-1} (≈8.5C).

Item label	R_b (Ω)	R_{SEI} (Ω)	R_{ct} (Ω)	R_{ct1}(Ω)	R_{Total} (Ω)
LTO 0	48.00	10.90	9.60	0.50	69.00
LTO 24	11.30	5.90	13.80	2.30	33.30
LTO 48	4.70	1.60	3.80	13.80	23.90
LTO 72	3.60	1.10	3.00	1.30	9.00
LTO 96	5.30	6.10	0.50	1.00	12.90
LTO 144	7.70	5.40	6.80	5.60	25.50

LTO 72 shows the conductivity among the samples, indicating that the stirring time was well-optimized for improved performance. Besides LTO 24 and LTO 48 exhibit decreased resistance compared to LTO 0 initially. Longer stirring times for samples, such as LTO 96 and LTO 144, show higher resistance values than LTO 72. This suggests that excessive stirring beyond a point may have negative effects on electrode structure and performance. Overall, the results highlight that LTO 72 has the lowest impedance and internal resistance. The improved ion and electron transport within the material is evident and causes the reduced impedance and resistance values of LTO 72 compared to samples. This enhanced transport is essential for achieving high-rate performance and overall battery efficiency.

The lower resistance in LTO 72 could be due to some level of tension within the matrix, which helps integrate LTO and carbon particles better and leads to improved conductivity and operational efficiency. Optimizing stirring enhances the dispersion and interaction between LTO and carbon particles in the binding matrix, contributing to conductivity and overall electrochemical performance. These findings are consistent with studies in optical microscopy (**Figure 53** and **Figure 54**) and scanning electron microscopy (**Figure 55** and **Figure 56**) that also highlighted particle distribution and reduced clustering in the case of the LTO 72 sample.

4.4.4.3. Post-mortem Characterization

The sample LTO 72 electrodes were analyzed, and 5000 cycles were applied at a rate of 10.0 A g^{-1} to complement our data. The X-ray diffraction examination, depicted in **Figure 63**, indicated that the electrochemical performance aligned with the crystalline structure of the LTO 72 electrodes, which remained unchanged throughout the mentioned rough cycling process. The X-ray diffractogram revealed consistent unit cell dimensions, with the value persisting at 8.364 Å without alterations.

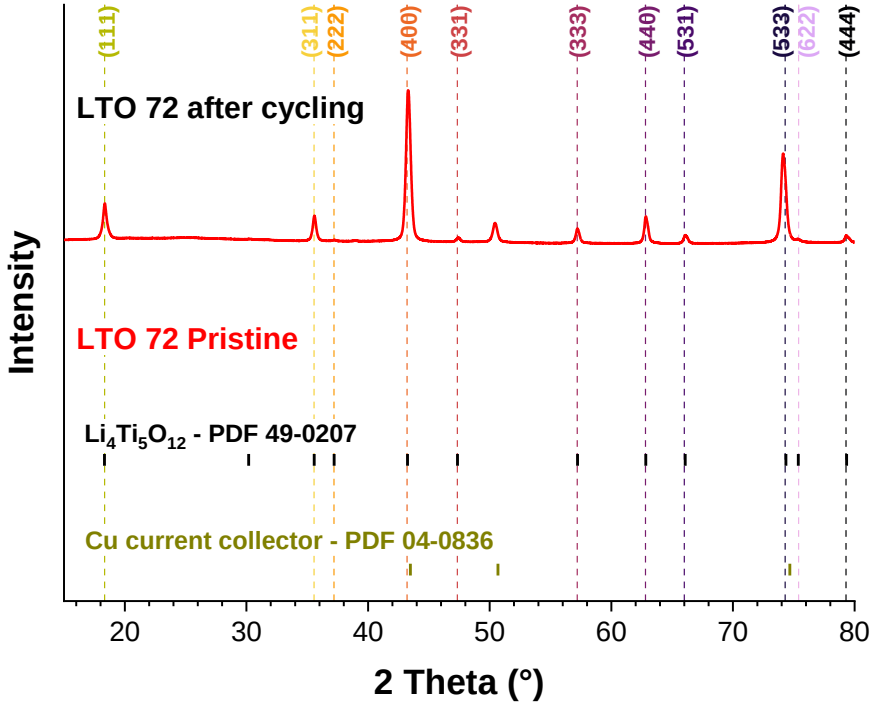

Figure 63. X-ray diffractograms using Cu-Kα radiation of pristine and cycled LTO 72 (5000 cycles at 10.0 A g^{-1} (≈34C)) electrodes. Cu reflections relate to the Cu current collector.

Furthermore, there was no broadening related to domain size (as the domain size of the sample stayed in the range of 82±16 nm) confirming the durability of the electrodes post-

mortem cycling. Scanning electron microscopy was utilized to examine the structure of the LTO 72 electrodes. Before cycling, **Figure 64A** depicts the particle structure in the LTO 72 electrode. Following 5000 cycles, examination of the LTO 72 electrode (**Figure 64B**) showed no morphological changes. The particle structure remained without signs of degradation or clumping. The sustained crystalline structure and consistent particle morphology after prolonged cycling at the high applied current rate, emphasize the robustness of the LTO 72 electrode material.

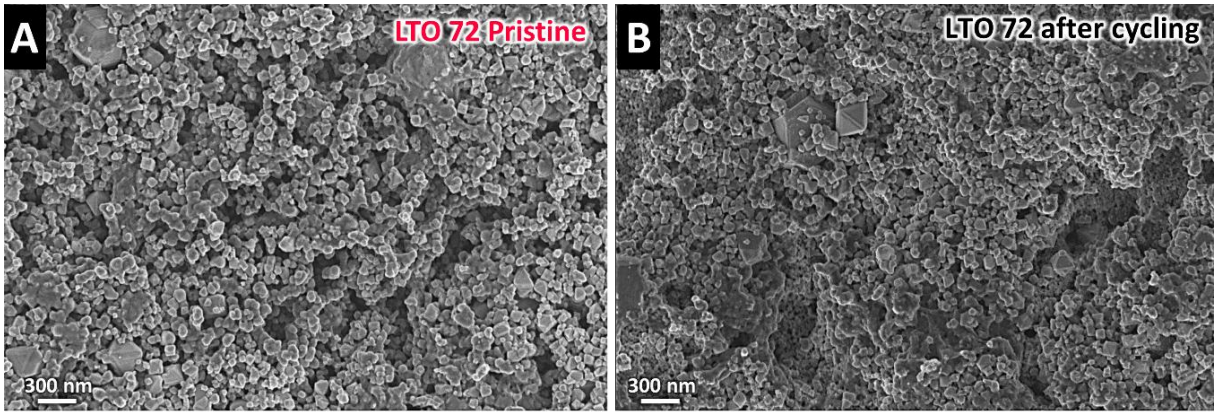

Figure 64. Scanning electron micrographs of **(A)** pristine LTO 72 and (**B)** LTO 72 after 5000 cycles at 10.0 A g^{-1} (≈34C).

4.4.4.4. Comparative study of optimized LTO with other studies

To present a reasonable comparative study, we first convert the C-rate to specific currents to simplify the comparison, as shown in **Table 8**. The obtained values in this work show promising performance, particularly at high rates, compared to state-of-the-art literature, as depicted in **Figure 65**. For example, Temeche et al. improved the electrochemical performance of LTO nanopowder by adding $LiAlO_2$ and Li_6SiON and reported capacities of 130 mAh g^{-1} and 70 mAh g^{-1} at 1.3 A g^{-1} and 2.6 A g^{-1}, respectively. The optimized LTO anode of this work at the higher specific currents of 2.0 A g^{-1} and 2.9 A g^{-1} delivered way higher capacities of 255 mAh g^{-1} and 232 mAh g^{-1}, respectively.

Lim et al. prepared a binder-free hybrid LTO anode and obtained a capacity of 143 mAh g^{-1} at 1.3 A g^{-1}. Our optimized LTO 72 at a 54% higher specific current of 2 A g^{-1} delivered 255 mAh g^{-1}. Ding et al. synthesized an LTO composite with TiO_2 and tested it at an extended potential range, delivering a capacity of 40 mAh g^{-1} at 2.9 A g^{-1}. For the same specific current, our LTO 72 delivered 232 mAh g^{-1}. Gu et al. synthesized $Li_4Ti_{4.95}Zr_{0.05}O_{12}$/C and reported 100 mAh g^{-1} at

1.5 A g^{-1}. Such a result is lower compared to our optimized LTO, which delivered nearly 155% higher capacity at 2 A g^{-1} specific current.

Table 8. Converting the C-rate to specific currents for comparison. Gu et al., Han et al., Lim et al., Temeche et al. Ding et al.

Author	The C-rate has been calculated based on the theoretical capacity of	C-rate	Specific current (mA g^{-1})	Specific capacity (mAh g^{-1})
Gu et al.	293 mAh g^{-1}	0.2	58.6	275.0
		0.5	146.5	242.0
		1.0	293.0	200.0
		2.0	586.0	159.0
		5.0	1465.0	100.0
Han et al.	293 mAh g^{-1}	0.1	29.3	260.0
		0.5	146.5	223.0
		1.0	293.0	205.0
		2.0	586.0	198.0
		5.0	1465.0	183.0
		10.0	2930.0	160.0
		20.0	5860.0	95.0
Lim et al.	260 mAh g^{-1}	0.1	26.0	220.4
		0.2	52.0	210.4
		0.5	130.0	199.5
		1.0	260.0	178.1
		5.0	1300.0	143.0
Temeche et al.	260 mAh g^{-1}	0.5	130.0	240.0
		1.0	260.0	198.0
		2.0	520.0	170.0
		5.0	1300.0	130.0
		10.0	2600.0	70.0
Ding et al.	293 mAh g^{-1}	0.2	58.6	410.0
		0.5	146.5	198.0
		1.0	293.0	160.0
		2.0	586.0	126.0
		5.0	1465.0	90.0
		10.0	2930.0	40.0

Zeng et al. synthesized nano-M embedded $Li_4Ti_5O_{12}$/C composites and reported 110 mAh g^{-1} at 1.0 A g^{-1}. Our LTO 72 delivered 143% more capacity for the same specific current. Han et al., by extending the potential range to 0 V, showed that at 5.9 A g^{-1}, there was a sharp drop in capacity after 10 cycles from 112 mAh g^{-1} to around 58 mAh g^{-1}. While they showed 56.2% capacity retention at 1.5 A g^{-1} after 300 cycles, our best-performing electrode demonstrated capacity retention of 80% after 300 cycles at a specific current of 10.0 A g^{-1}. Overall, our optimized LTO 72 electrode delivered notable and prominent electrochemical performances.

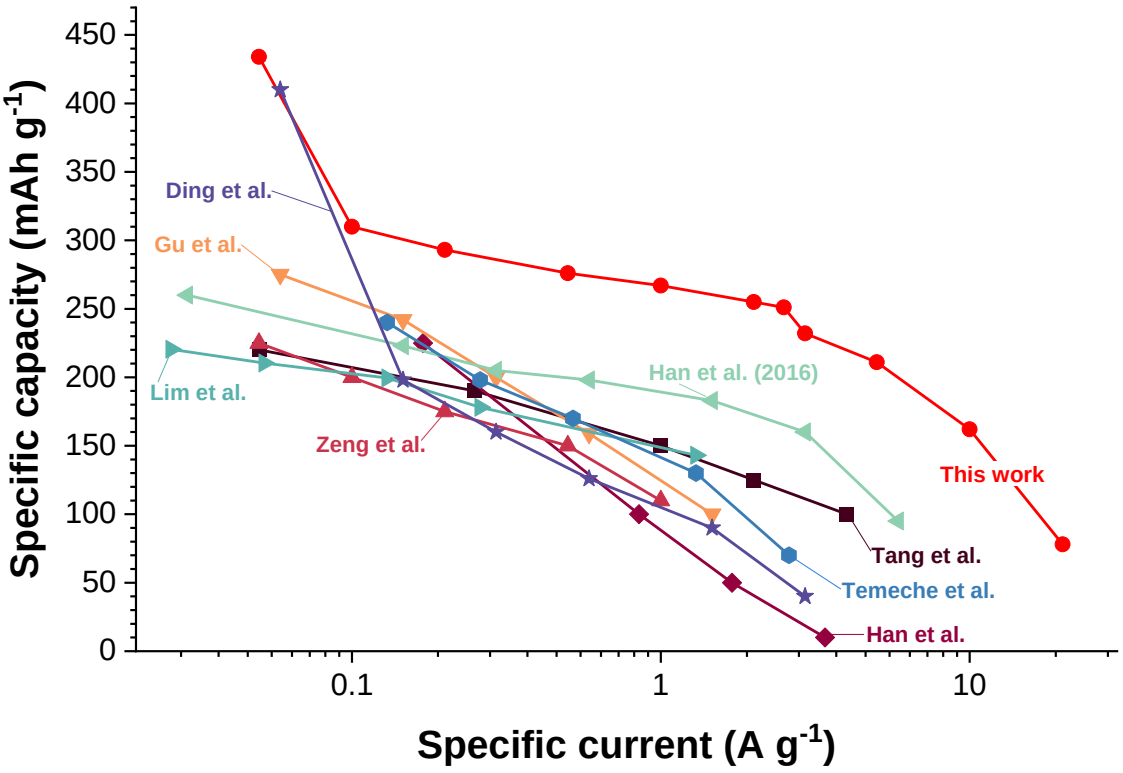

Figure 65. Comparison of optimized LTO electrode (LTO 72) performance in this work with state-of-the-art literature.

5. LITHIUM IRON PHOSPHATE (LFP), LITHIUM MANGANESE OXIDE (LMO), AND LITHIUM MANGANESE OXIDE//ACTIVATED CARBON (LMO//AC) ELECTRODE PREPARATION

The manufacturing of electrode materials plays a vital role in advancing high-performing LIBs. This section of the report focuses on three electrode materials. Lithium Iron Phosphate (LFP) Lithium Manganese Oxide (LMO) and a hybrid electrode of LMO with Activated Carbon (LMO//AC). These materials were selected for their electrochemical properties and cost-effectiveness while being environmentally friendly options for energy storage purposes such as powering electric vehicles and storing energy, in grid systems. This chapter will describe the materials and techniques we used to create the materials for our experiments without purifying the chemicals since they were obtained from trustworthy sources for consistency in our tests. The section also explains the procedures it has been followed to produce the LFP, LMO, and LMO //AC electrodes that serve as the foundation, for our electrochemical assessments.

5.1. Materials

All chemicals were purchased commercially and used as received without any purification. $LiFePO_4$ nanopowder (LFP) was synthesized as discussed below. LMO powder (98%, ~0.5 µm) was purchased from Sigma-Aldrich. Super C65 (C65) conductive carbon black was from IMERYS Graphite & Carbon. Dimethyl sulfoxide solvent (DMSO, ≥99.9%, anhydrous) and polyvinylidene fluoride binder (PVdF) were procured from Sigma-Aldrich, respectively. Battery-grade carbon-coated aluminum foil current collectors with 18 µm thickness were obtained from MTI Corporation.

5.2. LFP cathode

5.2.1. Synthesis of lithium iron phosphate

Lithium iron phosphate (LFP) was synthesized by Dr. Hitoshi Nakamura using a hydrothermal method. In a process, phosphoric acid, iron sulfate (heptahydrate), and lithium hydroxide were mixed in molar ratios of 1:1:3 and dissolved in distilled water at room temperature to make a solution, with a concentration of 1.0 mol L^{-1}. The mixture was then placed in a polytetrafluoroethylene reactor heated to 150°C for 20 h and left to cool to room temperature.

After filtering and washing the solution using a Buchner funnel, the final product was dried in an oven under a vacuum.

5.2.2. LFP cathode preparation

Figure 66 shows the preparation steps for LFP cathodes. First, 80 mass% as-synthesized LFP nanopowder was mixed with 10 mass% conductive carbon black (C65) by manually grinding in a mortar for 10 min, followed by speed mixing using an SM at 1000 rpm for 5 min. DMSO solvent was added dropwise to the dry mixture and subsequently placed in the SM at 1500 rpm and 2500 rpm for 5 min each, respectively. A 10 mass% PVdF solution was added to the slurry, and the mixture was further mixed at 800 rpm for 10 min. The mixtures were mechanically stirred continuously at 500 rpm for 24 h.

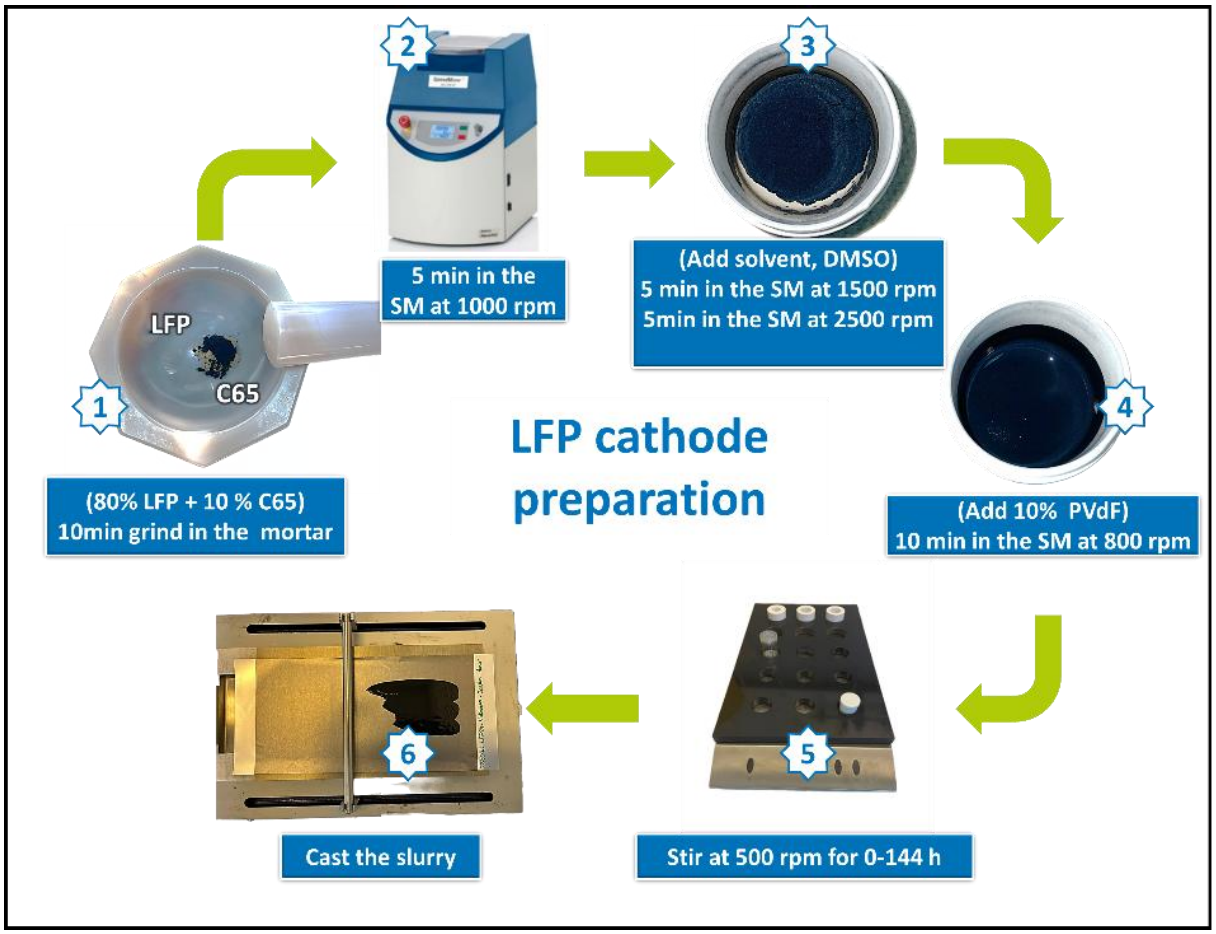

Figure 66. The manufacturing mixing routines of lithium iron phosphate cathode

The mixtures obtained were applied onto the aluminum foil coated with carbon using a Micrometer blade. Subsequently, the coated samples were left to dry in a ventilated cabinet for 12 h, followed by a drying step in a vacuum oven at 80°C and 60 mbar for another 12 h to

guarantee drying. After that, these cathodes were set for utilization in LIBs, and their efficiency relied on how evenly and consistently they were prepared.

5.2.3. Half-cell assembly using LFP cathode

Figure 67 displays the illustration of a CR2032-type Li-ion battery coin helf cell assembly using LFP cathodes. All of our cells are assembled with high precision and quality, making them suitable for use in LIB testing and applications. Our thorough preparation and controlled environment are critical for obtaining consistent, reliable, and reproducible results in subsequent experimental evaluations and practical energy storage solutions. The LFP half-cell assembly was carried out in an MBRAUN Argon-filled glove box, where oxygen and water levels were maintained below 0.1 ppm to ensure a controlled environment.

The cells were fabricated in coin cell format using commercial CR2032 enclosures from PI-KEM. Lithium chips (Ø = 15 mm, MTI Corporation) were used as both the counter and reference electrodes, while LFP discs (Ø = 10 mm, approximately 16 mg cm^{-2}, with a dried thickness of around 210 µm) were used as the working electrodes. Whatman GF/F glass fiber discs (Ø = 18 mm) were punched and used as separators between the electrodes. For each coin cell, 150 µL of an electrolyte solution consisting of 1 M $LiPF_6$ salt in a mixture of ethylene carbonate and dimethyl carbonate (EC:DMC 1:1 by volume, Sigma-Aldrich), was injected. Two stainless steel 304 spacers (thickness = 0.5 mm, PI-KEM) were used for each coin cell, and the cells were sealed under a pressure of 1000 psi using a hydraulic crimping machine (MSK-110, MTI Corporation).

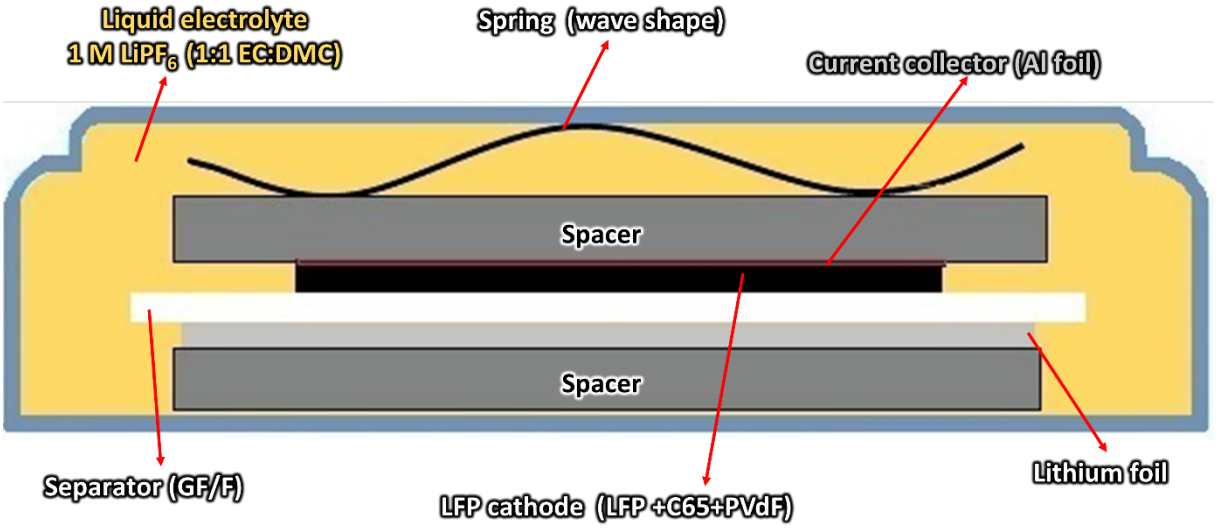

Figure 67. Illustration of a CR2032-type Li-ion battery coin cell assembly using LFP cathode.

5.3. LMO cathode

5.3.1. LMO cathode preparation

Figure 68 shows the preparation steps for LMO cathodes. In parallel to the above procedures, 80 mass% LMO powder was first mixed with 10 mass% C65 conductive carbon black by manual grinding in a mortar for 10 min, followed by speed mixing at 1500 rpm for 5 min. DMSO solvent and a 10 mass% PVdF binder solution were then added sequentially to the mixture and placed in a speed mixer at 2500 rpm and 800 rpm for 10 min each, respectively. Finally, the mixtures were stirred continuously at 500 rpm for 24 h. The final slurries were then carefully coated onto a battery-grade carbon-coated aluminum foil current collector using a micrometer doctor blade at a speed of 7.5 mm s^{-1} to maintain 200 µm wet thickness. The wet thickness of the coating was maintained to ensure uniformity. The coated foils were subjected to a 2-step drying process steps to finalize the cathodes for use in LIBs.

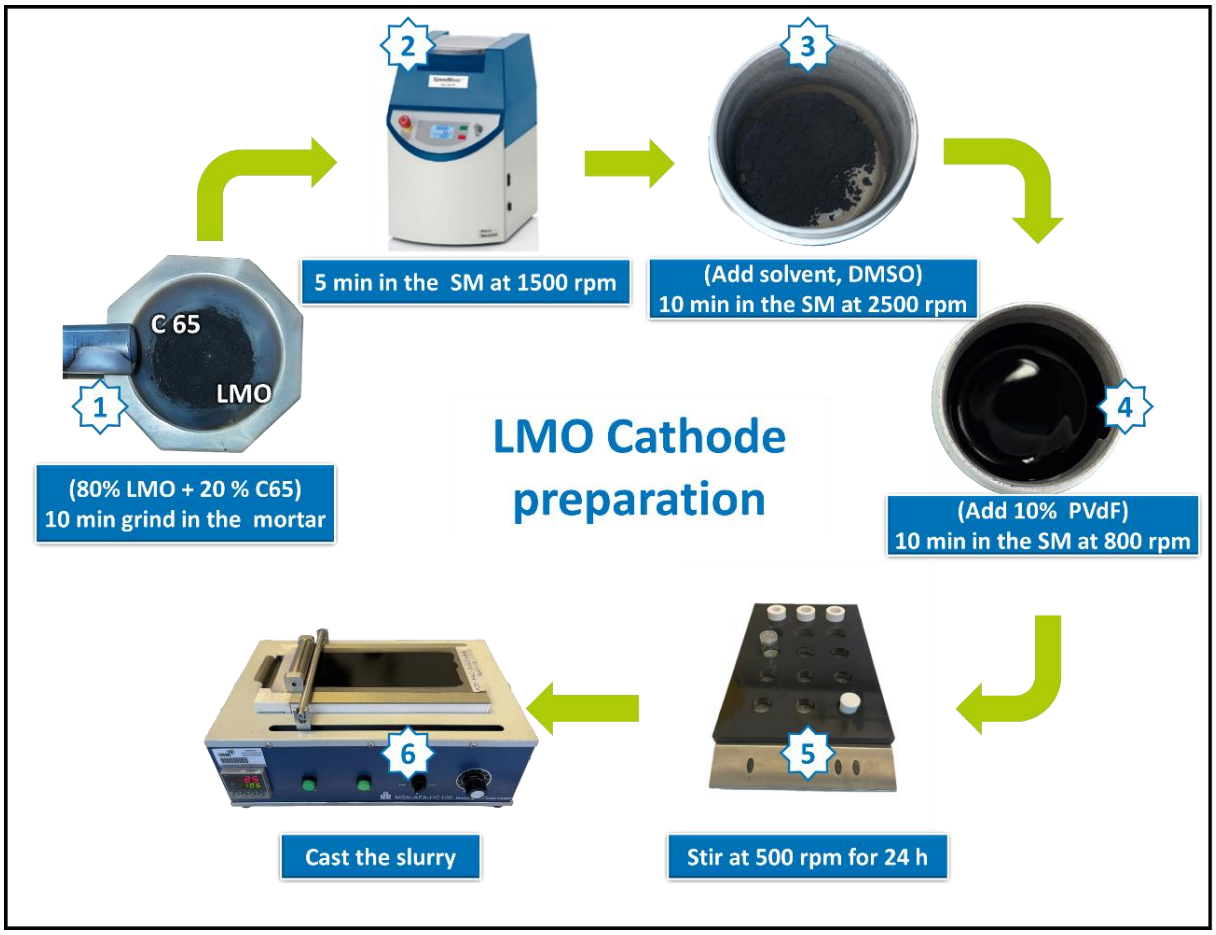

Figure 68. The manufacturing of lithium manganese oxide cathode mixing routines.

5.3.2. Half-cell assembly using LMO cathode

A similar configuration like **Figure 69** and replacing LFP with an LMO cathode was used to build a CR2032-type LIB coin half-cell assembly with LMO cathodes. The cells are put together with care and quality, making them suitable for testing and use in LIB applications. Our planning and controlled setting is crucial for achieving dependable and repeatable outcomes in experiments. The LMO half-cell assembly took place in an MBRAUN Argon-filled glove box where oxygen and water levels were kept below 0.1 ppm. The cells were created in coin cell format using CR2032 provided by PI-KEM. Lithium chips (diameter = 15 mm from MTI Corporation) were used as both the counter and reference electrodes. In comparison, LMO discs (diameter = 10 mm weighing 4.4 mg cm^2 with a thickness of about 35 µm) served as the working electrodes. Whatman GF/F glass fiber discs (diameter = 18 mm) were cut out. Used as separators between the electrodes. Each coin cell received a solution amount of 150 µL containing 1 M LiPF6 salt in a mix of ethylene carbonate and dimethyl carbonate (EC:DMC 1:1 by volume, from Sigma Aldrich). This electrolyte is necessary to help Li-ion move inside the battery. We placed two steel 304 spacers (each with a thickness of 0.5 mm, from PI-KEM) in every coin cell. After that, we sealed the cells using a crimping machine (MSK-110 from MTI Corporation at a pressure of 1000 psi.

5.4. Hybrid lithium manganese oxide//activated carbon cathode

5.4.1. Hybrid LMO//AC cathode preparation

The hybrid LMO//AC cathode was prepared to enhance the battery's performance by leveraging the strengths of both materials. LMO because of high energy density and stable electrochemical properties and AC provides a large surface area and great conductivity facilitating quicker charge/discharge cycles and improved power output. The hybrid cathode is designed to boost energy and power density to enhance the device's overall performance for applications that demand both high capacity and high-rate capabilities. **Figure 70** shows the preparation steps for the LMO//AC cathodes. 30% LMO powder was finely mixed and blended with 50% activated carbon (YP-80F, Kuraray) and 10% conductive carbon black (C65) by manual grinding for 10 min and speed mixing at 1000 rpm for 5 min, respectively.

DMSO solvent was added dropwise to control the consistency of the slurry before placing it in a speed mixer at 2500 rpm for 10 min. A 10% PVdF binder solution was then added, and the mixture was subjected to one more round of speed mixing at 800 rpm for 10 min. The wet

mixture was continuously stirred for 24 h at 500 rpm to ensure the uniform blending of LMO powder, active carbon, and conductive carbon black.

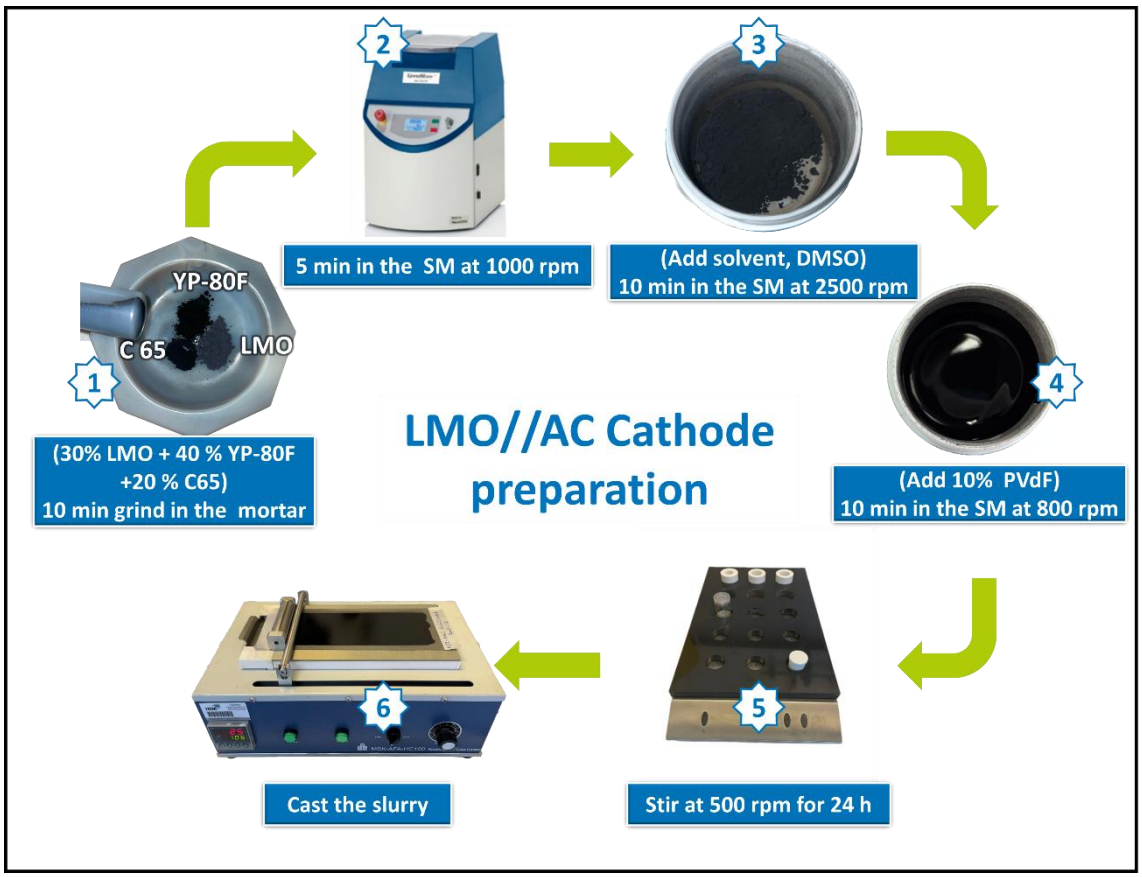

Figure 69. The manufacturing of hybrid cathode including lithium manganese oxide and activated carbon mixing routines.

The final slurries were coated onto a battery-grade carbon-coated aluminum foil (18 µm, MTI Corporation) current collector using a micrometer doctor-blade at a speed of 7.5 mm s^{-1}. The wet thickness of the coating was maintained at 200 µm to ensure uniformity and consistency. A defined drying process was applied to the coated foils (air-drying and vacuum drying at 80 °C and 60 mbar) to finalize the cathodes for use in LIBs.

5.4.2. Half-cell assembly using hybrid LMO//AC cathode

A similar configuration, like **Figure 67**, was used to replace LFP with an LMO//AC cathode to build a CR2032-type Li-ion battery coin half-cell assembly using hybrid LMO//AC cathodes. The LMO//AC hybrid half-cell assembly was carried out in an MBRAUN Argon-filled glove box, where oxygen and water levels were maintained below 0.1 ppm to ensure a controlled environment. The cells were fabricated in coin cell format using commercial CR2032

enclosures from PI-KEM. Lithium chips (Ø = 15 mm, MTI Corporation) were used as both the counter and reference electrodes, while LMO//AC discs (Ø = 10 mm, approximately 5.1 mg cm^2, with a dried thickness of around 56 µm) were used as the working electrodes. Whatman GF/F glass fiber discs (Ø = 18 mm) were punched and used as separators between the electrodes. For each coin cell, 150 µL of an electrolyte solution consisting of 1 M $LiPF_6$ salt in a mixture of ethylene carbonate and dimethyl carbonate (EC:DMC 1:1 by volume, Sigma-Aldrich) was injected (by using a pipette). This electrolyte solution is essential for facilitating Li-ion movement within the cell. Two stainless steel 304 spacers (thickness = 0.5 mm, PI-KEM) were used for each coin cell. The cells were then sealed with a hydraulic crimping machine (MSK-110, MTI Corporation).

5.5. Results and Discussion

In the following section, we will investigate the characterization analysis of each mentioned cathode type, including LFP, LMO, and LMO//AC.

5.5.1. Lithium iron phosphate

This section explores the features and electrochemical performance of LFP cathode materials. Scanning electron micrographs showcase the size and structural organization of the LFP particles. Insights into the material's chemical composition and crystalline structure are obtained through Raman spectroscopy and X-ray diffraction. Moreover, cyclic voltammetry and cycling performance assessments assess the LFP cathode's capacity to undergo reactions maintain capacity, over time, and achieve high Coulombic efficiency. This discovery underscores the material's promise, for being utilized in energy storage purposes.

5.5.1.1. Characterization analysis of LFP cathode

In **Figure 70** we can observe scanning electron micrographs of the LFP sample, providing a view of its particle morphology. **Figure 70A** displays the particles of the LFP sample which demonstrate a rod-like shape with particle diameters ranging from 0.1 µm to 2.0 µm and lengths between 0.5 µm to 3.0 µm. The consistent rod-like structure indicates a degree of crystallinity, which can be advantageous for the material's electrochemical performance.

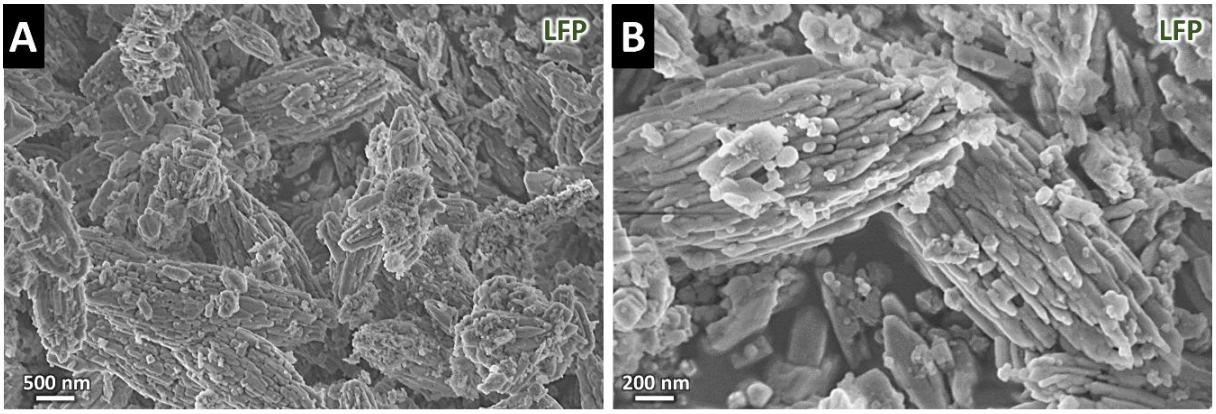

Figure 70. The lithium iron phosphate powder **(A-B)** scanning electron micrographs of the top view

In **Figure 70B** there is a close-up scanning electron micrographs of the LFP particles showing their rod shape. The image reveals surface details and consistent particle sizes and shapes, offering insights into the structure and dimensions of the particles. The uniform distribution of carbon in rod-shaped particles can boost the performance of the material in applications by

ensuring pathways for the free movement of ions and electrons. The close-up view in **Figure 70B** displays the rod-shaped structure of the LFP particles in detail. These particles have a distinct rod shape, with dimensions typically falling between 200 nm and 500 nm as indicated by the scale bars provided. The precise surface features and uniform particle sizes indicate a spread that might impact how well the material performs in electrochemical processes. The consistent size and shape of particles and the carbon coating on these rod-shaped LFP particles may boost the ability of the material to conduct electricity and its performance in reactions involving electricity transfer. This arrangement could assist in creating paths for ions and electrons to move through more efficiently leading to better long-term durability and increased speed, in storing energy for various uses.

The Raman pattern of the LFP samples is illustrated in **Figure 71A**, which provides information about the chemical properties. Various peaks were identified within ranges, such as 200 cm^{-1} -300 cm^{-1}, 450 cm^{-1} -600 cm^{-1}, and around 950 cm^{-1}, each related to vibrations. For instance, peaks in the 200 cm^{-1} and 300 cm^{-1} range correspond to FeO_x group vibrations, those in the 450 cm^{-1} and 600 cm^{-1} range relate to P-O bond vibrations, and the peak around 950 cm^{-1} is linked to $(PO_4)^{-3}$ anion vibration. Further peaks, at 1350 cm^{-1} and 1600 cm^{-1}, were observed, corresponding to A_{1g} and E_{2g} vibration modes associated with D-band and G-band characteristics. The X-ray pattern of the LFP samples showed two structures: $LiFePO_4$ according to PDF 40-1499 and $Li_3Fe_2(PO_4)_3$ according to PDF 43-0526 (which is shown in **Figure 71B**). These discoveries offer details about the makeup and features of the lithium iron phosphate samples, helping to acquire knowledge of their properties and possible uses.

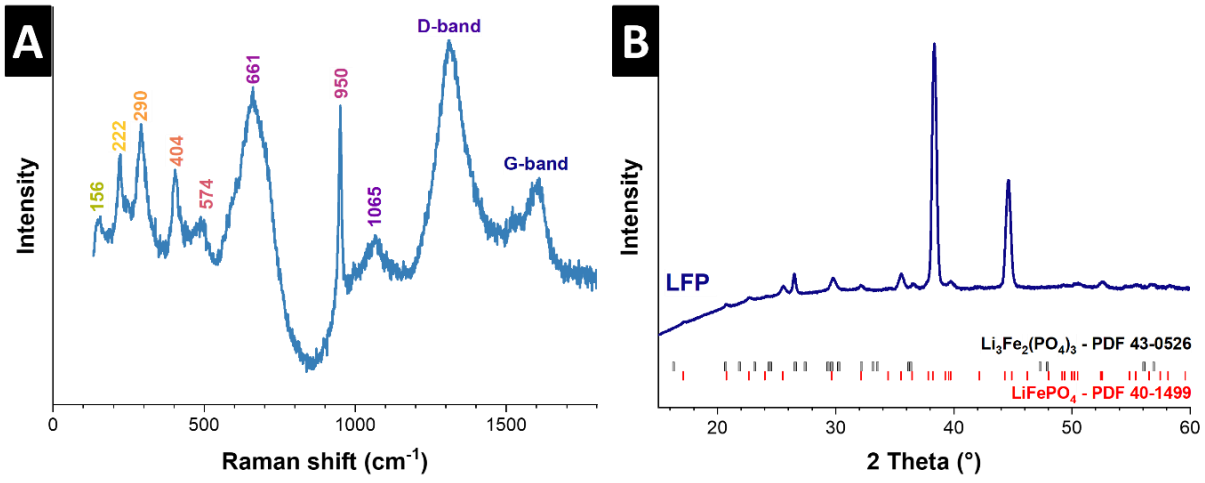

Figure 71. The dried lithium iron phosphate cathode **(A)** Raman pattern **(B)** X-ray diffractogram using Cu-Kα radiation.

5.5.1.2. Electrochemical measurements of LFP cathode

Figure 72A shows the results of the cyclic voltammetry tests applied at the rates of 0.10 mV s^{-1}, 0.25 mV s^{-1}, 0.50 mV s^{-1}, 0.75 mV s^{-1}, and 1.00 mV s^{-1}. The redox reactions observed follow a pattern. At a rate of 0.10 mV s^{-1}, there was evidence of Li-ion intercalation, around 3.3 V vs. Li^+/Li, indicating Li-ions entered the LFP structure. Conversely, Li-ion deintercalation occurred at 3.6 V vs. Li^+/Li, representing where Li-ions exited the LFP structure. As the scan rates increase, peak shifts occur. Both intercalation and deintercalation peaks move slightly, showing changes in electrochemical kinetics with higher scan rates. The cyclic voltammograms suggest that the LFP material shows electrochemical behavior with clear redox peaks that correspond with the insertion and removal of Li-ions.

The peak position variations at rates show that the kinetics of Li-ion transport within the LFP structure are affected by the scan rate. Higher scan rates could accelerate reactions. It may also exhibit increased resistance and polarization effects as the initial capacity. Higher scan rates may lead to faster electrochemical reactions and show greater resistance and polarization effects. By referencing **Figure 72B,** specific capacity and Coulombic efficiency tests were conducted on LFP cells at a rate of 25 mA g^{-1}, throughout 50 cycles. The specific capacity started at a high value and gradually declined over the cycles, stabilizing around 70 mAh g^{-1} by the 50th cycle. The Coulombic efficiency remained consistently high, close to 87%, throughout the cycling, indicating efficient and reversible charge-discharge processes with minimal losses.

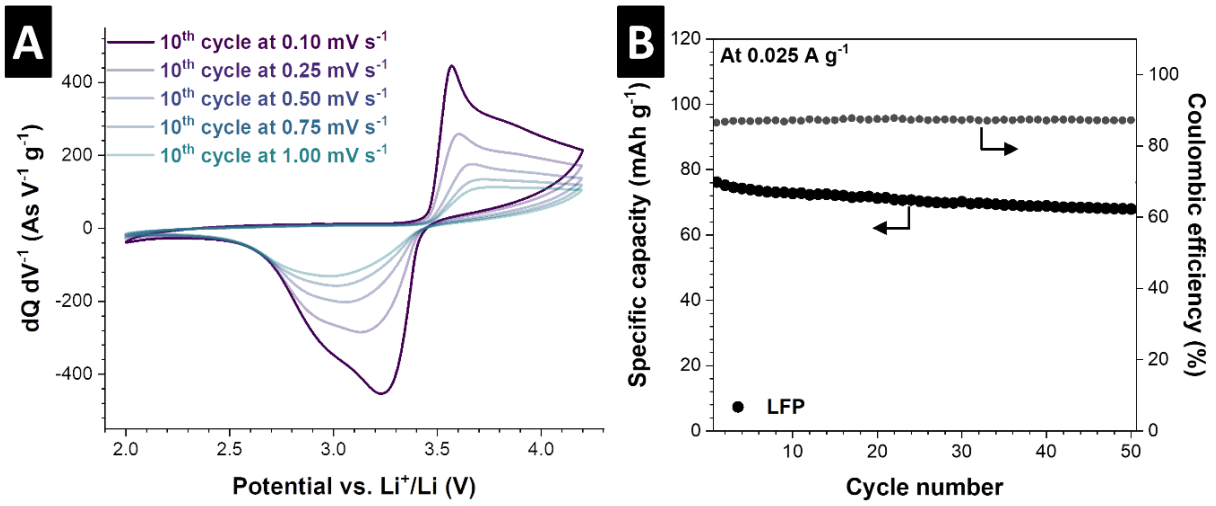

Figure 72. The lithium iron phosphate cathode **(A)** cyclic voltammetry profile at a scan rate of 0.1-1.00 mV s^{-1} normalized to scan rate, and **(B)** 50 cycles at 25 mA g^{-1}.

The Coulombic efficiency of around 87%, which is shown consistently across cycles, proves the material's stable electrochemical properties and the success of the LFP half-cell setup.

Although there is a decrease in capacity (around 8%) after 50 cycles, a significant portion of the initial capacity is maintained, which suggests cycling stability. The thorough examination of voltammograms and cycling performance validates the redox reactions, high Coulombic efficiency, and reliable cycling performance at a low rate. When analyzing the cycling performance for 50 cycles at 25 mA g^{-1}, we observed an initial capacity of 76 mAh g^{-1}. Furthermore, 87% of the capacity was retained with a Coulombic efficiency of around 87%. These findings provide a clear picture of the behavior and functionality of LFP half-cells, indicating their potential suitability for diverse applications that require dependable and efficient energy storage.

5.5.2. Lithium manganese oxide (LMO)

This part explores the features and effectiveness of LMO electrodes in LIBs. Optical and structural examination using scanning electron microscopy, X-ray diffraction patterns, and Raman patterns provides insights into particle shape and size and confirms the crystalline structure and chemical characteristics of LMO. Additionally, the impact of mixing conditions on particle size distribution inside the electrode is discussed. Lastly, electrochemical analysis shows the capacity retention and structural durability of LMO electrodes.

5.5.2.1. Characterization analysis of raw LMO powder

This part delves into studying the properties of LMO powder and how they impact the performance of LMO in Li-ion systems. The examination depicted in **Figure 73A-F** utilizes scanning electron micrographs. It looks into factors like particle size, shape, and distribution in the LMO powder since these aspects play a role, in determining its electrochemical performance. In **Figure 73A-F** it can be observed LMO crystals of varying sizes with diameters below 10 µm in size. Upon inspection of the images revealed that the particles tend to cluster within a range of approximately 5 µm.

Moreover, the images depict an evenly distributed arrangement of particles that plays a significant role, in ensuring consistent electrochemical performance. Upon examination of the scanning electron micrographs in **Figures 73D**, to **73F**, more intricate features of the particle arrangement become apparent. When viewed at a scale of 500 nm the particles display geometric forms notably showcasing the octahedral configuration of the LMO particles. The

consistent size and shape exhibited by these particles across scales ranging from 300 nm to 200 nm underscore the crystalline quality of the LMO powder.

These findings indicate that having defined and evenly spread particles can improve the materials' effectiveness in various uses by aiding smoother ion movement and reducing any hindrances from uneven particle sizes. The uniformity and absence of flaws in the particles further confirm that this LMO powder possesses a well-coordinated and ideal microstructure suitable, for energy storage purposes.[431-433]

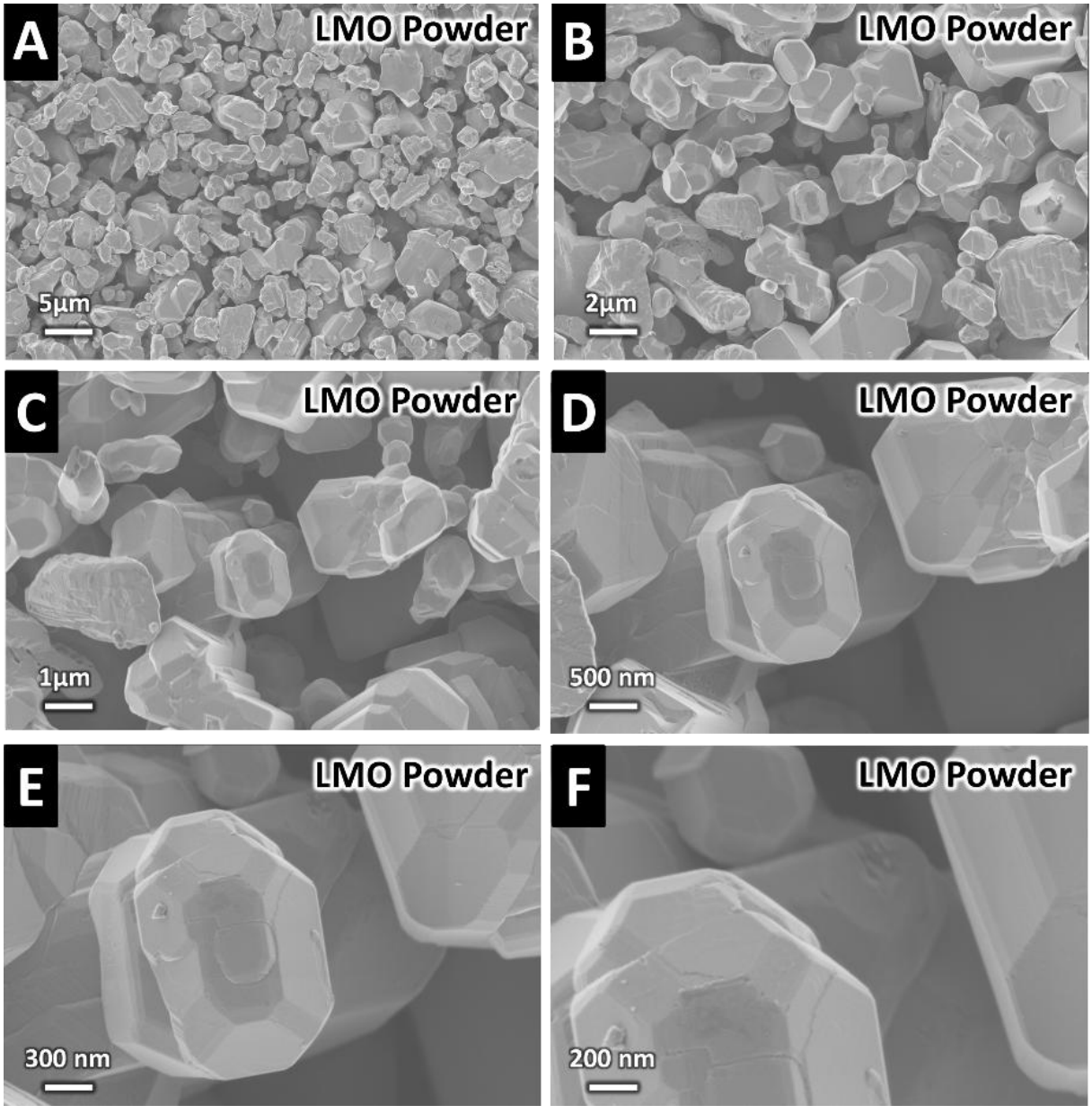

Figure 73. The scanning electron micrographs of lithium manganese oxide powder (Sigma-Aldrich).

As shown in **Figure 74A**, the X-ray diffractograms of several peaks related to LMO powder are consistent with the reference JCPDS card 35-0782. The XRD pattern of the sample indicates

that the face-centered cubic spinel structure of LMO, belonging to the space group $Fd\bar{3}m$, is preserved.[431-433] Reflections at 18.62° 2θ, 36.08° 2θ, 37.72° 2θ, 43.88° 2θ, 48.12° 2θ, 58.30° 2θ, 63.86° 2θ, 67.10° 2θ, 75.64° 2θ, 76.80° 2θ, 80.62° 2θ and 83.72° 2θ can indicate the planes of cubic LMO at (111), (311), (222), (400), (331), (511), (440), (531), (533), (622), (444) and (551) respectively. The identified peaks confirm the presence of the characteristic planes of the cubic spinel LMO structure, with primary orientations such as (111) at 18.62° 2θ, and others like (311), (222), and (400) at 36.08° 2θ, 37.72° 2θ, and 43.88° 2θ. Higher-order reflections, including (511) and (440) at 58.30° 2θ and 63.86° 2θ, further validate the face-centered cubic arrangement of the LMO crystal structure.

Figure 74B shows the Raman pattern of LMO in the spectral region of 100-800 cm^{-1} with a strong band around 625 cm^{-1}, which is related to Mn-O, the vibration of MnO_6 groups associated with A_{1g} spectroscopic symmetry.[434-438]The charge disproportionation (including $LiMn^{3+}Mn^{4+}O_4$) of manganese ions due to the Jahn-Teller effect in $LiMn_2O_4$ causes isotropic.[434-438] These isotropies include $Mn^{4+}O_6$ octahedra and locally distorted $Mn^{3+}O_6$ octahedra, which causes the broadness of the A_{1g} mode vibration related to MnO_6^{9-} and MnO_6^{8-} occur.[434-438]

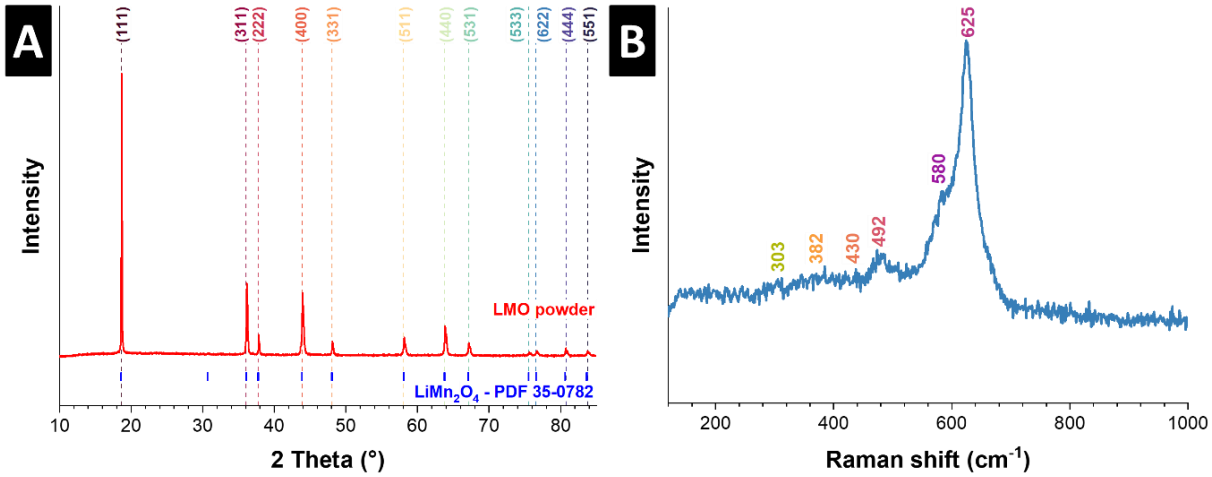

Figure 74. (A) X-ray diffractogram using Cu-Kα radiation and **(B)** Raman pattern of the LMO powder.

The Raman pattern shows minor bands around 303 cm^{-1}, 382 cm^{-1}, 430 cm^{-1}, 492 cm^{-1}, and 580 cm^{-1}.[434-438] The shoulder peak at 580 cm^{-1} is associated with F_{2g} mode and is related to the manganese average oxidation state in the spinel phase, which is not widening due to low intensity.[434-438] The peak at 483 cm^{-1} shows medium intensity and is associated with F_{2g} symmetry, along with peaks at 426 cm^{-1} and 382 cm^{-1} are related to the E_g and F_{2g} symmetry, respectively.[434-438] The F_{2g} symmetry is related to the movement of $Li - O$ in a manner.[434-438]. By analyzing both XRD and Raman spectroscopy results together we gain insights, into the

characteristics of LMO powder. The XRD findings confirm that the LMO powder maintains its face-centered cubic spinel structure, with reflections corresponding to the Fd$\bar{3}$m space group. The key peaks observed include (111) at 18.62° 2θ, (311) at 36.08° 2θ, (222) at 37.72° 2θ, and (400) at 43.88° 2θ. The crystallite size, calculated using the Scherrer equation, is approximately [insert size] nm, indicating a well-defined crystalline structure. Additionally, Raman spectroscopy reveals the Jahn-Teller distortion, with broadened A_{1g} mode around 625 cm^{-1} due to the coexistence of $Mn^{4+}O_6$ octahedra and locally distorted $Mn^{4+}O_6$ octahedra.

5.5.2.2. Effect of mixing time and speed to LMO/C65 dry mixture

First, the effect of dry mixing on LMO particle sizes was investigated. In this regard, four types of procedures were applied to LMO powder based on **Table 9**.

Table 9. The dry mixing steps for the LMO mixtures (including C65 and LMO powders) in the SpeedMixer.

Sample	Dry mixing in a mortar (Time, min)	Dry mixing with SpeedMixer (Speed, rpm)	Dry mixing with SpeedMixer (Time, min)
LMO-Mixture A	10	-	-
LMO-Mixture B	10	3500	5
LMO-Mixture C	10	3500	10
LMO-Mixture D	10	3500	20

Various blends were prepared by combining LMO powder (the ingredient). C65 (the conductive agent), in a ratio of 8:1 by mass. The ingredients were added to the mortar in quantities corresponding to the ratio of 80% LMO powder and 10% C65 as illustrated in **Figure 75**. This consistent mass ratio was upheld for all electrodes manufactured. In the mixing phase, the LMO and C65 blends were stirred together in the mortar for 10 min.

In the next step, 0.9 g of the mixture was transferred into the SpeedMixer container. Sealed it with PARAFILM (a wax and polyolefin product) before placing it in the SpeedMixer to ensure the accuracy of our mixing process. Apart from LMO Mixture A, we mixed the remaining samples in the SpeedMixer for durations of 5 min, 10 min, and 20 min. For LMO-Mixture B, LMO-Mixture C, and LMO-Mixture D, we set the mixing speed at 3500 rpm as per the SpeedMixers capability. Each mixture followed the procedures;

- **LMO-Mixture A**: Mixed in a mortar for 10 min without using the SpeedMixer in the next step.

- **LMO-Mixture B**: Mixed in a mortar for 10 min followed by additional mixing in the SpeedMixer at 3500 rpm for 5 min.
- **LMO-Mixture C**: Mixed in a mortar for 10 min followed by further mixing in the SpeedMixer at 3500 rpm for 10 min.
- **LMO-Mixture D**: Mixed in a Mortar for 10 min and then mixed at 3500 rpm for 20 min.

These procedures were designed to investigate how mixing time and speed using a centrifuge mixer will impact particle sizes of LMO powder. By ensuring the balance of materials and careful mixing conditions, the main aim was to ensure that the results could be consistently reproduced. The SpeedMixer was used to enhance the consistency and uniformity of the blends, which could potentially improve how well the resulting electrodes work. Understanding how different mixing times and speeds affect the process allows us to adjust and tune production. **Figures 75A-D** and **Figure 76** give an overview of the structure and size distribution of the LMO and C65 mixtures.

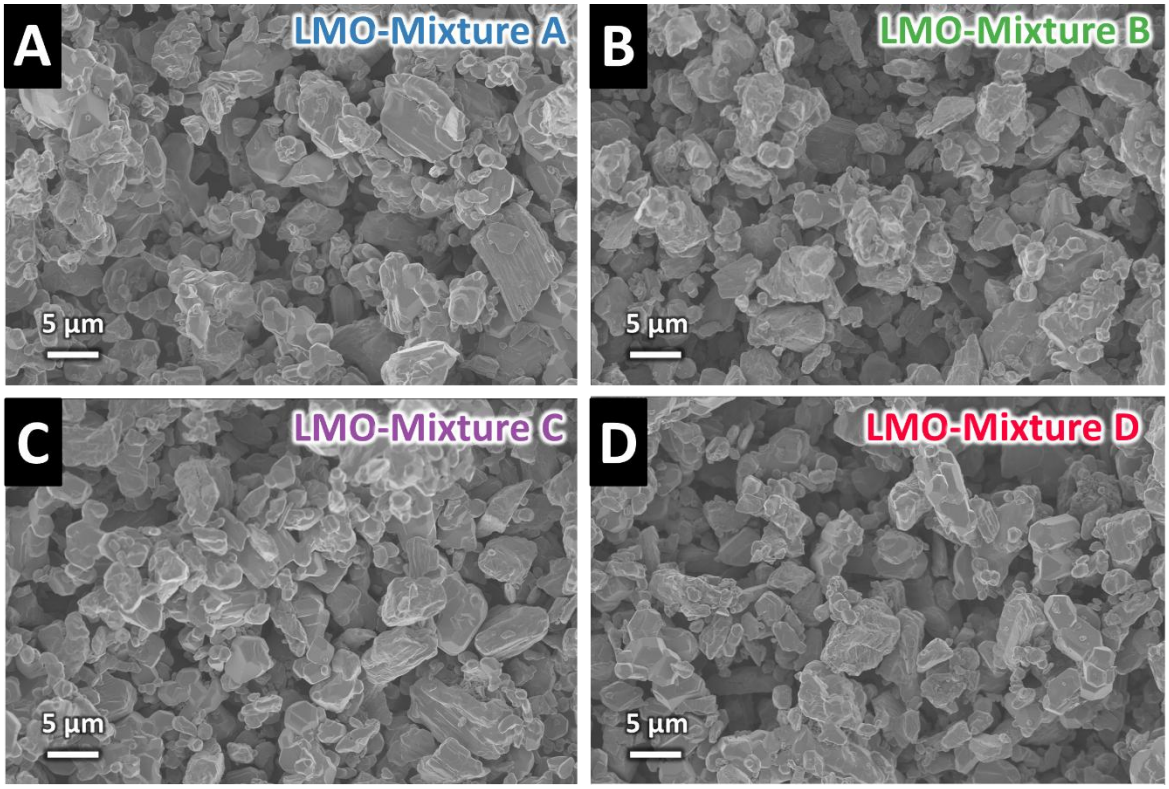

Figure 75. Scanning electron micrographs for different applied speeds and durations in the mixture of powder samples, **(A)** LMO-Mixture A, **(B)** LMO-Mixture B, **(C)** LMO-Mixture C, and **(D)** LMO-Mixture D.

The images show a view of both mixed structures and compositions. All these images are magnified to a scale indicated by a 5 µm bar. Each sample contains particles with shapes and surfaces forming a mix of sized particles. The scanning electron micrographs in **Figure 75** show

that all blends consist of particles with sizes ranging from 500 nm to 20 µm, regardless of the mixing speed and duration used during the process. The scanning electron micrographs in **Figure 75** stayed consistent within a range of 500 nm to 20 µm of the mixing speed and duration used during the process. There was no variation, in particle size across the various mixing conditions tested on the LMO powder. In LMO-Mixture A which was hand mixed in a mortar for 10 min, without mixing in the SpeedMixer the particle sizes varied between 500 nm and 20 µm and showed a relatively wide range of distribution.

In the way as before with LMO-Mixture B after an extra 5 min of blending at 3500 rpm in the SpeedMixer device it showed a similar distribution of particle sizes. There was no decrease in the average particle size or any obvious alterations, in the general shape of the particles. As the stirring duration rose in LMO-Mixture C and LMO-Mixture D (10 min and 20 min each at 3500 rpm) the particle sizes stayed consistent between 500 nm to 20 µm throughout the process with no breakage or decrease, in size despite the prolonged mixing times. Therefore the ingredients combined did not have an impact on the distribution of particle sizes. The uniform spread of particle sizes ranging from 500 nm to 20 µm is indicative that the shape of the LMO powder remained mostly unchanged by the mixing methods tested in this experiment.

Figure 76 summarizes the light scattering measurements on LMO and C65 powder Mixtures. The graph illustrates how particle volume percentages vary across sizes in each LMO blend. Each blend shows a peak around a specific particle size, indicating primary particle sizes among them. The primary particle dimensions pertain to the LMO particles that consistently fall within the range of 500 nm, to 20 µm as validated by both DLS and scanning electron micrographs examinations. The DLS data presented here suggests that the sizes of the particles did not undergo notable alterations regardless of shifts in mixing speeds and durations employed in the process. When operated at the maximum speed setting on the SpeedMixer device used in this study shows that there was a considerable overlap in distribution patterns across all mixtures tested; this overlap indicates that neither the original particle sizes nor the collective sizes were impacted by variations, in mixing conditions.

According to the data from DLS analysis; adjusting the mixing speed and duration did not notably affect the size distribution of LMO particles and their clusters. The mixing speed of 1500 rpm was selected to ensure the mixing of LMO and C65 powders without changing the particle size. The scanning electron micrographs back up these results by displaying a

consistent shape of particles and clusters under all circumstances. The curves representing the distribution patterns of all mixes overlap, suggesting that when operating at the highest speed of the SpeedMixer, the particle size distribution within LMO mixtures did not significantly alter. The data from DLS supports this by indicating that the SpeedMixer did not affect the particle sizes in the material, showing size distributions regardless of mixing speeds and durations. Therefore a mixing speed of 1500 rpm was chosen to ensure a blend of LMO and C65 powders in their form. Detailed insights into the morphology and distribution of particle sizes for LMO and C65 mixtures are provided by scanning electron micrographs and DLS measurements. The analysis demonstrates that while mixing influences how evenly particles are distributed, it does not change their sizes, which remain constant under conditions.

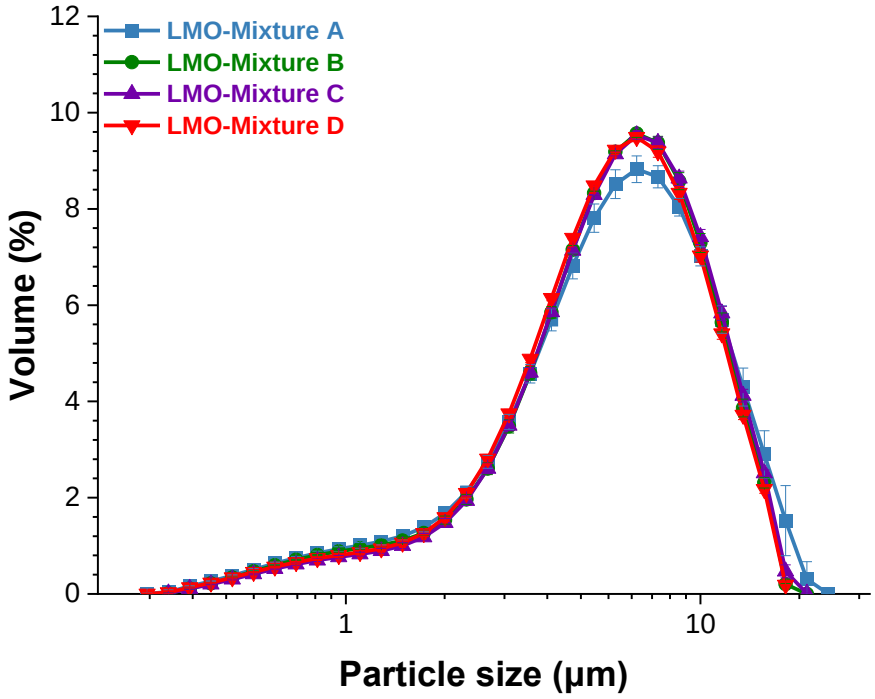

Figure 76. Dynamic light scattering measurements to identify the particle sizes for different applied speeds and durations in the mixture of powder samples, LMO-Mixture A, LMO-Mixture B, LMO-Mixture C, LMO-Mixture D.

5.5.2.3. Characterization analysis of LMO electrode

Following the calendering procedure, scanning electron micrographs were conducted to gain an understanding of the features and physical appearance of the LMO electrodes at levels of magnification, as shown in **Figure 77**. In **Figure 77A**, there is a scanning electron micrograph demonstrating a consistent surface, suggesting a well-compressed structure and successful compaction. **Figure 77B** shows that the surface is covered with the varied distribution of pores

that influence how the electrode functions in processes. In **Figures 77C** and **D**, the microspheres are made up of nanoparticles, which indicate that these nanoparticles are densely packed, with boundaries between them aiding in electron flow.

Figures 77E-F show the structure of the LMO microspheres. These pores play a role by accommodating volume changes during charge and discharge cycles and shortening the paths for Li-ions to diffuse. These pores serve a role by providing room for volume changes during charge-discharge cycles and shortening the diffusion paths for Li-ions.

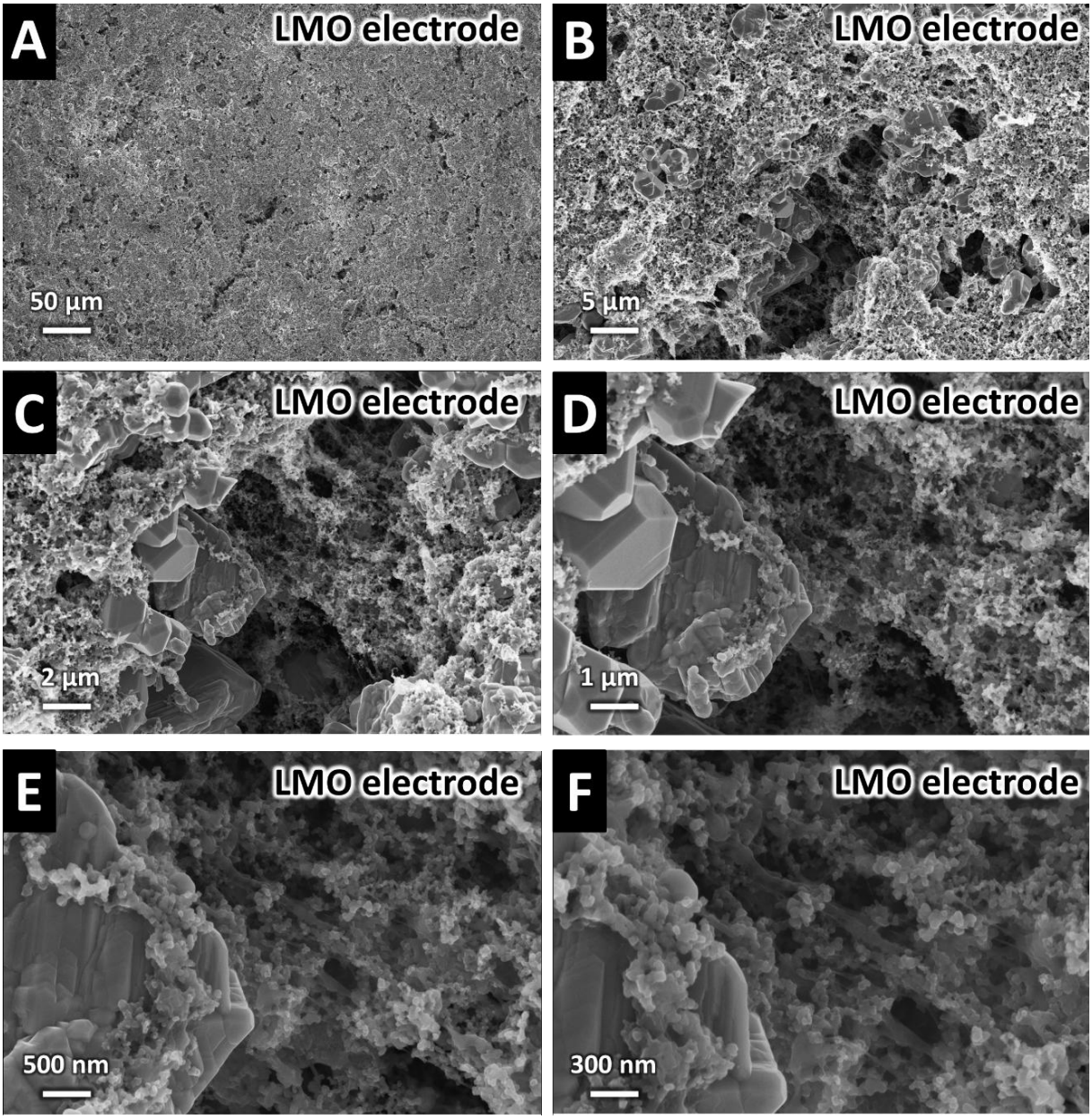

Figure 77. Scanning electron micrographs of the LMO 0 and LMO dried electrodes after calendering (A-F), top view.

Looking at **Figure 78A** displays X-ray diffractograms of the LMO electrode to analyze its coating structure. The patterns seen in XRD align with the cubic spinel phase of the $Fd\bar{3}m$ space group (JCPDS 35-0782) showing planes such as (111), (311), (222), (400), (331), (511), (440), and (531). Within this spinel structure, lithium atoms are located in the 8a positions, manganese atoms fill the 16d octahedral sites, and finally, oxygen atoms are situated in the 32e Wyckoff sites. The XRD patterns do not show peaks from the conductive carbon due to its quantity and amorphous nature, resulting in diffraction peaks.

Figure 78B displays the Raman pattern of the LMO samples. In general, LMO, with the $Fd\bar{3}m$ space group shows five Raman modes denoted by A_{1g}, E_g, and $3F_{2g}$. The prominent peak at 630 cm^{-1} in the LMO samples is linked to the Mn-O mode in the MnO_6 structure. Moreover, there are two bands around 492 cm^{-1} and 585 cm^{-1} representing frequency scattering bands of $F_{2g}(2)$ and $F_{2g}(3)$ stemming from vibrations of large and small Mn atoms, respectively. The E_g band at 382 cm^{-1} corresponds to oxygen vibrations. Notably, no significant peak shifts were observed post-manufacturing process, indicating that the fundamental characteristics of the LMO structure remained unchanged.

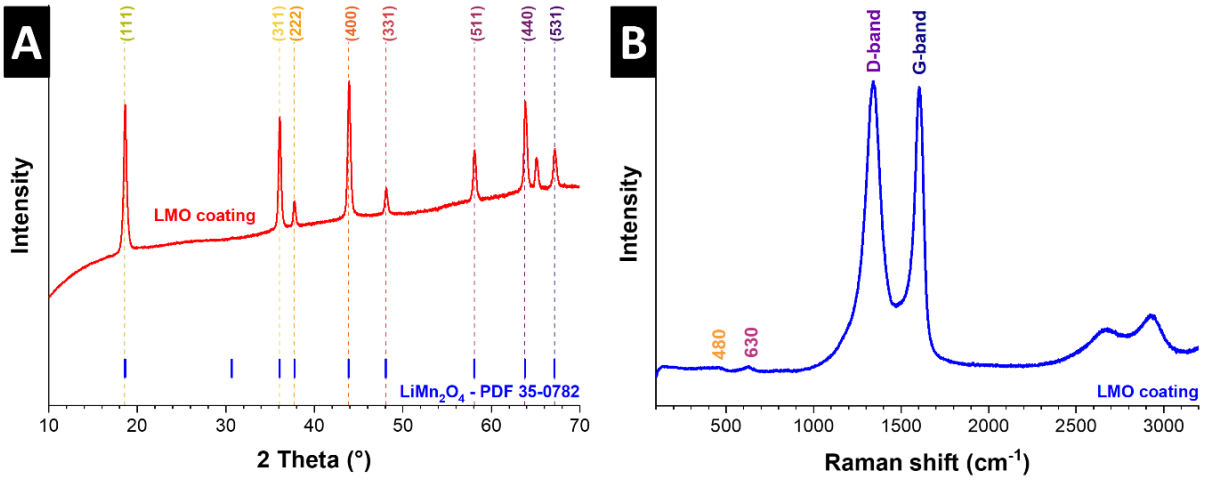

Figure 78. (A) X-ray diffractogram using Cu-Kα radiation (Cu reflections relate to the Cu current collector) and **(B)** Raman pattern of LMO coating.

Two noticeable peaks at 1360 cm^{-1} and 1592 cm^{-1} were detected in the LMO electrode spectrum. These peaks correspond to A_{1g} and E_{2g} vibrational modes D-band (disorder band) at 1360 cm^{-1} and the G-band (graphitic band) at 1592 cm^{-1}, which are characteristic of carbon-based materials. The D-band is associated with defects and disorder in the carbon structure, often originating from sp^3 hybridized carbon atoms, while the G-band is related to the in-plane vibrations of sp^2 carbon atoms in graphitic materials. These bands confirm the presence of

carbon in the LMO electrode coating. Furthermore, a broad peak was observed at 2700 cm^{-1} points towards the presence of a carbon 2D band originating from the agent used in the electrode. The identification of the I_D, I_G, and 2D bands, in the Raman pattern of the LMO electrode indicates that carbon from the agent is present in the structure of the LMO electrode. With the addition of carbon, XRD analysis reveals that the crystal structure of LMO remains unchanged, retaining its cubic spinel phase (space group $Fd\bar{3}m$). The main diffraction peaks were observed at 18.62° 2θ, 36.08° 2θ, 43.88° 2θ, 58.30° 2θ, and 63.86° 2θ, corresponding to the (111), (311), (400), (511), and (440) planes, respectively. The intensity and position of these peaks confirm that the incorporation of carbon did not induce any significant structural changes in the LMO. This examination confirms that although the structure of the LMO coating remains intact, the presence of carbon added during production is evident in the Raman pattern.

5.5.2.4. Electrochemical measurements of LMO electrode

The test for cycling performance involved running at a current of 200 mA g^{-1} for 500 cycles, as depicted in **Figure 79**. Following these cycles, the LMO sample showed a capacity retention of 69%. Several factors can be involved in this capacity retention.

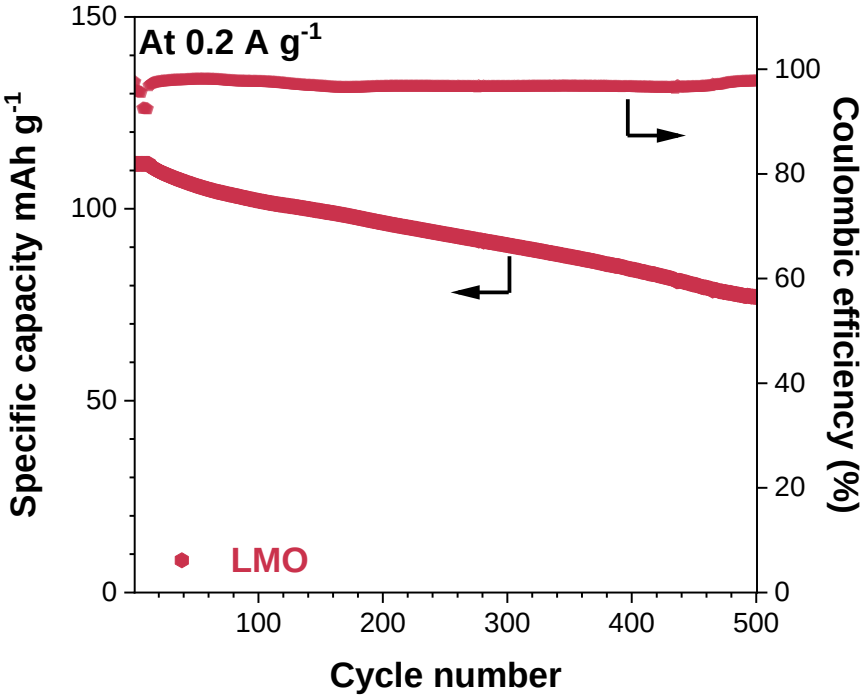

Figure 79. The cycling performance of the lithium manganese oxide for 500 cycles at 200 mA g^{-1}.

Initially, the dissolution of manganese and its subsequent redeposition at the location played a role in reducing capacity.[439, 440] This dissolution and redeposition process causes a deterioration of the material, ultimately lowering its total capacity.[439, 440]

Furthermore, the changes in the structure of LMO after each cycle can affect its ability to store a charge. The cycling performance of LMO shows that after 500 cycles at 200 mA g^{-1}, the specific capacity decreases from an initial value of approximately 120 mAh g^{-1} to around 65 mAh g^{-1}, representing a capacity retention of approximately 54%. The Coulombic efficiency remains above 95%, demonstrating efficient charge and discharge processes, though the capacity fade is evident. This modification in structure as it cycles can impact how stable the material is, which in turn influences its ability to retain capacity over the term. Also, the limited electrical conductivity of LMO plays a role in the decrease in capacity during each cycle. When considering all these factors together, it results in a 69% preservation of capacity after 500 cycles, highlighting the drawbacks of the LMO sample during performance assessments, under cycling conditions.

5.5.3. Hybrid electrode Lithium manganese oxide (LMO)//Activated carbon

This section studies hybrid electrodes containing activated carbon and LMO. By using scanning electron microscopy, X-ray diffraction, and Raman spectroscopy, the research provides in-depth insights into the morphology, structure, and surface properties of the particles.

5.5.3.1. Characterization analysis of raw activated carbon

The YP-80F activated carbon manufactured by Kuraray was analyzed using scanning electron microscopy to understand its characteristics and particle sizes. The scanning electron micrographs displayed in **Figures 80A-F** show the material's morphology.

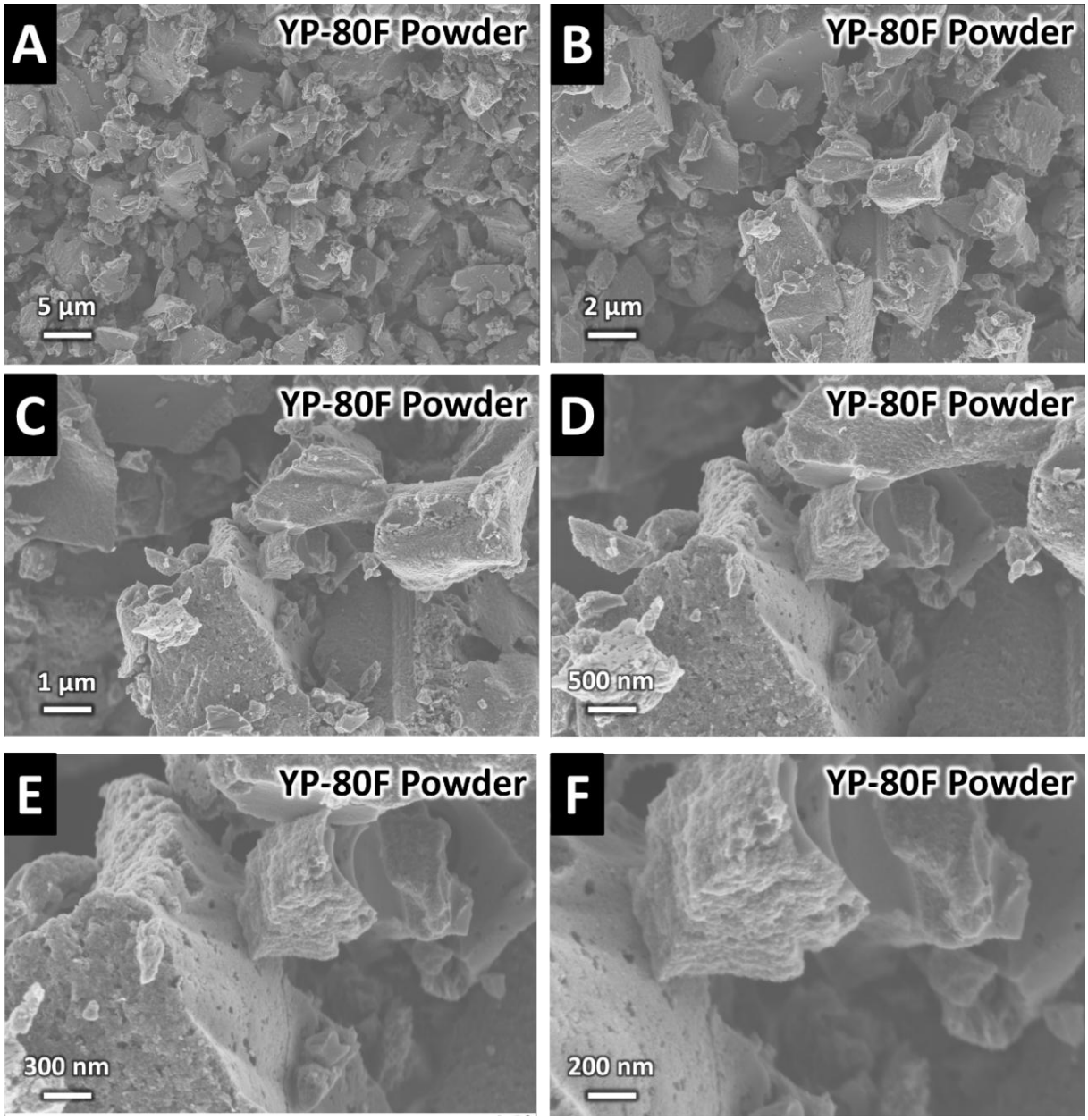

Figure 80. The scanning electron micrographs of activated carbon (YP-80F, Kuraray).

In **Figures 80A-B**, the YP-80F activated carbon particles display an uneven distribution of shapes and sizes. The particle sizes range from approximately 2 µm to 10 µm, with some larger aggregates visible. As the magnification increases, **Figures 80C-D** highlight more detailed structural features, showing the rough, porous surface texture of the YP-80F particles. The pores range from approximately 500 nm to 2 µm, contributing to a larger surface area, which enhances ion and molecule adsorption. Furthermore, Figures 80E-F reveal significant voids and channels on the scale of 200 nm to 500 nm, which further improve the porosity and accessible surface area, crucial for adsorption processes.

Figure 81A shows X-ray diffractograms of YP-80F activated carbon powder with peaks at 25.6° 2θ (002 plane). 44.2° 2θ (101 plane) indicating a graphite structure that has some crystallinity in the carbon matrix based on PDF 41-1487. The peak at 25.6° 2θ linked to the (002) plane is a feature of carbon materials nature showing the spacing between layers.[428, 429] Another prominent peak, at 44.2° 2θ associated with the (101) plane further indicates the presence of disordered carbon.

Figure 81B presents the Raman pattern of YP-80F powder. The spectrum displays two peaks around 1350 cm^{-1} and 1580 cm^{-1}, representing the D-band and G-band respectively. [428, 429] The D-band at 1350 cm^{-1} indicates defects and disorder in carbon structures often found in regions or edges of graphene layers.[428, 429] The G-band at 1580 cm^{-1} means vibrations of sp^2 bonded carbon atoms within a lattice.[428, 429]

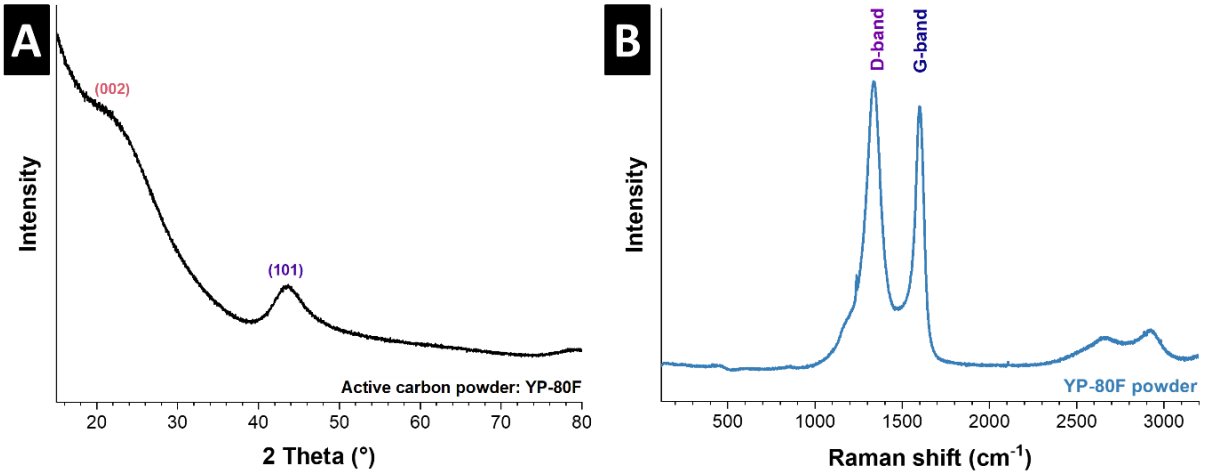

Figure 81. Activated carbon YP-80F (Kuraray) **(A)** X-ray diffractogram using Cu-Kα radiation, **(B)** Raman pattern.

The XRD analysis of YP-80F activated carbon powder, shown in **Figure 81A**, reveals diffraction peaks at 25.6° 2θ (002 plane) and 44.2° 2θ (101 plane), indicating a graphitic structure with a

degree of crystallinity. In the Raman spectrum (**Figure 81B**), two prominent peaks are observed at 1350 cm^{-1} (D-band) and 1590 cm^{-1} (G-band). The intensity ratio I_D/I_G was used to evaluate the defective nature arising from the presence of sp^2 defective sites in activated carbon.[441]

5.5.3.2. Characterization analysis of LMO//AC

In the characterization analysis of LMO//AC shown in **Figure 82,** the scanning electron micrographs provide a look at the morphology and structure of the LMO//AC hybrid electrode post-calendering.

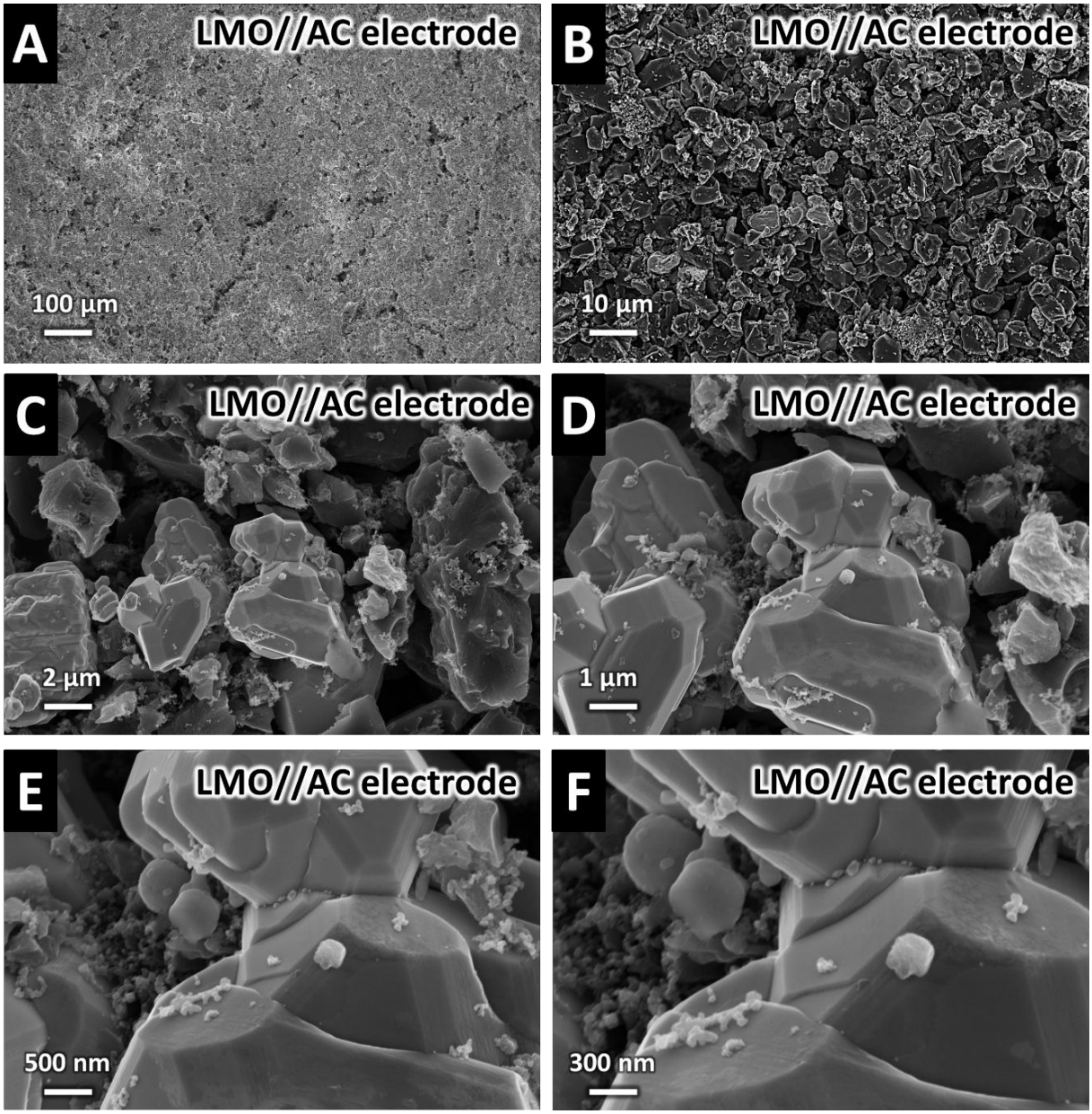

Figure 82. Scanning electron micrographs of LMO//AC hybrid electrode after calendering **(A-F)** top view.

In **Figure 82A** we observe a compact surface on the LMO//AC electrode with some cracks or gaps indicating proper compaction (20%) for ensuring stable electrochemical performance. **Figure 82B** there is a combination of activated carbon and LMO particles dispersed across the matrix contributing to the surface. **Figure 82C** LMO particles and activated carbon particles based on their appearance can be distinguished. **Figure 82D** we can see how LMO particles blend into the activated carbon matrix suggesting a connection, between electron movement and electrode function. **Figure 82E** gives us insights into the features of LMO particles and any surface imperfections. **Figure 82F** pores and surface irregularities have been observed.

Figure 83A displays an X-ray diffraction pattern of a cathode containing LMO revealing peaks corresponding to crystal planes in its structure. The peaks at angles like 18.6° 2θ, 36.1° 2θ, 38.0° 2θ, 44.3° 2θ, 48.4° 2θ, 58.5° 2θ, and 64.1° 2θ indicate the presence of the LMO phase based on the reference pattern (JCPDS card no. 35-0782).

Moreover, it can be seen how the LMO particles are incorporated into the activated carbon matrix, suggesting a connection and interaction that aid in electron transport and the overall function of the electrode. It also shows insight into the properties of LMO particles and any surface imperfections. Lastly, there are pores and surface irregularities that might affect performance by acting as locations for Li-ion insertion and extraction.

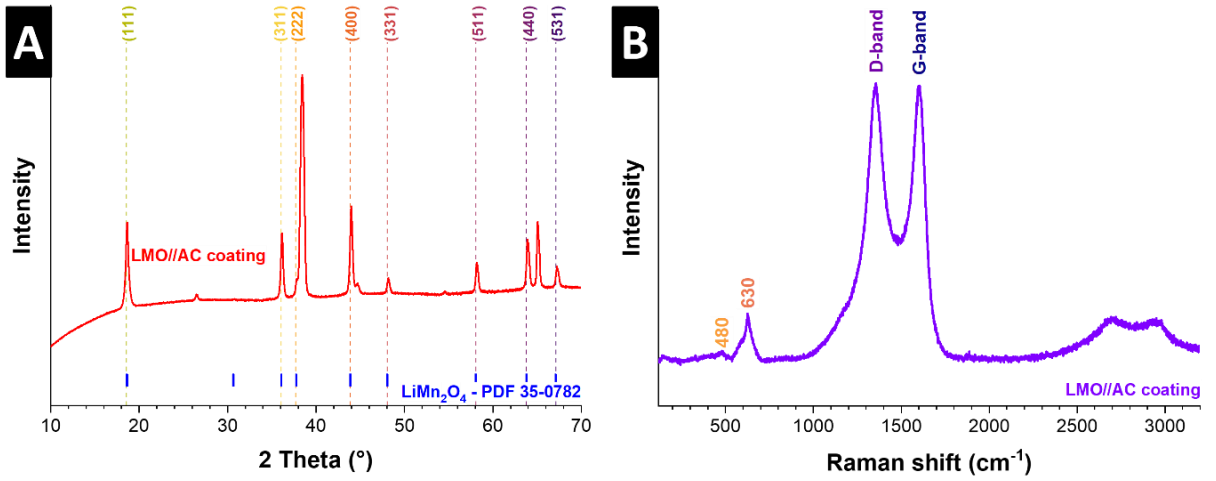

Figure 83(A) X-ray diffractogram using Cu-Kα radiation (Cu reflections relate to the Cu current collector) and **(B)** Raman pattern of LMO//AC hybrid electrode coating.

In **Figure 83B** the Raman pattern of the LMO//AC cathode shows insights into its composition. The spectrum displays peaks at 630 cm^{-1} along with a band at 1350 cm^{-1} and a G-band at 1590 cm^{-1}. The peak at 630 cm^{-1} is linked to oxide stretching vibrations in MnO_6 octahedra suggesting the presence of a spinel LMO structure. The D-band at 1350 cm^{-1} suggests

imperfections in the carbon material, while the G-band at 1590 cm^{-1} indicates the presence of ordered graphitic domains within the activated carbon. Together, these bands confirm the hybrid nature of the LMO//AC electrode, where the carbon components contribute both defect sites for ion adsorption and graphitic regions that enhance conductivity.

5.5.3.3. Electrochemical measurements of LMO//AC

Figure 84 shows how the LMO//AC behaves when exposed to an applied current of 200 mA g^{-1} for 300 cycles. At the start, the specific capacity is 165 mAh g^{-1} during charging and 145 mAh g^{-1} during discharging. However, after around 50 cycles, there is a decline in capacity for both charging and discharging processes, which continues to decrease throughout the remaining cycles. At the conclusion of the 300 cycles, the specific capacity drops to 60 mAh g^{-1} for both charging and discharging.

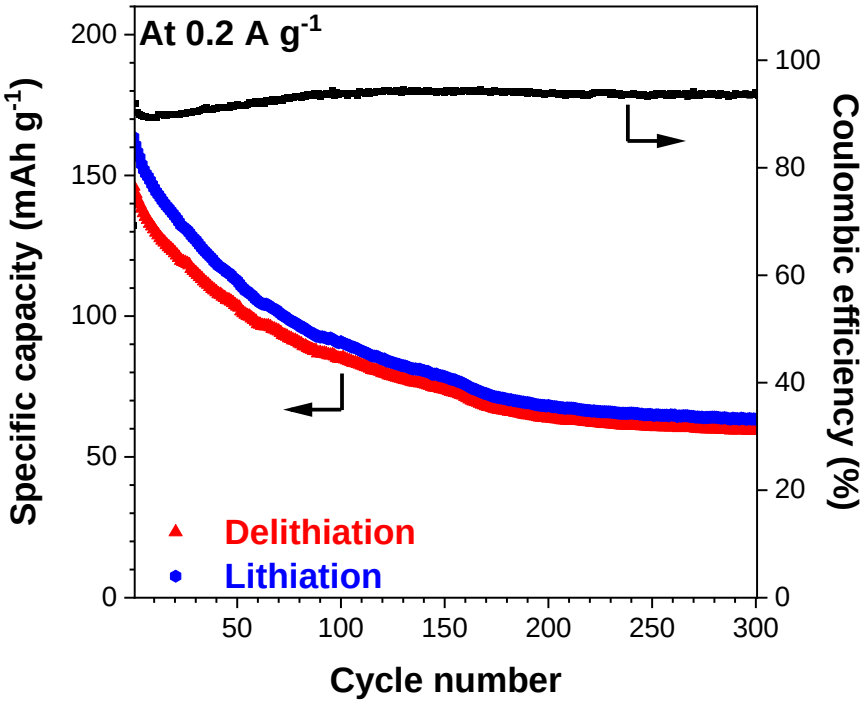

Figure 84. The LMO//AC hybrid electrode cycling performance at 200 mA g^{-1} for 300 cycles.

The Coulombic efficiency begins below 90%. Shows improvement after around 100 cycles, and reaching higher than the 90% mark. Nevertheless, it doesn't stay consistent. Instead fluctuates during the rest of the cycling period. This graph indicates that although the electrode maintains charge and discharge processes, there are shifts in efficiency over time. In summary, the results suggest that throughout 300 cycles, at this rate, there is capacity degradation observed in the

LMO//AC hybrid electrode. While Coulombic efficiency shows improvement over time, it remains inconsistent.

6. FULL-CELL ASSEMBLY AND TESTING

In this part, we discuss the process of preparing and testing full cells using LTO as anode LMO and LFP as the cathode materials. The goal of this study is to create and enhance high-performance configurations, for LIBs. These cells go through tests to evaluate their performance. Tests such as cyclic voltammetry, galvanostatic charge/discharge cycles, and electrochemical impedance spectroscopy.

6.1. Full-cell assembly

A similar configuration like **Figure 67** was used to build CR2032 type coin cell assembly (LIB) with LMO or LFP as cathode materials and LTO as the material. The construction of the full cell assemblies including LTO//LFP and LTO//LMO was done inside an MBRAUN Argon filled glove box to maintain oxygen and water levels below 0.1 ppm for a controlled environment. The battery cells were assembled in coin cell format using CR2032 casings from PI-KEM. An LTO disk, with a diameter of 12 mm, is utilized as the anode while LFP or LMO disks with a diameter of 10 mm each are used as the cathodes. The LTO, LMO, and LFP disks were cut using EL-Cut devices from EL-CELL. Separators made of Whatman GF/F glass fiber disks with an 18 mm diameter were interposed between the electrodes.

Each coin cell was filled with 150 µL of a solution containing 1 M $LiPF_6$ salt in a combination of ethylene carbonate and dimethyl carbonate (EC:DMC, 1:1 ratio by volume sourced from Sigma Aldrich). This electrolyte solution plays a role in enabling the movement of Li-ions within the cell. Additionally, two stainless steel 304 spacers measuring 0.5 mm in thickness from PI-KEM were utilized for each coin cell assembly. The cells were subsequently sealed using a crimping machine (MSK 110, from MTI Corporation).

6.2. Results and Discussion

6.2.1. LTO//LMO full cell

Figure 85 shows how well the LTO//LMO full cells perform when cycling at a current of 0.5 A g^{-1} for 300 cycles. The initial specific capacity is around 250 mAh g^{-1}. It drops after the 50 cycles to about 100 mAh g^{-1}. From there, it gradually decreases over the remaining cycles. The Coulombic efficiency remains steady at over 90% throughout all 300 cycles. This indicates a charge/discharge efficiency despite the decline in capacity of about 68%. This can be translated

in that while the cell maintains its efficiency in charging and discharging, its ability to store charge diminishes with time.

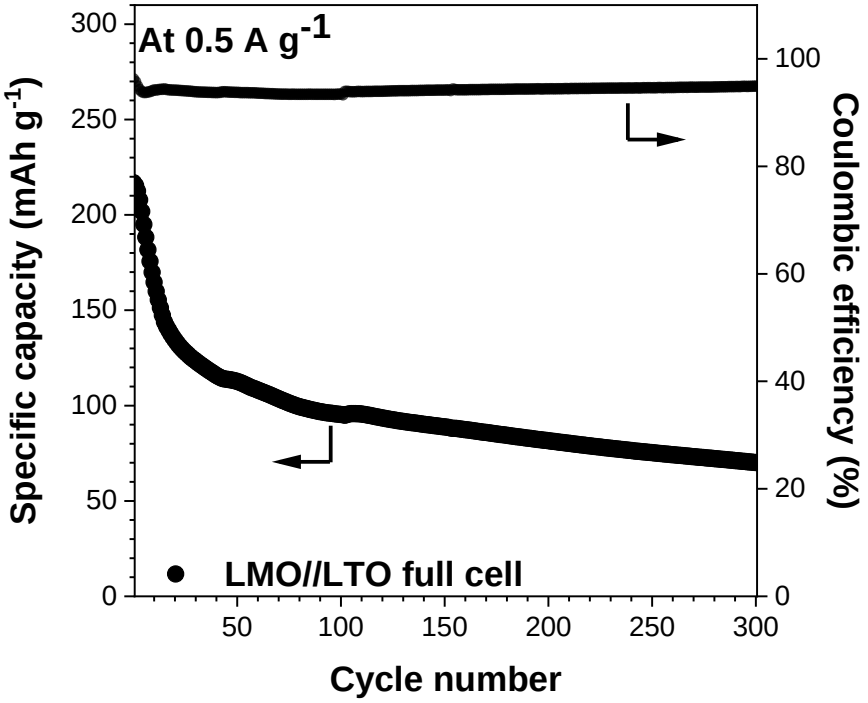

Figure 85. The LMO//LTO full cell data cycling performance at 0.5 A g^{-1} for 300 cycles.

6.2.2. LTO//LFP full cell

The optimized LTO anode performance, in cell testing, was examined versus LFP cathodes using a solution of 1 M $LiPF_6$ in EC/DMC as electrolyte. **Figures 86A** and **B** show cyclic voltammograms at rates from 0.10 mV s^{-1} to 1.00 mV s^{-1} showing symmetric redox reactions that indicate a reversible process. At a rate of 0.10 mV s^{-1} Li-ion intercalation occurs around 1.6 V and deintercalation at 2.0 V. With increasing scan rates the voltage gap between the anodic and cathodic peaks widens and the specific current peak shifts that show greater electrode polarization and reduced electrochemical kinetic reaction efficiency.

Figure 86C illustrates the cycling performance of LFP//LTO cells at a current of 0.2 A g^{-1}. The cell exhibited an initial capacity of 138 mAh g^{-1} at the mentioned specified current rate. After going through 200 cycles, it retained 81% of the initial capacity, highlighting its long-term durability. Moreover, the Coulombic efficiency consistently exceeded 97%, indicating charge and discharge processes throughout the testing phases. **Figure 86D** shows electrochemical impedance spectra for the cell in a pristine state after 100 cycles and finally after completing

500 cycles. These measurements were conducted using an input current of 0.2 A g^{-1} and analyzed via a circuit model (ECM) to interpret the spectra accurately. In the high-frequency range, a resistance known as ohmic resistance (cap R sub b) is observed, which is related to the resistances of cables, electrolytes, contact points between the material and the current collector, and resistance within the separators. Furthermore, two semicircles and a 45° inclined line in the impedance patterns can be observed. The initial semicircle is related to the transport of Li-ions through the interphase (SEI) film, symbolized by R_{SEI}.

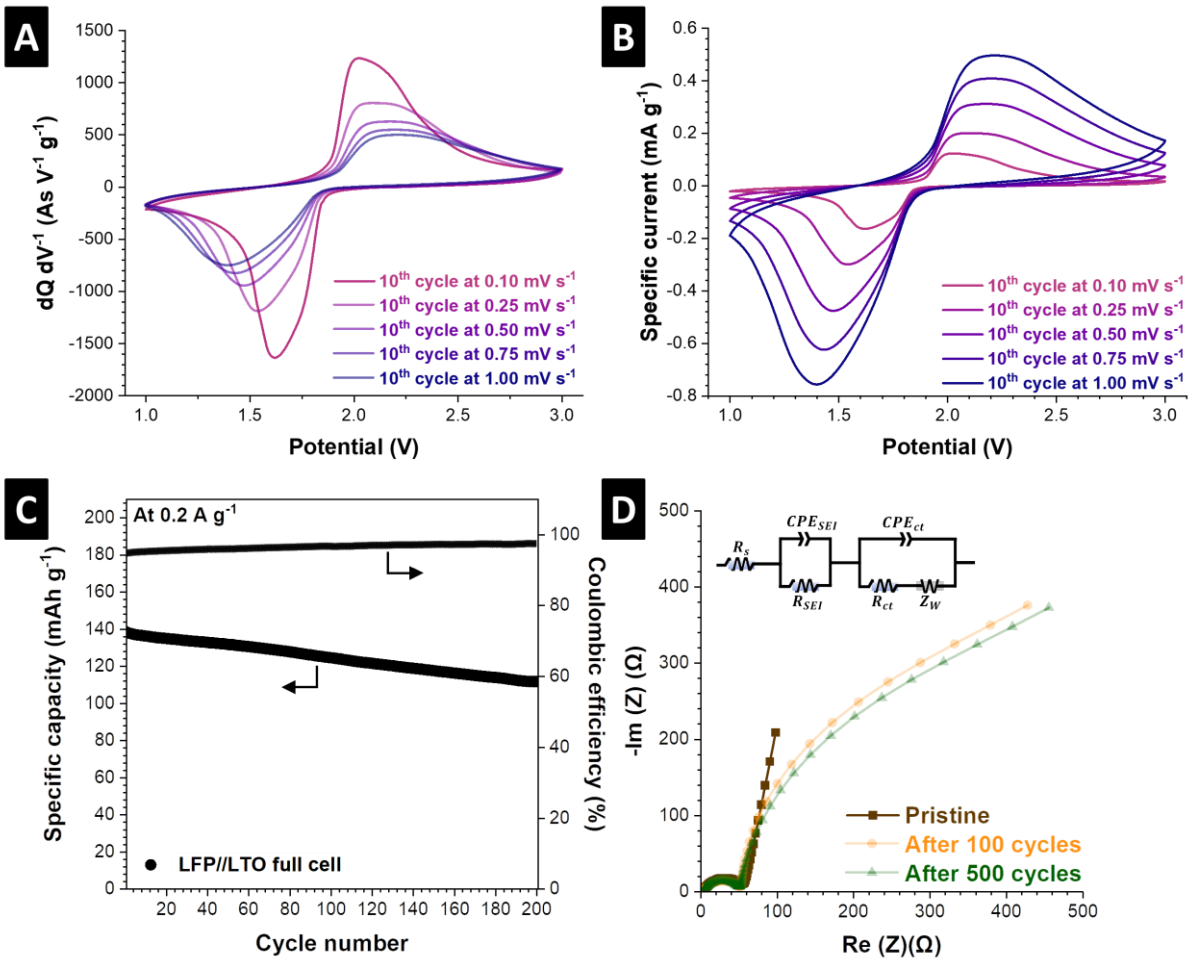

Figure 86. The LFP/LTO full cell data. Cyclic voltammetry profile **(A)** at a scan rate of 0.1-1.00 mV s^{-1} normalized to scan rate **(B)** at a scan rate of 0.1-1.0 mV s^{-1} **(C)** cycling performance at 0.2 A g^{-1} for 200 cycles (**D)** electrochemical impedance spectroscopy results at pristine state, after 100, and 500 cycles at 0.2 A g^{-1} and the equivalent circuit model was utilized for fitting.

The second semicircle is related to the charge transfer resistance at the interface between the anode, cathode, and electrolyte (R_{ct}), and the Warburg impedances (Z_W) in the lower-frequency region due to solid-state Li-ion diffusion into the electrodes. **Table 10** summarizes the total internal resistance (R_{Total}) of the LFP//LTO full cell. The data indicates that as the number of cycles increases, the overall resistance of the cell also increases, which is consistent

with electrochemical findings. This rise in resistance during cycling suggests a deterioration of cell components and an increase in resistance. These results offer insights into how the LTO anode behaves and interacts with the LFP cathode within a complete cell configuration. It was noted that the internal resistance of the cell rose as cycle numbers increased, signaling a degradation of the cell over time.

Table 10. Electrochemical impedance spectroscopy results of LFP//LTO full cell, in the pristine state, after 100 and 500 lithiation and delithiation cycles at 0.2 A g^{-1}.

Samples	R_b (Ω)	R_{SEI} (Ω)	R_{ct} (Ω)	R_{total} (Ω)
Pristine	3.39	54.45	0.13	57.95
After 100 cycles	4.16	50.60	353.50	408.26
After 500 cycles	4.06	49.34	399.90	453.30

7. DRY-PROCESS ELECTRODE PREPARATION

In this part, a method for preparing electrodes that do not use solvents (solvent-free electrode), known as the dry process electrode, has been discussed. It includes blending the material, conductive agents, and binders in a dry form and then pressing them mechanically to create the electrode film. The study looks into how factors like mixing duration, pressure, and temperature impact the performance of the electrode.

7.1. Hybrid lithium manganese oxide//activated carbon (LMO//AC)

Figure 87 summarizes the dry process for LMO//AC cathodes. In a typical experiment, 30 mass% LMO powder was mixed with 40 mass% active carbon (YP-80F, Kuraray) and 20 mass% C65 conductive carbon black by manual grinding in the mortar for 30 min. It was further blended via a speed mixer at different rates (800 rpm, 1000 rpm, 1500 rpm, and 2500 rpm) for 5 min each.

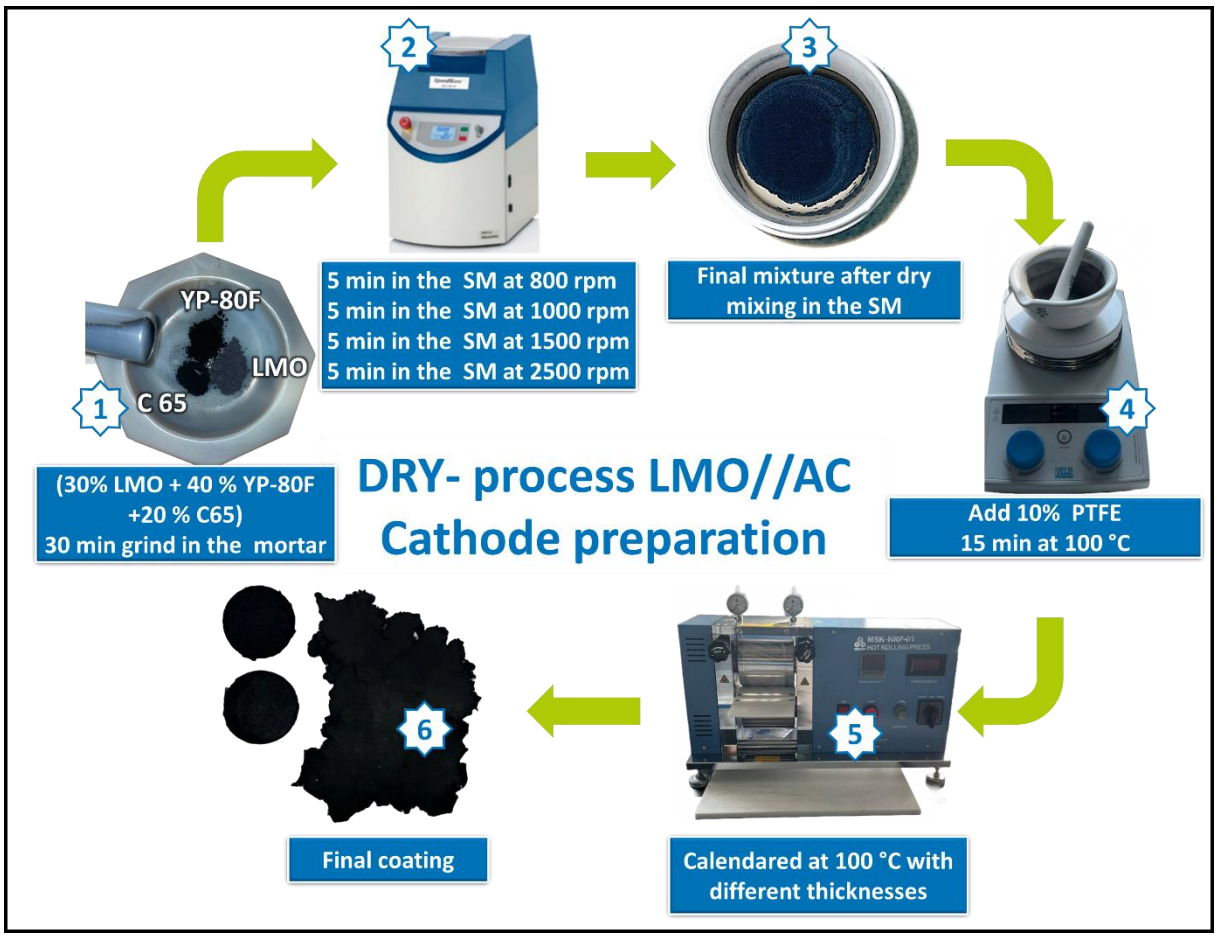

Figure 87. The manufacturing of hybrid cathode including lithium manganese oxide and activated carbon mixing routines.

The powder mix was moved to a mortar heated to 180°C (the temperature of the mixture material in the mortar reached 100°C) and mixed with a binder comprising 10% Polytetrafluoroethylene. After that, by heating the mixture, the PTFE effectively bonded all the components together, creating a blended and unified cathode material. This careful process of mixing and production steps ensured that the resulting LMO//AC cathodes were performing well, which makes them suitable for application in LIBs.

7.2. Half-cell assembly using dry hybrid LMO//AC cathode

A similar configuration like **Figure 67** was used to build CR2032 type coin cells assembly (LIB) with LMO//AC as cathode materials and LTO as the anode material used to assemble dry-process cathode half-cells. The dry LMO//AC hybrid half-cell assembly was carried out in an MBRAUN Argon-filled glove box, where oxygen and water levels were maintained below 0.1 ppm to ensure a controlled environment. The cells were fabricated in coin cell format using commercial CR2032 enclosures from PI-KEM. Lithium chips (Ø = 15 mm, MTI Corporation) were used as both the counter and reference electrodes, while LMO//AC discs (Ø = 10 mm, in the range of 10 mg cm² to 139 mg cm², with a dried thickness from 190 µm to 987 µm) were used as the working electrodes.

Whatman GF/F glass fiber discs (Ø = 18 mm) were punched and used as separators between the electrodes. For each coin cell, 150 µL of an electrolyte solution consisting of 1 M $LiPF_6$ salt in a mixture of ethylene carbonate and dimethyl carbonate (EC:DMC 1:1 by volume, Sigma-Aldrich), was injected. This electrolyte solution is essential for facilitating Li-ion movement within the cell. Two stainless steel 304 spacers (thickness = 0.5 mm, PI-KEM) were used for each coin cell. The cells were then sealed with a hydraulic crimping machine (MSK-110, MTI Corporation).

7.3. Results and Discussion

7.3.1. Characterization analysis of dry hybrid LMO//AC cathode

In **Figure 88,** scanning electron micrographs of the hybrid LMO//AC cathode after the manufacturing process are shown. These images give us a look, at the shape and structure of the material. In following will explain all the observations in Scanning electron micrographs. **Figure 88A:** It shows the surface appearance of the electrode showing that the particles are

evenly spread out. **Figure 88B** zoom in for a view focusing on the texture of the electrode surface that shows AC and LMO particles grouped together evenly all over the electrode.

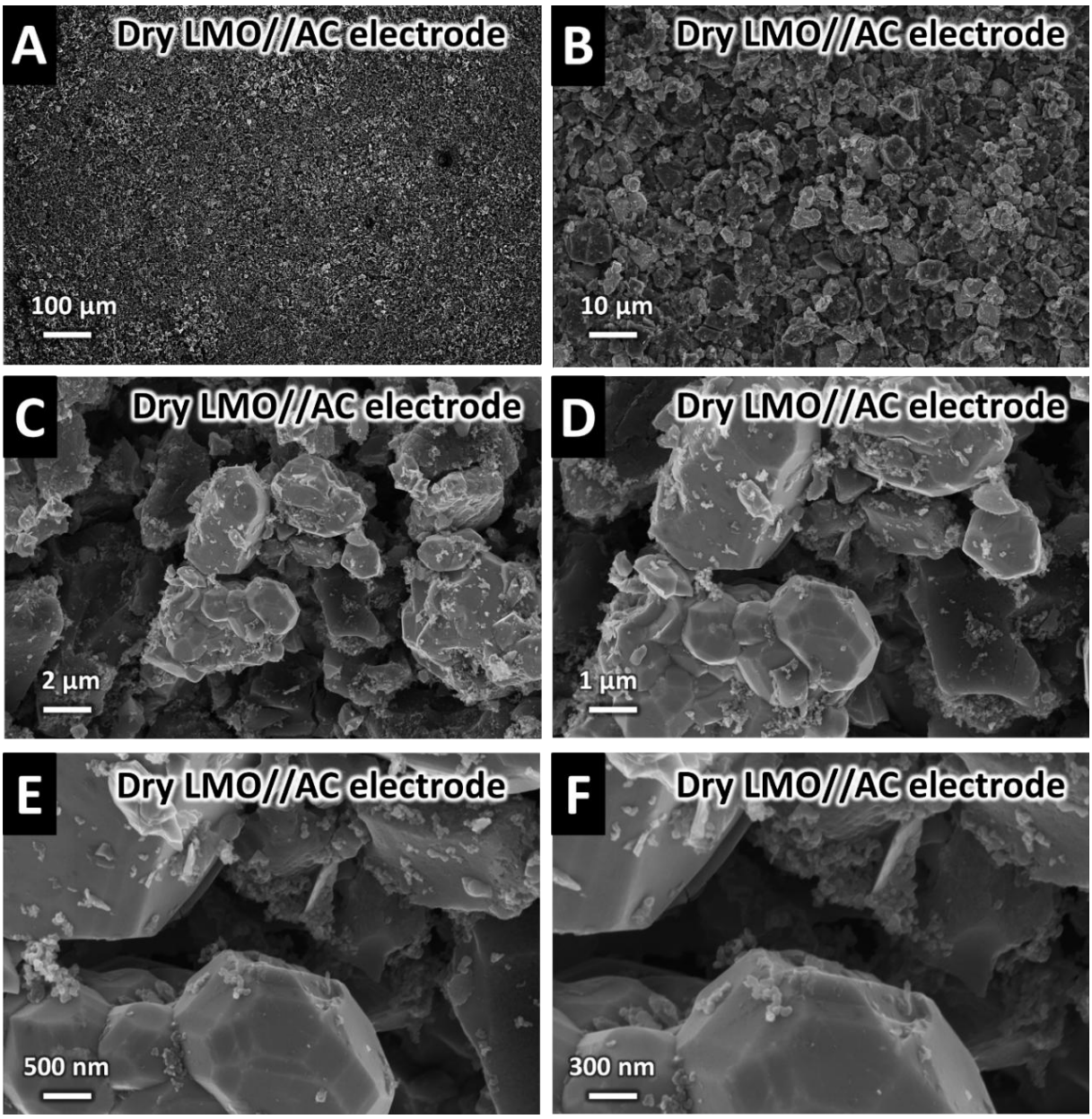

Figure 88. Scanning electron micrographs of LMO//AC hybrid electrode after calendering **(A-F)** top view.

Figure 88C-D: Displaying scales of 2 µm and 1 µm respectively provide a look, at the electrode features showcasing how the LMO particles are grouped with activated carbon. The particles seem evenly spread out and tightly packed. **Figure 88E-F:** Captured at magnifications of 500 nm and 300 nm respectively Showing the structures and surface qualities of individual particles. These images highlight the uniformity and even distribution of both LMO and AC in the electrode indicating a well preparation process.

In **Figure 89,** analytical data including X-ray diffractogram and Raman pattern for the LMO//AC hybrid coating is presented. **Figure 89A** displays X-ray diffractograms using Cu radiation. The diffraction peaks correspond to the phases of the LMO material with peaks identified at different positions on the 2 Theta (°) scale. These peaks align well with the diffraction pattern of reference in PDF 35-0782 confirming the presence of the expected crystalline structure in the coating.

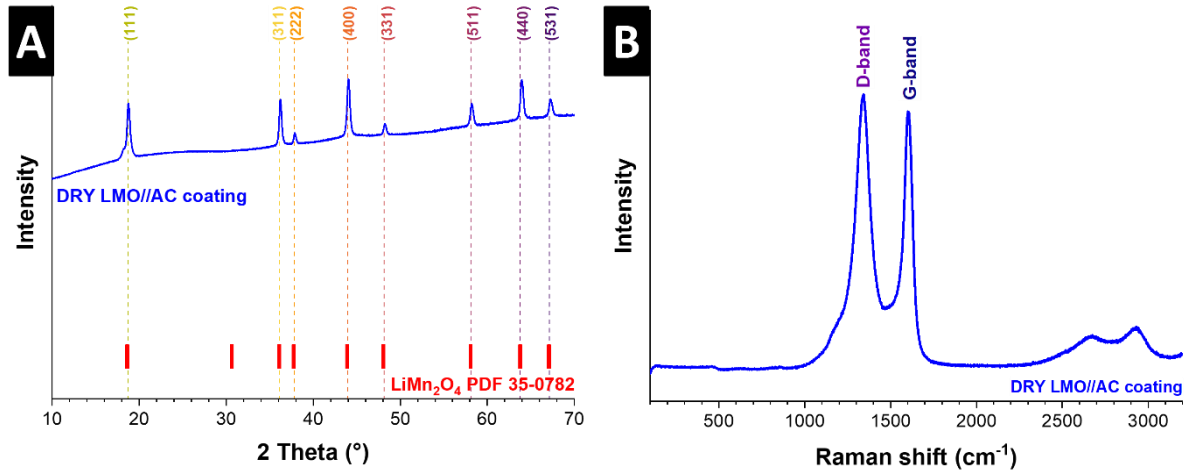

Figure 89. Dry LMO//AC hybrid electrode coating **(A)** X-ray diffractogram using Cu-Kα radiation (Cu reflections relate to the Cu current collector) and **(B)** Raman pattern.

Figure 89B shows the Raman pattern of the LMO//AC coating. The spectrum displays D-band and G-band peaks that are typical of carbon materials. The D-band, at 1350 cm^{-1} indicates the presence of disordered carbon, while the G-band, around 1580 cm^{-1} represents activated carbon materials. These findings confirm that activated carbon is present in the electrode and offer insights into the characteristics of the carbon component.

7.3.2. Electrochemical measurements of dry hybrid LMO//AC cathode

By testing the performance of our custom-made electrodes (30:50:10:10 LMO:AC:C65:PVdF), with varying thicknesses, we observed how the manufacturing process affects their performance. In **Figure 90A** the results of cycling tests for thicknesses ranging from 190 µm to 720 µm have been shown that carried out over 20 cycles at a rate of 1C. All electrodes show a capacity of about 50 mAh g^{-1} with only slight differences during short-term cycling tests. This suggests that the thickness of the electrode does not have an impact on cycling performance within this range. Additionally, we evaluated the performance of two electrodes with

thicknesses of 230 µm and 500 µm (these two were considered as the thickness became nearly doubled) over 100 cycles at a rate of 1C, as depicted in **Figure 90B**.

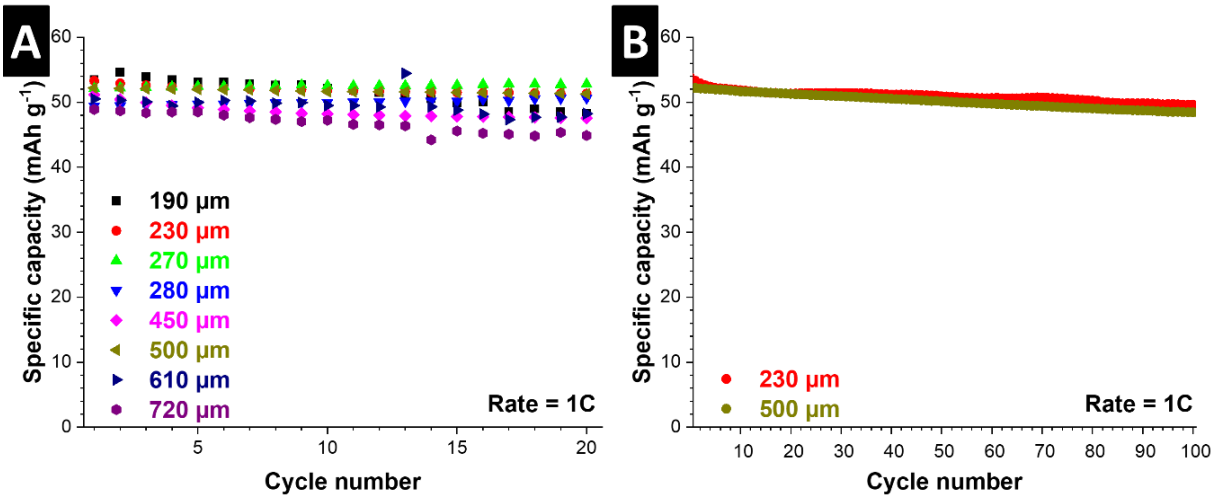

Figure 90. Dry LMO//AC hybrid electrode (30:50:10:10 LMO:AC: SC65:PVdF) **(A)** Cycling test for different thicknesses from 190 µm to 720 µm **(B)** Long cycling test for samples with 230 µm and 500 µm.

Both electrodes initially could provide a capacity of 54 mAh g^{-1}. This value gradually decreased over time during extended cycling tests and remained stable overall. Over the cycling tests, this value showed a gradual decline. For the thinner electrode (230 µm), the capacity decreased to 52 mAh g^{-1} after 20 cycles, whereas the thicker electrode (500 µm) maintained a relatively stable capacity of around 50 mAh g^{-1} over the same period. The thicker electrode demonstrated nearly the same capacity retention during longer cycles, with the capacity stabilizing at around 48 mAh g^{-1} after 100 cycles compared to the thinner electrode, which showed a similar capacity of 47 mAh g^{-1}. These results indicate that the manufacturing process can play an important role in the electrode where in the long-term cycling stability, the thicker electrodes exhibit the same performance over extended cycles. The thicker electrode (500 µm) maintained a specific capacity compared to the thinner one (230 µm) throughout the test period. This indicates that while both thicknesses offer performance, the thicker electrode may have an advantage in retaining capacity over time.

To investigate more on our initial findings, a dry hybrid LMO//AC cathode with 40:40:10:10 LMO:AC:C65:PVdF composition, 23.12 mg active mass, and 612.0 µm thickness has been fabricated. **Figure 91** shows the cycling performance of such hybrid cathode 200 cycles at a rate of 1C. The initial specific capacity is around 65 mAh g^{-1} (after formation) for both lithiation and delithiation processes. Over the 200 cycles, the specific capacity declined to 58 mAh g^{-1} and retained 89% of its initial capacity by the end of the test period. Moreover, the Coulombic

efficiency remains consistently close to 100% throughout the cycling, which indicates efficient charge/discharge processes. The combined results of our electrochemical tests show the successful fabrication of stable and high-performing dry electrodes based on hybrid LMO//AC. The results prove that the presented preparation process is effective and could reproduce electrodes with varying content combinations, thicknesses, and mass loading.

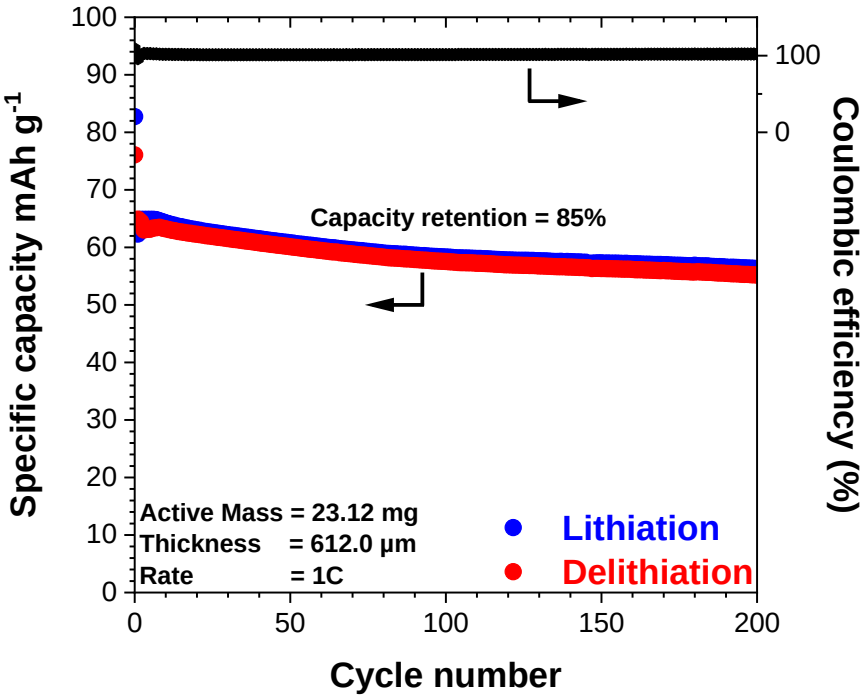

Figure 91. Cycling performance of the dry hybrid LMO//AC electrode (40:40:10:10 LMO:AC:C65:PVdF) at 1C for 200 cycles

8. DIGIBATMAT

Some of the details in **Section 8** are extracted from the scientific publication „ Developing an ontology on battery production and characterization with the help of key use cases from battery research.“ All specific contributions are thoroughly listed and acknowledged in **Section 12**.

8.1. DigiBatMat Project Overview

The DigiBatMat initiative has successfully built a platform that merges information, on battery components and production procedures by bringing together battery tech experts with digitalization and AI professionals to work hand in hand on this endeavor. Utilizing data to establish a connection, between materials used and manufacturing techniques through thorough analysis and exploration of their correlations is what the project has accomplished. In Key Use Case 3 my work contributions stood out when I devised and executed a plan to streamline the process of generating data throughout production phases. By pinpointing zones, with potential, for valuable data collection, I made sure that the information gathered would directly enhance production effectiveness and analysis of material performance.

8.2. Summary of achievements on the DigiBatMat platform

The DigiBatMat platform has made enhancements to the efficiency and evaluation of materials and procedures, in LIBs manufacturing operations. By working with specialists in battery technology along, with digitalization and AI expertise we have developed a system that harmonizes different facets of LIB production thus simplifying the handling and examination of data.

8.2.1. Platform Development:

In the platform’s growth process, I made an impact by working on crafting a user interface dedicated to data management excellence. Essential, to this endeavor was the design of a template system allowing users to seamlessly import Excel data files and cutting down data entry efforts by a quarter. My dedication to ensuring ease of use meant that researchers could easily handle and organize volumes of data efficiently – enhancing the usability of the platform for day-to-day activities.

8.2.2. Data Analysis and Reference Data Production

A machine learning algorithm to examine the gathered data and uncover findings and trends that steered the research paths and decision-making processes effectively has been utilized. Moreover, developed reference data enhanced the accuracy of comparisons and validations thus ensuring evaluations of materials and processes.

8.2.3. Key use cases:

In my role, at the company I worked on Key Use Case 3 which focused on consolidating data generation throughout phases of the battery manufacturing process. This targeted approach was instrumental in streamlining data gathering in areas with potential for positive change leading to enhanced efficiency and outcomes. By pinpointing these zones aimed to ensure that our data-centric strategy had an impact, on guiding research initiatives and refining production processes.

8.3. Implementation of key use cases

The uses of the DigibatMat platform have greatly contributed to its ability to assist in research and development activities across fields by combining data knowledge with studies successfully. I have played a role, in advancing the effectiveness of the platform in managing data and planning experiments with a focus, on Key Use Case 3. The DigiBatMat Ontologies offer a foundation, for shaping and enhancing research ideas. With its method for formulating hypotheses, the system aids in laying the groundwork for research endeavors, in R&D making it easier to conduct systematic and evidence-based studies.

The process of planning experiments has been made efficient with the help of DigiBatMat ontologies to ensure that experiment designs follow established standards and practices, in the industry consistently and effectively improved R&D workflows as a result contributing to integration of reference data that offers crucial benchmarks for comparison and validation, on the platform. After conducting experiments are finished and completed all steps involving combining information and examining them are carefully saved in the system to manage data smoothly. In a key use case 3, I played a part, in bringing together the process of generating data throughout various stages of production with a focus placed specifically on key spots, for collecting data and securing its accuracy. This work has guaranteed that the information collected is accurately verified and confirmed, making it easier to use for examination and

understanding. The platform is always being improved with suggestions, for growth opportunities in mind. By building upon the infrastructure and expanding its functionalities the platform boosts researchers' capacity to assess workflows and discover insights. My input has secured the platform flexibility allowing researchers to widen their research horizons while upholding standards, for data accuracy and analysis.

8.4. Key use case 3

Key use case 3 (KUC 3) primarily focused on enhancing the performance of lithium titanate oxide, lithium manganese oxide, and lithium manganese oxide//activated carbon hybrid electrodes by refining their manufacturing processes. Dry and wet mixing methods along with variations in mixing speeds and durations (in centrifuge mixer) were investigated to determine their influence on particle size distribution and electrode structure, subsequently impacting the electrochemical performance of each electrode.

8.4.1. Hypotheses for LTO, LMO, and LMO//AC electrodes

Two hypotheses were. Studied for LTO, LMO, and LMO//AC electrodes. **Hypothesis 1**: Extensive optimization of the mixing method will reduce capacity degradation in LTO, LMO, and LMO//AC electrodes when subjected to applied current in the appointed potential range. **Hypothesis 2**: Modifying mixing parameters, such as speed and duration of centrifuge mixer, in both wet processes will result in electrode structures with varying particle sizes and distributions. To find the conditions for improving the performance of LTO, LMO, and LMO//AC electrodes we experimented with different mixing parameters like speed and duration using both dry and wet methods. Here are the steps we followed.

Gathering and organizing Data: information on materials mixing techniques and characterization methods has been collected. In the next step, we uploaded the results to the DigiBatMat platform. The DigiBatMat ontology was used to organize the relationships between materials and processes for clarity and easy access. **Characterization methods**: We analyzed properties such as structure, particle size, and uniformity using techniques listed in **Table 11** and **Table 12**. Methods, like Scanning Electron Microscopy, X-ray Diffraction, and Raman spectroscopy were used to study the structure, morphology, and surface composition of the electrodes. **Electrochemical testing**: The prepared electrodes underwent testing to assess how the optimized manufacturing process affected their performance. Tests included Cyclic

Voltammetry, Galvanostatic Charge/Discharge cycles, and Electrochemical Impedance Spectroscopy for evaluation.

Table 11. List of characterization techniques

Properties	Characterization techniques	Instrument
Particle size distribution	Dynamic light scattering (DLS) Grindometer	Malvern Mastersizer 2000 BEVS Fineness
Shear rate	Rheometer	Anton-Paar MCR302e
Morphology	Scanning electron microscopy	Geminin 500, Zeiss
Crystal phase and structure	X-ray Diffraction (XRD) Raman spectroscopy	D8 Discover (Bruker AXS) Renishaw inVia Raman

8.4.2. Detailed flow and implementation

The detailed flow of the DigiBatMat platform's implementation, as shown in **Figure 92, Table 11,** and **Table 12**, shows the process of characterizing and optimizing battery materials. This approach showed that the data collection process was reliable and practical for enhancing the manufacturing process of high-performance LIBs. By focusing on KUC 3 the system facilitated an examination of how various mixing techniques and factors impact the structure and efficiency of the electrodes and, particularly the LTO anode.

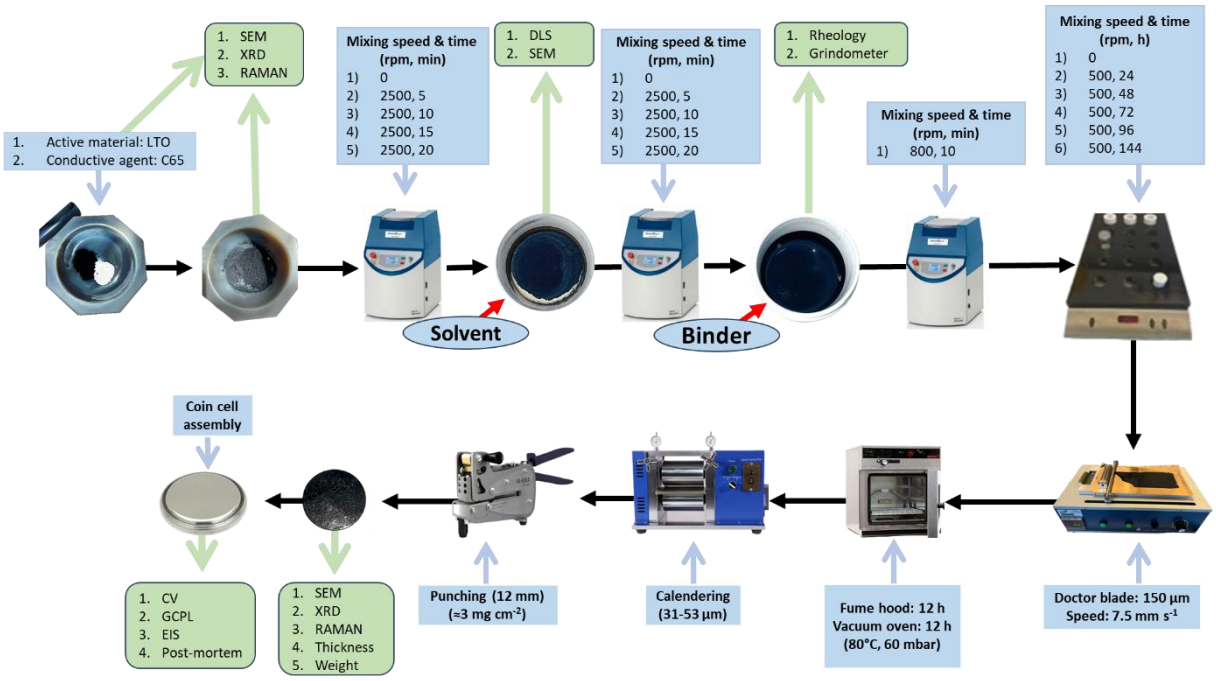

Figure 92. Summary of the electrode preparation with relevant parameters. *Legend:* Blue box – mixing parameters; Green box –characterization techniques; Insets – actual photos.

In the following section, we have discussed the findings and results. **Mixing Methods:** We thoroughly investigated how mixing techniques such as the duration of mixing and the speed of mixing (in a centrifuge mixer) influence particle size distribution and electrode structure. It was noted that optimized mixing factors play a role, in the consistency and electrochemical performance of the electrodes. **Electrode Properties:** With characterization analyses, we uncovered how varying mixing speeds and durations can influence structures and particle size distributions. These structural changes were linked to the performance of the electrodes that confirmed the defined hypotheses. **Electrochemical Performance:** The improved performance of the optimized electrodes was apparent showing capacity degradation and enhanced stability under high-rate conditions. The data presented on the DigiBatMat platform provided a summary of these findings that enables an evaluation and validation process.

Table 12. List of electrochemical measurements and conditions

Battery testing	The **BioLogic** battery cycler BCS-810 is equipped with BT-Lab software. VMP3 multi-channel potentiostat and galvanostat (Biologic) were analyzed using the EC-Lab software.
Testing conditions	@25±1°C in Binder Climate chamber
Battery Chemistry (CR2032)	
Separator	Whatman GF/F glass fiber discs (Ø = 18 mm)
Electrolyte	1 M $LiPF_6$ in 1:1 EC:DMC, Sigma Aldrich(150 µL)
Working Electrode	LTO (Ø = 12 mm, ≈ 3.0 mg cm^{-2})
Counter Electrode	Li chips, MTI (Ø = 15 mm)
Half-cell tests	
Cyclic Voltammetry (CV)	Potential window: 0.01 – 3.00 V vs. Li^+/Li Scan rate: 0.1 and 5.0 mV s^{-1}
Galvanostatic Charge and Discharge (GCD)	Potential window: 0.01 – 3.00 V vs. Li^+/Li Specific current: 0.1 and 20.0 A g^{-1}
Electrochemical impedance spectroscopy (EIS)	Frequency: 10^{-2} -10^5 Hz Open Voltage: 5 mV

9. SUMMARY, CONCLUSION, AND OUTLOOK

9.1. Summary

The detailed work on electrodes for LIBs discussed in this thesis has given insights into improving the electrode manufacturing processes and boosting the performance of metal oxide electrodes for LIBs. The research mainly focused on optimizing the preparation of five types of electrodes; LTO, LFP, LMO, a hybrid electrode made of a combination of lithium manganese oxide and activated carbon, and a dry process electrode that was a mix of lithium manganese oxide and activated carbon. Our results confirmed the significance of adjusting mixing techniques and parameters during preparation to enhance the efficiency and longevity of these electrodes.

9.1.1. LTO anode

The first part of the investigation of this thesis (**Section 4**) discusses the experiments conducted to find the parameters for improving the performance of the LTO anode. Different conditions were tested to prepare dry mixture and wet mixture (slurry) of LTO and C65 combination. By using Dynamic light scattering (DLS) measurements, Scanning electron microscopy, X-ray Diffraction (XRD), Raman analysis, Electrochemical impedance spectroscopy (EIS), etc., we evaluated how mixing time and speed affect the compositional and electrochemical properties of the LTO electrode. Our systematic research identified parameters that result in enhanced performance across a wide potential range for LTO electrodes:

The optimal mixing time for the LTO/C65 powder mixture in a mortar is 10 min. It was observed that mixing beyond 10 min caused powder adhesion making it challenging to collect the mixture from the mortar. For mixing LTO/C65 powders using a centrifuge mixer (SpeedMixer), the speed and time are 2500 rpm and 15 min. These settings effectively reduced particle size. Ensured coverage of LTO particles by the conductive agent (C65). The best ratio for solvent and powder mixture is 8:5 by mass percent. This amount of solvent proved sufficient for uniform coating of mixtures, resulting in a slurry with viscosity and consistency. The optimal speed and duration for wet mixing of LTO and C65 powder mixture and DMSO solvent in the SpeedMixer (SM) are 2500 rpm and 10 min. With these settings, the average particle size in the final slurry remains below 5 µm.

Through a combination of characterization and electrochemical analyses, it was observed that extending the final mixing of the optimized mixture by 72 h under a mechanical stirrer (magnetic stirrer) enhances the structural properties of the LTO electrode. This process leads to improvements in particle size distribution and homogeneity of the LTO active materials. Overall, the optimized LTO anode (LTO 72) demonstrated superior electrochemical performance, including initial capacities of 232 mAh g^{-1} at 2.9 A g^{-1} (10C), 190 mAh g^{-1} at 5.0 A g^{-1} (≈17C), 162 mAh g^{-1} at 10.0 A g^{-1} (≈34C), and 78 mAh g^{-1} at 20.0 A g^{-1} (≈68C). This electrode maintained 60% and 57% of its initial capacity after 2000 cycles at specific currents of 5.0 A g^{-1} (≈17C) and 10.0 g^{-1} (≈34C), respectively. The homogeneous distribution of electrode materials, as confirmed by scanning electron microscopy (with post-mortem analysis), played a crucial role in these results.

9.1.2. LFP, LMO, and hybrid LMO//AC cathodes

In the second part of this thesis (**Section 5**), we studied enhancing the capabilities of LFP, LMO, and hybrid LMO//AC cathodes by refining the electrode preparation methods that have shown promising results for enhancing LTO anodes. The findings shared are preliminary and ongoing. Despite that, we have gained insights that lay the groundwork for further advancements in battery research.

9.1.2.1. LFP cathode

The preparation of LFP cathodes employed in this work involves a manual mixing of 80% as-synthesized LFP nanopowder with 10% conductive carbon black for 10 min, followed by speed mixing at 1000 rpm for 5 min. DMSO solvent is gradually added and mixed at 1500 rpm and 2500 rpm for 5 min each, and then PVdF binder is added. The variations in the mixing speed and time of wet LFP/C65 mixtures have not yet been included in this thesis. The final slurry was mechanically stirred for 24 h at 500 rpm. The variations in the mixing speed and time of dry and wet LFP/C65 mixtures were not yet included in this thesis. The cycling performance of the as-prepared LFP cathode at 25 mA g^{-1} for 50 cycles delivered an initial capacity of 76 mAh g^{-1}. The specific capacity gradually decreased to 66 mAh g^{-1} and stabilized throughout the cycles retaining 87% of the initial capacity. The Coulombic efficiency remained close to 100% across the whole cycling process, indicating efficient and reversible charge-discharge processes with minimal losses.

9.1.2.2. LMO cathode

During our initial investigation using the DLS measurement and scanning electron micrographs, we learned that the SM parameters did not affect the particle sizes of the dry LMO/C65 mixture, as the particle size distributions remain consistent across different mixing speeds and durations. With this, the preparation process of LMO cathodes in this work proceeds by mixing 80% LMO powder and 10% C65 by manual grinding for 10 min and speed mixing at 1500 rpm for 5 min. DMSO solvent and 10 mass% PVdF binder solution are then added, mixed at 2500 rpm and 800 rpm for 10 min each, and stirred at 500 rpm for 24 h.

In the case of the LMO cathodes, a capacity retention of 69% after 500 cycles at 200 A g^{-1} was obtained. Such stability was influenced by manganese dissolution and redeposition at the anode, phase transitions within the LMO structure, and the material's electrical conductivity. Even though the LMO electrode showed limitations, the electrochemical performance remained stable under prolonged cycling conditions, indicating its potential for long-term energy storage applications.

9.1.2.3. Hybrid LMO//AC cathode

The LMO//AC hybrid electrode with 30:50:10:10 LMO:AC:C65:PVdF ratio was prepared parallel to the preparation mentioned above process. The combined results of scanning electron micrographs, XRD, and Raman analyses revealed a well-structured and uniform composite material with good dispersion and adhesion between LMO and activated carbon particles. Although we successfully prepared the hybrid LMO//AC electrode with a uniform presence of the LMO phase and graphitic nature of the activated carbon component, the result of its cycling performance at 0.2 A g^{-1} for 300 cycles showed limited electrochemical performance. The hybrid LMO//AC electrode delivered an initial specific capacity of ~165 mAh g^{-1} for lithiation and 145 mAh g^{-1} for delithiation.

Then a noticeable capacity fading starts after 50 cycles, which drops to ~60 mAh g^{-1} after 300 cycles. While the Coulombic efficiency improves to above 90% after 100 cycles, it remains unstable and shifts throughout the rest of the cycling period. We believe that the structural, compositional, and electrochemical properties of the hybrid LMO//AC electrode could be improved through further optimization of the electrode preparation process. This investigation is not yet included in this work.

9.1.2.4. Full-cell test (LTO//LMO and LTO//LFP)

In the third part of the study (**Section 6**), by using the improved LTO, LMO, and LFP electrodes, we assembled LIBs in full-cell configuration using LTO as anode and LMO (LTO//LMO) and LFP (LTO//LFP) as cathode, respectively. The LTO//LMO full cell starts with a specific capacity of about 250 mAh g^{-1} at the applied current of 0.5 A g^{-1}, which drops significantly to around 100 mAh g^{-1} after 50 cycles and continues to decrease. Despite this capacity fading, the Coulombic efficiency remains stable above 90%, indicating consistent charge/discharge efficiency. Likewise, the full-cell performance of the optimized LTO anode against an LFP cathode showed an initial capacity of 138 mAh g^{-1} at 0.2 A g^{-1} and retained 81% of its capacity after 200 cycles. The Coulombic efficiency remained above 97%, demonstrating efficient charge and discharge processes.

9.1.3. Dry process electrode

In **Section 7** we recognize the progress made in improving the method of preparing dry process electrodes. Exploring this procedure is essential as it can lead to cost eco eco-friendly and high-performance batteries. Understanding this technique will enable us to develop energy storage solutions supporting initiatives, in combating climate change and achieving energy self-sufficiency. Our initial investigations using a hybrid LMO//AC cathode with a 30:50:10:10 ratio of LMO:AC:C65:PVdF showed outcomes. We observed that the thickness of the electrode does not significantly affect its performance as all electrodes maintained a consistent specific capacity of around 50 mAh g^{-1} during short-term cycling. Thicker electrodes (500 µm) displayed an advantage in retaining capacity over 100 cycles at a rate of 1C compared to ones (230 µm). Furthermore, we fabricated a hybrid LMO//AC cathode with a ratio of 40:40:10:10 for LMO, AC, C65, and PVdF and a thickness of 612 µm to confirm the versatility of our preparation method. Interestingly, our cells exhibited a capacity of around 80 mAh g^{-1} and maintained good stability with an 85% capacity retention after 200 cycles, along with consistently high Coulombic efficiency. In conclusion, we have successfully demonstrated a dry process preparation technique of producing electrodes, with varying thicknesses and mass loadings.

9.1.4. DigiBatMat

Finally, in **Section 8**, we introduce the DigiBatMat platform. This platform plays a role in moving forward battery research and development (R&D) by focusing on applications. It makes it easy to gather historical data and analyze them, resulting in innovative insights for optimizing LIB systems. Through its data management capabilities, it has significantly smoothed the research

process, showing its potential to fuel innovation and scientific advancement in battery technology. This systematic approach shows the significance of DigiBatMat in supporting R&D initiatives and its impact, on the development of high-performance LIBs that shape the future of energy storage solutions.

9.2. Conclusions

In **Section 7,** we recognize the progress made in improving the method of preparing dry process electrodes. Exploring this procedure is important as it can lead to cost-effective and eco-friendly and also high-performance batteries. Understanding this technique will enable us to develop energy storage solutions that support the capability of combating climate change and achieving energy self-sufficiency. Our initial investigations using a hybrid LMO//AC cathode with a 30:50:10:10 ratio of LMO:AC:C65:PVdF showed outcomes. We observed by optimizing the manufacturing process, the thickness of the electrode does not significantly affect its performance as all electrodes maintained a consistent specific capacity of around 50 mAh g^{-1} during short-term cycling. In another study, a thicker electrode (500 µm) displayed an advantage in retaining capacity over 100 cycles at a rate of 1C compared to a thinner one, which had a thickness of 230 µm.

Furthermore, we fabricated a hybrid LMO//AC cathode with a ratio of 40:40:10:10 for LMO:AC:C65:PVdF and a thickness of 612 µm to confirm the reliability of our preparation method. The cells exhibited a capacity of around 65 mAh g^{-1} and maintained good stability with an 89% capacity retention after 200 cycles, and also with consistent and high Coulombic efficiency. In conclusion, we have shown a dry process preparation technique for producing electrodes with varying thicknesses and mass loadings.

9.2.1. Impact of mixing methods and parameters

It was distinguished that when **dry mixing** is done carefully, it can effectively disperse the active material and the other components. Otherwise, there are challenges with agglomeration if not managed well. Optimized dry mixing can create electrodes with a particle size distribution and improved electrochemical performance. Achieving these results in our study required finding a balance between **mixing speed** and **duration** in a centrifuge mixer. **Wet mixing** techniques allow for control, over the size and distribution of particles by adjusting the **speed and duration** to achieve a mixture, ultimately enhancing the properties of the electrode. This

method is crucial for ensuring a distribution of the material within the electrode. Both mixing speed and duration play roles in determining the properties of the electrodes. High-speed mixing results in particles and uniform distribution, which are advantageous for performance. However prolonged mixing may cause material properties to degrade due to stress. The optimal conditions strike a balance between achieving particle sizes without compromising the integrity of the materials.

9.2.2. Effect of the optimized manufacturing process

Ongoing efforts are necessary to develop novel energy storage systems and enhance current ones to meet the growing demands. The presented study showed how modifying the manufacturing process impacts the electrochemical performance of LTO anode half-cells. Variations in wet and dry mixing steps (in centrifuge mixer) resulted in various particle dispersions and sizes being obtained. The improvement in the manufacturing procedure reduced the amount of solvent required for electrode production by up to 50%, potentially lowering the electrode production costs on an industrial scale.

9.2.3. Effect of hybridization

Adding AC as a supercapacitor material in the LMO//AC hybrid electrodes was beneficial. The conductive network provided by AC facilitated rapid electron transport, reducing the internal resistance and enhancing the overall performance. This hybrid approach demonstrated the potential of combining different materials to leverage their strengths, resulting in electrodes with superior electrochemical properties.

9.2.4. Machine learning insights

Analyzing data with machine learning algorithms helped determine the mixing parameters. By using this method, researchers could find the conditions for electrode preparation, lowering the need for numerous trial and error tests. Combining machine learning with historical data improved the efficiency and success of the research attempt.

9.3. Outlook

The results of this thesis offer directions for research and advancement. First of all, advanced mixing techniques with the following studies could investigate innovative mixing methods like

ultrasonication or high-energy ball milling to achieve more refined particle distributions and improved material integration. These methods could boost performance by establishing better electrode structures. Secondly, the exploration of alternative materials by exploring alternative metal oxides and hybrid materials may provide a better view of potentially superior electrode materials. For example, examining the utilization of nickel cathodes or silicon-based anodes could result in batteries with increased energy densities and enhanced performance qualities. Thirdly, scaling up and commercialization means the methodologies and discoveries from this study need to be evaluated on a scale to determine their suitability for commercial battery manufacturing. Expanding the optimized blending techniques and assessments will play a role in evaluating the potential for applications. Fourthly, the integration of Advanced Analytical Techniques by Integrating advanced characterization techniques like in situ XRD or scanning electron microscopy during cycling can offer a deeper understanding of the structural changes within electrodes and degradation mechanisms. This knowledge is important for formulating strategies to enhance the durability and performance of LIBs further.

Fifthly, sustainability and cost-effectiveness, which is important for future studies to consider the sustainability and cost-effectiveness of the materials and methods used in making electrodes. Creating cost-efficient electrode materials is key to making advanced LIB technologies more widely accessible. Finally, the further development of the DigiBatMat Platform by ongoing enhancement of the DigiBatMat platform has proven to be useful for organizing and analyzing data. By continuing to improve this platform, for example, by integrating data analysis tools and machine learning algorithms, we can achieve new discoveries.

10. REFERENCES

1. G. d. A. E. E.-S. A.-S. a. Umweltbundesamt, Renewable energies continue to pick up speed in 2023, https://www.umweltbundesamt.de/en/topics/renewable-energies-continue-to-pick-up-speed-in).
2. Y. Liu, R. Zhang, J. Wang and Y. Wang, *iScience*, 2021, **24**, 102332.
3. H. Niu, N. Zhang, Y. Lu, Z. Zhang, M. Li, J. Liu, N. Zhang, W. Song, Y. Zhao and Z. Miao, *Journal of Energy Storage*, 2024, **88**, 111666.
4. W. Tong, Z. Lu, J. Sun, G. Zhao, M. Han and J. Xu, *Energy Reports*, 2022, **8**, 926-934.
5. Y. Zou, L. Bo and Z. Li, *Fundamental Research*, 2021, **1**, 364-382.
6. O. Gerard, A. Numan, S. Krishnan, M. Khalid, R. Subramaniam and R. Kasi, *Journal of Energy Storage*, 2022, **50**, 104283.
7. M. Tawalbeh, A. Farooq, R. Martis and A. Al-Othman, *International Journal of Hydrogen Energy*, 2023, DOI: https://doi.org/10.1016/j.ijhydene.2023.06.264.
8. Q. Abbas, M. Mirzaeian, M. R. C. Hunt, P. Hall and R. Raza, *Energies*, 2020, **13**.
9. S. Khalid, I. Raouf, A. Khan, N. Kim and H. S. Kim, *International Journal of Precision Engineering and Manufacturing-Green Technology*, 2019, **6**, 821-851.
10. E. Ostadzadeh, A. Elshorbagy, M. Tuninetti, F. Laio and A. Abdelkader, *Economic Systems Research*, 2023, **35**, 354-375.
11. J. Bateman, 2023 was the world's warmest year on record, by far, https://www.noaa.gov/news/2023-was-worlds-warmest-year-on-record-by-far#:~:text=%E2%80%9CNot%20only%20was%202023%20the,both%20more%20frequent%20and%20severe.).
12. M. Ryder, S. Evro, C. Brown and O. Tomomewo, *American Journal of Energy Research*, 2023, **11**, 63-81.
13. A. Z. Al Shaqsi, K. Sopian and A. Al-Hinai, *Energy Reports*, 2020, **6**, 288-306.
14. C. Kang and L. Yao, *Dianli Xitong Zidonghua/Automation of Electric Power Systems*, 2017, **41**, 2-11.
15. O. Haas and E. J. Cairns, *Annual Reports Section "C" (Physical Chemistry)*, 1999, **95**, 163-198.
16. A. Dutta, S. Mitra, M. Basak and T. Banerjee, *Energy Storage*, 2023, **5**.
17. B. D. McCloskey, *The Journal of Physical Chemistry Letters*, 2015, **6**, 3592-3593.
18. H. Zhang, L. Wang, H. Li and X. He, *ACS Energy Letters*, 2021, **6**, 3719-3724.
19. T. Placke, R. Kloepsch, S. Dühnen and M. Winter, *Journal of Solid State Electrochemistry*, 2017, **21**, 1939-1964.
20. Y. Liu, Q. H. Wu, L. Y. Liu, P. Manasa, L. Kang and F. Ran, *Journal of Materials Chemistry A*, 2020, **8**, 8218-8233.
21. Y. Meesala, A. Jena, H. Chang and R.-S. Liu, *ACS Energy Letters*, 2017, **2**.
22. S. Sarmah, Lakhanlal, B. K. Kakati and D. Deka, *Wiley Interdisciplinary Reviews-Energy and Environment*, 2023, **12**.
23. M. Nasrollahzadeh, N. Shafiei and Z. Nezafat, in *Biopolymer-Based Metal Nanoparticle Chemistry for Sustainable Applications*, ed. M. Nasrollahzadeh, Elsevier, 2021, DOI: https://doi.org/10.1016/B978-0-323-89970-3.00001-9, pp. 1-44.
24. S. Hemavathi, S. Srirama and A. S. Prakash, *Chembioeng Reviews*, 2023, **10**, 1123-1145.
25. M. Gambini, F. Guarnaccia, M. Manno and M. Vellini, *Journal of Energy Storage*, 2024, **76**, 109815.
26. E. Catenaro, D. M. Rizzo and S. Onori, *Applied Energy*, 2021, **291**, 116473.
27. T. Christen and M. W. Carlen, *Journal of Power Sources*, 2000, **91**, 210-216.
28. S. C. Lee and W. Y. Jung, *Energy Procedia*, 2016, **88**, 526-530.
29. D. V. Ragone, *Sae Transactions*, 1968, **77**, 131-&.
30. R. Zhou, S. Wei, Y. Liu, N. Gao, G. Wang, J. Lian and Q. Jiang, *Scientific Reports*, 2019, **9**, 3980.
31. I. Beyers, A. Bensmann and R. Hanke-Rauschenbach, *Journal of Energy Storage*, 2023, **73**, 109097.

32. D. Wu, X. Xiubo, Y. Zhang, D. Zhang, W. Du, X. Zhang, and B. Wang, *Frontiers in Materials*, 2020, **7**, 2.
33. R. J. Chen, R. Luo, Y. X. Huang, F. Wu and L. Li, *Advanced Science*, 2016, **3**.
34. P. J. Hall and E. J. Bain, *Energy Policy*, 2008, **36**, 4352-4355.
35. J. Fleischmann, M. Hanicke, E. Horetsky, D. Ibrahim, S. Jautelat, M. Linder, P. Schaufuss, L. Torscht and A. van de Rijt, *McKinsey & Company*, 2023, 2-18.
36. F. Omenya, M. Paiss, X. Li and D. Reed, *ACS Energy Letters*, 2023, **8**, 2707-2710.
37. R. Borah, F. R. Hughson, J. Johnston, and T. Nann, *Materials Today Advances*, 2020, **6**, 100046.
38. N. Nitta, F. Wu, J. T. Lee and G. Yushin, *Materials Today*, 2015, **18**, 252-264.
39. J. Yao and T. Han, *Energy*, 2023, **271**, 127033.
40. A. Jain, S. P. Ong, G. Hautier, W. Chen, W. D. Richards, S. Dacek, S. Cholia, D. Gunter, D. Skinner, G. Ceder and K. A. Persson, *APL Materials*, 2013, **1**.
41. H. Ibrahim, A. Ilinca and J. Perron, *Renewable and Sustainable Energy Reviews*, 2008, **12**, 1221-1250.
42. X. R. Chen, X. Liu, Q. C. Le, M. X. Zhang, M. Liu and A. Atrens, *Journal of Materials Chemistry A*, 2021, **9**, 12367-12399.
43. Y. Nishi, *Chemical Record*, 2001, **1**, 406-413.
44. A. Noori, M. F. El-Kady, M. S. Rahmanifar, R. B. Kaner and M. F. Mousavi, *Chemical Society Reviews*, 2019, **48**, 1272-1341.
45. Y. Cao, M. Li, J. Lu, J. Liu and K. Amine, *Nature Nanotechnology*, 2019, **14**, 200-207.
46. Y. Chen, Y. Kang, Y. Zhao, L. Wang, J. Liu, Y. Li, Z. Liang, X. He, X. Li, N. Tavajohi and B. Li, *Journal of Energy Chemistry*, 2021, **59**, 83-99.
47. M. Patel, K. Mishra, R. Banerjee, J. Chaudhari, D. K. Kanchan and D. Kumar, *Journal of Energy Chemistry*, 2023, **81**, 221-259.
48. X. M. Yang and A. L. Rogach, *Advanced Energy Materials*, 2019, **9**.
49. T. Bashir, S. A. Ismail, Y. H. Song, R. M. Irfan, S. Q. Yang, S. W. Zhou, J. Q. Zhao and L. J. Gao, *Energy Materials*, 2021, **1**.
50. A. J. Smith, J. C. Burns and J. R. Dahn, *Electrochemical and Solid-State Letters*, 2010, **13**, A177.
51. P. G. Balakrishnan, R. Ramesh and T. Prem Kumar, *Journal of Power Sources*, 2006, **155**, 401-414.
52. T. Wang, C. Li, X. Xie, B. Lu, Z. He, S. Liang and J. Zhou, *ACS Nano*, 2020, **14**, 16321-16347.
53. S. J. An, J. Li, C. Daniel, D. Mohanty, S. Nagpure and D. L. Wood, *Carbon*, 2016, **105**, 52-76.
54. V. Etacheri, R. Marom, R. Elazari, G. Salitra and D. Aurbach, *Energy & Environmental Science*, 2011, **4**, 3243-3262.
55. M. M. Kabir and D. E. Demirocak, *International Journal of Energy Research*, 2017, **41**, 1963-1986.
56. D. Deng, *Energy Science & Engineering*, 2015, **3**, 385-418.
57. L. J. Zhang, H. T. Wang, X. M. Zhang and Y. B. Tang, *Advanced Functional Materials*, 2021, **31**.
58. X. L. Chen, Y. H. Zheng, W. J. Liu, C. Zhang, S. Li and J. Li, *Nanoscale*, 2019, **11**, 22196-22205.
59. R. Marom, S. F. Amalraj, N. Leifer, D. Jacob and D. Aurbach, *Journal of Materials Chemistry*, 2011, **21**, 9938-9954.
60. F. Beck, H. Krohn, and W. Kaiser, *Journal of Applied Electrochemistry*, 1982, **12**, 505-515.
61. M. S. Palagonia, C. Erinmwingbovo, D. Brogioli and F. La Mantia, *Journal of Electroanalytical Chemistry*, 2019, **847**, 113170.
62. L. Driscoll, S. de la Torre and J. A. Gomez-Ruiz, *Journal of Energy Storage*, 2022, **50**, 104584.
63. D. Choi, N. Shamim, A. Crawford, Q. Huang, C. K. Vartanian, V. V. Viswanathan, M. D. Paiss, M. J. E. Alam, D. M. Reed and V. L. Sprenkle, *Journal of Power Sources*, 2021, **511**, 230419.
64. J. F. Rusling and S. L. Suib, *Advanced Materials*, 1994, **6**, 922-930.
65. M. D. Levi and D. Aurbach, *The Journal of Physical Chemistry B*, 1997, **101**, 4630-4640.
66. Z.-y. Chen, H.-l. Zhu, W. Zhu, J.-l. Zhang and Q.-f. Li, *Transactions of Nonferrous Metals Society of China*, 2010, **20**, 614-618.
67. A. Vadivel Murugan, M. V. Reddy, G. Campet and K. Vijayamohanan, *Journal of Electroanalytical Chemistry*, 2007, **603**, 287-296.

68. N. Mahmood, T. Y. Tang, and Y. L. Hou, *Advanced Energy Materials*, 2016, **6**.
69. K. Kleiner and H. Ehrenberg, *Topics in Current Chemistry*, 2017, **375**, 54.
70. P. Peljo and H. H. Girault, *Energy & Environmental Science*, 2018, **11**, 2306-2309.
71. A. M. Divakaran, M. Minakshi, P. A. Bahri, S. Paul, P. Kumari, A. M. Divakaran and K. N. Manjunatha, *Prog Solid State Ch*, 2021, **62**.
72. T. Hosaka, K. Kubota, A. S. Hameed and S. Komaba, *Chemical Reviews*, 2020, **120**, 6358-6466.
73. M. Li, J. Lu, Z. W. Chen and K. Amine, *Advanced Materials*, 2018, **30**.
74. Y. Li, Y. Lu, P. Adelhelm, M.-M. Titirici and Y.-S. Hu, *Chemical Society Reviews*, 2019, **48**, 4655-4687.
75. Y. Jung, Y. Zhou and J. J. Cha, *Inorganic Chemistry Frontiers*, 2016, **3**, 452-463.
76. M.-S. Balogun, W. Qiu, Y. Luo, H. Meng, W. Mai, A. Onasanya, T. K. Olaniyi and Y. Tong, *Nano Research*, 2016, **9**, 2823-2851.
77. Y.-M. Kang, M.-S. Song, J.-H. Kim, H.-S. Kim, M.-S. Park, J.-Y. Lee, H. K. Liu and S. X. Dou, *Electrochimica Acta*, 2005, **50**, 3667-3673.
78. E. Buiel and J. R. Dahn, *Electrochimica Acta*, 1999, **45**, 121-130.
79. M. Wagemaker and F. M. Mulder, *Accounts of Chemical Research*, 2013, **46**, 1206-1215.
80. A. Moradabadi and P. Kaghazchi, *Physical Chemistry Chemical Physics*, 2015, **17**, 22917-22922.
81. M. S. Dresselhaus and G. Dresselhaus, *Advances in Physics*, 1981, **30**, 139-326.
82. S.-H. Yu, X. Feng, N. Zhang, J. Seok and H. D. Abruña, *Accounts of Chemical Research*, 2018, **51**, 273-281.
83. Z. Yang, M. H. Xu, Y. Liu, F. J. He, F. Gao, Y. J. Su, H. Wei and Y. F. Zhang, *Nanoscale*, 2014, **6**, 1890-1895.
84. T. Yang, T. Qian, J. Liu, N. Xu, Y. Li, N. Grundish, C. Yan and J. B. Goodenough, *ACS Nano*, 2019, **13**, 9067-9073.
85. A. Jana, D. R. Ely and R. E. García, *Journal of Power Sources*, 2015, **275**, 912-921.
86. W.-J. Zhang, *Journal of Power Sources*, 2011, **196**, 877-885.
87. P. K. Choubey, M.-s. Kim, R. R. Srivastava, J.-c. Lee and J.-Y. Lee, *Minerals Engineering*, 2016, **89**, 119-137.
88. B. Tadesse, F. Makuei, B. Albijanic and L. Dyer, *Minerals Engineering*, 2019, **131**, 170-184.
89. J. Wang, X. Yue, P. Wang, T. Yu, X. Du, X. Hao, A. Abudula and G. Guan, *Renewable and Sustainable Energy Reviews*, 2022, **154**, 111813.
90. P. Meshram, B. D. Pandey and T. R. Mankhand, *Hydrometallurgy*, 2014, **150**, 192-208.
91. L. V. Garcia, Y. C. Ho, M. M. M. Thant, D. S. Han and J. W. Lim, *Processes*, 2023, **11**.
92. W. Yu, Y. Guo, S. Xu, Y. Yang, Y. Zhao and J. Zhang, *Energy Storage Materials*, 2023, **54**, 172-220.
93. C. E. L. Foss, 2014.
94. G. E. Blomgren, *Journal of the Electrochemical Society*, 2017, **164**, A5019-A5025.
95. J. B. Goodenough and K. S. Park, *Journal of the American Chemical Society*, 2013, **135**, 1167-1176.
96. A. Manthiram, *Nature Communications*, 2020, **11**.
97. R. Mehek, N. Iqbal, N. Tayyaba, M. Z. Amjad, G. Ali, K. Vignarooban and M. Khan, *RSC Advances*, 2021, **11**, 29247-29266.
98. T. Kim, W. Song, D.-Y. Son, L. K. Ono and Y. Qi, *Journal of Materials Chemistry A*, 2019, **7**, 2942-2964.
99. C. Dai, Z. Wang, K. Liu, X. Zhu, X. Liao, X. Chen and Y. Pan, *Engineering Failure Analysis*, 2019, **101**, 193-205.
100. C. K. Lee and K.-I. Rhee, *Journal of Power Sources*, 2002, **109**, 17-21.
101. X. Liu, G. Zhu, K. Yang and J. Wang, *Journal of Power Sources*, 2007, **174**, 1126-1130.
102. J. Lu, Z. H. Chen, Z. F. Ma, F. Pan, L. A. Curtiss and K. Amine, *Nature Nanotechnology*, 2017, **12**, 90-90.
103. H. Liu, Z. Wei, W. He and J. Zhao, *Energy Conversion and Management*, 2017, **150**, 304-330.
104. B. F. Ji, F. Zhang, M. H. Sheng, X. F. Tong and Y. B. Tang, *Advanced Materials*, 2017, **29**.
105. X. Zhang, *Electrochimica Acta*, 2011, **56**, 1246-1255.
106. L. Li, R. Chen, F. Sun, F. Wu and J. Liu, *Hydrometallurgy*, 2011, **108**, 220-225.

107. P. U. Nzereogu, A. D. Omah, F. I. Ezema, E. I. Iwuoha and A. C. Nwanya, *Applied Surface Science Advances*, 2022, **9**, 100233.
108. W. Qi, J. G. Shapter, Q. Wu, T. Yin, G. Gao, and D. Cui, *Journal of Materials Chemistry A*, 2017, **5**, 19521-19540.
109. Y. Kim, W. Song, S. Y. Lee, C. Jeon, W. Jung, M. Kim and C. Y. Park, *Applied Physics Letters*, 2011, **98**.
110. L. Ji, Z. Lin, M. Alcoutlabi and X. Zhang, *Energy & Environmental Science*, 2011, **4**, 2682-2699.
111. M. Winter, J. O. Besenhard, M. E. Spahr and P. Novak, *Advanced Materials*, 1998, **10**, 725-763.
112. Z. Xiao, R. H. Wang, D. T. Jiang, Z. F. Qian, Y. Li, K. S. Yang, Y. L. Sun, Z. Y. Zeng and F. X. Wu, *ACS Applied Energy Materials*, 2021, **4**, 7440-7461.
113. S. K. Sharma, G. Sharma, A. Gaur, A. Arya, F. S. Mirsafi, R. Abolhassani, H. G. Rubahn, J. S. Yu and Y. K. Mishra, *Energy Advances*, 2022, **1**, 457-510.
114. A. Eftekhari, *Energy Storage Materials*, 2017, **7**, 157-180.
115. F. Yang, D. Wang, Y. Zhao, K.-L. Tsui and S. J. Bae, *Energy*, 2018, **145**, 486-495.
116. R. Xu, X. Shen, X. X. Ma, C. Yan, X. Q. Zhang, X. Chen, J. F. Ding and J. Q. Huang, *Angewandte Chemie-International Edition*, 2021, **60**, 4215-4220.
117. J. Yang, M. Winter and J. O. Besenhard, *Solid State Ionics*, 1996, **90**, 281-287.
118. J. Z. Niu, Z. H. Zhang and D. Aurbach, *Advanced Energy Materials*, 2020, **10**.
119. S. Imtiaz, I. S. Amiinu, Y. Xu, T. Kennedy, C. Blackman and K. M. Ryan, *Materials Today*, 2021, **48**, 241-269.
120. C.-M. Park, J.-H. Kim, H. Kim and H.-J. Sohn, *Chemical Society Reviews*, 2010, **39**, 3115-3141.
121. M. Mayo and A. J. Morris, *Chemistry of Materials*, 2017, **29**, 5787-5795.
122. M. M. Lao, Y. Zhang, W. B. Luo, Q. Y. Yan, W. P. Sun and S. X. Dou, *Advanced Materials*, 2017, **29**.
123. P. Limthongkul, Y.-I. Jang, N. J. Dudney and Y.-M. Chiang, *Acta Materialia*, 2003, **51**, 1103-1113.
124. M. Gu, Y. He, J. Zheng and C. Wang, *Nano Energy*, 2015, **17**, 366-383.
125. P. Roy and S. K. Srivastava, *Journal of Materials Chemistry A*, 2015, **3**, 2454-2484.
126. H. K. Liu, Z. P. Guo, J. Z. Wang and K. Konstantinov, *Journal of Materials Chemistry*, 2010, **20**, 10055-10057.
127. H. Jung, M. Park, Y.-G. Yoon, G.-B. Kim and S.-K. Joo, *Journal of Power Sources*, 2003, **115**, 346-351.
128. C. Z. Zhang, F. Wang, J. Han, S. Bai, J. Tan, J. S. Liu and F. Li, *Small Structures*, 2021, **2**.
129. K. Feng, M. Li, W. W. Liu, A. G. Kashkooli, X. C. Xiao, M. Cai and Z. W. Chen, *Small*, 2018, **14**.
130. D. Shao, D. Tang, Y. Mai and L. Zhang, *Journal of Materials Chemistry A*, 2013, **1**, 15068-15075.
131. M. Zeilinger, I. M. Kurylyshyn, U. Häussermann and T. F. Fässler, *Chemistry of Materials*, 2013, **25**, 4623-4632.
132. Y. Sun, Q. J. Wu, X. Liang and H. F. Xiang, *Materials Chemistry Frontiers*, 2021, **5**, 4089-4106.
133. S. Yuan, Q. Lai, X. Duan, and Q. Wang, *Journal of Energy Storage*, 2023, **61**, 106716.
134. X. J. Wang, L. L. Liu, and Z. Q. Niu, *Materials Chemistry Frontiers*, 2019, **3**, 1265-1279.
135. S. Nardecchia, D. Carriazo, M. L. Ferrer, M. C. Gutiérrez and F. del Monte, *Chemical Society Reviews*, 2013, **42**, 794-830.
136. L. Li, D. Zhang, J. Deng, Y. Gou, J. Fang, H. Cui, Y. Zhao and M. Cao, *Carbon*, 2021, **183**, 721-734.
137. D. Puthusseri, M. Wahid and S. Ogale, *ACS Omega*, 2018, **3**, 4591-4601.
138. L. Wang, J. Światowska, S. Dai, M. Cao, Z. Zhong, Y. Shen and M. Wang, *Materials Today Energy*, 2019, **11**, 46-60.
139. H. Wang, S. Chen, C. Fu, Y. Ding, G. Liu, Y. Cao and Z. Chen, *ACS Materials Letters*, 2021, **3**, 956-977.
140. Z. Q. Qi, Y. D. Wu, X. F. Li, Y. Qu, Y. Y. Yang and D. J. Mei, *Ionics*, 2020, **26**, 33-42.
141. M. J. Aragón, B. León, C. P. Vicente and J. L. Tirado, *Inorganic Chemistry*, 2008, **47**, 10366-10371.
142. N. Li, Q. Li, X. Guo, M. Yuan and H. Pang, *Chemical Engineering Journal*, 2019, **372**, 551-571.
143. J. S. Yeoh, C. F. Armer and A. Lowe, *Materials Today Energy*, 2018, **9**, 198-222.
144. K. Zhang, F. Liang, Y. Wang, Y. Dai, and Y. Yao, *Journal of Alloys and Compounds*, 2019, **779**, 91-99.

145. Q. He, H. Wang, X. Zhao and L. Chen, *Materials Today Chemistry*, 2021, **22**, 100564.
146. T. Yamada and T. Nankawa, *Inorganic Chemistry*, 2016, **55**, 8267-8270.
147. L. Lv, M. Peng, L. Wu, Y. Dong, G. You, Y. Duan, W. Yang, L. He and X. Liu, *Nanoscale Research Letters*, 2021, **16**, 138.
148. N. Yan, L. Hu, Y. Li, Y. Wang, H. Zhong, X. Hu, X. Kong and Q. Chen, *The Journal of Physical Chemistry C*, 2012, **116**, 7227-7235.
149. Y. Meng, Y. Liu, J. He, X. Sun, A. Palmieri, Y. Gu, X. Zheng, Y. Dang, X. Huang, W. Mustain, and S. L. Suib, *ACS Applied Energy Materials*, 2021, **4**, 5424-5433.
150. R. Ata ur, M. Iftikhar, S. Latif, V. Jevtovic, I. M. Ashraf, A. A. El-Zahhar, E. Abdu Musad Saleh and S. Mustansar Abbas, *Sustainable Energy Technologies and Assessments*, 2022, **53**, 102376.
151. B. Y. Guan, Y. Lu, Y. Wang, M. H. Wu and X. W. Lou, *Advanced Functional Materials*, 2018, **28**.
152. D. Y. Chen, G. Ji, B. Ding, Y. Ma, B. H. Qu, W. X. Chen and J. Y. Lee, *Industrial & Engineering Chemistry Research*, 2014, **53**, 17901-17908.
153. M. Sajjad, F. Cheng and W. Lu, *RSC Advances*, 2021, **11**, 25450-25460.
154. R. Sahoo, M. Singh and T. N. Rao, *Chemelectrochem*, 2021, **8**, 2358-2396.
155. L. Wang, X. Zhang, C. Li, X.-Z. Sun, K. Wang, F.-Y. Su, F.-Y. Liu and Y.-W. Ma, *Rare Metals*, 2022, **41**, 2971-2984.
156. Y. X. Zhang, L. Zhang, T. A. Lv, P. K. Chu and K. F. Huo, *Chemsuschem*, 2020, **13**, 1114-1154.
157. H. Yuan, L. Kong, T. Li and Q. Zhang, *Chinese Chemical Letters*, 2017, **28**, 2180-2194.
158. M. Mojtabavi, A. VahidMohammadi, W. T. Liang, M. Beidaghi and M. Wanunu, *Acs Nano*, 2019, **13**, 3042-3053.
159. D. Q. Li, X. F. Chen, P. Xiang, H. Y. Du and B. B. Xiao, *Applied Surface Science*, 2020, **501**.
160. M. Naguib, M. Kurtoglu, V. Presser, J. Lu, J. J. Niu, M. Heon, L. Hultman, Y. Gogotsi and M. W. Barsoum, *Advanced Materials*, 2011, **23**, 4248-4253.
161. A. S. Arico, P. Bruce, B. Scrosati, J. M. Tarascon and W. Van Schalkwijk, *Nature Materials*, 2005, **4**, 366-377.
162. H. Aghamohammadi, R. Eslami-Farsani and E. Castillo-Martinez, *Journal of Energy Storage*, 2022, **47**, 103572.
163. M. Naguib, J. Come, B. Dyatkin, V. Presser, P.-L. Taberna, P. Simon, M. W. Barsoum and Y. Gogotsi, *Electrochemistry Communications*, 2012, **16**, 61-64.
164. Q. Tang, Z. Zhou and P. Shen, *Journal of the American Chemical Society*, 2012, **134**, 16909-16916.
165. Z. Wu, S. Zhu, X. Bai, M. Liang, X. Zhang, N. Zhao and C. He, *Electrochimica Acta*, 2022, **407**, 139916.
166. S. J. Kim, M. Naguib, M. Zhao, C. Zhang, H.-T. Jung, M. W. Barsoum and Y. Gogotsi, *Electrochimica Acta*, 2015, **163**, 246-251.
167. A. Sengupta, B. V. B. Rao, N. Sharma, S. Parmar, V. Chavan, S. K. Singh, S. Kale and S. Ogale, *Nanoscale*, 2020, **12**, 8466-8476.
168. H. Abdurehman Tariq, U. Nisar, J. James Abraham, Z. Ahmad, S. AlQaradawi, R. Kahraman and R. A. Shakoor, *Applied Surface Science*, 2022, **583**, 152441.
169. Y. Wang, T. Guo, Z. Tian, K. Shirazi, Y. Zhang and H. Alshareef, *Advanced Materials*, 2022, **34**, 2108560.
170. N. Thakur, P. Kumar, and P. Sharma, in *Age of MXenes, Volume 3. Applications in Energy Storage: Batteries and Supercapacitors*, American Chemical Society, 2023, vol. 1444, ch. 1, pp. 1-25.
171. J. Zhu, Y. Ding, Z. Ma, W. Tang, X. Chen and Y. Lu, *Journal of Electronic Materials*, 2022, **51**, 3391-3417.
172. J. P. Liu, L. W. Dong, D. J. Chen, Y. P. Han, Y. F. Liang, M. Q. Yang, J. C. Han, C. H. Yang and W. D. He, *Small Methods*, 2020, **4**.
173. H. B. Wu, J. S. Chen, H. H. Hng and X. Wen Lou, *Nanoscale*, 2012, **4**, 2526-2542.
174. J. Jiang, Y. Li, J. Liu and X. Huang, *Nanoscale*, 2011, **3**, 45-58.
175. W. Xia, F. Xu, C. Zhu, H. L. Xin, Q. Xu, P. Sun and L. Sun, *Nano Energy*, 2016, **27**, 447-456.
176. J. S. Chen and X. W. Lou, *Small*, 2013, **9**, 1877-1893.
177. S. Natarajan, K. Subramanyan and V. Aravindan, *Small*, 2019, **15**.

178. N. Delaporte, P. Chevallier, S. Rochon, G. Lajoie, J.-C. Daigle, V. Gariepy, D. Clément, R. Veillette, M.-C. Mathieu, M. Provencher, M. L. Trudeau and K. Zaghib, *Materials Advances*, 2020, **1**, 854-872.
179. H. Liu, Z. Zhu, J. Huang, X. He, Y. Chen, R. Zhang, R. Lin, Y. Li, S. Yu, X. Xing, Q. Yan, X. Li, M. J. Frost, K. An, J. Feng, R. Kostecki, H. Xin, S. P. Ong and P. Liu, *ACS Materials Letters*, 2019, **1**, 96-102.
180. H. Zhang, Y. Yang, H. Xu, L. Wang, X. Lu and X. M. He, *Infomat*, 2022, **4**.
181. A. Ghosh and F. Ghamouss, *Frontiers in Materials*, 2020, **7**.
182. C. Han, Y.-B. He, S. Wang, C. Wang, H. Du, X. Qin, Z. Lin, B. Li and F. Kang, *ACS Applied Materials & Interfaces*, 2016, **8**, 18788-18796.
183. Z. Wang, Y. Yu, W. Kong, L. He, L. Sun and X. Liu, *The Journal of Physical Chemistry C*, 2022, **126**, 12283-12293.
184. C. P. Han, Y. B. He, S. Wang, C. Wang, H. D. Du, X. Y. Qin, Z. Q. Lin, B. H. Li and F. Y. Kang, *ACS Applied Materials & Interfaces*, 2016, **8**, 18788-18796.
185. H. Ge, N. Li, D. Li, C. Dai and D. Wang, *The Journal of Physical Chemistry C*, 2009, **113**, 6324-6326.
186. L. Mo and H. Zheng, *Energy Reports*, 2020, **6**, 2913-2918.
187. N. Takami, H. Inagaki, Y. Tatebayashi, H. Saruwatari, K. Honda and S. Egusa, *Journal of Power Sources*, 2013, **244**, 469-475.
188. X. Wang, B. Liu, X. Hou, Q. Wang, W. Li, D. Chen and G. Shen, *Nano Research*, 2014, **7**, 1073-1082.
189. B. Zhao, R. Ran, M. Liu and Z. Shao, *Materials Science and Engineering: R: Reports*, 2015, **98**, 1-71.
190. T.-F. Yi, Z.-K. Fang, L. Deng, L. Wang, Y. Xie, Y.-R. Zhu, J.-H. Yao and C. Dai, *Ceramics International*, 2015, **41**, 2336-2341.
191. C. Wang, S. Wang, L. Tang, Y.-B. He, L. Gan, J. Li, H. Du, B. Li, Z. Lin and F. Kang, *Nano Energy*, 2016, **21**, 133-144.
192. H. S. Bhatti, D. H. Anjum, S. Ullah, B. Ahmed, A. Habib, A. Karim and S. K. Hasanain, *The Journal of Physical Chemistry C*, 2016, **120**, 9553-9561.
193. G. Xu, P. Han, S. Dong, H. Liu, G. Cui and L. Chen, *Coordination Chemistry Reviews*, 2017, **343**, 139-184.
194. V. Siller, J. C. Gonzalez-Rosillo, M. Nuñez Eroles, M. Stchakovsky, R. Arenal, A. Morata and A. Tarancón, *Materials Today Energy*, 2022, **25**, 100979.
195. C. P. Sandhya, B. John and C. Gouri, *Ionics*, 2014, **20**, 601-620.
196. F. Gu, G. Chen and Z. H. Wang, *Journal of Solid State Electrochemistry*, 2012, **16**, 375-382.
197. S. Chauque, F. Y. Oliva, A. Visintin, D. Barraco, E. P. M. Leiva and O. R. Cámara, *Journal of Electroanalytical Chemistry*, 2017, **799**, 142-155.
198. C. P. Sandhya, B. John and C. Gouri, *Journal of Alloys and Compounds*, 2016, **655**, 238-243.
199. B. E. Murdock, K. E. Toghill and N. Tapia-Ruiz, *Advanced Energy Materials*, 2021, **11**.
200. N. Nitta, F. X. Wu, J. T. Lee and G. Yushin, *Materials Today*, 2015, **18**, 252-264.
201. T. Chen, Y. Jin, H. Lv, A. Yang, M. Liu, B. Chen, Y. Xie, and Q. Chen, *Transactions of Tianjin University*, 2020, **26**, 208-217.
202. J. W. Liu, M. Yue, S. Q. Wang, Y. F. Zhao and J. J. Zhang, *Advanced Functional Materials*, 2022, **32**.
203. J. J. Xu, W. Ding, G. H. Yin, Z. L. Tian, S. N. Zhang, Z. L. Hong and F. Q. Huang, *Materials Today Energy*, 2018, **9**, 240-246.
204. N. Nitta, F. Wu, J. Lee and G. Yushin, *Materials Today*, 2014, **18**.
205. Y. Ding, Z. P. Cano, A. Yu, J. Lu and Z. Chen, *Electrochemical Energy Reviews*, 2019, **2**, 1-28.
206. W. Xu and Y. Wang, *Nano-Micro Letters*, 2019, **11**.
207. J. Jyoti, B. P. Singh and S. K. Tripathi, *Journal of Energy Storage*, 2021, **43**, 103112.
208. R. Alcántara, P. Lavela, J. L. Tirado, E. Zhecheva and R. Stoyanova, *Journal of Solid State Electrochemistry*, 1999, **3**, 121-134.
209. C. Tian, F. Lin, and M. M. Doeff, *Accounts of Chemical Research*, 2018, **51**, 89-96.

210. P. He, H. Yu, D. Li and H. Zhou, *Journal of Materials Chemistry*, 2012, **22**, 3680-3695.
211. Z. Li, A. Li, H. Zhang, F. Ning, W. Li, A. Zangiabadi, Q. Cheng, J. J. Borovilas, Y. Chen, H. Zhang, X. Xiao, C. Ouyang, X. Huang, W.-K. Lee, M. Ge, Y. S. Chu, X. Chuan and Y. Yang, *Energy Storage Materials*, 2020, **29**, 71-77.
212. B. Hu, X. Lou, C. Li, F. Geng, C. Zhao, J. Wang, M. Shen and B. Hu, *Journal of Power Sources*, 2019, **438**, 226954.
213. M. Duffiet, D. Goonetilleke, F. Fauth, T. Brezesinski, J. Janek and M. Bianchini, *Chemistry of Materials*, 2022, **34**, 9955-9969.
214. G. Assat and J.-M. Tarascon, *Nature Energy*, 2018, **3**, 373-386.
215. J. Kim, H. Lee, H. Cha, M. Yoon, M. Park, and J. Cho, *Advanced Energy Materials*, 2018, **8**.
216. A. Rougier, P. Gravereau and C. Delmas, *Journal of The Electrochemical Society*, 1996, **143**, 1168.
217. H. Arai, S. Okada, Y. Sakurai and J.-i. Yamaki, *Solid State Ionics*, 1998, **109**, 295-302.
218. T. Ohzuku, A. Ueda and M. Nagayama, *Journal of The Electrochemical Society*, 1993, **140**, 1862.
219. M. Guilmard, A. Rougier, M. Grüne, L. Croguennec and C. Delmas, *Journal of Power Sources*, 2003, **115**, 305-314.
220. A. R. Armstrong and P. G. Bruce, *Nature*, 1996, **381**, 499-500.
221. J. W. Fergus, *Journal of Power Sources*, 2010, **195**, 939-954.
222. B. Ammundsen and J. Paulsen, *Advanced Materials*, 2001, **13**, 943-+.
223. W. Li, H. Y. Asl, Q. Xie and A. Manthiram, *Journal of the American Chemical Society*, 2019, **141**, 5097-5101.
224. Z.-Y. Li, H. Guo, X. Ma, K. Sun, D. Chen, L. He and S. Han, *The Journal of Physical Chemistry C*, 2019, **123**, 19298-19306.
225. Y.-M. Jiang, K.-X. Wang, X.-Y. Wu, H.-J. Zhang, B. M. Bartlett and J.-S. Chen, *ACS Applied Materials & Interfaces*, 2014, **6**, 19791-19796.
226. M. M. Thackeray, S. H. Kang, C. S. Johnson, J. T. Vaughey, R. Benedek and S. A. Hackney, *Journal of Materials Chemistry*, 2007, **17**, 3112-3125.
227. P. Oh, M. Ko, S. Myeong, Y. Kim and J. Cho, *Advanced Energy Materials*, 2014, **4**.
228. L. L. Ma, L. Mao, X. F. Zhao, J. H. Lu, F. Zhang, P. C. Ding, L. F. Chen and F. Lian, *Chemelectrochem*, 2017, **4**, 3068-3074.
229. A. R. Armstrong, M. Holzapfel, P. Novak, C. S. Johnson, S. H. Kang, M. M. Thackeray and P. G. Bruce, *Journal of the American Chemical Society*, 2006, **128**, 8694-8698.
230. B. Xu, C. R. Fell, M. Chi and Y. S. Meng, *Energy & Environmental Science*, 2011, **4**, 2223-2233.
231. M. T. Paques-Ledent and P. Tarte, *Spectrochimica Acta Part A: Molecular Spectroscopy*, 1974, **30**, 673-689.
232. A. K. Padhi, K. S. Nanjundaswamy and J. B. Goodenough, *Journal of The Electrochemical Society*, 1997, **144**, 1188.
233. J.-Z. Wang, S.-L. Chou, J. Chen, S.-Y. Chew, G.-X. Wang, K. Konstantinov, J. Wu, S.-X. Dou and H. K. Liu, *Electrochemistry Communications*, 2008, **10**, 1781-1784.
234. Y. Jiang, S. Liao, Z. Liu, G. Xiao, Q. Liu and H. Song, *Journal of Materials Chemistry A*, 2013, **1**, 4546-4551.
235. Y. Guan, J. Shen, X. Wei, Q. Zhu, X. Zheng, S. Zhou and B. Xu, *Applied Surface Science*, 2019, **481**, 1459-1465.
236. J. Oh, J. Lee, T. Hwang, J. M. Kim, K.-d. Seoung and Y. Piao, *Electrochimica Acta*, 2017, **231**, 85-93.
237. M. S. Islam, D. J. Driscoll, C. A. J. Fisher and P. R. Slater, *Chemistry of Materials*, 2005, **17**, 5085-5092.
238. N. N. Bramnik, K. Nikolowski, C. Baehtz, K. G. Bramnik and H. Ehrenberg, *Chemistry of Materials*, 2007, **19**, 908-915.
239. T. Shiratsuchi, S. Okada, T. Doi and J.-i. Yamaki, *Electrochimica Acta*, 2009, **54**, 3145-3151.
240. X. Li, F. Jiang, K. Qu, Y. Wang, Y. Pan, M. Wang, Y. Liu, H. Xu, J. Chen, Y. Huang, J. Zheng, P. Gao, M. Chen, J. Li, Y. Peng and D. Mitlin, *The Journal of Physical Chemistry Letters*, 2020, **11**, 4608-4617.

241. H. Tian, X. Zhao, J. Zhang, M. Li and H. Lu, *ACS Applied Energy Materials*, 2018, **1**, 3497-3504.
242. H. Matsui, T. Nakamura, Y. Kobayashi, M. Tabuchi and Y. Yamada, *Journal of Power Sources*, 2010, **195**, 6879-6883.
243. Z. Guo, D. Zhang, H. Qiu, T. Zhang, Q. Fu, L. Zhang, X. Yan, X. Meng, G. Chen, and Y. Wei, *ACS Applied Materials & Interfaces*, 2015, **7**, 13972-13979.
244. M. Ati, M. Sathiya, S. Boulineau, M. Reynaud, A. Abakumov, G. Rousse, B. Melot, G. Van Tendeloo and J.-M. Tarascon, *Journal of the American Chemical Society*, 2012, **134**, 18380-18387.
245. G. Rousse and J. M. Tarascon, *Chemistry of Materials*, 2014, **26**, 394-406.
246. J. Wu, Y. Xu, Y. Chen, L. Li, H. Wang and J. Zhao, *Journal of Power Sources*, 2018, **401**, 142-148.
247. J. Wu, Y. Xu, X. Sun, C. Wang, B. Zhang and J. Zhao, *Journal of Power Sources*, 2018, **396**, 155-163.
248. N. R. Khasanova, A. N. Gavrilov, E. V. Antipov, K. G. Bramnik and H. Hibst, *Journal of Power Sources*, 2011, **196**, 355-360.
249. K. R. Stroukoff and A. Manthiram, *Journal of Materials Chemistry*, 2011, **21**, 10165-10170.
250. S. P. Ong, A. Jain, G. Hautier, B. Kang and G. Ceder, *Electrochemistry Communications*, 2010, **12**, 427-430.
251. M. E. Arroyo-de Dompablo, M. Armand, J. M. Tarascon and U. Amador, *Electrochemistry Communications*, 2006, **8**, 1292-1298.
252. C. Lyness, B. Delobel, A. R. Armstrong and P. G. Bruce, *Chemical Communications*, 2007, DOI: 10.1039/B711552K, 4890-4892.
253. L.-L. Zhang, S. Duan, X.-L. Yang, G. Peng, G. Liang, Y.-H. Huang, Y. Jiang, S.-B. Ni and M. Li, *ACS Applied Materials & Interfaces*, 2013, **5**, 12304-12309.
254. A. Kokalj, R. Dominko, G. Mali, A. Meden, M. Gaberscek and J. Jamnik, *Chemistry of Materials*, 2007, **19**, 3633-3640.
255. R. Dominko, M. Bele, M. Gaberšček, A. Meden, M. Remškar, and J. Jamnik, *Electrochemistry Communications*, 2006, **8**, 217-222.
256. A.-H. Marincaş, F. Goga, S.-A. Dorneanu and P. Ilea, *Journal of Solid State Electrochemistry*, 2020, **24**, 473-497.
257. P. Selinis and F. Farmakis, *Journal of the Electrochemical Society*, 2022, **169**.
258. A. B. Haruna, D. H. Barrett, C. B. Rodella, R. M. Erasmus, A. M. Venter, Z. N. Sentsho and K. I. Ozoemena, *Electrochimica Acta*, 2022, **426**.
259. Z. Zhang, T. Zeng, Y. Q. Lai, M. Jia and J. Li, *Journal of Power Sources*, 2014, **247**, 1-8.
260. M. J. Lee, S. Lee, P. Oh, Y. Kim and J. Cho, *Nano Letters*, 2014, **14**, 993-999.
261. M. Jayalakshmi, M. M. Rao and F. Scholz, *Langmuir*, 2003, **19**, 8403-8408.
262. Y. Miao, P. Hynan, A. von Jouanne and A. Yokochi, *Energies*, 2019, **12**.
263. T. C. Liu, A. Dai, J. Lu, Y. F. Yuan, Y. G. Xiao, L. Yu, M. Li, J. Gim, L. Ma, J. J. Liu, C. Zhan, L. X. Li, J. X. Zheng, Y. Ren, T. P. Wu, R. Shahbazian-Yassar, J. G. Wen, F. Pan and K. Amine, *Nature Communications*, 2019, **10**.
264. Y. M. Huang, Y. H. Dong, S. Li, J. Lee, C. Wang, Z. Zhu, W. J. Xue, Y. Li, and J. Li, *Advanced Energy Materials*, 2021, **11**.
265. M. M. Thackeray, A. Dekock, M. H. Rossouw, D. Liles, R. Bittihn and D. Hoge, *Journal of the Electrochemical Society*, 1992, **139**, 363-366.
266. Y. F. Deng, L. N. Wan, Y. Xie, X. S. Qin and G. H. Chen, *RSC Advances*, 2014, **4**, 23914-23935.
267. M. Jeong, M. J. Lee, J. Cho and S. Lee, *Advanced Energy Materials*, 2015, **5**.
268. K. Schroder, J. Alvarado, T. A. Yersak, J. Li, N. Dudney, L. J. Webb, Y. S. Meng and K. J. Stevenson, *Chemistry of Materials*, 2015, **27**, 5531-5542.
269. K. Xu, *Nature Energy*, 2021, **6**, 763-763.
270. K. Xu, *Chemical Reviews*, 2004, **104**, 4303-4418.
271. B. Flamme, G. Rodriguez Garcia, M. Weil, M. Haddad, P. Phansavath, V. Ratovelomanana-Vidal and A. Chagnes, *Green Chemistry*, 2017, **19**, 1828-1849.
272. E. Perricone, M. Chamas, J. C. Leprêtre, P. Judeinstein, P. Azais, E. Raymundo-Pinero, F. Béguin and F. Alloin, *Journal of Power Sources*, 2013, **239**, 217-224.

273. A. Abouimrane, I. Belharouak and K. Amine, *Electrochemistry Communications*, 2009, **11**, 1073-1076.
274. H. Dietz, G. Hoogestraat, S. Laibach, D. von Borstel and K. Wiesener, *Journal of Power Sources*, 1995, **53**, 359-365.
275. P. Ruetschi, *Journal of Power Sources*, 2004, **127**, 33-44.
276. Y. G. Wang, J. Yi, and Y. Y. Xia, *Advanced Energy Materials*, 2012, **2**, 830-840.
277. C. D. Wessells, S. V. Peddada, R. A. Huggins and Y. Cui, *Nano Letters*, 2011, **11**, 5421-5425.
278. F. Wang, O. Borodin, T. Gao, X. Fan, W. Sun, F. Han, A. Faraone, J. A. Dura, K. Xu and C. Wang, *Nature Materials*, 2018, **17**, 543-549.
279. D. W. Su, A. McDonagh, S. Z. Qiao and G. X. Wang, *Advanced Materials*, 2017, **29**.
280. N. Alias and A. A. Mohamad, *Journal of Power Sources*, 2015, **274**, 237-251.
281. A. Eftekhari, *Advanced Energy Materials*, 2018, **8**.
282. X. W. Yu, Z. H. Bi, F. Zhao and A. Manthiram, *Advanced Energy Materials*, 2016, **6**.
283. F. Ding, W. Xu, G. L. Graff, J. Zhang, M. L. Sushko, X. Chen, Y. Shao, M. H. Engelhard, Z. Nie, J. Xiao, X. Liu, P. V. Sushko, J. Liu and J.-G. Zhang, *Journal of the American Chemical Society*, 2013, **135**, 4450-4456.
284. Y. Ren, Y. Shen, Y. Lin and C.-W. Nan, *Electrochemistry Communications*, 2015, **57**, 27-30.
285. W. Zhou, S. Wang, Y. Li, S. Xin, A. Manthiram and J. B. Goodenough, *Journal of the American Chemical Society*, 2016, **138**, 9385-9388.
286. A. Manthiram, X. Yu and S. Wang, *Nature Reviews Materials*, 2017, **2**, 16103.
287. H. Zhang, C. Li, M. Piszcz, E. Coya, T. Rojo, L. M. Rodriguez-Martinez, M. Armand and Z. Zhou, *Chemical Society Reviews*, 2017, **46**, 797-815.
288. J. Mindemark, M. J. Lacey, T. Bowden and D. Brandell, *Progress in Polymer Science*, 2018, **81**, 114-143.
289. T. Jiang, M. J. Chollier Brym, G. Dubé, A. Lasia and G. M. Brisard, *Surface and Coatings Technology*, 2006, **201**, 1-9.
290. M.-C. Lin, M. Gong, B. Lu, Y. Wu, D.-Y. Wang, M. Guan, M. Angell, C. Chen, J. Yang, B.-J. Hwang and H. Dai, *Nature*, 2015, **520**, 324-328.
291. A. Lewandowski and A. Świderska-Mocek, *Journal of Power Sources*, 2007, **171**, 938-943.
292. H. Sakaebe and H. Matsumoto, *Electrochemistry Communications*, 2003, **5**, 594-598.
293. C. Xu, S. M. Zhao, Y. Q. Du, W. Y. Zhang, P. Li, H. X. Jin, Y. J. Zhang, Z. H. Wang and J. X. Zhang, *Chemelectrochem*, 2019, **6**, 3350-3354.
294. H. Sun, W. Wang, Z. Yu, Y. Yuan, S. Wang and S. Jiao, *Chemical Communications*, 2015, **51**, 11892-11895.
295. C. Chiappe and D. Pieraccini, *Journal of Physical Organic Chemistry*, 2005, **18**, 275-297.
296. G. B. Appetecchi, M. Montanino and S. Passerini, in *Ionic Liquids: Science and Applications*, American Chemical Society, 2012, vol. 1117, ch. 4, pp. 67-128.
297. P. Zhu, D. Gastol, J. Marshall, R. Sommerville, V. Goodship and E. Kendrick, *Journal of Power Sources*, 2021, **485**, 229321.
298. A. Jossen, *Journal of Power Sources*, 2006, **154**, 530-538.
299. T. Liu, X. Li, S. Sun, X. Sun, F. Cao, T. Ohsaka and J. Wu, *Electrochimica Acta*, 2018, **269**, 422-428.
300. J. Entwistle, R. Ge, K. Pardikar, R. Smith and D. Cumming, *Renewable and Sustainable Energy Reviews*, 2022, **166**, 112624.
301. K. Wang, Y. Wu, S. Luo, X. He, J. Wang, K. Jiang and S. Fan, *Journal of Power Sources*, 2013, **233**, 209-215.
302. J. Wang, Z. Shen and M. Yi, *Carbon*, 2019, **153**, 156-163.
303. J. Wang, Y. Yamada, K. Sodeyama, C. H. Chiang, Y. Tateyama and A. Yamada, *Nature Communications*, 2016, **7**, 12032.
304. T. A. Assefa, A. F. Suzana, L. Wu, R. J. Koch, L. Li, W. Cha, R. J. Harder, E. S. Bozin, F. Wang and I. K. Robinson, *ACS Applied Energy Materials*, 2021, **4**, 111-118.
305. D. Muñoz-Torrero, M. Anderson, J. Palma, R. Marcilla and E. Ventosa, *Chemelectrochem*, 2019, **6**, 2766-2770.

306. K. Wang, S. Luo, Y. Wu, X. F. He, F. Zhao, J. P. Wang, K. L. Jiang, and S. S. Fan, *Advanced Functional Materials*, 2013, **23**, 846-853.
307. J. Guo and C. Wang, *Chemical Communications*, 2010, **46**, 1428-1430.
308. D. P. Wong, R. Suriyaprabha, R. Yuvakumar, V. Rajendran, Y.-T. Chen, B.-J. Hwang, L.-C. Chen and K.-H. Chen, *Journal of Materials Chemistry A*, 2014, **2**, 13437-13441.
309. H. Wang, Y. Bai, S. Chen, X. Luo, C. Wu, F. Wu, J. Lu, and K. Amine, *ACS Applied Materials & Interfaces*, 2015, **7**, 80-84.
310. D. Leanza, C. A. F. Vaz, P. Novák and M. El Kazzi, *Helvetica Chimica Acta*, 2021, **104**.
311. J. Pan, Y.-T. Cheng and Y. Qi, *Physical Review B*, 2015, **91**, 134116.
312. R. Wang, L. Feng, W. Yang, Y. Zhang, Y. Zhang, W. Bai, B. Liu, W. Zhang, Y. Chuan, Z. Zheng, and H. Guan, *Nanoscale Research Letters*, 2017, **12**, 575.
313. M. C. Rehwoldt, Y. Wang, F. Xu, P. Ghildiyal and M. R. Zachariah, *ACS Applied Materials & Interfaces*, 2022, **14**, 8938-8946.
314. S. Mishra, L. Unnikrishnan, S. K. Nayak and S. Mohanty, *Macromolecular Materials and Engineering*, 2019, **304**.
315. E. Markevich, G. Salitra and D. Aurbach, *Electrochemistry Communications*, 2005, **7**, 1298-1304.
316. S. Behera, S. Ippili, V. Jella, N. Y. Kim, S. C. Jang, J. W. Jung, S. G. Yoon and H. S. Kim, *Energy & Environmental Materials*, 2024, DOI: 10.1002/eem2.12734.
317. B. Balli, A. Şavk and F. Şen, in *Nanocarbon and its Composites*, eds. A. Khan, M. Jawaid, Inamuddin and A. M. Asiri, Woodhead Publishing, 2019, DOI: https://doi.org/10.1016/B978-0-08-102509-3.00005-5, pp. 123-151.
318. W. B. Huang, W. Wang, Y. Wang, Q. T. Qu, C. C. Jin and H. H. Zheng, *Journal of Materials Chemistry A*, 2021, **9**, 1541-1551.
319. B. B. Damdinov, V. A. Danilova, A. V. Minakov and M. I. Pryazhnikov, *Journal of Siberian Federal University-Mathematics & Physics*, 2021, **14**, 265-272.
320. S. S. Zhang, *Journal of Power Sources*, 2007, **164**, 351-364.
321. J. P. Serra, J. Uranga, R. Gonçalves, C. M. Costa, K. de la Caba, P. Guerrero and S. Lanceros-Mendez, *Electrochimica Acta*, 2023, **462**, 142746.
322. Y. Song, L. Sheng, L. Wang, H. Xu and X. He, *Electrochemistry Communications*, 2021, **124**, 106948.
323. J. Sheng, S. Tong, Z. He and R. Yang, *Cellulose*, 2017, **24**, 4103-4122.
324. Z. Cai, Y. Ma, X. Huang, X. Yan, Z. Yu, S. Zhang, G. Song, Y. Xu, C. Wen and W. Yang, *Journal of Energy Storage*, 2020, **27**, 101036.
325. F. Liu and X. Chuan, *RSC Advances*, 2021, **11**, 16633-16644.
326. M. F. Lagadec, R. Zahn and V. Wood, *Nature Energy*, 2019, **4**, 16-25.
327. L. Zhang, X. Hu, Z. Wang, F. Sun and D. G. Dorrell, *Renewable and Sustainable Energy Reviews*, 2018, **81**, 1868-1878.
328. N. Devillers, S. Jemei, M.-C. Péra, D. Bienaimé and F. Gustin, *Journal of Power Sources*, 2014, **246**, 596-608.
329. Z. S. Iro, C. Subramani and S. S. Dash, *International Journal of Electrochemical Science*, 2016, **11**, 10628-10643.
330. Poonam, K. Sharma, A. Arora and S. K. Tripathi, *Journal of Energy Storage*, 2019, **21**, 801-825.
331. D. Ruan, Y. Huang, L. Li, J. Yuan and Z. Qiao, *Journal of Alloys and Compounds*, 2017, **695**, 1685-1690.
332. W. Raza, F. Ali, N. Raza, Y. Luo, K.-H. Kim, J. Yang, S. Kumar, A. Mehmood and E. E. Kwon, *Nano Energy*, 2018, **52**, 441-473.
333. S. Karthikeyan, B. Narenthiran, A. Sivanantham, L. D. Bhatlu and T. Maridurai, *Materials Today: Proceedings*, 2021, **46**, 3984-3988.
334. Y. Xu, W. Lu, G. Xu and T.-W. Chou, *Composites Science and Technology*, 2021, **204**, 108636.
335. R. Drummond, C. Huang, P. S. Grant and S. R. Duncan, *Journal of Power Sources*, 2019, **433**, 126579.
336. D. Chen, Q. Wang, R. Wang and G. Shen, *Journal of Materials Chemistry A*, 2015, **3**, 10158-10173.

337. F. Béguin, V. Presser, A. Balducci and E. Frackowiak, *Advanced Materials*, 2014, **26**, 2219-2251.
338. Y. Shao, M. F. El-Kady, J. Sun, Y. Li, Q. Zhang, M. Zhu, H. Wang, B. Dunn and R. B. Kaner, *Chemical Reviews*, 2018, **118**, 9233-9280.
339. L. Kouchachvili, W. Yaïci and E. Entchev, *Journal of Power Sources*, 2018, **374**, 237-248.
340. H. A. Catherino, J. F. Burgel, P. L. Shi, A. Rusek and X. Zou, *Journal of Power Sources*, 2006, **162**, 965-970.
341. H. S. Choi, J. H. Im, T. Kim, J. H. Park and C. R. Park, *Journal of Materials Chemistry*, 2012, **22**, 16986-16993.
342. X. Z. Sun, X. Zhang, B. Huang and Y. W. Ma, *Acta Physico-Chimica Sinica*, 2014, **30**, 485-491.
343. W. H. Zuo, R. Z. Li, C. Zhou, Y. Y. Li, J. L. Xia and J. P. Liu, *Advanced Science*, 2017, **4**.
344. M. Hagen, J. Yan, W. J. Cao, X. J. Chen, A. Shellikeri, T. Du, J. A. Read, T. R. Jow and J. P. Zheng, *Journal of Power Sources*, 2019, **433**, 126689.
345. L. Chen, X. Zheng, C. Hao, Y. Wei, J. Cheng, H. Zhang, J. Wu, P. Si and L. Ci, *Journal of Alloys and Compounds*, 2021, **877**, 160273.
346. M. B. Ahsan, S. Mekhilef, T. K. Soon, M. B. Mubin, P. Shrivastava and M. Seyedmahmoudian, *International Journal of Energy Research*, 2022, **46**, 19826-19854.
347. S. R. Sivakkumar and A. G. Pandolfo, *Electrochimica Acta*, 2012, **65**, 280-287.
348. N. Omar, M. Daowd, O. Hegazy, M. Al Sakka, T. Coosemans, P. Van den Bossche and J. Van Mierlo, *Electrochimica Acta*, 2012, **86**, 305-315.
349. M. Zeiger, N. Jäckel, V. N. Mochalin and V. Presser, *Journal of Materials Chemistry A*, 2016, **4**, 3172-3196.
350. E. Zhao, C. Qin, H.-R. Jung, G. Berdichevsky, A. Nese, S. Marder and G. Yushin, *ACS Nano*, 2016, **10**, 3977-3984.
351. M. Widmaier, K. Pfeifer, L. Bommer and V. Presser, *Batteries & Supercaps*, 2018, **1**, 11-26.
352. X. Meng, J. Liu, X. Li, M. N. Banis, J. Yang, R. Li and X. Sun, *RSC Advances*, 2013, **3**, 7285-7288.
353. J. Shu, L. Hou, R. Ma, M. Shui, L. Shao, D. Wang, Y. Ren and W. Zheng, *RSC Advances*, 2012, **2**, 10306-10309.
354. J.-H. Choi, W.-H. Ryu, K. Park, J.-D. Jo, S.-M. Jo, D.-S. Lim and I.-D. Kim, *Scientific Reports*, 2014, **4**, 7334.
355. S. Goriparti, E. Miele, F. De Angelis, E. Di Fabrizio, R. Proietti Zaccaria and C. Capiglia, *Journal of Power Sources*, 2014, **257**, 421-443.
356. K. Naoi, *Fuel Cells*, 2010, **10**, 825-833.
357. K. Naoi, W. Naoi, S. Aoyagi, J.-i. Miyamoto and T. Kamino, *Accounts of Chemical Research*, 2013, **46**, 1075-1083.
358. M. Secchiaroli, R. Marassi, M. Wohlfahrt-Mehrens and S. Dsoke, *Electrochimica Acta*, 2016, **219**, 425-434.
359. B. Wang, Q. Wang, B. Xu, T. Liu, D. Wang and G. Zhao, *RSC Advances*, 2013, **3**, 20024-20033.
360. N. Böckenfeld, R. S. Kühnel, S. Passerini, M. Winter and A. Balducci, *Journal of Power Sources*, 2011, **196**, 4136-4142.
361. N. Böckenfeld, T. Placke, M. Winter, S. Passerini and A. Balducci, *Electrochimica Acta*, 2012, **76**, 130-136.
362. G. A. dos Santos Junior, V. D. S. Fortunato, G. A. A. Bastos, G. G. Silva, P. F. R. Ortega and R. L. Lavall, *ACS Applied Energy Materials*, 2020, **3**, 9028-9039.
363. A. Shellikeri, S. Yturriaga, J. S. Zheng, W. Cao, M. Hagen, J. A. Read, T. R. Jow and J. P. Zheng, *Journal of Power Sources*, 2018, **392**, 285-295.
364. Y. Wang, L. Wang, M. Li and Z. Chen, *eTransportation*, 2020, **4**, 100064.
365. H. Shim, O. Budak, V. Haug, M. Widmaier and V. Presser, *Electrochimica Acta*, 2020, **337**.
366. W. Jin, G. Song, J. K. Yoo, S. K. Jung, T. H. Kim and J. Kim, *Chemelectrochem*, 2024, DOI: 10.1002/celc.202400288.
367. Y. Zhang, S. Lu, F. Lou and Z. Yu, *Electrochimica Acta*, 2023, **456**, 142469.
368. Y. Zhang, S. Lu, Z. Wang, V. Volkov, F. Lou and Z. Yu, *Renewable and Sustainable Energy Reviews*, 2023, **183**, 113515.
369. Y. Lu, C.-Z. Zhao, H. Yuan, J.-K. Hu, J.-Q. Huang and Q. Zhang, *Matter*, 2022, **5**, 876-898.

370. K. Astafyeva, C. Dousset, Y. Bureau, S. L. Stalmach and D. B. Dufour, *Batteries & Supercaps*, 2020, **3**, 341-343.
371. M. E. Sotomayor, C. d. l. Torre-Gamarra, B. Levenfeld, J.-Y. Sanchez, A. Varez, G.-T. Kim, A. Varzi and S. Passerini, *Journal of Power Sources*, 2019, **437**, 226923.
372. S. El Khakani, N. Verdier, D. Lepage, A. Prébé, D. Aymé-Perrot, D. Rochefort and M. Dollé, *Journal of Power Sources*, 2020, **454**, 227884.
373. L. Helmers, L. Froböse, K. Friedrich, M. Steffens, D. Kern, P. Michalowski and A. Kwade, *Energy Technology*, 2021, **9**.
374. D. W. Park, N. A. Canas, N. Wagner and K. A. Friedrich, *Journal of Power Sources*, 2016, **306**, 758-763.
375. Z. H. Zhang, L. P. Wu, D. Zhou, W. Weng and X. Y. Yao, *Nano Letters*, 2021, **21**, 5233-5239.
376. T. Kawaguchi, H. Nakamura and S. Watano, *Powder Technology*, 2017, **305**, 241-249.
377. W. Bauer, D. Nötzel, V. Wenzel and H. Nirschl, *Journal of Power Sources*, 2015, **288**, 359-367.
378. H. Zhou, M. Liu, H. Gao, D. Hou, C. Yu, C. Liu, D. Zhang, J.-c. Wu, J. Yang and D. Chen, *Journal of Power Sources*, 2020, **473**, 228553.
379. G. Li, R. Xue and L. Chen, *Solid State Ionics*, 1996, **90**, 221-225.
380. C. Wang, R. Yu, H. Duan, Q. Lu, Q. Li, K. R. Adair, D. Bao, Y. Liu, R. Yang, J. Wang, S. Zhao, H. Huang and X. Sun, *ACS Energy Letters*, 2022, **7**, 410-416.
381. G.-T. Kim, G. B. Appetecchi, F. Alessandrini and S. Passerini, *Journal of Power Sources*, 2007, **171**, 861-869.
382. S. Boulineau, J.-M. Tarascon, J.-B. Leriche and V. Viallet, *Solid State Ionics*, 2013, **242**, 45-48.
383. S. Yubuchi, W. Nakamura, T. Bibienne, S. Rousselot, L. W. Taylor, M. Pasquali, M. Dollé, A. Sakuda, A. Hayashi and M. Tatsumisago, *Journal of Power Sources*, 2019, **417**, 125-131.
384. X. Han, Z. Yang, B. Zhao, S. Zhu, L. Zhou, J. Dai, J.-W. Kim, B. Liu, J. W. Connell, T. Li, B. Yang, Y. Lin and L. Hu, *ACS Nano*, 2017, **11**, 3189-3197.
385. D. J. Kirsch, S. D. Lacey, Y. Kuang, G. Pastel, H. Xie, J. W. Connell, Y. Lin and L. Hu, *ACS Applied Energy Materials*, 2019, **2**, 2990-2997.
386. K. Kwon, J. Kim, S. Han, J. Lee, H. Lee, J. Kwon, J. Lee, J. Seo, P. J. Kim, T. Song and J. Choi, *Small Science*, 2024, **4**.
387. W. B. Hawley and J. Li, *Journal of Energy Storage*, 2019, **25**, 100862.
388. A. L. Phan, C. Jayawardana, P. M. L. Le, J. X. Zhang, B. Nan, W. R. Zhang, B. L. Lucht, S. Y. Hou and C. S. Wang, *Advanced Functional Materials*, 2023, **33**.
389. K. Y. Wang, Y. L. Wu, C. Yang, M. S. Yu, C. Lei, Y. C. Zhang, T. Z. Ding, Y. Z. Long, K. Liu, M. C. Li and H. Wu, *Advanced Energy Materials*, 2024, DOI: 10.1002/aenm.202400589.
390. A. Gyulai, W. Bauer and H. Ehrenberg, *Acs Applied Energy Materials*, 2023, **6**, 5122-5134.
391. Y. Nikodimos, M. Ihrig, B. W. Taklu, W.-N. Su and B. J. Hwang, *Energy Storage Materials*, 2023, **63**, 103030.
392. Y. T. Liu, X. T. Gong, C. Podder, F. Wang, Z. Y. Li, J. Z. Liu, J. Z. Fu, X. T. Ma, P. Vanaphuti, R. Wang, A. Hitt, Y. Savsatli, Z. Z. Yang, M. Y. Ge, W. K. Lee, B. Yonemoto, M. Tang, H. Pan and Y. Wang, *Joule*, 2023, **7**.
393. R. M. Tao, B. Steinhoff, X. G. Sun, K. Sardo, B. Skelly, H. I. I. I. Meyer, C. Sawicki, G. Polizos, X. Lyu, Z. J. Du, J. Yang, K. L. Hong and J. L. Li, *Chemical Engineering Journal*, 2023, **471**.
394. B. Paredes-Goyes, F. M. Zanotto, V. Boudeville, S. Grugeon, L. Dupont and A. A. Franco, *Batteries & Supercaps*, 2024, **7**.
395. E. Ayerbe, M. Berecibar, S. Clark, A. A. Franco and J. Ruhland, *Advanced Energy Materials*, 2022, **12**.
396. P. Mayer, M. Oberle and S. Gärtner, in *Handbook on Smart Battery Cell Manufacturing*, WORLD SCIENTIFIC, 2021, DOI: doi:10.1142/9789811245626_0014
10.1142/9789811245626_0014, pp. 275-300.
397. Q. S. Wang, L. Velasco, B. Breitung and V. Presser, *Advanced Energy Materials*, 2021, **11**.
398. P. K. Dammala, K. B. Dermenci, A. R. Kathribail, P. Yadav, J. Van Mierlo and M. Berecibar, *Journal of Energy Storage*, 2023, **74**, 109209.

399. S. Singh, C. Schneider and S. Baazouzi, in *Handbook on Smart Battery Cell Manufacturing*, WORLD SCIENTIFIC, 2021, DOI: doi:10.1142/9789811245626_0017
10.1142/9789811245626_0017, pp. 337-345.
400. S. Haghi, A. Summer, P. Bauerschmidt and R. Daub, *Energy Technology*, 2022, **10**.
401. J. Wessel, A. Schoo, A. Kwade and C. Herrmann, *Energy Technology*, 2023, **11**.
402. R. Y. Zhong, X. Xu, E. Klotz and S. T. Newman, *Engineering*, 2017, **3**, 616-630.
403. A. C. Ngandjong, T. Lombardo, E. N. Primo, M. Chouchane, A. Shodiev, O. Arcelus and A. A. Franco, *Journal of Power Sources*, 2021, **485**, 229320.
404. L. Dong, H. Kumar, B. Anasori, Y. Gogotsi and V. B. Shenoy, *The Journal of Physical Chemistry Letters*, 2017, **8**, 422-428.
405. A. A. Franco, A. Rucci, D. Brandell, C. Frayret, M. Gaberscek, P. Jankowski and P. Johansson, *Chemical Reviews*, 2019, **119**, 4569-4627.
406. M. Fichtner, K. Edström, E. Ayerbe, M. Berecibar, A. Bhowmik, I. E. Castelli, S. Clark, R. Dominko, M. Erakca, A. A. Franco, A. Grimaud, B. Horstmann, A. Latz, H. Lorrmann, M. Meeus, R. Narayan, F. Pammer, J. Ruhland, H. Stein, T. Vegge and M. Weil, *Advanced Energy Materials*, 2022, **12**.
407. M. Perno, L. Hvam and A. Haug, *Computers in Industry*, 2022, **134**, 103558.
408. F. Tao and Q. L. Qi, *Nature*, 2019, **573**, 490-491.
409. Y. Wang, R. Xu, C. Zhou, X. Kang and Z. Chen, *Journal of Manufacturing Systems*, 2022, **62**, 124-134.
410. X. V. Wang and L. H. Wang, *International Journal of Production Research*, 2019, **57**, 3892-3902.
411. A. Angrish, B. Starly, Y.-S. Lee and P. H. Cohen, *Journal of Manufacturing Systems*, 2017, **45**, 236-247.
412. S. M. Bazaz, M. Lohtander and J. Varis, *Procedia Manufacturing*, 2019, **38**, 1705-1712.
413. F. Gregori, A. Papetti, M. Pandolfi, M. Peruzzini and M. Germani, *Procedia CIRP*, 2017, **63**, 436-442.
414. A. Kwade, W. Haselrieder, R. Leithoff, A. Modlinger, F. Dietrich and K. Droeder, *Nature Energy*, 2018, **3**, 290-300.
415. P. Zheng, H. wang, Z. Sang, R. Y. Zhong, Y. Liu, C. Liu, K. Mubarok, S. Yu and X. Xu, *Frontiers of Mechanical Engineering*, 2018, **13**, 137-150.
416. S. Haghi, M. Leeb, A. Molzberger and R. Daub, *Energy Technology*, 2023, **11**.
417. J. Huang, L. Albero Blanquer, J. Bonefacino, E. R. Logan, D. Alves Dalla Corte, C. Delacourt, B. M. Gallant, S. T. Boles, J. R. Dahn, H.-Y. Tam and J.-M. Tarascon, *Nature Energy*, 2020, **5**, 674-683.
418. A. J. Ilott, M. Mohammadi, H. J. Chang, C. P. Grey and A. Jerschow, *Proceedings of the National Academy of Sciences of the United States of America*, 2016, **113**, 10779-10784.
419. J. M. Griffin, A. C. Forse, W.-Y. Tsai, P.-L. Taberna, P. Simon and C. P. Grey, *Nature Materials*, 2015, **14**, 812-819.
420. Alexander C. Forse, John M. Griffin, C. Merlet, J. Carretero-Gonzalez, A.-Rahman O. Raji, Nicole M. Trease and Clare P. Grey, *Nature Energy*, 2017, **2**, 16216.
421. S. H. Kim, K. H. Lee, B. S. Seong, G.-H. Kim, J. S. Kim and Y. S. Yoon, *Korean Journal of Chemical Engineering*, 2006, **23**, 961-964.
422. A. S. Prakash, P. Manikandan, K. Ramesha, M. Sathiya, J. M. Tarascon and A. K. Shukla, *Chemistry of Materials*, 2010, **22**, 2857-2863.
423. B. Vikram Babu, K. Vijaya Babu, G. Tewodros Aregai, L. Seeta Devi, B. Madhavi Latha, M. Sushma Reddi, K. Samatha and V. Veeraiah, *Results in Physics*, 2018, **9**, 284-289.
424. I. A. Leonidov, O. N. Leonidova, L. A. Perelyaeva, R. F. Samigullina, S. A. Kovyazina and M. V. Patrakeev, *Physics of the Solid State*, 2003, **45**, 2183-2188.
425. D. V. Pelegov, A. A. Koshkina, B. N. Slautin and V. S. Gorshkov, *Journal of Raman Spectroscopy*, 2019, **50**, 1015-1026.
426. J. R. Dahn, A. K. Sleigh, H. Shi, J. N. Reimers, Q. Zhong and B. M. Way, *Electrochimica Acta*, 1993, **38**, 1179-1191.
427. A. C. Ferrari and J. Robertson, *Physical Review B*, 2000, **61**, 14095-14107.

428. A. Laheäär, P. Przygocki, Q. Abbas and F. Béguin, *Electrochemistry Communications*, 2015, **60**, 21-25.
429. P. Srimuk, F. Kaasik, B. Krüner, A. Tolosa, S. Fleischmann, N. Jäckel, M. C. Tekeli, M. Aslan, M. E. Suss and V. Presser, *Journal of Materials Chemistry A*, 2016, **4**, 18265-18271.
430. H. Liu, X. Cheng, Y. Chong, H. Yuan, J.-Q. Huang and Q. Zhang, *Particuology*, 2021, **57**, 56-71.
431. L. Tian and A. Yuan, *Journal of Power Sources*, 2009, **192**, 693-697.
432. J. Akimoto, Y. Takahashi, Y. Gotoh and S. Mizuta, *Chemistry of Materials*, 2000, **12**, 3246-3248.
433. J. Abou-Rjeily, I. Bezza, N. A. Laziz, C. Autret-Lambert, M. T. Sougrati and F. Ghamouss, *Energy Storage Materials*, 2020, **26**, 423-432.
434. P. R. Ilango, K. Prasanna, S. J. Do, Y. N. Jo and C. W. Lee, *Scientific Reports*, 2016, **6**, 29826.
435. A. Paolone, A. Sacchetti, P. Postorino and R. Cantelli, *The Journal of Physical Chemistry B*, 2005, **109**, 7587-7588.
436. C. M. Julien, F. Gendron, A. Amdouni and M. Massot, *Materials Science and Engineering: B*, 2006, **130**, 41-48.
437. M. A. Camacho-Lopez, L. Escobar-Alarcon, E. Haro-Ponlatowski and C. Julien, *MRS Online Proceedings Library*, 2011, **617**, 317.
438. N. Kuwata, Y. Matsuda, T. Okawa, G. Hasegawa, O. Kamishima and J. Kawamura, *Solid State Ionics*, 2022, **380**, 115925.
439. D. Kim, S. Park, O. B. Chae, J. H. Ryu, Y. U. Kim, R. Z. Yin and S. M. Oh, *Journal of the Electrochemical Society*, 2012, **159**, A193-A197.
440. T. Aoshima, K. Okahara, C. Kiyohara and K. Shizuka, *Journal of Power Sources*, 2001, **97-98**, 377-380.
441. O. E. Eleri, K. U. Azuatalam, M. W. Minde, A. M. Trindade, N. Muthuswamy, F. Lou and Z. Yu, *Electrochimica Acta*, 2020, **362**, 137152.

11. ABBREVIATIONS

11.1. Abbreviations

CE	**Coulombic efficiency**
CMC	**carboxymethyl cellulose**
CV	**cyclic voltammetry**
DEC	**diethyl carbonate**
DMC	**dimethyl carbonate**
DMSO	**dimethyl sulfoxide**
EC	**ethylene carbonate**
EES	**electrochemical energy storage**
EMC	**ethyl methyl carbonate**
ESR	**equivalent series resistance**
GCPL	**galvanostatic cycling with potential limitation**
LFP	**lithium iron phosphate**
LIB	**lithium-ion battery**
LMO	**lithium manganese oxide**
LTO	**lithium titan oxide**
NMC	**lithium nickel manganese cobalt oxide**
OLC	**onion-like carbon**
PC	**propylene carbonate**
PE	**polyethylene**
PP	**polypropylene**
PVdF	**polyvinylidene fluoride**
SEI	**solid electrolyte Interphase**
SEM	**scanning electron microscopy**
SHE	**standard hydrogen electrode**
VC	**vinylene carbonate**
XRD	**X-ray diffraction**

11.2. Symbols and constants

%	percent
°C	degree Celsius
A	Ampere
A g^{-1}	Ampere per gram
C	C-rate
cm^2	square centimeter
Eo	redox potential
F	Farad
F	Faraday constant
g	gram
h	hours
I	electric current
kt	kiloton
M	molar
M	molar mass
m	mass
m^2 g^{-1}	square meter per gram
mAh g^{-1}	milli-ampere-hour per gram
min	minutes
mm	millimeter
n	amount of substance (mol)
NA	Avogadro constant
nm	nanometer
Q	charge
t	time
TWh	terawatt hour
U	Voltage in volt
V	Volt
Wh g^{-1}	Watt-hour per gram
µm	micrometers

12. LIST OF PUBLICATIONS

12.1. Optimized preparation and potential range for spinel lithium titanate anode for high-rate performance lithium-ion batteries

Authors: Amir Haghipour, Stefanie Arnold, Jonas Oehm, Dominik Schmidt, Lola Gonzalez-Garcia, Hitoshi Nakamura, Tobias Kraus, Volker Knoblauch, Volker Press

Publication date: 24 October 2024

Journal: Advanced Energy and Sustainability Research

https://doi.org/10.1002/aesr.202400239

12.2. Developing an ontology on battery production and characterization with the help of key use cases from battery research

Authors: Vincent Nebel,* Lisa Beran, Veit Königer, Amir Haghipour, Marcel Mutz, Andriy Taranovskyy, Dirk Werth, Volker Knoblauch, Tobias Kraus.

Publication date: 19 November 2024

Journal: Advanced Engineering Materials

https://doi.org/10.1002/adem.202401540

12.3. On the development of a digital data management platform for battery material and processing data

Authors: Jonas Oehm, Vincent Nebel, Lisa Beran, Milena Perovic, Laura Gottschalk, Amir Haghipour, Veit Königer, Philip Gümbel, Marcel Mutz, Arno Kwade, Volker Presser, Volker Knoblauch, Tobias Kraus

2024 ECS - The Electrochemical Society

https://doi.org/10.1149/MA2024-0163084mtgabs